DISSERTATION

DESIGN OF A NONHYDROSTATIC ATMOSPHERIC MODEL BASED ON A GENERALIZED VERTICAL COORDINATE

Submitted by

Michael D. Toy

Department of Atmospheric Science

In partial fulfillment of the requirements

for the degree of Doctor of Philosophy

Colorado State University

Fort Collins, CO

Summer 2008

COLORADO STATE UNIVERSITY

July 9, 2008

WE HEREBY RECOMMEND THAT THE DISSERTATION PREPARED UNDER OUR SUPERVISION BY MICHAEL D. TOY ENTITLED DESIGN OF A NONHYDROSTATIC ATMOSPHERIC MODEL BASED ON A GENERALIZED VERTICAL COORDINATE BE ACCEPTED AS FULFILLING IN PART THE REQUIREMENTS FOR THE DEGREE OF DOCTOR OF PHILOSOPHY.

Committee on Graduate Work

_____

_____

_____

_____
Advisor

_____
Department Head

ABSTRACT OF DISSERTATION

DESIGN OF A NONHYDROSTATIC ATMOSPHERIC MODEL BASED ON A GENERALIZED VERTICAL COORDINATE

The isentropic system of equations has particular advantages in the numerical modeling of weather and climate. These include the elimination of the vertical velocity in adiabatic flow, which simplifies the motion to a two-dimensional problem and greatly reduces the numerical errors associated with vertical advection. Vertical resolution is enhanced in regions of high static stability which leads to better resolving of features such as the tropopause boundary. Also, sharp horizontal gradients of atmospheric properties found along frontal boundaries in traditional Eulerian coordinate systems are nonexistent in the isentropic coordinate framework.

The extreme isentropic overturning that can occur in fine-scale atmospheric motion presents a challenge to nonhydrostatic modeling with the isentropic vertical coordinate. This dissertation presents a new nonhydrostatic atmospheric model based on a generalized vertical coordinate. The coordinate is specified in a similar manner as Konor and Arakawa, but elements of arbitrary Eulerian-Lagrangian methods are added to provide the flexibility to maintain coordinate monotonicity in regions of negative static stability and return the coordinate levels to their isentropic targets in statically stable

regions. The model is mass-conserving and implements a vertical differencing scheme that satisfies two additional integral constraints for the limiting case of z-coordinates.

The hybrid vertical coordinate model is tested with mountain wave experiments which include a downslope windstorm with breaking gravity waves. The results show that the advantages of the isentropic coordinate are realized in the model with regards to vertical tracer and momentum transport. Also, the isentropic overturning associated with the wave breaking is successfully handled by the coordinate formulation.

Michael D. Toy
Department of Atmospheric Science
Colorado State University
Fort Collins, CO 80523
Summer 2008

ACKNOWLEDGEMENTS

I wish to express my deepest gratitude to my advisor, Dr. David Randall, for his guidance and support in this research. His encouragement through the struggle to tame the unruly coordinate surfaces in the model made this dissertation possible. I also thank my committee members, Drs. Richard Johnson, Wayne Schubert and Allan Kirkpatrick, for their interest and enthusiasm during my research.

I am fortunate to have been able to work with the wonderful group of people – students, research and administrative staff – who make up the Randall research group. I am especially grateful to Dr. Celal Konor, on whose work my research is largely based, for his encouragement and the many hours of consultation he provided me along the way. To Dr. Marat Khairoutdinov (with whom I shared an office for a time) I owe special thanks for the many stimulating discussions that helped me gain insight into the workings of the atmosphere and the models we use to represent it. I appreciate the computer programming and hardware support I received from Mark Branson, Don Dazlich, Mostafa El-Kady, Dr. Ross Heikes and Kelley Wittmeyer. I am also thankful for the help of the administrative staff including Cindy Carrick, Connie Hale, Michelle Beckman, and Beth White.

Special thanks go to Norm Wood of our department for helping me learn the CDAT visualization software used to produce the plots in the dissertation.

I am honored to have had contact with Dr. Akio Arakawa of UCLA and am very grateful for his comments on my work as it progressed. I hope that in some way this research will build on his legacy.

Drs. Stanley Benjamin, John Brown, and Jin-Luen Lee of the NOAA Earth System Research Laboratory, as well as Dr. Gunther Zangl of the University of Munich, provided valuable suggestions at a critical point in the model development.

Finally, I am grateful for the support and encouragement from family and friends, most importantly from my wife, Monica, whose unwavering confidence in me I will always appreciate. Her proofreading of the drafts of this dissertation was an invaluable help. My children, Benjamin and Dominique, were also an inspiration to this work, and I thank them for all the joy they bring to our lives.

This research was supported by the Office of Science (BER), U. S. Department of Energy, Grant No. DE-FC02-06ER64302.

CONTENTS

Chapter 1 INTRODUCTION 1

1.1 The quasi-Lagrangian θ coordinate 2
1.2 Numerical modeling with the θ coordinate 4
1.3 Advantages and disadvantages of isentropic-coordinate modeling 6
1.4 Hybrid vertical coordinate models 7
1.5 Nonhydrostatic modeling with hybrid vertical coordinates 10
1.6 A new approach to nonhydrostatic modeling with a hybrid vertical coordinate. 12
1.7 Design of the vertical discretization 14
1.7.1 Vertical staggering 14
1.7.2 Integral constraints 17
1.8 Outline of the dissertation 18

Chapter 2 CONTINUOUS EQUATIONS 20

2.1 Introduction 20
2.2 Governing equations 20
2.3 Integral constraints 24
2.3.1 Conservation of mass ("Constraint 0") 25
2.3.2 Vertically integrated momentum circulation constraint on the HPGF ("Constraint I") 26
2.3.3 Conservation of total energy ("Constraint II") 28
2.3.3.1 Kinetic energy equation 28
2.3.3.2 Internal energy equation 30
2.3.3.3 Geopotential energy equation 32
2.3.3.4 Total energy equation 32
2.4 A summary of the continuous system of equations 33
2.5 Specification of the vertical coordinate and diagnosis of the vertical velocity ... 35
2.5.1 The vertical coordinate 36
2.5.2 Diagnosis of the vertical velocity 42
2.5.2.1 "Target-seeking" component of the vertical velocity 43
2.5.2.2 "Smoothing" component of the vertical velocity 45
2.6 Vertical flux of horizontal momentum in a generalized vertical coordinate 46
2.7 Summary 50

Chapter 3 VERTICAL DISCRETIZATION 52

3.1 Introduction 52
3.2 Vertical grid 53
3.2.1 Linearized, steady-state equations 54
3.2.1.1 Discrete linearized equations in z coordinates 56
3.2.1.2 Discrete linearized equations in θ coordinates 58
3.2.1.3 Closing remarks 61
3.2.2 Model grid 63
3.3 Governing equations 64
3.3.1 Continuity equation 64
3.3.2 Pressure gradient forces 66
3.3.2.1 Vertical pressure gradient force 66
3.3.2.2 Horizontal pressure gradient force 67
3.3.3 Horizontal momentum equation 68
3.3.4 Vertical momentum equation 68
3.3.5 Thermodynamic energy equation 68
3.3.6 Geopotential tendency equation 68
3.3.7 Diagnostic relations 69
3.4 Integral constraints for the generalized vertical coordinate η: The "η-scheme" 70
3.4.1 Work done by the pressure gradient forces: Part I 70
3.4.2 Vertically integrated momentum circulation constraint on the HPGF (Constraint I) 74
3.4.3 Conservation of total energy (Constraint II) 76
3.4.3.1 Work done by the pressure gradient forces: Part II 77
3.4.3.2 Thermodynamic energy equation 77
3.4.3.3 Geopotential energy equation 84
3.4.4 Implications of the "η-scheme" 85
3.5 Alternative scheme: The "z-scheme" 86
3.5.1 Vertically integrated momentum circulation constraint on the HPGF 87
3.5.2 Conservation of total energy 87
3.5.2.1 Work done by the pressure gradient forces 87
3.5.2.2 Thermodynamic energy equation 88
3.5.2.3 Geopotential energy equation 91
3.5.3 Implications of the "z-scheme" 92
3.6 Summary of the design features of the two vertical schemes 92
3.7 Summary of the *"z*-scheme" vertically discrete governing equations 93

Chapter 4 VERTICAL VELOCITY DIAGNOSIS AND ADVECTION IN THE DISCRETE EQUATIONS 99

4.1 Introduction 99
4.2 A closer look at the advection of θ and z by the generalized vertical velocity . 100
4.2.1 The role of the vertical θ-advection term in the z-coordinate domain 101

4.2.2 The role of the vertical θ-advection term in the θ-coordinate domain 101
4.2.3 The role of the vertical z-advection term in the θ-coordinate domain 102
4.2.4 The role of the vertical z-advection term in the z-coordinate domain 102
4.2.5 Two components of the generalized vertical velocity 103
4.3 Vertical velocity diagnosis and the advection of θ and ϕ in the model 105
4.3.1 Advection of θ and ϕ by the "target-seeking" vertical velocity component 106
4.3.2 Advection of θ and ϕ by the "smoothing" vertical velocity component 108
4.3.3 The final determination of the vertical velocity 109
4.3.4 Final forms of the vertical advection of θ and ϕ and the vertical velocity .. 112
4.4 Summary 113

Chapter 5 RESULTS 114

5.1 Introduction 114
5.2 Mountain waves in an isothermal atmosphere 114
5.2.1 Linear hydrostatic waves 119
5.2.2 Linear nonhydrostatic waves 126
5.2.3 Finite-amplitude nonhydrostatic waves 126
5.3 The 11 January 1972 Boulder, Colorado Downslope Windstorm 143
5.3.1 Model configuration and initialization 145
5.3.2 Potential temperature field and static stability 149
5.3.3 Bulk Richardson number 159
5.3.4 Zonal wind field and surface drag 159
5.3.5 Tracer advection 164
5.3.6 Integral property evaluation 171
5.4 Summary and conclusions 174

Chapter 6 SUMMARY AND CONCLUSIONS 178

Appendix A SUPPLEMENTAL MODEL INFORMATION 183

A.1 Upstream-weighted vertical advection schemes for θ and ϕ 183
A.1.1 Vertical θ-advection scheme 183
A.1.2 Vertical ϕ-advection scheme 185
A.2 Horizontal finite-difference schemes used in the model 186
A.2.1 The horizontal grid 186
A.2.2 Horizontal momentum advection 187
A.2.3 Horizontal mass advection 187
A.2.4 Horizontal θ-advection 188
A.2.5 Horizontal ϕ-advection 190
A.2.6 Time discretization 191
A.2.7 Subgrid-scale turbulence parameterization 191
A.2.8 Surface pressure diagnosis 191

Appendix B EFFECT OF THE FORM OF THE DESCRETE PRESSURE GRADIENT FORCES ON ACCURACY AND SATISFACTION OF THE INTEGRAL CONSTRAINTS: "*p*- vs. Π-FORM"..... 194

B.1 Introduction 194
B.2 Integral constraints in the vertically continuous, horizontally discrete quasi-static (primitive) equations in the generalized vertical coordinate 196
B.2.1 Energy conversion term of the thermodynamic energy equation 197
B.2.2 The "p-form" of the HPGF 199
B.2.3 The "Π-form" of the HPGF 202
B.2.4 Discussion 204
B.3 Comparison of the truncation error between the "*p-"* and "Π-forms" of the HPGF and VPGF 204
B.3.1 A closer look at Constraint I (the "mountain torque" constraint) 204
B.3.2 Analysis of HPGF truncation error 205
B.3.3 Analysis of the truncation error of the VPGF 209

Appendix C LINEAR WAVE EQUATIONS 215

Appendix D 3D EXPERIMENTS WITH AN EARLY VERSION OF THE σ-COORDINATE MODEL 219

D.1 Rising thermal experiment 219
D.1 Amplifying 3D baroclinic wave in a β-channel 223

REFERENCES 226

Chapter 1 INTRODUCTION

The theoretical framework for atmospheric modeling with the isentropic vertical coordinate was first worked out over 60 years ago (e.g., Starr 1945). This coordinate has particular advantages in improving the accuracy of numerical weather forecasting and climate models. Despite this, its use has been slow to develop, due in part to the technical challenges of handling the quasi-Lagrangian isentropic surfaces. These challenges are more difficult in nonhydrostatic models designed to simulate fine scale motion where isentropic overturning often occurs. It has only been in the last decade that the isentropic coordinate has been implemented in nonhydrostatic models.

The isentropic vertical coordinate is classified as quasi-Lagrangian because, under adiabatic processes, surfaces of constant potential temperature are material surfaces. Therefore, numerical errors associated with vertical transport across coordinate surfaces are virtually eliminated. One of the drawbacks to modeling with the isentropic coordinate is the intersection of potential temperature surfaces with the ground. Hybrid vertical coordinate models provide a means to overcome this issue by incorporating a terrain-following Eulerian coordinate near the surface. They combine the optimum features of the quasi-Lagrangian and Eulerian coordinate systems.

This dissertation presents a new approach to nonhydrostatic finite-difference modeling with a hybrid vertical coordinate. It combines the generalized vertical coordinate technique of Konor and Arakawa (1997) with the arbitrary Lagrangian-

Eulerian methods used in previous hybrid models. With the former method, a smooth transition between the coordinate types is specified, while the latter method provides the flexibility to allow the coordinate to adapt "on the fly" to changing atmospheric conditions. The result is that the benefits of the isentropic coordinate are achieved as much as possible while allowing nonmonotonic vertical profiles of potential temperature to exist in the free atmosphere.

1.1 The quasi-Lagrangian θ coordinate

The benefits of transforming the equations of atmospheric motion into the isentropic (θ) coordinate were recognized as early as the 1930's (e.g., Montgomery 1937, Rossby 1938). Potential temperature increases monotonically with height in the standard, stably stratified atmosphere, making it useable as a vertical coordinate. Furthermore, the fact that air parcels conserve their value of θ under adiabatic processes means that there is no vertical velocity in isentropic coordinates. Here, the potential temperature is defined as

$$\theta \equiv T\left(\frac{p_0}{p}\right)^{\kappa}, \tag{1.1}$$

where T is temperature, p is pressure, p_0 is a reference pressure (usually 1000 mb), and $\kappa \equiv R/c_p$, where R is the gas constant and c_p is the specific heat at constant pressure. Isentropic weather charts, which are plotted on surfaces of constant θ, provided a new way of visualizing atmospheric motion since the flow on isentropic surfaces is two-dimensional for adiabatic processes.

The physical insight gained from the isentropic coordinate framework led to the advancement of PV theory (see Rossby 1940). In θ coordinates, the effect of stretching on the absolute vorticity of vertical cylindrical fluid elements bounded by material surfaces can be clearly expressed. Ertel (1942) derived a form of the PV that is materially conserved for adiabatic, frictionless motion. It is written as

$$P = \frac{\boldsymbol{\zeta}_{\mathbf{a}} \cdot \nabla \theta}{\rho}, \tag{1.2}$$

where P is Ertel's potential vorticity, $\boldsymbol{\zeta}_{\mathbf{a}}$ is the absolute vorticity vector, ∇ is the three-dimensional gradient operator, and ρ is density. In isentropic coordinates, Ertel's PV takes on a simple form when the hydrostatic assumption is applied. It becomes

$$P = -g\left(f + \zeta_\theta\right)\left(\frac{\partial p}{\partial \theta}\right)^{-1}, \tag{1.3}$$

where g is gravity, f is the Coriolis parameter, and ζ_θ is the isentropic relative vorticity given by

$$\zeta_\theta = \mathbf{k} \cdot \nabla_\theta \times \mathbf{v}, \tag{1.4}$$

where $\mathbf{k}$ is the unit vertical vector, ∇_θ is the horizontal gradient operator on constant-θ surfaces, and $\mathbf{v} = (u, v, 0)$ is the horizontal wind velocity. When P is plotted on isentropic charts, the visualization of the flow field evolution is aided since both θ and P are nearly conserved. Through the invertibility principle, the complete three-dimensional motion field can be diagnosed from the PV field. A history of the development of PV theory and isentropic potential vorticity maps can be found in Hoskins et al. (1985).

The merits of performing dynamical analysis with the isentropic vertical coordinate led to the development of a quasi-Lagrangian system of hydrodynamical equations (Starr 1945). In his paper, Starr combined the Eulerian Cartesian coordinate in the horizontal, and a Lagrangian coordinate in the vertical. Isosurfaces of the vertical coordinate (referred to as c) are fixed to a particular set of fluid particles. The vertical velocity $\dot{c}$ in the system is identically zero, so all motion is horizontal in the coordinate framework. Over the years the term "quasi-Lagrangian vertical coordinate" has been used to describe quasi-conservative vertical coordinates for which the vertical velocity is usually small. These include isopycnal coordinates used in ocean dynamics, and isentropic coordinates used in dry atmospheric dynamics.

1.2 Numerical modeling with the θ coordinate

The advent of digital computing in the 1940's and 1950's made numerical methods for solving the hydrodynamical equations practicable. The first weather forecasting and general circulation models (GCMs) used Eulerian vertical coordinate systems based on geometric height and pressure. (See Randall (2000) for a historical overview of GCM development.) The use of material layers in a model was proposed by Eliassen (1962), in part to reduce the numerical error associated with vertical advection.

Eliassen and Raustein (1968) built a two-layer finite-difference θ-coordinate model based on the primitive equations. In their model, the lower boundary was a model surface, and the lower isentropic model surface would intersect the ground. The intersection of model layers with the lower boundary required special attention and it became one of the most challenging design features of subsequent θ-coordinate models.

In Eliassen and Raustein (1968, 1970) and Shapiro (1975), the Exner function, $\Pi \equiv c_p(p/p_0)^{\kappa}$, and also the velocity components were linearly extrapolated below the surface. These subterranean values were used in the horizontal difference terms.

Bleck (1984) implemented an alternative to the "linear extrapolation" technique of handling intersecting θ-coordinate surfaces at the ground. In this "massless-layer" approach, which originated from Lorenz (1955), isentropic surfaces intersecting the lower boundary are extended along the ground, as shown in Figure 1.1. These may be collocated with adjacent isentropic layers and they are filled identically by zero mass. With this technique, the surface value of potential temperature, which is needed to determine the horizontal position of ground intersection in the "linear extrapolation" method, need not be calculated from the thermodynamic energy equation. Instead, the location of layer intersection is determined from the mass continuity equation with the lower boundary condition $\dot{\theta}_S = 0$, where θ_S is an arbitrarily assigned lower bound of potential temperature.

The massless-layer approach was also used by Hsu and Arakawa (1990), hereafter HA90, in the development of their θ-coordinate model. They formulated a vertical

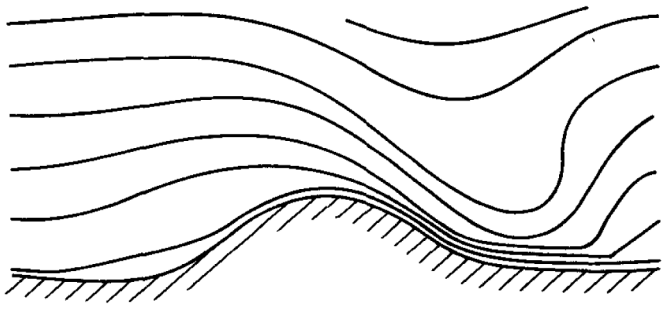


Figure 1.1: Illustration of massless isentropic layers along the lower boundary [Fig. 2 from Hsu and Arakawa (1990)].

discretization scheme which conserved total energy and angular momentum, and they achieved long-term simulations of baroclinic wave growth on a β-plane with a 25-layer model. Randall et al. (2000) developed a θ-coordinate global model using the scheme of HA90.

1.3 Advantages and disadvantages of isentropic-coordinate modeling

HA90 discussed advantages and disadvantages of the isentropic coordinate. Some of the advantages are summarized below.

1) The vertical velocity is zero for adiabatic flow, which simplifies the motion to a two-dimensional problem and greatly reduces the numerical errors associated with vertical advection.

2) Sharp horizontal gradients of atmospheric properties, which are found along frontal boundaries in traditional Eulerian coordinate systems, are nonexistent in the isentropic coordinate framework.

3) Ertel's potential vorticity, given by equation (1.3), is more easily expressed since it does not involve vertical derivatives of **v**. This makes the conservation of PV more straightforward in the discrete, quasi-static framework.

4) A quasi-Lagrangian view of the general circulation of the atmosphere is readily obtained with the isentropic coordinate. This follows from the fact that mean vertical transport is due only to diabatic heating with no contribution from eddy transport. For example, under adiabatic conditions, the pressure form drag acting on isentropic surfaces is the only mechanism for the vertical transfer of momentum.

Some of the disadvantages pointed out by HA90 are listed below. The solutions to these will be addressed later.

1) As pointed out earlier, isentropic coordinate surfaces can intersect the lower boundary, even without topography. These intersections are difficult to handle in a discrete model.

2) The mass between adjacent isentropic layers can become infinitesimally small which can cause computational difficulties.

3) In the planetary boundary layer (PBL), isentropic surfaces can become vertical due to mixing, resulting in a lack of vertical resolution.

4) Unstable layers with $\partial\theta/\partial z<0$ cannot be represented in the model because of the requirement that the vertical coordinate be a monotonic function of height.

1.4 Hybrid vertical coordinate models

The disadvantages listed above can be solved with the hybrid vertical coordinate approach. In this method, the θ coordinate is used in the free atmosphere, where the static stability is generally positive, and an Eulerian *p*- or *z*-based coordinate is used near the surface. The latter is typically a terrain-following (σ) coordinate, which eliminates the issue with intersecting coordinate surfaces with the lower boundary. Also, the PBL can be well resolved with an arbitrary number of model levels. The hybrid method was developed in the 1970's (e.g., Deaven 1976, Friend et al. 1977, Uccellini et al. 1979). In these early hybrid models there was an interface between the isentropic and σ coordinate domains (see Figure 1.2). In general, isentropic model surfaces would intersect the interface, and, therefore, the finite-difference schemes would have to handle this in a

similar manner to isentropic ground intersections with the "pure" θ coordinate models. In Deaven (1976), this was done using a linear extrapolation method where θ-surfaces are extrapolated into the σ-domain. Uccellini et al. (1979) designed their model to conserve mass, momentum and energy in association with transport across the interface between the isentropic and sigma domains. This reduced the pressure and wind perturbations caused by truncation errors with the discrete handling of the interface.

Bleck (1978a) introduced a method of joining the isentropic and sigma domains that avoids the intersection of isentropic surfaces with the interface (see Figure 1.2). This was to have the interface coincide with an arbitrary isentropic surface which is high enough to avoid intersection with the lower boundary (310K was chosen). While this method has the advantage of avoiding coordinate surface intersections, it has the

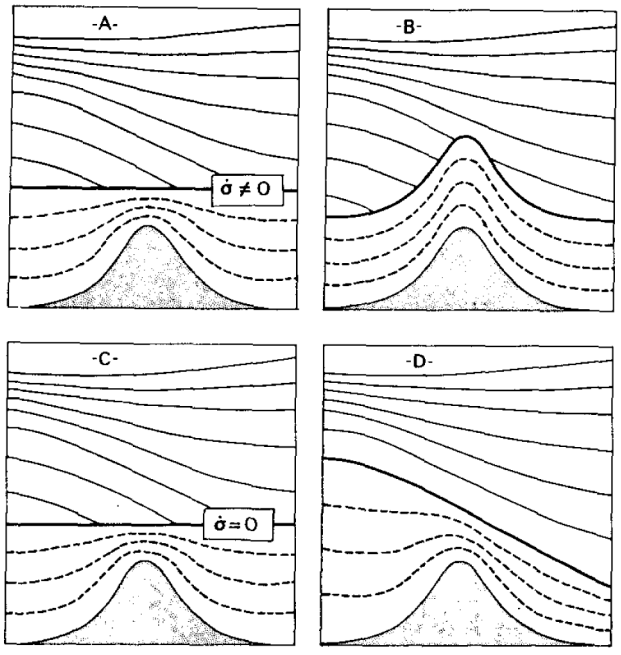


Figure 1.2: Four ways of joining the σ and θ domains: (A) Friend et al. (1977), (B) Uccellini et al. (1979), (C) Deaven (1976), and (D) Bleck (1978a) [Fig.1 from Bleck (1978a)].

disadvantage that the interface height would vary considerably with latitude. For the choice of $\theta_{\text{INTERFACE}} = 310\,\text{K}$, the height would typically be about 3 km in the tropics, while near the poles, it is located at almost 10 km. Therefore, the benefit of the θ coordinate would not be realized throughout most of the troposphere in the higher latitudes.

The method of transition from the σ coordinate to the θ coordinate in Bleck's model logically led to the use of a generalized vertical coordinate. In two subsequent papers, Bleck (1978b, 1979) formulated a system of finite-difference equations based on the generalized vertical coordinate for use in hybrid coordinate models. Under this framework, the vertical coordinate may be specified as a function of two or more variables. For example, Zhu et al. (1992) defined their coordinate in terms of σ, θ and p. The generalized vertical coordinate is also used in the NOAA Rapid Update Cycle (RUC) operational weather prediction model for regional forecasts (Bleck and Benjamin 1993; Benjamin et al. 2004). In this model, the coordinate is specified as purely isentropic in the free atmosphere, while near the surface, a minimum pressure spacing between coordinate surfaces is maintained through a process of regridding. Therefore, the coordinate behaves as a pressure-based terrain-following σ coordinate near the surface. The coordinate-relative vertical velocity associated with the regridding process is calculated and used in the vertical advection terms of the prognostic equations. Another quasi-static atmosphere model based on this coordinate is the Flow-following finite-volume Icosahedral Model (FIM) global model developed at NOAA/ESRL (documentation at http://fim.noaa.gov/fimdocu_rb.pdf).

Konor and Arakawa (1997), hereafter KA97, used a coordinate defined as a linear function of σ and θ, with a smooth transition from the σ coordinate near the surface to the θ coordinate. The functional relationship was specified to maintain vertical coordinate monotonicity for a given degree of static instability, i.e., $\partial\theta/\partial z<0$, without the need for regridding. Models based on the vertical coordinate of KA97 include Heikes et al. (2006) and Dowling et al. (2006).

1.5 Nonhydrostatic modeling with hybrid vertical coordinates

In the quasi-static models discussed so far, the folding of isentropic surfaces in the free atmosphere was generally not considered a major difficulty. Eliassen and Raustein (1968) stated that there was no reason to believe that these surfaces would fold during integration of their isentropic coordinate model. HA90 pointed out that in θ-coordinate models, mass is automatically redistributed in such a way as to prevent unstable layers from developing, which is equivalent to a built-in dry convective adjustment process. These are valid arguments for large-scale quasi-static motion. However, on the small scales resolved by nonhydrostatic models, the existence of statically unstable layers and isentropic overturning are common physical features which must be accommodated.

In the last decade, nonhydrostatic models using the quasi-Lagrangian θ coordinate have been developed. Skamarock (1998) and He (2002) extended the hybrid coordinate method of Bleck and Benjamin (1993). In their regridding algorithms they imposed both minimum and maximum Δz requirements on adjacent layers to prevent layers from crossing and to provide vertical resolution in statically unstable regions,

respectively. Therefore, the generalized vertical coordinate used in these nonhydrostatic models are hybrids of potential temperature and a height-based terrain-following coordinate. In addition to the layer thickness requirements, coordinate surfaces were horizontally and vertically filtered to maintain grid smoothness and to prevent layers from having infinite slope. Successful two-dimensional mountain wave breaking experiments were achieved by both Skamarock (1998) and He (2002). With the latter model, a three-dimensional simulation of baroclinic wave growth on a β-plane was also performed.

Zangl (2007) developed an adaptive vertical coordinate formulation with flux-form equations and implemented it in the nonhydrostatic Weather Research and Forecasting Model (WRF) (Skamarock et al. 2005). The value of the vertical coordinate, which is based on WRF's terrain-following hydrostatic-pressure vertical coordinate (see Laprise 1992), is calculated at each grid point using a prognostic equation. This equation is a relaxation-diffusion equation that applies a Newtonian relaxation toward a "target" field. The specification of the target field determines the nature of the coordinate. Zangl specified it to be terrain-following near the surface and isentropic in the free atmosphere. The diffusive aspect of the prognostic equation maintains a smooth layer spacing and smoothness in the horizontal, in addition to maintaining coordinate monotonicity in regions of isentropic overturning.

The handling of the vertical coordinate in these nonhydrostatic models, as well as the quasi-static models that use a regridding method, are characteristic of arbitrary Lagrangian-Eulerian (ALE) methods (Hirt et al. 1974) and adaptive grid techniques (Dietachmayer and Droegemeier 1992). With the ALE method, the three dimensional

model grid is attached to grid points whose positions in space are predicted in a Lagrangian manner. To prevent the grid from becoming too irregular, mass is allowed to cross grid cell walls in an Eulerian manner. The hybrid coordinate models apply these techniques only in the vertical dimension. In contrast, the hybrid coordinate method of KA97 is not derivative of ALE or adaptive grid techniques as the combination of the quasi-Lagrangian (i.e., θ) and Eulerian (i.e., σ) components are strictly prescribed at each model level.

1.6 A new approach to nonhydrostatic modeling with a hybrid vertical coordinate

For the nonhydrostatic model developed in this dissertation we started with the hybrid vertical coordinate of KA97. We did so because of the straightforwardness of its formulation and the smoothly prescribed transition from terrain-following (sigma) to isentropic coordinates. In the final design, however, we ended up incorporating elements of ALE. Therefore, our formulation can be viewed as an "adaptive" version of the statically-defined coordinate of KA97. Next, we briefly explain the development process of the vertical coordinate used in the model.

Recall that in KA97, a specified degree of static instability can be accommodated while maintaining the monotonicity of the vertical coordinate. This is achieved by retaining some "sigma-ness" in the vertical coordinate and not allowing it to become exactly isentropic, which results in sacrificing some of the quasi-Lagrangian nature of the θ coordinate. In testing their model, KA97 allowed for a small enough amount of static instability that the deviation from isentropic coordinates was small. In their model, dry-

convective adjustment helped to maintain statically stable vertical profiles as is observed on the large scale.

When we implemented the KA97 hybrid vertical coordinate in our nonhydrostatic model, it functioned well for small-scale cases in which static stability is maintained, such as gravity wave formation in flow over a small obstacle. For more severe cases, such as nonlinear wave breaking over a taller obstacle, we ran into problems. Our hope had been that it would be possible to achieve a numerical solution to the pure θ-coordinate representation of wave breaking. We had theorized that the waves would amplify to the point mathematically allowed with a monotonic θ coordinate, that is just before isentropes overturn and the static stability becomes zero, and then they would die out. Instead, the model would not run unless enough of a σ-component remained in the vertical coordinate to allow the waves to develop and break as they do in the physical realm. In fact the coordinate had to deviate from θ to the point that the generalized vertical velocity, and therefore the dispersion error associated with vertical advection, was indistinguishable from a pure σ coordinate. This, of course, defeats the purpose of the hybrid-coordinate.

The problem that occurred in the pure θ-coordinate runs was that large-amplitude noise would develop in the motion field which caused coordinate surfaces to cross each other, resulting in negative mass. We implemented an upstream mass-advection scheme to try to prevent negative values of mass, but this merely delayed the problem. We then imposed a minimum layer thickness by using a "regridding" method, but this only further delayed the model crash. We speculate that the root problem was that the spatial gradients of the prognostic variable fields in the coordinate space became too sharp for

the numerical schemes to handle, particularly the advection schemes. The way to get past the barrier was to prevent these sharp gradients from developing by spatially smoothing the coordinate surfaces, that is by incorporating an adaptive grid technique. We will show evidence of the reduction of these gradients in the next chapter, where the details of the smoothing method will be described.

1.7 Design of the vertical discretization

This section outlines the design criteria for the vertical discretization used in the model. A description of the vertical staggering of the prognostic variables will be given. This will be followed by a discussion of the integral constraints, such as mass conservation, that will be used as a guide in developing the discrete form of the governing equations.

1.7.1 Vertical staggering

Determining the spatial grid distribution of the predicted variables is an important early step in the design of a numerical model. The way these variables are staggered with respect to each other directly affects the forms of the discrete difference terms in the model equations. These, in turn, affect the accuracy of the model solutions, as well as the satisfaction of conservation properties. They also can determine whether or not nonphysical computational modes exist. Various grid staggerings on horizontal, quadrilateral grids, and their effects on gravity wave motion, are analyzed in Arakawa and Lamb (1977) and Randall (1994). Their results provide a framework for determining the optimal grid staggering for representing geostrophic adjustment.

Proper prognostic variable staggering in the vertical is also important for the accurate representation of wave propagation and the avoidance of computational modes. The various arrangements for quasi-static models have been analyzed (e.g., Tokioka 1978, Arakawa and Moorthi 1988, Arakawa and Konor 1996). Two general classes of vertical grids exist for the primitive equation models using a pressure-based vertical coordinate – the Charney-Phillips (CP) grid and the Lorenz grid. These are illustrated in Figure 1.3. The CP grid was used in Charney and Phillips (1953) for a discrete three-dimensional quasigeostrophic model. In this grid, the thermodynamic variable θ is vertically staggered with respect to the horizontal velocity (**v**). Lorenz (1960) placed θ at

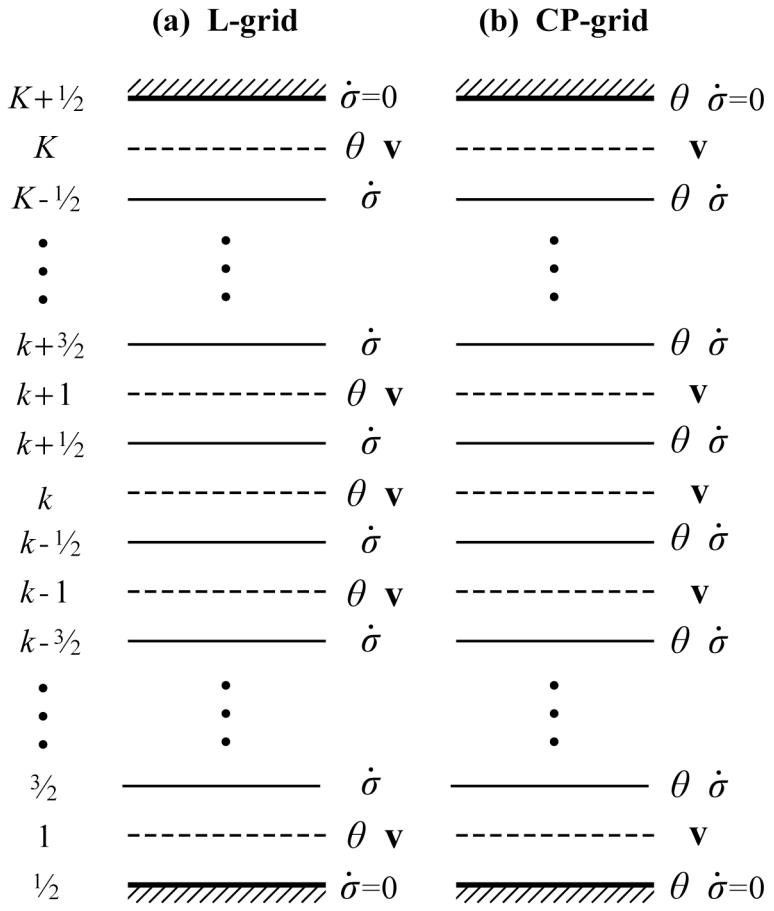


Figure 1.3: Variable staggerings of (a) the Lorenz grid and (b) the Charney-Phillips grid for a σ coordinate.

the same level as the horizontal velocity in order to facilitate conservation of total energy, mean potential temperature and potential temperature variance. The Lorenz grid became the typical standard in GCMs because of these conservation properties. However, this grid supports a computational mode in the potential temperature field which is described in Arakawa and Moorthi (1988). This mode was found to cause spurious baroclinic wave growth in discrete models. The computational mode does not exist in the CP grid, as demonstrated by Arakawa and Konor (1996). In that paper, it was also shown that total energy conservation can be achieved with the CP grid.

In nonhydrostatic modeling, the replacement of the hydrostatic relation with a prognostic equation for the vertical velocity w, changes the analysis of the vertical staggering. In this system of equations, there is an additional vertical wave mode – the acoustic mode – which, although not of meteorological significance, has an important role in the hydrostatic adjustment process (e.g., Bannon 1995). The choice of vertical coordinate also has a role in determining the optimal grid staggering. Woollings (2004) and Thuburn and Woollings (2005) analyzed the discrete linear normal modes for various staggerings with the compressible, nonhydrostatic system of equations expressed in three different coordinate systems – the height coordinate, the isentropic coordinate and a terrain-following mass-based coordinate. The staggerings which provided the most accurate representation of wave motion as well as being free of computational modes were those in which potential temperature is staggered with respect to horizontal velocity, i.e., the CP-like grids.

Partly based on the results of Thuburn and Woollings, we chose to implement the CP grid in the height-based coordinate domain of the hybrid vertical coordinate model.

There is also precedent for using the CP grid in nonhydrostatic atmospheric models based on a terrain-following height-based vertical coordinate in the "unified model" developed at the United Kingdom's Met Office (Davies et al. 2005).

1.7.2 Integral constraints

The discrete forms of the governing equations used in numerical models are often designed to satisfy various integral properties found in the continuous system of equations. These properties include the conservation of mass, momentum, total energy, potential temperature, and concentrations of water and chemical species. As there is a limited number of degrees of freedom in the algebraic model equations, it is not possible to satisfy all of the integral properties found with the continuous system. Therefore, trade-offs must be made in designing the vertical discretization. The vertical discretization we developed for the model conserves the total mass through the direct prediction of the mass variable with a flux-form of the continuity equation. Total energy and the vertically integrated momentum circulation about a closed contour of topography is also conserved under the special case of pure height coordinates and centered-differencing schemes. The satisfaction of these constraints for the generalized vertical coordinate is traded-off in order to avoid the existence of a computational mode in the thermal field. Another constraint that is compromised is the conservation of potential temperature, which appears to be due to the use of the CP grid.

1.8 Outline of the dissertation

The purpose of this dissertation is to present the design and tests of a new nonhydrostatic atmosphere model which takes advantage of a quasi-Lagrangian vertical coordinate. The tests demonstrate its capability to represent fine-scale nonhydrostatic motions including those involving isentropic overturning. Results with the hybrid coordinate are compared to those with the conventional σ coordinate, revealing both advantages and disadvantages of the hybrid coordinate.

In Chapter 2 the continuous system of equations is presented. The governing equations in z coordinates are transformed into the generalized vertical coordinate (η). We then derive some of the integral properties of the continuous system in this coordinate. The details of the vertical coordinate specification and the method of diagnosing the generalized vertical velocity $\dot{\eta}$ are presented. Finally, the vertical flux of horizontal momentum is analyzed and the Eliassen-Palm flux in a generalized vertical coordinate is derived. This expression is used for the analysis of the momentum transport in the model.

Chapter 3 describes the design of the vertical discretization scheme. The vertical staggering and the discrete form of the governing equations are presented. Various integral constraints are satisfied by these equations under certain conditions. Compromises made between the various design criteria are highlighted. The method of diagnosing the generalized vertical velocity in the model is detailed in Chapter 4. Also, we will describe the special handling of the vertical advection of potential temperature and geopotential.

In Chapter 5, a series of two-dimensional mountain wave experiments are performed with the model. Results from runs with the hybrid vertical coordinate and the σ coordinate are compared in regard to the overall fields, as well as momentum and tracer transport. Finally, Chapter 6 provides a summary of the dissertation along with concluding remarks.

Chapter 2 CONTINUOUS EQUATIONS

2.1 Introduction

This chapter describes the compressible Eulerian equations of fluid motion in a generalized vertical coordinate on which the model is based. We develop the nonhydrostatic equations starting in z coordinates, and transform them to the generalized vertical coordinate following the work of Kasahara (1974) for the quasi-static equations. The integral constraints that will form the basis of the vertical discretization scheme are then derived. The vertical coordinate is presented, along with the method for diagnosing the generalized vertical velocity. Finally, we will analyze the vertical flux of horizontal momentum in the generalized vertical coordinate, and derive an expression for the Eliassen-Palm flux in this coordinate.

2.2 Governing equations

We start with the governing equations in z-coordinates. The laws of momentum, energy and mass conservation make up the prognostic equations. The horizontal momentum equation is

$$\frac{D\mathbf{v}}{Dt} + f\mathbf{k}\times\mathbf{v} = -\frac{1}{\rho}\nabla_z p + \mathbf{F}, \tag{2.1}$$

where ∇ is the horizontal gradient operator, **F** is the horizontal friction force, and D/Dt is the material time derivative given by

$$\frac{D}{Dt} = \left(\frac{\partial}{\partial t} + \mathbf{v} \cdot \nabla \right)_z + w \frac{\partial}{\partial z}. \tag{2.2}$$

The subscript z on the differential operators denotes derivatives at constant geopotential height. The vertical momentum equation is

$$\frac{Dw}{Dt} = -\frac{1}{\rho} \frac{\partial p}{\partial z} - g + F_z, \tag{2.3}$$

where F_z is the vertical component of the friction force.

Mass conservation is given by

$$\left(\frac{\partial \rho}{\partial t} \right)_z + \nabla_z \cdot (\rho \mathbf{v}) + \frac{\partial}{\partial z}(\rho w) = 0. \tag{2.4}$$

The first law of thermodynamics for quasiequilibrium, frictionless processes can be expressed as

$$\frac{D\theta}{Dt} = \frac{Q}{\Pi}, \tag{2.5}$$

where Q is the rate of diabatic heating and Π is the Exner function defined below.

The diagnostic equations that close the system are the ideal gas law,

$$p = \rho R T, \tag{2.6}$$

the definition of the Exner function,

$$\Pi \equiv c_p \left(\frac{p}{p_0} \right)^{\kappa}, \tag{2.7}$$

and the definition of potential temperature,

$$\theta \equiv \frac{c_p T}{\Pi}. \tag{2.8}$$

To transform these equations to a generalized vertical coordinate η we use the following chain-rule identities:

$$\left(\frac{\partial}{\partial t}\right)_z = \left(\frac{\partial}{\partial t}\right)_\eta + \left(\frac{\partial \eta}{\partial t}\right)_z \frac{\partial}{\partial \eta}, \tag{2.9}$$

$$\nabla_z = \nabla_\eta + \nabla_z \eta \frac{\partial}{\partial \eta}, \tag{2.10}$$

$$\left(\frac{\partial \eta}{\partial t}\right)_z = -\frac{\partial \eta}{\partial z}\left(\frac{\partial z}{\partial t}\right)_\eta, \tag{2.11}$$

$$\nabla_z \eta = -\frac{\partial \eta}{\partial z} \nabla_\eta z, \tag{2.12}$$

and

$$\frac{\partial}{\partial z} = \frac{\partial \eta}{\partial z}\frac{\partial}{\partial \eta}. \tag{2.13}$$

Applying equations (2.9) - (2.13) in equations (2.1) - (2.4) gives the governing equations in the generalized vertical coordinate η. First, the horizontal momentum equation becomes

$$\frac{D\mathbf{v}}{Dt} + f\mathbf{k} \times \mathbf{v} = -\frac{1}{\rho}\nabla_\eta p + \frac{1}{m}\frac{\partial p}{\partial \eta}\nabla_\eta z + \mathbf{F}. \tag{2.14}$$

Note that the horizontal pressure gradient force has become a two-term expression, and a new quantity is introduced – the pseudo-density (m) given by

$$m \equiv \rho \frac{\partial z}{\partial \eta}. \tag{2.15}$$

This is the analog of the conventional density, referred to the generalized vertical coordinate, i.e., the amount of mass per unit volume of the generalized space. Using the expression

$$\dot{\eta} \equiv \frac{D\eta}{Dt} = \left(\frac{\partial \eta}{\partial t} \right)_z + \mathbf{v} \cdot \nabla_z \eta + w \frac{\partial \eta}{\partial z}, \tag{2.16}$$

where $\dot{\eta}$ is the generalized vertical velocity, the material time derivative becomes

$$\frac{D}{Dt} = \left(\frac{\partial}{\partial t} + \mathbf{v} \cdot \nabla \right)_\eta + \dot{\eta} \frac{\partial}{\partial \eta}. \tag{2.17}$$

The vertical momentum equation is

$$\frac{Dw}{Dt} = -\frac{1}{m} \frac{\partial p}{\partial \eta} - g + F_z. \tag{2.18}$$

Finally, the flux form of the mass continuity equation is written as

$$\left(\frac{\partial m}{\partial t} \right)_\eta + \nabla_\eta \cdot (m\mathbf{v}) + \frac{\partial}{\partial \eta}(m\dot{\eta}) = 0, \tag{2.19}$$

where we used

$$w = \frac{Dz}{Dt} = \left(\frac{\partial z}{\partial t} + \mathbf{v} \cdot \nabla z \right)_\eta + \dot{\eta} \frac{\partial z}{\partial \eta}. \tag{2.20}$$

At this point, it is illustrative to consider these equations in the framework of some commonly used vertical coordinate systems, and to briefly discuss the formulation of the generalized vertical velocity in each. For the *z*-coordinate ($\eta = z$), the original governing equations are recovered, as equation (2.15) becomes $m = \rho$, and the vertical velocity, as given by (2.16), becomes $\dot{\eta} = w$. In this system, the vertical velocity is simply the prognostic quantity governed by (2.18). This is in contrast to the diagnosis of

w in the z-coordinate, quasi-static system of equations, which is quite complicated (Richardson 1922).

In pressure coordinates ($\eta = p$), the vertical velocity $\dot{\eta} = \dot{p}$ is not straightforward to calculate in the nonhydrostatic system. In the quasi-static system, it can readily be diagnosed from the vertically integrated horizontal divergence (Sutcliffe 1947; Eliassen 1949). The reason for the complication in the nonhydrostatic system is that pressure is no longer tied to the mass through the hydrostatic equation. Also, the continuity equation is prognostic instead of diagnostic as in the quasi-static system.

In isentropic coordinates ($\eta = \theta$), the vertical velocity is $\dot{\eta} = \dot{\theta}$, which is diagnosed from the diabatic heating rate through equation (2.5). In θ-coordinates the vertical velocity diagnosis is the same in both the nonhydrostatic and quasi-static systems.

In summary, the vertical velocity calculation in the nonhydrostatic system is simple with z-coordinates, while in the quasi-static system it is simpler to use the p-coordinate. For the θ-coordinate, the vertical velocity diagnosis is the same in both the nonhydrostatic and quasi-static systems.

2.3 Integral constraints

The equations numerical models solve are approximations of the continuous governing equations. Usually there is sufficient freedom in the finite difference approximations of the governing equations to not only satisfy the convergence criterion, i.e., that as the grid size becomes infinitely small the equations converge to the continuous form, but also to satisfy certain integral properties of the continuous

equations, such as conservation of the global sum of mass, potential temperature, vorticity and total energy. An example of this "mimetic" method can be found in Arakawa and Lamb (1977). This section describes the integral constraints that our numerical scheme will be designed to mimic.

The upper and lower boundaries are assumed to be impermeable; therefore, the boundary conditions are that the vertical mass flux is zero at these boundaries. The generalized vertical coordinate, as well as the generalized vertical velocity, are left undefined in the derivation of the integral properties. The mathematical expression for the impermeable upper and lower boundary conditions will be presented in the following analysis of mass conservation. (Note that in the following derivations, the time and horizontal derivatives will be on constant η-coordinate surfaces, so the subscript η will be omitted from the differential operators unless otherwise necessary.)

2.3.1 Conservation of mass ("Constraint 0")

The global conservation of mass is easy to demonstrate when the flux form of the continuity equation given by (2.19) is used. The goal is to show that $\frac{d}{dt}\int_{\mathcal{V}} m\, d\mathcal{V} = 0$, where $\mathcal{V}$ is the total volume of the domain, and $d\mathcal{V} = dA\, d\eta$ is a differential volume element in η-space. Using the Leibniz integral rule we can write

$$\frac{d}{dt}\int_{\mathcal{V}} m\, d\mathcal{V} = \int_A \left(\int_{\eta_S}^{\eta_T} \frac{\partial m}{\partial t}\, d\eta + m_T \frac{\partial \eta_T}{\partial t} - m_S \frac{\partial \eta_S}{\partial t} \right) dA\,, \tag{2.21}$$

where the subscripts S and T represent the bottom and top boundaries respectively. Applying equation (2.19), this becomes

$$\frac{d}{dt}\int_{\mathcal{V}} m\, d\mathcal{V} = -\int_{A} \nabla \cdot \int_{\eta_S}^{\eta_T} (m\mathbf{v})\, d\eta\, dA \qquad (2.22)$$
$$+\int_{A} m_T \left(\frac{\partial \eta_T}{\partial t} + \mathbf{v}_T \cdot \nabla \eta_T - \dot{\eta}_T \right) dA - \int_{A} m_S \left(\frac{\partial \eta_S}{\partial t} + \mathbf{v}_S \cdot \nabla \eta_S - \dot{\eta}_S \right) dA .$$

The first term on the right-hand side of (2.22) vanishes when integrated over any closed surface or any horizontal domain in which there is no horizontal mass flux at the boundaries. The integrands of the second and third terms on the right-hand side are the vertical mass fluxes at the top and bottom boundaries respectively. We consider that there is no mass flux across the top and bottom boundaries, so these terms are zero, and therefore we have proven that mass is conserved.

2.3.2 Vertically integrated momentum circulation constraint on the HPGF ("Constraint I")

The horizontal pressure gradient force term of the horizontal momentum equation is the largest contributor to the momentum tendency on many scales of atmospheric motion. Therefore its accurate representation in numerical models is important. As will be shown in Section 2.3.3, the HPGF plays an important role in total energy conservation through the conversion term between thermodynamic and kinetic energy. In the design of the discrete system of equations, while we have limited control over the accuracy of the HPGF at a given location, we can express the HPGF in a form which mimics the continuous form in its satisfaction of integral constraints. This is especially important for two-term expressions of the HPGF in the generalized vertical coordinate, as in equation (2.14), in which the error between the opposition of the two large terms with opposite

sign can be large. We now discuss the effect of surface topography, through the HPGF, on the vertically integrated circulation of momentum about a closed contour.

Following Arakawa and Lamb (1977), we wish to derive a useful expression for the HPGF that will facilitate the calculation of the vertically integrated momentum tendency. The horizontal pressure gradient force is represented by the first two terms on the right-hand side of the horizontal momentum equation (2.14). Using (2.15) we can express it in the form

$$\begin{aligned} \mathbf{HPGF} &= \frac{1}{mg}\left(-\frac{\partial \phi}{\partial \eta}\nabla p + \frac{\partial p}{\partial \eta}\nabla \phi \right) \\ &= \frac{1}{mg}\left[-\nabla\left(p\frac{\partial \phi}{\partial \eta} \right) + \frac{\partial}{\partial \eta}\left(p\nabla \phi \right) \right], \end{aligned} \tag{2.23}$$

where $\phi \equiv gz$ is the geopotential. Now multiply (2.23) by m and integrate across the vertical domain to get

$$\int_{\eta_S}^{\eta_T} m(\mathbf{HPGF})\, d\eta = -\nabla \int_{\eta_S}^{\eta_T} \left(\frac{p}{g}\frac{\partial \phi}{\partial \eta} \right) d\eta - p_S \nabla z_S , \tag{2.24}$$

where we neglected the upper boundary and used the identity

$$\nabla z_{S,T} = \left(\nabla z \right)_{S,T} + \left(\frac{\partial z}{\partial \eta} \right)_{S,T} \nabla \eta_{S,T} . \tag{2.25}$$

When the line integral of the tangential component of (2.24) is taken along any closed curve, the first term on the right-hand side has a zero contribution because it is a gradient vector. The only contribution to the vertically integrated circulation of momentum comes from the last term, which is called the "mountain torque" term. When the closed curve is a contour of surface topography, it is zero. Also, for $p_s = p_s(z_s)$, the contribution to the line integral is zero.

2.3.3 Conservation of total energy ("Constraint II")

In the absence of diabatic heating and friction the total energy of a fluid system is constant. Total energy is defined as the sum of mechanical and internal energy. Mechanical energy is the sum of the kinetic energy associated with the macroscopic motion of the fluid (i.e., the wind) and the gravitational potential energy. Internal energy is the energy associated with the molecular motion of the fluid. Various conversions can take place between the forms of energy. The rate at which these conversions take place appear in the derivation of the total energy equation as "conversion" terms which cancel out to keep the total energy constant. A method to conserve total energy in a numerical model is to ensure that the discrete analogs of these conversion terms cancel. In the formulation of the discrete equations, which will be shown in the following chapter, the energy conversion terms will be analyzed. For now we derive the continuous form of the energy equations.

2.3.3.1 Kinetic energy equation

The kinetic energy associated with the three-dimensional bulk motion of the air is

$$K = \frac{1}{2}\left(\mathbf{v}\cdot\mathbf{v} + w^2\right). \tag{2.26}$$

In the nonhydrostatic system, the vertical velocity w contributes to the kinetic energy, so we must include the work done by the vertical pressure gradient force (VPGF) in our analysis. From the vertical momentum equation (2.18) we can write

$$\text{VPGF} = -\frac{1}{m}\frac{\partial p}{\partial \eta}. \tag{2.27}$$

Note that in the hydrostatic approximation VPGF $= +g$.

In the development of the vertical discretization, we will consider alternate forms of the HPGF and VPGF expressed in terms of the Exner function instead of pressure. Using the definition of the Exner function given by equation (2.7), we can write

$$d\Pi = \frac{\kappa \Pi}{p} dp \,. \tag{2.28}$$

Using (2.6) and (2.8), the vertical pressure gradient force then becomes

$$\text{VPGF} = -\frac{\rho}{m} \theta \frac{\partial \Pi}{\partial \eta} \,. \tag{2.29}$$

Similarly, the horizontal pressure gradient force may be written

$$\textbf{HPGF} = -\theta \nabla \Pi + \frac{1}{g} \frac{\rho}{m} \theta \frac{\partial \Pi}{\partial \eta} \nabla \phi \,. \tag{2.30}$$

The flux form of the kinetic energy equation is derived from the momentum equations by taking the dot product of $m\mathbf{v}$ and (2.14), and adding mw times (2.18) which, using the notation above, gives

$$\frac{\partial}{\partial t}(mK) + \nabla \cdot (m\mathbf{v}K) + \frac{\partial}{\partial \eta}(m\dot{\eta}K) = m\mathbf{v} \cdot (\text{HPGF}) + mw(\text{VPGF}) - mwg \,, \tag{2.31}$$

where we have neglected friction. The first two terms on the right-hand side represent the kinetic energy generated by the pressure gradient forces. These terms deserve special focus as they have an important role in the consistency of the energy conversion terms in the discretization scheme. The last term on the right-hand side is the rate of energy conversion between kinetic and geopotential energy.

Now we analyze the work done by the pressure-gradient force. From equations (2.15), (2.20) and (2.23) we get

$$m\mathbf{v}\cdot(\mathbf{HPGF}) = -m\alpha\omega - \frac{\partial}{\partial\eta}\left(\frac{p}{g}\frac{\partial\phi}{\partial t}\right) + \frac{\partial}{\partial t}\left(\frac{p}{g}\frac{\partial\phi}{\partial\eta}\right) + w\frac{\partial p}{\partial\eta}, \tag{2.32}$$

where

$$\omega \equiv \frac{Dp}{Dt}. \tag{2.33}$$

From equation (2.27), the work done by the vertical pressure gradient force is simply

$$mw(\text{VPGF}) = -w\frac{\partial p}{\partial\eta}. \tag{2.34}$$

Adding equations (2.32) and (2.34) we get the work done by the pressure gradient force as

$$m\mathbf{v}\cdot(\mathbf{HPGF}) + mw(\text{VPGF}) = -m\alpha\omega - \frac{\partial}{\partial\eta}\left(\frac{p}{g}\frac{\partial\phi}{\partial t}\right) + \frac{\partial}{\partial t}\left(\frac{p}{g}\frac{\partial\phi}{\partial\eta}\right). \tag{2.35}$$

Plugging (2.35) into (2.31), the kinetic energy equation becomes

$$\frac{\partial}{\partial t}(mK) + \nabla\cdot(m\mathbf{v}K) + \frac{\partial}{\partial\eta}(m\dot{\eta}K) = -m\alpha\omega - \frac{\partial}{\partial\eta}\left(\frac{p}{g}\frac{\partial\phi}{\partial t}\right) + \frac{\partial}{\partial t}\left(\frac{p}{g}\frac{\partial\phi}{\partial\eta}\right) - mwg. \tag{2.36}$$

As will be seen shortly, the first term on the right-hand side is the conversion term between thermodynamic and kinetic energy, and the last term on the right-hand side is the conversion term between kinetic and geopotential energy.

2.3.3.2 Internal energy equation

The processes that directly affect the internal energy of a fluid parcel are heating and work done by the parcel through expansion. The first law of thermodynamics states that the rate of change of the internal energy is equal to the difference between the heat

added to the parcel and the work done by the parcel. For quasiequilibrium, frictionless processes this is expressed as

$$\frac{De}{Dt} = Q - p\frac{D\alpha}{Dt}. \tag{2.37}$$

where α is the specific volume. Here e is the internal energy which can be expressed as $c_v T$, where c_v is the specific heat at constant volume. Equation (2.37) can be converted to a flux form by multiplying by the pseudo-density m, applying equations (2.15), (2.19), and the product rule of differentiation to get

$$\begin{aligned}\frac{\partial}{\partial t}(me) + \nabla\cdot(m\mathbf{v}e) + \frac{\partial}{\partial \eta}(m\dot{\eta}e) = mQ + m\alpha\omega \\ -\frac{\partial}{\partial t}\left(\frac{p}{g}\frac{\partial\phi}{\partial\eta}\right) - \nabla\cdot\left(\frac{p}{g}\frac{\partial\phi}{\partial\eta}\mathbf{v}\right) - \frac{\partial}{\partial\eta}\left(\frac{p}{g}\frac{\partial\phi}{\partial\eta}\dot{\eta}\right).\end{aligned} \tag{2.38}$$

Note that the second term on the right-hand side is the conversion term between thermodynamic and kinetic energy which now appears with the opposite sign as in equation (2.36). Equation (2.38) can be rewritten in terms of enthalpy, defined as $h \equiv e + p\alpha$, for which $dh = c_p\, dT$. It becomes

$$\frac{\partial}{\partial t}\left(mc_p T\right) + \nabla\cdot\left(m\mathbf{v}c_p T\right) + \frac{\partial}{\partial\eta}\left(m\dot{\eta}c_p T\right) = mQ + m\alpha\omega. \tag{2.39}$$

Finally, it can be shown that the internal energy equation can be written as the potential temperature prediction equation (2.5), which is the form of the thermodynamic energy equation used in the model. This is done by using the relation $de = c_v dT$ in equation (2.37), and using the ideal gas law $p\alpha = RT$ and the definition of potential temperature $\theta = T\left(p_0/p\right)^{\kappa}$, which gives equation (2.5).

2.3.3.3 Geopotential energy equation

The rate of change of a fluid parcel's geopotential is calculated by multiplying *mg* by equation (2.20) and using the continuity equation (2.19) to get

$$\frac{\partial}{\partial t}(m\phi) + \nabla \cdot (m\mathbf{v}\phi) + \frac{\partial}{\partial \eta}(m\dot{\eta}\phi) = mwg\,. \tag{2.40}$$

Now note the energy conversion term between kinetic energy and geopotential energy *mwg* which appears with the opposite sign as in equation (2.36).

2.3.3.4 Total energy equation

The total energy equation is obtained by adding equations (2.36), (2.38), and (2.40), and canceling terms to get

$$\frac{\partial}{\partial t}(m\varepsilon) + \nabla \cdot (m\mathbf{v}\varepsilon) + \frac{\partial}{\partial \eta}(m\dot{\eta}\varepsilon) = mQ - \nabla \cdot \left(\frac{p}{g}\frac{\partial \phi}{\partial \eta}\mathbf{v} \right) - \frac{\partial}{\partial \eta}\left[\frac{p}{g}\left(\frac{\partial \phi}{\partial t} + \dot{\eta}\frac{\partial \phi}{\partial \eta} \right) \right], \tag{2.41}$$

where $\varepsilon \equiv c_v T + K + \phi$ is the total energy. The last two terms on the right-hand side are flux divergence terms that represent the spatial redistribution of energy. When integrated over the domain, they contribute nothing to the global total energy budget except for contributions from the boundaries. The time rate of change of the global mass-weighted integral of total energy for an adiabatic atmosphere is obtained by integrating (2.41) over the domain and requiring that no mass cross the upper and lower boundaries. A necessary identity is

$$\frac{\partial z_{S,T}}{\partial t} = \left(\frac{\partial z}{\partial t} \right)_{S,T} + \left(\frac{\partial z}{\partial \eta} \right)_{S,T} \frac{\partial \eta_{S,T}}{\partial t}\,. \tag{2.42}$$

The result is

$$\frac{d}{dt}\int_V m\varepsilon\, dV = -\int_A \nabla\cdot\int_{\eta_S}^{\eta_T}(m\mathbf{v}\varepsilon)\,d\eta\, dA - \int_A \nabla\cdot\int_{\eta_S}^{\eta_T}\left(\frac{p}{g}\frac{\partial\phi}{\partial\eta}\mathbf{v}\right)d\eta\, dA$$
$$-\int_A p_T\frac{\partial z_T}{\partial t}dA + \int_A p_S\frac{\partial z_S}{\partial t}dA. \tag{2.43}$$

For a closed surface, the first two terms are identically zero. The last two terms are the work done by the pressure force at the upper and lower boundaries. These terms would have a contribution over the ocean where waves keep the lower boundary in motion, but we will assume that the boundaries are fixed, so these terms are zero. Therefore, we have proven that for an adiabatic, frictionless atmosphere, the global total energy is conserved.

2.4 A summary of the continuous system of equations

Here we summarize the governing equations in the generalized vertical coordinate as well as the boundary conditions. We discuss system closure and begin to introduce the specification of the generalized vertical coordinate η and diagnosis of the generalized vertical velocity $\dot{\eta}$. From this point forward we will assume that the top and bottom boundaries are generalized vertical coordinate surfaces, i.e., η_T=constant and η_S=constant. Therefore, from equation (2.22), the impermeable upper and lower boundary conditions are expressed as

$$\left(m\dot{\eta}\right)_T = \left(m\dot{\eta}\right)_S = 0\,. \tag{2.44}$$

Continuity equation:

$$\frac{\partial m}{\partial t} + \nabla\cdot(m\mathbf{v}) + \frac{\partial}{\partial\eta}(m\dot{\eta}) = 0\,. \tag{2.45}$$

Horizontal momentum equation:

$$\frac{D\mathbf{v}}{Dt} + f\mathbf{k}\times\mathbf{v} = -\frac{1}{\rho}\nabla p + \frac{1}{m}\frac{\partial p}{\partial \eta}\nabla z + \mathbf{F}\,, \tag{2.46}$$

where

$$\frac{D}{Dt} = \frac{\partial}{\partial t} + \mathbf{v}\cdot\nabla + \dot{\eta}\frac{\partial}{\partial \eta}\,. \tag{2.47}$$

Vertical momentum equation:

$$\frac{Dw}{Dt} = -\frac{1}{m}\frac{\partial p}{\partial \eta} - g + F_z\,. \tag{2.48}$$

Thermodynamic energy equation:

$$\frac{D\theta}{Dt} = \frac{Q}{\Pi}\,. \tag{2.49}$$

Geopotential equation:

$$\frac{D\phi}{Dt} = wg\,. \tag{2.50}$$

Ideal gas law:

$$p = \rho RT\,. \tag{2.51}$$

Definition of the Exner function:

$$\Pi \equiv c_p\left(\frac{p}{p_0}\right)^{\kappa}\,. \tag{2.52}$$

Definition of potential temperature:

$$\theta \equiv \frac{c_p T}{\Pi}\,. \tag{2.53}$$

Definition of pseudo-density:

$$m \equiv \frac{\rho}{g}\frac{\partial \phi}{\partial \eta}. \tag{2.54}$$

Relation between geopotential and height:

$$\phi = gz\,. \tag{2.55}$$

We introduce a normalized height variable:

$$\sigma \equiv \frac{z - z_S}{z_T - z_S}\,. \tag{2.56}$$

This is a terrain-following variable which has the value σ=0 at the surface and σ=1 at the model top. It is based on the pressure-based σ coordinate of Phillips (1957), and is similar to the z-based terrain-following coordinate of Gal-Chen and Somerville (1975).

Finally, we introduce the definition of the vertical coordinate in terms of a relationship between θ and σ to be specified in the next subsection:

$$\eta \equiv f(\theta, \sigma). \tag{2.57}$$

Equations (2.45), (2.46), and (2.48)-(2.57) represent a system of 12 equations in 12 unknowns, i.e., the dependent variables: $\mathbf{v}, w, m, \theta, \phi, z, p, \rho, T, \Pi, \sigma, \dot{\eta}$. The independent variables are the three spatial coordinates x, y and η, and time t. In the present dynamical analysis we do not consider the heating (Q) and friction ($\mathbf{F}$ and F_z) to be unknowns as these are obtained from physics parameterizations.

2.5 Specification of the vertical coordinate and diagnosis of the vertical velocity

Up to this point, we have not specified the form of the vertical coordinate η, other than prescribing the upper and lower boundaries as coordinate surfaces. In this section

we describe how it is defined in the model and explain the method for diagnosing the vertical velocity $\dot{\eta}$.

2.5.1 The vertical coordinate

The starting point for designing our vertical coordinate is the work of Konor and Arakawa (1997), hereafter KA97. As with various hybrid vertical coordinate models, they take advantage of the quasi-Lagrangian nature of the θ-coordinate as much as possible in the free atmosphere. Near the surface, the coordinate is terrain-following to avoid coordinate intersections with the lower boundary. Also, since θ may have a vertically constant value due to a mixed layer, the σ coordinate provides vertical resolution for resolving boundary layer processes. Like KA97, the basis for our vertical coordinate is a prescribed function (equation (2.57)) of θ and the terrain-following height-based coordinate σ defined in equation (2.56).

In the free atmosphere, on the fine scales that we wish to resolve with our nonhydrostatic model, localized turbulence can develop in which the vertical profile of θ is highly nonmonotonic. Although the vertical coordinate of KA97 can remain monotonic for such cases, it does so at a significant expense to the quasi-Lagrangian quality of the coordinate throughout the domain. Therefore, we have generalized their method to accommodate localized static instabilities, i.e., where $\partial\theta/\partial z<0$, while elsewhere retaining the coordinate as pure θ. Our method includes techniques similar to the arbitrary Lagrangian-Eulerian (ALE) scheme of Hirt et al. (1974), and is influenced by the adaptive vertical coordinate approach of Zangl (2007).

Before fully describing the method, we briefly review the vertical coordinate developed by KA97. (Note that we denote the coordinate by η in place of their designation of ζ). KA97 defines the vertical coordinate as

$$\eta \equiv F(\theta,\sigma) \equiv f(\sigma) + g(\sigma)\theta\,, \tag{2.58}$$

where the functions $f(\sigma)$ and $g(\sigma)$ are chosen such that

$$\left.\begin{array}{ll} g(\sigma) \to 0; & \sigma \to \sigma_S \\ f(\sigma) \to 0, \quad g(\sigma) \to 1; & \sigma \to \sigma_T \end{array}\right\}. \tag{2.59}$$

They also must facilitate the condition that the coordinate increase monotonically with height, that is

$$\frac{\partial \eta}{\partial \sigma} > 0\,. \tag{2.60}$$

The monotonicity requirement (2.60) can be achieved if $f(\sigma)$ and $g(\sigma)$ satisfy the relation

$$\frac{df}{d\sigma} + \frac{dg}{d\sigma}\theta_{\min} + g\left(\frac{\partial \theta}{\partial \sigma}\right)_{\min} = 0\,, \tag{2.61}$$

where $g(\sigma)$ is chosen as a monotonically increasing function of σ, and $\theta_{\min}$ and $(\partial\theta/\partial\sigma)_{\min}$ are suitably chosen constants representing the lower bounds of the potential temperature and static stability, respectively. Equation (2.61) is solved for the function $f(\sigma)$. The form of $g(\sigma)$ that we use in the model is

$$g(\sigma) = 1 - (1-\sigma)^r\,, \tag{2.62}$$

where r is a constant greater than unity. This choice satisfies (2.59), and the thickness of the σ-like domain near the surface can be controlled by the value of r – the larger its value, the nearer the surface the coordinate becomes fully isentropic. In KA97, the

function $g(\sigma)$ is expressed in terms of an exponential function. The power function we use in (2.62) achieves basically the same result.

In KA97 the derivation of the vertical mass flux diagnosis is based on the requirement that the value of F given by (2.58) remain constant on level surfaces, that is

$$\left(\frac{\partial}{\partial t}\right)_{\eta} F(\theta,\sigma) = 0\,. \tag{2.63}$$

This maintains the monotonicity of the vertical coordinate η in time.

In our generalized method, we allow $F(\theta,\sigma)$ to deviate from η, as needed, to allow the vertical profile of η to remain monotonic for non-monotonic F. We do so by employing an adaptive vertical grid technique similar to He (2002) and Zangl (2007), which allows the coordinate to be fully isentropic except where isentropes tend to overturn or become irregularly distributed horizontally. The vertical coordinate η is therefore a "target value" for the function $F(\theta,\sigma)$, instead of its specification. The starting point for diagnosing the vertical mass flux, corresponding to equation (2.63), is

$$\left(\frac{\partial}{\partial t}\right)_{\eta} F(\theta,\sigma) = \frac{\eta - F(\theta,\sigma)}{\tau} - \dot{\eta}_S \frac{\partial F}{\partial \eta}\,, \tag{2.64}$$

where τ is a relaxation time constant, and η is the vertical coordinate, which behaves as the target value for $F(\theta,\sigma)$. The first term on the right-hand side serves to relax the value of F toward the target value. The second term on the right-hand side acts to force F away from η in order to maintain coordinate monotonicity. The specification of $\dot{\eta}_S$, which is the "smoothing" portion of the total vertical velocity $\dot{\eta}$, will be described below. When

the target has been met, and $\dot{\eta}_S = 0$, then the right-hand side of (2.64) is zero and we have equation (2.63). The system is then equivalent to KA97.

We now discuss the mechanisms by which $F(\theta,\sigma)$ is forced away from η. Basically the coordinate system and vertical mass flux diagnosis follows KA97 until either the geopotential height on coordinate surfaces becomes horizontally irregular, i.e., when

$$\left|\nabla^4 z\right| > \left(\nabla^4 z\right)_{\max}, \tag{2.65}$$

or when the "relative vertical curvature" of the z-profile becomes large, i.e., when

$$\left|\frac{\dfrac{\partial^2 z}{\partial \eta^2}}{\dfrac{\partial z}{\partial \eta}}\right| > \left(\frac{\dfrac{\partial^2 z}{\partial \eta^2}}{\dfrac{\partial z}{\partial \eta}}\right)_{\max}. \tag{2.66}$$

The $(\ )_{\max}$ values in the above equations are specified maximum limits. Equation (2.65) describes the "horizontal smoothness" criterion, and is designed to limit the existence of sharp horizontal gradients and their associated truncation errors in the discrete model. Equation (2.66) is the "vertical smoothness" criterion which eliminates the possibility of z and therefore η from becoming non-monotonic (overturning) with height, and in the discrete model, it prevents the relative difference in thickness of adjacent layers from becoming too large. It basically serves to keep the distribution of layer thicknesses in a model column evenly distributed.

The mathematical form of the "vertical smoothness" criterion of equation (2.66) is derived from the above statement about the relative difference in thickness of adjacent layers in a discrete model. Figure 2.1 shows a representative continuous relationship

between z and η. Three points are shown along the curve which represent discrete model locations. The relative difference in thickness of adjacent layers is expressed by the nondimensional parameter

$$\frac{\delta^2 z}{\delta z} \equiv \frac{\left(z_3 - z_2\right) - \left(z_2 - z_1\right)}{\frac{1}{2}\left(z_3 - z_1\right)}, \tag{2.67}$$

where the δ^2 operator refers to the difference operator δ recursively applied twice. Applying a Taylor series expansion to (2.67) we get

$$\frac{\delta^2 z}{\delta z} = \frac{\frac{1}{2}\left(\frac{\partial^2 z}{\partial \eta^2}\right)_2 \left[\left(\delta\eta\right)_B^{\,2} + \left(\delta\eta\right)_A^{\,2}\right] + \left(\frac{\partial z}{\partial \eta}\right)_2 \left[\left(\delta\eta\right)_B - \left(\delta\eta\right)_A\right] + \cdots}{\left(\frac{\partial z}{\partial \eta}\right)_2 \frac{1}{2}\left[\left(\delta\eta\right)_B + \left(\delta\eta\right)_A\right] + \frac{1}{4}\left(\frac{\partial^2 z}{\partial \eta^2}\right)_2 \left[\left(\delta\eta\right)_B^{\,2} - \left(\delta\eta\right)_A^{\,2}\right] + \cdots}, \tag{2.68}$$

where the subscript "2" denotes continuous derivatives at the discrete point "2", $(\delta\eta)_A \equiv \eta_2 - \eta_1$ and $(\delta\eta)_B \equiv \eta_3 - \eta_2$. For $(\delta\eta)_A = (\delta\eta)_B = (\delta\eta)$, and truncating the Taylor series, we have

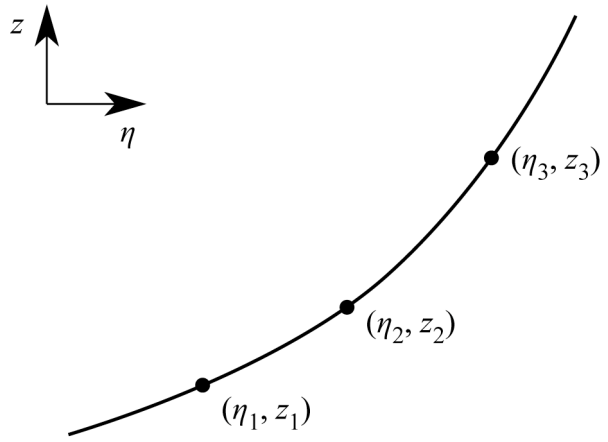


Figure 2.1: Three discrete points along a continuous profile of z as a function of η. Used to derive the mathematical form of the "vertical smoothness parameter".

$$\frac{\delta^2 z}{\delta z} \cong \frac{\left(\frac{\partial^2 z}{\partial \eta^2}\right)}{\left(\frac{\partial z}{\partial \eta}\right)}(\delta\eta), \tag{2.69}$$

which is the mathematical representation of the "vertical smoothness" parameter.

As mentioned in Chapter 1, one of the reasons for spatially smooth the coordinate isolines is to limit the magnitude of spatial gradients in the prognostic variable fields. This is to avoid large truncation errors associated with the representation of sharp gradients in the model's numerical schemes. We speculate that this is the root cause of problems with the model run with pure θ coordinates in regions where isentropes are about to overturn. Figure 2.2 shows model results of a two-dimensional mountain wave experiment to be presented in Chapter 5. The pseudo-density field is plotted in

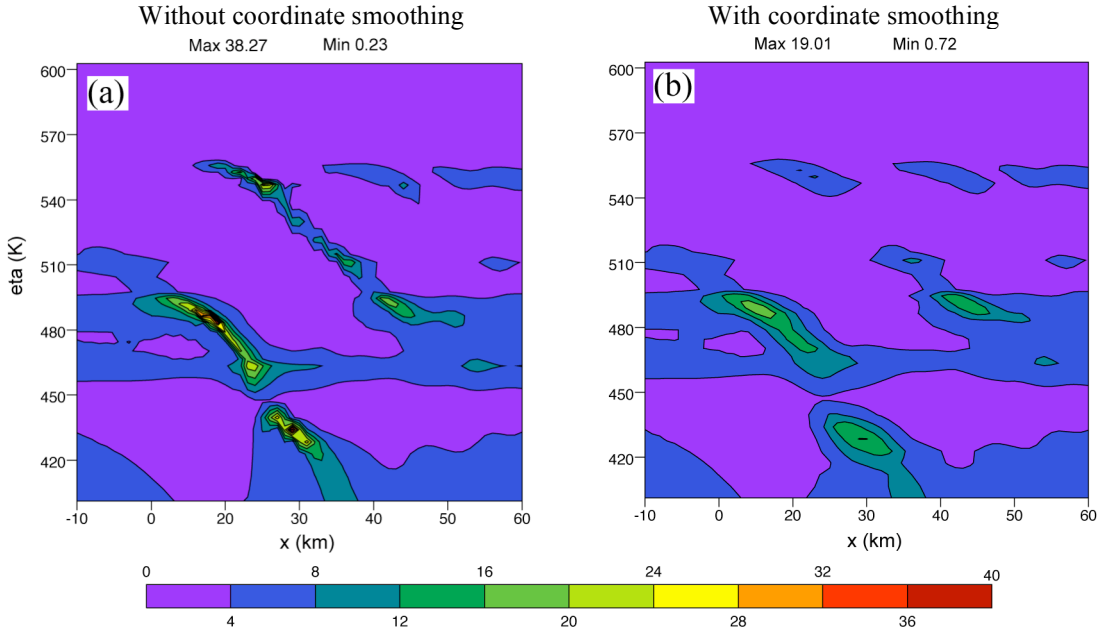


Figure 2.2: Pseudo-density ($\mathrm{kg\,m^{-2}\,K^{-1}}$) at time $t = 78$ minutes in a region of wave-breaking from the 11 January 1972 Boulder, Colorado windstorm simulation to be presented in Chapter 5. Panel (a) shows results without coordinate smoothing, and panel (b) is with coordinate smoothing applied.

η-coordinate space, with and without coordinate smoothing applied, in a region where gravity waves are about to break in the θ-coordinate domain. The spatial gradients in the field are reduced as a result of coordinate smoothing. Therefore, we expect that the numerical accuracy of processes such as mass advection to be improved.

We point out here that the smoothing applied to the geopotential height field does not affect the governing equations, and therefore, the representation of physical processes in the model. That is, we are not adding artificial terms to the geopotential equation (2.50). Instead, we adjust the fields through the appropriate values of vertical velocity and the associated vertical advection. The method of calculating the vertical velocity is the topic of the following subsection. Also, we point out that in smoothing the geopotential we break the relationship given by (2.58), yet the vertical coordinate could still be expressed as some function (f) of θ and σ, as in (2.57), to mathematically close the system. However, it is not necessary to formally calculate this relationship since the equations are self-consistent and they share the same vertical velocity field $\dot{\eta}$.

2.5.2 Diagnosis of the vertical velocity

In this subsection we describe the diagnosis of the vertical velocity that is consistent with the above treatment of the vertical coordinate. As the vertical velocity has multiple roles to play, it is best to subdivide it into separate components. The broadest distinction of the roles is between: 1) the "target seeking" component which maintains the relationship (2.58) (as in KA97) or relaxes the system back toward this relationship, which we designate as $\dot{\eta}_T$, and 2) the "smoothing" component which is

responsible for smoothing the geopotential height field, which we designate as $\dot{\eta}_S$. Note that this second component appeared in equation (2.64). The total vertical velocity is expressed as

$$\dot{\eta} = \dot{\eta}_T + \dot{\eta}_S . \tag{2.70}$$

2.5.2.1 "Target-seeking" component of the vertical velocity

First we consider the tendencies of θ and σ due to $\dot{\eta}_T$. Applying the chain rule of differentiation to equation (2.64), letting $\dot{\eta}_S = 0$, we have

$$\left(\frac{\partial}{\partial t}\right)_\eta F(\theta,\sigma) = \left(\frac{\partial F}{\partial \theta}\right)_\sigma \frac{\partial \theta}{\partial t} + \left(\frac{\partial F}{\partial \sigma}\right)_\theta \frac{\partial \sigma}{\partial t} = \frac{\eta - F(\theta,\sigma)}{\tau} . \tag{2.71}$$

Combining equations (2.47), (2.49), (2.50), (2.55) and (2.56) in (2.71), and solving for the vertical velocity, we get

$$\dot{\eta}_T = \left(\frac{\partial F}{\partial \eta}\right)^{-1}\left[\left(\frac{\partial F}{\partial \theta}\right)_\sigma\left(\frac{Q}{\Pi} - \mathbf{v}\cdot\nabla\theta\right) + \left(\frac{\partial F}{\partial \sigma}\right)_\theta\left(\frac{w}{H} - \frac{1}{gH}\mathbf{v}\cdot\nabla\phi\right) + \frac{F(\theta,\sigma)-\eta}{\tau}\right], \tag{2.72}$$

where

$$\frac{\partial F}{\partial \eta} = \frac{\partial \theta}{\partial \eta}\left(\frac{\partial F}{\partial \theta}\right)_\sigma + \frac{1}{gH}\frac{\partial \phi}{\partial \eta}\left(\frac{\partial F}{\partial \sigma}\right)_\theta , \tag{2.73}$$

and

$$H \equiv z_T - z_S , \tag{2.74}$$

is the height of the model column. Note that $\partial F/\partial\eta$ is equal to unity when F meets its target value, i.e., for $F=\eta$. However, when the target value is not met, it is possible for this term to equal zero in the case of $F\cong\theta$, and neutrally static environments

where $\partial\theta/\partial\eta \cong 0$. In this case the vertical velocity becomes infinite. (A physical interpretation for the case of a passing gravity wave, in which isentropes are nearly vertical, is that the vertical velocity tries to become infinite in order to vertically advect z fast enough to keep the level "stuck" to its target isentrope.) Therefore, we must modify the expression for the vertical velocity given by (2.72) to avoid the existence of such a singularity. We have considerable freedom in such a modification, so we can choose to have it effect the vertical velocity to position isolines of constant η in a particular manner. A straightforward choice is to "freeze" the isolines in space, such that $\partial\phi/\partial t = 0$, as $\partial\theta/\partial\eta$ approaches zero and for $\partial\theta/\partial\eta < 0$. In other words, the coordinate becomes a stationary, Eulerian coordinate in regions of negative static stability. The value of the vertical velocity which maintains $\partial\phi/\partial t = 0$, which we will use for $\partial F/\partial\eta \le 0$, is given by

$$\dot{\eta}_T = \left(\frac{\partial\phi}{\partial\eta}\right)^{-1}\left(wg - \mathbf{v}\cdot\nabla\phi\right) \qquad \text{for } \frac{\partial F}{\partial\eta} \le 0\,. \tag{2.75}$$

For $\partial F/\partial\eta \ge \beta$ we use equation (2.72), where β has a value, which we choose, between 0 and 1. For the transition zone where $0 < \partial F/\partial\eta < \beta$, we use a linear combination of (2.75) and (2.72) evaluated with $\partial F/\partial\eta = \beta$, i.e.,

$$\dot{\eta}_T = \left(1 - \frac{1}{\beta}\frac{\partial F}{\partial\eta}\right)\left(\text{r.h.s. eqn. (2.74)}\right) + \frac{1}{\beta}\frac{\partial F}{\partial\eta}\left(\text{r.h.s. eqn. (2.72) for } \frac{\partial F}{\partial\eta} = \beta\right) \qquad \text{for } 0 < \frac{\partial F}{\partial\eta} < \beta. \tag{2.76}$$

This gives

$$\dot{\eta}_T = \left(1 - \frac{1}{\beta}\frac{\partial F}{\partial \eta}\right)\left(\frac{\partial \phi}{\partial \eta}\right)^{-1}\left(wg - \mathbf{v}\cdot\nabla\phi\right) + \frac{1}{\beta^2}\frac{\partial F}{\partial \eta}\left[\left(\frac{\partial F}{\partial \theta}\right)_\sigma\left(\frac{Q}{\Pi} - \mathbf{v}\cdot\nabla\theta\right) + \left(\frac{\partial F}{\partial \sigma}\right)_\theta\left(\frac{w}{H} - \frac{1}{gH}\mathbf{v}\cdot\nabla\phi\right) + \frac{F(\theta,\sigma) - \eta}{\tau}\right] \quad (2.77)$$

$$\text{for } 0 < \frac{\partial F}{\partial \eta} < \beta.$$

2.5.2.2 "Smoothing" component of the vertical velocity

The vertical velocity field required to smooth the geopotential height fields, per the criteria described in subsection 2.5.1, can be calculated from

$$\dot{\eta}_S = -\left[\left(\frac{\partial z}{\partial t}\right)_{\text{smoothing},h} + \left(\frac{\partial z}{\partial t}\right)_{\text{smoothing},v}\right]\frac{\partial \eta}{\partial z}, \quad (2.78)$$

where the two terms in brackets are the geopotential height tendencies due to horizontal and vertical smoothing respectively.

We quantify the horizontal smoothing tendency in the form of a "del-4" diffusion equation

$$\left(\frac{\partial z}{\partial t}\right)_{\text{smoothing},h} = -\left(\max\left\{0, \kappa_h\left[\left|\nabla^4 z\right| - \left(\nabla^4 z\right)_{\max}\right]\right\}\text{sgn}\left(\nabla^4 z\right)\right), \quad (2.79)$$

where κ_h is a constant diffusion coefficient. This equation differs from typical diffusion equations in that diffusion acts not to eliminate the fourth-spatial derivative, but instead to limit its absolute value at a specified amount. Unlike He (2002) and Zangl (2007), diffusion only occurs where it is a necessary. In regions where the target vertical coordinate is isentropic, this allows the coordinate to be almost exactly isentropic as long as isentropes are reasonably smooth in the horizontal. The choice of ∇^4 over ∇^2 for the

horizontal diffusion follows from traditional numerical smoothing methods where higher order diffusion is used to selectively remove noise at the smaller scales.

The vertical smoothing tendency is described similarly, except second-order diffusion is used instead. In this case, the lower order-diffusion provided better results. We express the tendency as

$$\left(\frac{\partial z}{\partial t}\right)_{\text{smoothing},v} = \max\left\{0, \kappa_v\left[\left|\frac{\partial^2 z}{\partial \eta^2}\right| - \frac{\partial z}{\partial \eta}\left(\frac{\frac{\partial^2 z}{\partial \eta^2}}{\frac{\partial z}{\partial \eta}}\right)_{\max}\right]\right\}\text{sgn}\left(\frac{\partial^2 z}{\partial \eta^2}\right), \tag{2.80}$$

where κ_v is a constant diffusion coefficient. Vertical diffusion only acts when the absolute value of the ratio of the second and first derivatives of z with respect to η exceeds the specified limit.

2.6 Vertical flux of horizontal momentum in a generalized vertical coordinate

The interaction of atmospheric waves with the mean flow has important implications in weather and climate. Waves transport energy and momentum vertically throughout the atmospheric column. For example, the drag imparted by a mountain range on the airflow can be transported, via gravity waves, through the tropopause and into the stratosphere (and beyond) influencing the strength of the zonal flow (i.e., x-component winds) at these heights. In their influential paper, Eliassen and Palm (1960) analyzed linear wave-mean flow interactions and proposed a theory which determines conditions in which waves will or will not influence the mean flow.

In this section we perform a nonhydrostatic analysis of the vertical momentum transport in a generalized vertical coordinate. In the process, we derive a generalized

form of the Eliassen-Palm (EP) flux. The divergence of the EP flux is an important term in the tendency equation for the mean zonal flow. This will illustrate the different mechanisms in which momentum is transported vertically in the Eulerian (z-coordinate) versus the quasi-Lagrangian (θ-coordinate) frameworks. In the former, it is transported through the vertical eddy mass flux, while in the latter it is through the pressure form drag on isentropic (material) surfaces. Our work follows that of Andrews (1983) who derived the EP flux in isentropic coordinates for quasi-static flow.

In Chapter 5, we will use the expression for the EP flux, derived here, to diagnose the vertical momentum flux in two-dimensional (x-z) mountain wave model simulations. Such model simulations are useful in developing gravity wave drag parameterizations in general circulation models (e.g., Kim 1992, Kim and Arakawa 1995). Performing these experiments using a quasi-Lagrangian vertical coordinate provides a new view of the phenomenon which may be useful for GCM's based on such a coordinate.

We begin by writing the zonal momentum equation. Combining (2.14), (2.17), (2.23) and (2.55) we have

$$\frac{\partial u}{\partial t} + u\frac{\partial u}{\partial x} + v\frac{\partial u}{\partial y} + \dot{\eta}\frac{\partial u}{\partial \eta} - fv = \frac{1}{m}\left[-\frac{\partial}{\partial x}\left(p\frac{\partial z}{\partial \eta}\right) + \frac{\partial}{\partial \eta}\left(p\frac{\partial z}{\partial x}\right)\right] + F_u , \qquad (2.81)$$

where F_u is the zonal component of the friction force. Combining equation (2.81) with the continuity equation (2.19), the zonal momentum equation in flux form can be written as

$$\frac{\partial}{\partial t}(mu) + \frac{\partial}{\partial x}(muu) + \frac{\partial}{\partial y}(muv) + \frac{\partial}{\partial \eta}(mu\dot{\eta}) - fmv = -\frac{\partial}{\partial x}\left(p\frac{\partial z}{\partial \eta}\right) + \frac{\partial}{\partial \eta}\left(p\frac{\partial z}{\partial x}\right) + mF_u . \qquad (2.82)$$

The next step is to take the zonal average of the above equation. The zonal average of a given property a is defined as

$$\overline{a} \equiv \frac{1}{L}\int_{-L/2}^{L/2} a\,dx \tag{2.83}$$

where L is the length of the horizontal domain. Applying (2.83) to equation (2.82) we have

$$\frac{\partial}{\partial t}(\overline{mu}) + \frac{\partial}{\partial y}(\overline{muv}) + \frac{\partial}{\partial \eta}(\overline{mu\dot{\eta}}) - f\overline{mv} = \frac{\partial}{\partial \eta}\left(\overline{p\frac{\partial z}{\partial x}}\right) + \overline{mF_u}\,. \tag{2.84}$$

Here we used

$$\overline{\frac{\partial}{\partial x}(\ )} = 0\,. \tag{2.85}$$

In a similar manner, the zonally averaged continuity equation (2.19) is

$$\frac{\partial}{\partial t}\overline{m} + \frac{\partial}{\partial y}(\overline{mv}) + \frac{\partial}{\partial \eta}(\overline{m\dot{\eta}}) = 0\,. \tag{2.86}$$

Each fluid property can be divided into a mean and perturbation component. That is

$$a = \overline{a} + a'\,, \tag{2.87}$$

where the prime notation represents perturbations from the mean. Under Reynolds averaging, the zonal mean of the perturbation quantities are zero, i.e.,

$$\overline{a'} = 0\,. \tag{2.88}$$

This results in the relation

$$\overline{ma} = \overline{m}\,\overline{a} + \overline{m'a'}\,. \tag{2.89}$$

Applying (2.89) to the combination of equations (2.84) and (2.86), and rearranging terms, we can write the following expression for the tendency of the zonal momentum:

$$\frac{\partial}{\partial t}\bar{u} + \frac{\overline{mv}}{\bar{m}}\left(\frac{\partial}{\partial y}\bar{u} - f\right) + \frac{\overline{m\dot{\eta}}}{\bar{m}}\frac{\partial}{\partial \eta}\bar{u} = \frac{1}{\bar{m}}\left[-\frac{\partial}{\partial y}\overline{(mv)'u'} + \frac{\partial}{\partial \eta}\left[\overline{p'\frac{\partial z'}{\partial x}} - \overline{(m\dot{\eta})'u'}\right] - \frac{\partial}{\partial t}\overline{(m'u')}\right] + \frac{\overline{mF_u}}{\bar{m}}. \tag{2.90}$$

It is useful to introduce the "residual" mean velocities, defined as the mass-weighted means

$$\bar{v}^* \equiv \frac{\overline{mv}}{\bar{m}} \tag{2.91}$$

and

$$\bar{\dot{\eta}}^* \equiv \frac{\overline{m\dot{\eta}}}{\bar{m}}. \tag{2.92}$$

Using these relations, equation (2.90) is then written as

$$\frac{\partial}{\partial t}\bar{u} + \bar{v}^*\left(\frac{\partial}{\partial y}\bar{u} - f\right) + \bar{\dot{\eta}}^*\frac{\partial}{\partial \eta}\bar{u} = \frac{1}{\bar{m}}\left[\nabla^{(\eta)} \cdot \mathbf{F}^{(\eta)} - \frac{\partial}{\partial t}\overline{(m'u')}\right] + \frac{\overline{mF_u}}{\bar{m}}, \tag{2.93}$$

where $\mathbf{F}^{(\eta)} \equiv [0, F^{(\eta)}{}_y, F^{(\eta)}{}_\eta]$ is the EP flux vector in generalized vertical coordinates, which has the meridional and vertical components

$$F^{(\eta)}{}_y = \overline{(mv)'u'} \tag{2.94}$$

and

$$F^{(\eta)}{}_\eta = \overline{p'\frac{\partial z'}{\partial x}} - \overline{(m\dot{\eta})'u'}, \tag{2.95}$$

respectively. Equation (2.93) shows that the EP flux is non-divergent for steady-state, uniform, frictionless flow.

The vertical component of the EP flux given by (2.95) is the vertical flux of horizontal momentum. In z coordinates, the first term on the right-hand side is zero,

which leaves the eddy flux term $-\overline{(\rho w)' u'}$ as the means of vertical momentum transport. In θ coordinates, for adiabatic conditions, $\dot{\eta}' = \dot{\theta}' = 0$, which means the vertical momentum transport occurs through the first term on the right-hand side of (2.95), i.e., the pressure form drag term.

2.7 Summary

The nonhydrostatic, compressible Eulerian equations of fluid motion were transformed from z coordinates to a generalized vertical coordinate η. From these governing equations, we demonstrated various conservation properties such as the conservation of mass, total energy and the vertically integrated circulation of momentum about a closed contour of topography. In the following chapter these integral constraints will guide in the design of the vertical discretization scheme.

The vertical coordinate is terrain-following near the surface and transitions smoothly to θ with height. In the diagnosis of the generalized vertical velocity $\dot{\eta}$, a special contribution is calculated and included in the vertical advection terms; its purpose is to maintain smoothness of the coordinate surfaces. In this "smoothing" process, the values of geopotential and potential temperature on the coordinate surfaces deviate from their defined "target" values. However, these values are returned back to their target values through a Newtonian relaxation term.

The vertical flux of horizontal momentum and its effect on the mean flow was analyzed with the generalized vertical coordinate. In the θ coordinate, a quasi-Lagrangian interpretation is provided in which the vertical momentum flux is a result of

the horizontal component of pressure forces on material coordinate surfaces. This feature will be shown in the results of a mountain wave simulation in Chapter 5.

Chapter 3 VERTICAL DISCRETIZATION

3.1 Introduction

The design of the model's vertical discretization scheme includes determining the optimal arrangement of the prognostic variables on the grid and determining the vertically discrete governing equations. Our design goals for the vertical staggering are to avoid the existence of computational modes and to facilitate the accurate representation of wave motion. These goals are met through a normal mode analysis of the linearized system of discrete equations. A detailed analysis along these lines is provided in Thuburn and Woollings (2005), whose results we use as a guide.

The principal criterion for the formulation of the vertically discrete governing equations is that they satisfy certain integral properties found in the continuous system of equations discussed in Chapter 2. The integral constraints we seek to satisfy are conservation of mass (Constraint 0), conservation of the vertically integrated circulation of momentum about a closed contour of topography (Constraint I), and conservation of total energy (Constraint II). At that point, no degrees of freedom will remain; it turns out that the conservation of potential temperature (Constraint III) will not be met. The methods we follow include those developed by Arakawa and Lamb (1977), Simmons and

Burridge (1981), Hsu and Arakawa (1990), Arakawa and Konor (1996) and KA97 for quasi-static models.

As is often the case in numerical model design, it will turn out not to be possible to meet all of the design criteria simultaneously. We will derive two alternative schemes – the first scheme, which we refer to as the "η-scheme", satisfies integral Constraints 0, I, and II for any form of the generalized vertical coordinate, but has a computational mode involving the thermodynamic variables; the second scheme, referred to as the "z-scheme", supports no computational mode, but integral Constraints 0, I, and II are satisfied only for the case of non-sloping coordinate surfaces, i.e., z-coordinates. In both schemes, however, the mass conservation constraint is satisfied. The discretization we actually decided to implement in the model is the z-scheme. This was to achieve integrations free of computational modes, which we considered to be more important than unconditionally satisfying the integral Constraints I and II.

3.2 Vertical grid

The vertical staggering of the prognostic variables in the model is based on the Charney-Phillips (CP) grid (Charney and Phillips 1953). With this grid, the potential temperature is staggered with respect to the horizontal velocity (see Figure 1.3). The other commonly used staggering is the Lorenz (L) grid (Lorenz 1960) in which the potential temperature is carried at the same levels as the horizontal velocity (see Figure 1.3). The advantages of the CP grid over the L grid have been analyzed in various papers (e.g., Arakawa and Moorthi 1988; Arakawa and Konor 1996). These advantages pertain to quasi-static models based on the pressure coordinate and they involve the

avoidance of a computational mode in the θ field seen in the L grid, but not the CP grid. In the following analysis we show that these advantages carry over to nonhydrostatic z-coordinate models, which are relevant to the lower domain of our model. We also analyze the grid staggering for the θ-coordinate domain of the model.

3.2.1 Linearized, steady-state equations

We now test various vertical staggerings for the existence of zero-frequency computational modes in order to justify the use of the CP grid. The equations of motion are linearized with respect to a hydrostatic, horizontally homogeneous basic state at rest. Since steady-state solutions are sought, we can ignore partial time derivatives. The steady-state vertical momentum equation in generalized vertical coordinates can be obtained from equation (2.18). It is the hydrostatic relation given by

$$\frac{\partial p}{\partial \eta} = -mg\,. \tag{3.1}$$

We will refer to this as the "p-form" hydrostatic relation. We will also consider an alternate "Π-form", written in terms of the Exner function. It is obtained from equations (2.15) and (2.29), and is written as

$$-\theta \frac{\partial \Pi}{\partial \eta} = g \frac{\partial z}{\partial \eta}\,. \tag{3.2}$$

Expressing the dependent variables as the sum of the basic state and perturbation values, the linearized form of the p-form hydrostatic relation (3.1) is

$$\frac{\partial p'}{\partial \eta} = -m'g\,, \tag{3.3}$$

where the prime notation refers to the perturbation values. Here we used the hydrostatic relation on the basic state given by

$$\frac{d\bar{p}}{d\eta} = -\bar{m}g\,, \tag{3.4}$$

where the overbars represent the basic state. Similarly, the linearized form of the Π-form hydrostatic relation (3.2) is

$$-\theta' \frac{d\bar{\Pi}}{d\eta} - \bar{\theta}\frac{\partial \Pi'}{\partial \eta} = g\frac{\partial z'}{\partial \eta}\,, \tag{3.5}$$

where we have neglected products of perturbation variables.

The linearized diagnostic pseudo-density equation (2.15) is

$$m' = \rho' \frac{d\bar{z}}{d\eta} + \bar{\rho}\frac{\partial z'}{\partial \eta}\,, \tag{3.6}$$

where we have used the following expression for the basic state pseudo-density:

$$\bar{m} = \bar{\rho}\frac{d\bar{z}}{d\eta}\,. \tag{3.7}$$

The linearized equation of state (2.6) is

$$\frac{p'}{\bar{p}} = \frac{\rho'}{\bar{\rho}} + \frac{T'}{\bar{T}}\,. \tag{3.8}$$

The linearized expression for the potential temperature, given by the combination of (2.7) and (2.8), is

$$\frac{\theta'}{\bar{\theta}} = \frac{T'}{\bar{T}} - \kappa\frac{p'}{\bar{p}}\,. \tag{3.9}$$

The linearized definition of the Exner function, given by equation (2.7), is

$$\Pi' = \frac{\kappa\bar{\Pi}}{\bar{p}}p'\,. \tag{3.10}$$

In (3.9) and (3.10) we used the linear approximation $\left(1+p'/\bar{p}\right)^{\pm\kappa} \cong 1 \pm \kappa\, p'/\bar{p}$.

3.2.1.1 Discrete linearized equations in *z* coordinates

In height coordinates, $\eta=z$, $m=\rho$ and, by definition, $z'=0$. We use these expressions in the vertically discrete forms of the linearized equations (3.3)-(3.10). In our analysis, we consider both the CP and L grids, each using the *p*-form and Π-form hydrostatic relations. The resulting discrete equations for the four combinations are presented below:

⟨CP grid + *p*-form hydrostatic relation⟩

$$\left.\begin{aligned} &\frac{p'_{k+1}-p'_k}{\delta z} = -\frac{1}{2}\left(\rho'_{k+1}+\rho'_k\right)g, \\ &\frac{p'_k}{\bar{p}_k} = \frac{\rho'_k}{\bar{\rho}_k} + \frac{\mathrm{T}'_k}{\bar{T}_k}, \\ &\frac{1}{\bar{\theta}_\mathrm{k}}\frac{1}{2}\left(\theta'_{k+1/2}+\theta'_{k-1/2}\right) = \frac{T'_k}{\bar{T}_k} - \kappa\frac{p'_k}{\bar{p}_k}; \end{aligned}\right\} \tag{3.11}$$

⟨CP grid + Π-form hydrostatic relation⟩

$$\left.\begin{aligned} \frac{\Pi'_{k+1}-\Pi'_k}{\delta z} &= \frac{g}{\bar{\theta}_\mathrm{k}^{\,2}}\theta'_{k+1/2}, \\ \frac{p'_k}{\bar{p}_k} &= \frac{\rho'_k}{\bar{\rho}_k} + \frac{\mathrm{T}'_k}{\bar{T}_k}, \\ \frac{1}{\bar{\theta}_\mathrm{k}}\frac{1}{2}\left(\theta'_{k+1/2}+\theta'_{k-1/2}\right) &= \frac{T'_k}{\bar{T}_k} - \kappa\frac{p'_k}{\bar{p}_k}, \\ \Pi'_k &= \frac{\kappa\bar{\Pi}_k}{\bar{p}_k}\,p'; \end{aligned}\right\} \tag{3.12}$$

⟨L grid + p-form hydrostatic relation⟩

$$\left.\begin{aligned} \frac{p'_{k+1}-p'_k}{\delta z} &= -\frac{1}{2}\left(\rho'_{k+1}+\rho'_k\right), \\ \frac{p'_k}{\bar{p}_k} &= \frac{\rho'_k}{\bar{\rho}_k}+\frac{\mathrm{T}'_k}{\bar{T}_k}, \\ \frac{\theta'_k}{\bar{\theta}_{\mathrm{k}}} &= \frac{T'_k}{\bar{T}_k}-\kappa\frac{p'_k}{\bar{p}_k}; \end{aligned}\right\} \tag{3.13}$$

⟨L grid + Π-form hydrostatic relation⟩

$$\left.\begin{aligned} \frac{\Pi'_{k+1}-\Pi'_k}{\delta z} &= \frac{g}{\bar{\theta}_{\mathrm{k}}^{\,2}}\frac{1}{2}\left(\theta'_{k+1}+\theta'_k\right), \\ \frac{p'_k}{\bar{p}_k} &= \frac{\rho'_k}{\bar{\rho}_k}+\frac{\mathrm{T}'_k}{\bar{T}_k}, \\ \frac{\theta'_k}{\bar{\theta}_{\mathrm{k}}} &= \frac{T'_k}{\bar{T}_k}-\kappa\frac{p'_k}{\bar{p}_k}, \\ \Pi'_k &= \frac{\kappa\bar{\Pi}_k}{\bar{p}_k}p'_k. \end{aligned}\right\} \tag{3.14}$$

The subscripts k are whole number indices representing layer centers where mass and horizontal velocity are located. The half-integer indices are layer interfaces. Note that the CP and L grids are distinguished by differing θ grid indices. Note that the hydrostatic relations are defined at layer interfaces where the vertical velocity w resides. Arithmetic means are used to interpolate physical variables to levels where they are undefined. We assume that the grid spacing δz is constant. In each system of equations, the prognostic variables are θ and ρ. The variables p, T and Π, which reside at layer centers, are obtained from the prognostic variables through the diagnostic equations.

The discrete systems of equations (3.11)-(3.14) can be used to check for the existence of computational modes. This is done by considering the pressure field to be

unperturbed, i.e., $p'=0$ at all levels. In z coordinates ($z'=0$), the physical solution, given by the continuous equations (3.3)-(3.10), is that the remaining thermodynamic fields are also unperturbed, i.e., $\theta'=\rho'=\Pi'=T'=0$. (Similarly, in θ coordinates ($\theta'=0$), the solution is that the remaining thermodynamic fields are unperturbed, i.e., $z'=\rho'=\Pi'=T'=0$.) Therefore, solutions in which any of these fields are not identically zero are nonphysical computational modes. In general, these computational modes tend to appear as "zigzag" patterns in one or more of the thermodynamic fields.

Figure 3.1 summarizes the computational mode analysis for each of the four systems of equations shown above. With the L grid there are zero-frequency computational modes in both the perturbation density and potential temperature fields. With the CP grid, the existence of a computational mode depends on the form of the vertical pressure gradient force – there is no computational mode when the Π-form is used. This appears to be due to the absence of interpolated variables in the hydrostatic relation. Therefore, the use of the CP grid to avoid computational modes in z coordinates is justified, as long as the Π-form of the vertical pressure gradient force is used in the vertical momentum equation.

3.2.1.2 Discrete linearized equations in θ coordinates

In isentropic coordinates, $\eta=\theta$, and, by definition, $\theta'=0$. We use these expressions in the vertically discrete forms of the linearized equations (3.3)-(3.10). As in the z-coordinate analysis, we consider both the CP and L grids, each using the p-form and Π-form hydrostatic relations. In θ coordinates, the vertical thermal structure is

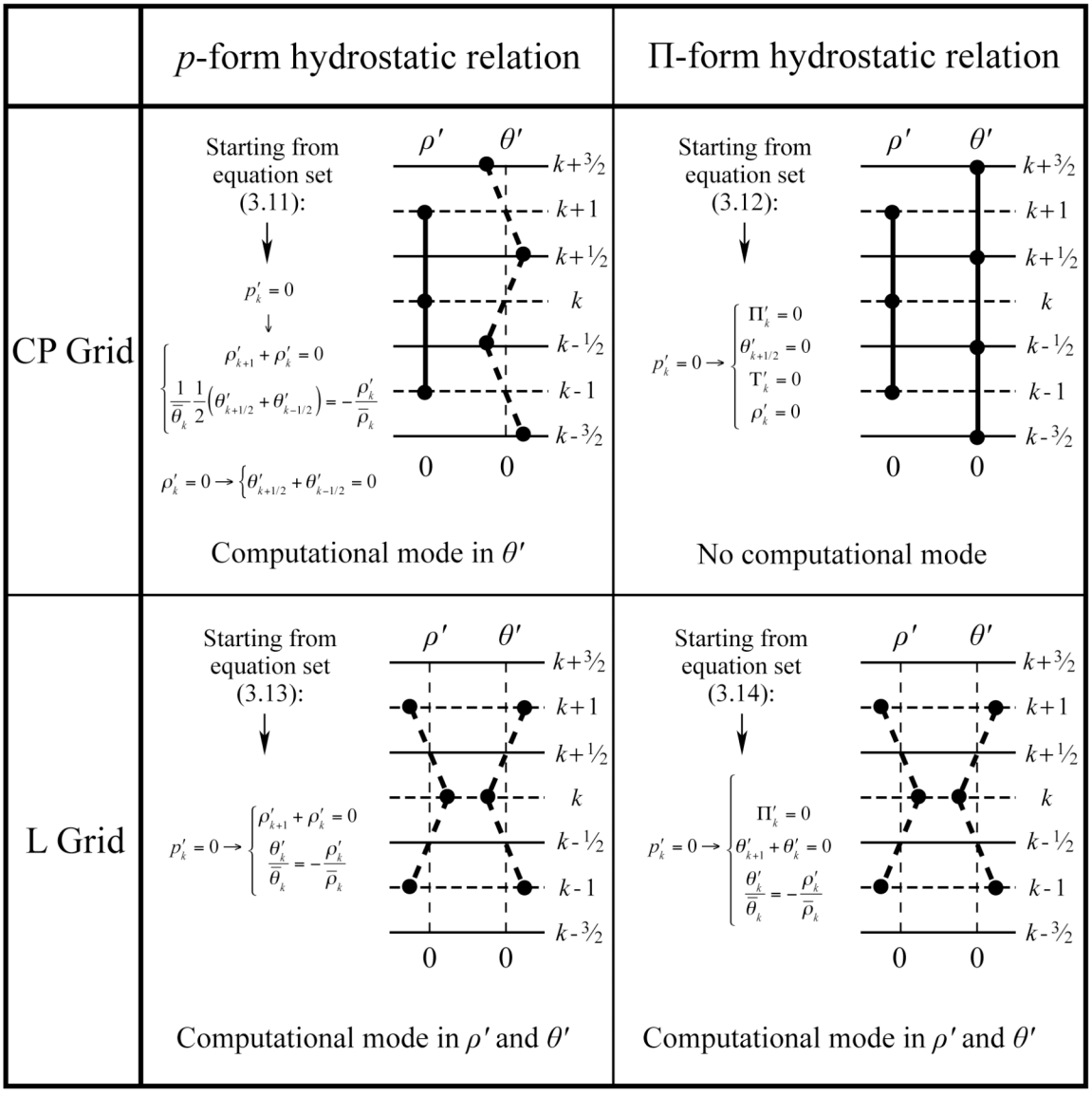


Figure 3.1: Analysis of zero-frequency computational modes in z coordinates. The CP and L grids are compared (rows), as well as the effect on the form of the discrete vertical pressure gradient (columns).

determined by the height field (z). Therefore, we define an analogous CP grid in θ coordinates which carries z at layer edges (i.e., staggered with respect to horizontal velocity), and an analogous L grid which has z located at layer centers. The resulting discrete equations for the four combinations are shown below:

⟨CP grid + p-form hydrostatic relation⟩

$$\left.\begin{aligned} \frac{p'_{k+1}-p'_k}{\delta\theta} &= -\frac{1}{2}\left(m'_{k+1}+m'_k\right)g, \\ \frac{m'_k}{\bar{m}_k} &= \frac{\rho'_k}{\bar{\rho}_k}+\left(\frac{d\bar{z}}{d\theta}\right)_k^{-1}\frac{z'_{k+1/2}-z'_{k-1/2}}{\delta\theta}, \\ \frac{1}{\gamma}\frac{p'_k}{\bar{p}_k} &= \frac{\rho'_k}{\bar{\rho}_k}; \end{aligned}\right\} \tag{3.15}$$

⟨CP grid + Π-form hydrostatic relation⟩

$$\left.\begin{aligned} \frac{1}{2}\frac{z'_{k+3/2}-z'_{k-1/2}}{\delta\theta} &= -\frac{\theta_{k+1/2}}{g}\frac{\Pi'_{k+1}-\Pi'_k}{\delta\theta}, \\ \frac{m'_k}{\bar{m}_k} &= \frac{\rho'_k}{\bar{\rho}_k}+\left(\frac{d\bar{z}}{d\theta}\right)_k^{-1}\frac{z'_{k+1/2}-z'_{k-1/2}}{\delta\theta}, \\ \frac{1}{\gamma}\frac{p'_k}{\bar{p}_k} &= \frac{\rho'_k}{\bar{\rho}_k}, \\ \Pi'_k &= \frac{\kappa\bar{\Pi}_k}{\bar{p}_k}p'_k; \end{aligned}\right\} \tag{3.16}$$

⟨L grid + p-form hydrostatic relation⟩

$$\left.\begin{aligned} \frac{p'_{k+1}-p'_k}{\delta\theta} &= -\frac{1}{2}\left(m'_{k+1}+m'_k\right)g, \\ \frac{m'_k}{\bar{m}_k} &= \frac{\rho'_k}{\bar{\rho}_k}+\left(\frac{d\bar{z}}{d\theta}\right)_k^{-1}\frac{1}{2}\frac{z'_{k+1}-z'_{k-1}}{\delta\theta}, \\ \frac{1}{\gamma}\frac{p'_k}{\bar{p}_k} &= \frac{\rho'_k}{\bar{\rho}_k}; \end{aligned}\right\} \tag{3.17}$$

⟨L grid + Π-form hydrostatic relation⟩

$$\left.\begin{aligned} \frac{z'_{k+1}-z'_k}{\delta\theta} &= -\frac{\theta_{k+1/2}}{g}\frac{\Pi'_{k+1}-\Pi'_k}{\delta\theta}, \\ \frac{m'_k}{\bar{m}_k} &= \frac{\rho'_k}{\bar{\rho}_k}+\left(\frac{d\bar{z}}{d\theta}\right)_k^{-1}\frac{1}{2}\frac{z'_{k+1}-z'_{k-1}}{\delta\theta}, \\ \frac{1}{\gamma}\frac{p'_k}{\bar{p}_k} &= \frac{\rho'_k}{\bar{\rho}_k}, \\ \Pi'_k &= \frac{\kappa\bar{\Pi}_k}{\bar{p}_k}p'_k. \end{aligned}\right\} \tag{3.18}$$

The computational mode analysis is summarized in Figure 3.2. With the θ coordinate, there appear to be computational modes associated with $p'=0$ which involve the perturbation pseudo-density and height fields. Note that the computational mode in z' for the "CP grid + Π-form hydrostatic relation" combination is a result of the $2\Delta z$ difference in z' of the hydrostatic relation in (3.16). With the CP grid, we speculate that the computational modes may be suppressed by the upper and lower boundary conditions $z'=0$. This is not the case with the L grid because z is defined at layer centers where the boundary conditions do not apply. In the model we will use the CP grid in the θ-coordinate domain.

3.2.1.3 Closing remarks

In the previous analysis, we linearized the forms of the governing equations that are used in the model. These are based on the integral constraint analysis presented in the following section. There are other forms of the equations, not analyzed here, that might

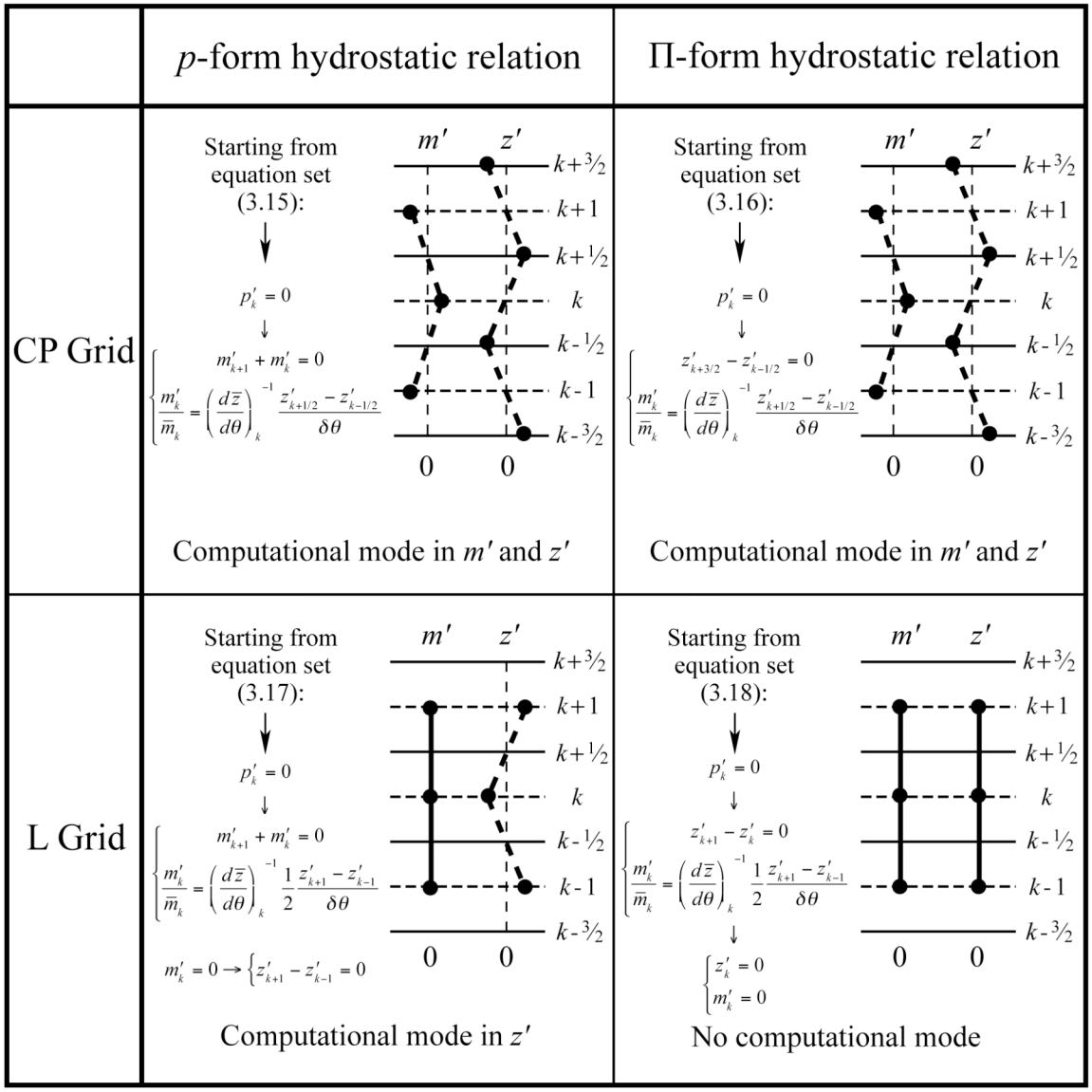


Figure 3.2: Analysis of zero-frequency computational modes in θ coordinates. The CP and L grids are compared (rows), as well as the effect on the form of the discrete vertical pressure gradient (columns). We speculate that the CP grid computational modes may be suppressed by the upper and lower boundary conditions $z'=0$.

avoid computational modes. Potentially, these could satisfy the integral constraints as well. For example, in θ coordinates, the hydrostatic relation can be expressed in terms of the Montgomery potential (M) as $\partial M/\partial\theta=\Pi$, where $M \equiv c_p T+\phi$. Alternative forms of the equations, such as these, deserve future consideration.

3.2.2 Model grid

Figure 3.3 shows the vertical staggering of the prognostic variables used in the model for the three coordinate domains – a) z-based sigma coordinates, b) isentropic coordinates, and c) the hybrid coordinate. These staggerings are based on the CP grid. This places θ and z together at layer edges – the appropriate location for the hybrid vertical coordinate which is a function of these two variables. The indexing convention used in the discretization is the same as that used in the linearized analysis, i.e., layer centers are numbered by whole integers k and layer edges by half-integers. The

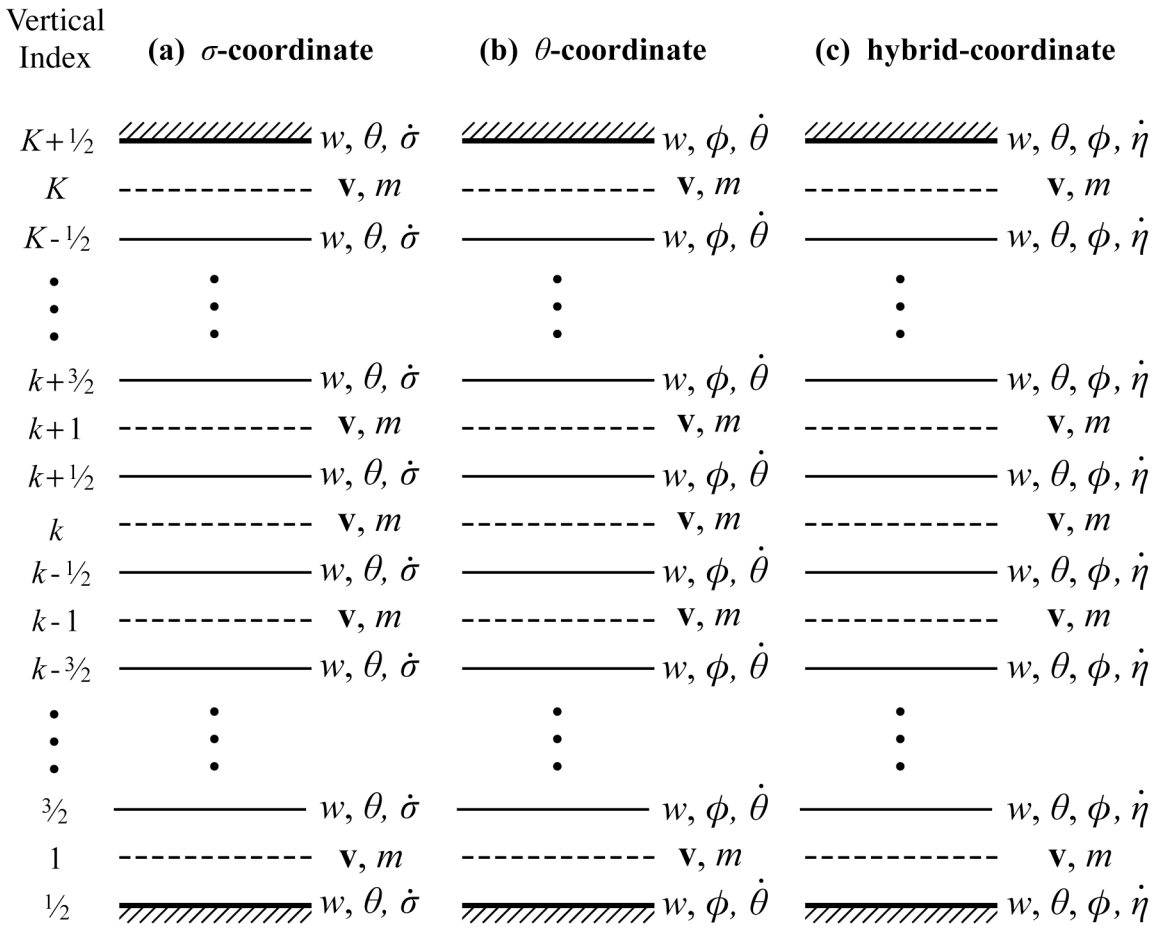


Figure 3.3: Layer indexing and vertical staggering of prognostic variables and diagnosed vertical velocities for (a) σ-coordinate, (b) θ-coordinate and (c) hybrid coordinate discretizations.

numbering of the K layers is from bottom to top.

3.3 Governing equations

3.3.1 Continuity equation

The discretization of the continuity equation is straightforward and is written for the mass at layer centers as

$$\frac{\partial m_k}{\partial t} + \nabla \cdot \left(m\mathbf{v} \right)_k + \frac{\left(m\dot{\eta} \right)_{k+1/2} - \left(m\dot{\eta} \right)_{k-1/2}}{\left(\delta\eta \right)_k} = 0 \qquad \text{for} \quad k = 1, 2, \cdots, K. \tag{3.19}$$

Note that the vertical velocity $\dot{\eta}$ is defined at layer edges, and that for vertical coordinates in which the top and bottom boundaries are coordinate and material surfaces

$$\dot{\eta}_{1/2} = \dot{\eta}_{K+1/2} = 0 . \tag{3.20}$$

Mass conservation (Constraint 0) is guaranteed due to the flux form of equation (3.19).

Following Arakawa and Konor (1996), hereafter AK96, a flux form continuity equation can be written in terms of mass interpolated to layer edges. This facilitates developing conservation properties of layer-edge quantities. The equation is

$$\frac{\partial m_{k+1/2}}{\partial t} + \nabla \cdot \left(m\mathbf{v} \right)_{k+1/2} + \frac{\left(m\dot{\eta} \right)_{k+1} - \left(m\dot{\eta} \right)_k}{\left(\delta\eta \right)_{k+1/2}} = 0 \qquad \text{for} \quad k = 1, 2, \cdots, K-1, \tag{3.21}$$

$$\frac{\partial m_{1/2}}{\partial t} + \nabla \cdot \left(m\mathbf{v} \right)_{1/2} + \frac{\left(m\dot{\eta} \right)_1}{\left(\delta\eta \right)_{1/2}} = 0, \tag{3.22}$$

and

$$\frac{\partial m_{K+1/2}}{\partial t} + \nabla \cdot \left(m\mathbf{v}\right)_{K+1/2} - \frac{\left(m\dot{\eta}\right)_K}{\left(\delta\eta\right)_{K+1/2}} = 0, \tag{3.23}$$

where the interpolated masses are

$$m_{k+1/2} \equiv \frac{1}{2}\frac{\left(\delta\eta\right)_k m_k + \left(\delta\eta\right)_{k+1} m_{k+1}}{\left(\delta\eta\right)_{k+1/2}} \qquad \text{for} \quad k = 1, 2, \cdots, K-1, \tag{3.24}$$

and

$$m_{1/2} \equiv m_1, \qquad m_{K+1/2} \equiv m_K. \tag{3.25}$$

The horizontal mass flux interpolated to layer edges is

$$\left(m\mathbf{v}\right)_{k+1/2} \equiv \frac{1}{2}\frac{\left(\delta\eta\right)_k \left(m\mathbf{v}\right)_k + \left(\delta\eta\right)_{k+1} \left(m\mathbf{v}\right)_{k+1}}{\left(\delta\eta\right)_{k+1/2}} \qquad \text{for} \quad k = 1, 2, \cdots, K-1, \tag{3.26}$$

and

$$\left(m\mathbf{v}\right)_{1/2} \equiv \left(m\mathbf{v}\right)_1, \qquad \left(m\mathbf{v}\right)_{K+1/2} \equiv \left(m\mathbf{v}\right)_K. \tag{3.27}$$

The vertical mass fluxes at layer centers is

$$\left(m\dot{\eta}\right)_k \equiv \frac{1}{2}\left[\left(m\dot{\eta}\right)_{k+1/2} + \left(m\dot{\eta}\right)_{k-1/2}\right] \qquad \text{for} \quad k = 2, 3, \cdots, K-1, \tag{3.28}$$

and

$$\left(m\dot{\eta}\right)_1 \equiv \frac{1}{2}\left(m\dot{\eta}\right)_{1/2}, \qquad \left(m\dot{\eta}\right)_K \equiv \frac{1}{2}\left(m\dot{\eta}\right)_{K-1/2}. \tag{3.29}$$

Finally, the layer thicknesses defined at layer edges are

$$\left(\delta\eta\right)_{k+1/2} \equiv \frac{1}{2}\left[\left(\delta\eta\right)_{k} + \left(\delta\eta\right)_{k+1}\right] \qquad \text{for} \quad k = 1, 2, \cdots, K-1, \tag{3.30}$$

and

$$\left(\delta\eta\right)_{1/2} \equiv \frac{1}{2}\left(\delta\eta\right)_{1}, \qquad \left(\delta\eta\right)_{K+1/2} \equiv \frac{1}{2}\left(\delta\eta\right)_{K}. \tag{3.31}$$

As stated in AK96, it can be shown that the vertical sum of the continuity equation (3.19), for *m* at layer centers, times $(\delta\eta)_k$ is equivalent to the vertical sum of the continuity equations (3.24) and (3.25), for *m* at layer edges, times $(\delta\eta)_{k+1/2}$.

3.3.2 Pressure gradient forces

In nonhydrostatic models, the discretized form of the vertical pressure gradient force (VPGF) requires attention in an analogous manner as the discrete hydrostatic equation in hydrostatic models. In such models the vertical velocity *w* is predicted and its contribution to the kinetic energy is accounted for. As with hydrostatic models, the horizontal pressure gradient force (HPGF) has a role in both the total energy conservation and the vertically integrated momentum circulation conservation integral constraints. We now analyze the pressure gradient forces.

3.3.2.1 Vertical pressure gradient force

The VPGF, expressed at the internal layer edges, is obtained from equation (2.29) as

$$(\text{VPGF})_{k+1/2} = -\frac{\hat{\rho}_{k+1/2}}{m_{k+1/2}}\theta_{k+1/2}\frac{\Pi_{k+1}-\Pi_k}{\left(\delta\eta\right)_{k+1/2}} \qquad \text{for} \quad k = 1, 2, \cdots, K-1, \tag{3.32}$$

where $\hat{\rho}_{k+1/2}$ is the value of density at layer edges. The upper boundary condition on the vertical velocity is $w_{K+1/2} = 0$, and, therefore, it is not necessary to compute the VPGF at the top edge. Doing so would provide a diagnostic relation for the pressure that the model top. However we would like to know what the surface pressure is, so we will need a diagnostic for the VPGF at the lower boundary. We write

$$(\text{VPGF})_{1/2} = -\frac{\hat{\rho}_{1/2}}{m_{1/2}}\theta_{1/2}\frac{\Pi_1-\hat{\Pi}_{1/2}}{\left(\delta\eta\right)_{1/2}}, \tag{3.33}$$

where $\hat{\Pi}_{1/2}$ is the surface Exner function, from which the surface pressure can be calculated.

3.3.2.2 Horizontal pressure gradient force

We discretize the HPGF, as given by equation (2.30), at layer centers to give

$$(\mathbf{HPGF})_k = -\tilde{\theta}_k\nabla\Pi_k + \frac{1}{\mathrm{g}}\left(\widetilde{\frac{\rho}{m}\theta\frac{\partial\Pi}{\partial\eta}\nabla\phi}\right)_k \qquad \text{for} \quad k = 1, 2, \cdots, K, \tag{3.34}$$

where the tildes represents layer-edge variables interpolated to layer centers. The coefficient in parentheses is a layer-center interpolation of the VPGF times the geopotential gradient, the form of which will be determined later.

3.3.3 Horizontal momentum equation

From equation (2.14) the horizontal momentum equation is written for layer centers as

$$\frac{D\mathbf{v}_k}{Dt} + f\mathbf{k}\times\mathbf{v}_k = (\mathbf{HPGF})_k + \mathbf{F}_k \qquad \text{for} \quad k = 1, 2, \cdots, K, \tag{3.35}$$

where the horizontal pressure gradient force is given by (3.34).

3.3.4 Vertical momentum equation

From equation (2.18) the vertical momentum equation is written for layer edges as

$$\frac{Dw_{k+1/2}}{Dt} = (\mathrm{VPGF})_{k+1/2} - g + \left(F_z\right)_{k+1/2} \qquad \text{for} \quad k = 0, 1, \cdots, K-1, \tag{3.36}$$

where the vertical pressure gradient force is given by (3.32) and (3.33).

3.3.5 Thermodynamic energy equation

The vertically discrete form of the potential temperature equation will be determined from the total energy conservation constraint derived in the next section.

3.3.6 Geopotential tendency equation

We obtain the vertically discrete version of the geopotential tendency equation from equation (2.20), which is

$$\frac{\partial \phi_{k+1/2}}{\partial t} + \left(\mathbf{v}\cdot\nabla\phi\right)_{k+1/2} + \dot{\eta}_{k+1/2}\frac{\tilde{\phi}_{k+1} - \tilde{\phi}_k}{\left(\delta\eta\right)_{k+1/2}} = g w_{k+1/2} \qquad \text{for} \quad k = 1, 2, \cdots, K-1. \tag{3.37}$$

We chose the simple, centered form of the vertical advection term to facilitate the diagnosis of the generalized vertical velocity, which will be discussed in the following chapter. For the bottom layer edge $\partial\phi/\partial t = 0$ and $\dot{\eta} = 0$ so we can write

$$\left(\mathbf{v}\cdot\nabla\phi\right)_{1/2} = g w_{1/2}. \tag{3.38}$$

The form of the horizontal advection terms, as well as the geopotential interpolated to layer centers, will be determined later.

3.3.7 Diagnostic relations

The diagnostic equation for temperature at layer centers is obtained from equation (2.8), and is based on the potential temperature interpolated to layer centers. We have

$$T_k = \frac{\tilde{\theta}_k \Pi_k}{c_p} \qquad \text{for} \quad k = 1, 2, \cdots, K. \tag{3.39}$$

The state variables in the ideal gas law are expressed at layer centers and are related by

$$p_k \alpha_k = R T_k \qquad \text{for} \quad k = 1, 2, \cdots, K. \tag{3.40}$$

The Exner function is

$$\Pi_k = c_p \left(\frac{p_k}{p_0}\right)^{\kappa} \text{ for} \quad k = 1, 2, \cdots, K. \tag{3.41}$$

The density at layer centers is diagnosed from the pseudo-density and geopotential using

$$\rho_k = \frac{m_k g \left(\delta\eta\right)_k}{\phi_{k+1/2} - \phi_{k-1/2}} \qquad \text{for} \quad k = 1, 2, \cdots, K. \tag{3.42}$$

3.4 Integral constraints for the generalized vertical coordinate η: The "η-scheme"

There is freedom left in the discretization to satisfy some of the integral constraints described at the beginning of this chapter. We have already shown above that the vertical scheme conserves total mass (Constraint 0) through the use of the flux form of the continuity equation. The discrete analysis of the remaining integral constraints will be analogous to the continuous analysis in Chapter 2.

As will be shown in following derivations, the "η-scheme" satisfies Constraints 0, I and II. However, this requires the use of the "*p*-form" of the vertical pressure gradient term in the vertical momentum equation. As shown in Section 3.2, this leads to the existence of a computational mode in the potential temperature (see Figure 3.1). This is not a desirable outcome; therefore, in the next section we will modify the "η-scheme" to use the Π-form of the vertical pressure gradient in order to avoid the computational mode. The tradeoff is that with the resulting "*z*-scheme", Constraints I and II will only be satisfied for the special case of *z* coordinates.

3.4.1 Work done by the pressure gradient forces: Part I

We now perform a preliminary analysis of the work done by the pressure gradient force, which will lead to the discrete form of the energy conversion term between

thermodynamic and kinetic energy as seen in the kinetic energy equation. Using (3.39)-(3.41) in (3.34), we can write the work done by the horizontal pressure gradient force as

$$\left[m\mathbf{v}\cdot(\mathbf{HGPF})\right]_k = -m_k\alpha_k\mathbf{v}_k\cdot\nabla p_k + \frac{1}{\mathrm{g}}(m\mathbf{v})_k\cdot\left(\widetilde{\frac{\rho}{m}\theta\frac{\partial\Pi}{\partial\eta}\nabla\phi}\right)_k \qquad (3.43)$$
$$\text{for}\quad k=1,2,\cdots,K.$$

Multiplying $w_{k+1/2}$ by equations (3.32) and (3.33) gives the work done by the vertical pressure gradient force

$$\left[mw\cdot(\mathrm{VGPF})\right]_{k+1/2} = -\left(gw_{k+1/2}\right)\frac{\hat{\rho}_{k+1/2}}{g}\theta_{k+1/2}\frac{\Pi_{k+1}-\Pi_k}{\left(\delta\eta\right)_{k+1/2}} \qquad (3.44)$$
$$\text{for}\quad k=1,2,\cdots,K-1,$$

and

$$\left[mw\cdot(\mathrm{VGPF})\right]_{1/2} = -\left(gw_{1/2}\right)\frac{\hat{\rho}_{1/2}}{g}\theta_{1/2}\frac{\Pi_1-\hat{\Pi}_{1/2}}{\left(\delta\eta\right)_{1/2}}. \qquad (3.45)$$

Note that we have not written an equation for the top boundary because $w_{K+1/2}=0$ and there is no contribution to the kinetic energy. Now multiply equations (3.44) and (3.45) by $(\delta\eta)_{k+1/2}$ and combine with (3.37) and (3.38) to obtain

$$\begin{aligned}\left[mw\cdot(\mathrm{VGPF})\right]_{k+1/2}\left(\delta\eta\right)_{k+1/2} = &-\frac{\partial\phi_{k+1/2}}{\partial t}\frac{\hat{\rho}_{k+1/2}}{g}\theta_{k+1/2}\left(\Pi_{k+1}-\Pi_k\right)\\ &-\left(\mathbf{v}\cdot\nabla\phi\right)_{k+1/2}\frac{\hat{\rho}_{k+1/2}}{g}\theta_{k+1/2}\left(\Pi_{k+1}-\Pi_k\right)\\ &-\dot{\eta}_{k+1/2}\left(\tilde{\phi}_{k+1}-\tilde{\phi}_k\right)\frac{\hat{\rho}_{k+1/2}}{g}\theta_{k+1/2}\frac{\Pi_{k+1}-\Pi_k}{\left(\delta\eta\right)_{k+1/2}}\end{aligned} \qquad (3.46)$$
$$\text{for}\quad k=1,2,\cdots,K-1,$$

and

$$\left[mw\cdot(\mathrm{VGPF})\right]_{1/2}\left(\delta\eta\right)_{1/2}=-\left(\mathbf{v}\cdot\nabla\phi\right)_{1/2}\frac{\hat{\rho}_{1/2}}{g}\theta_{1/2}\left(\Pi_1-\hat{\Pi}_{1/2}\right). \tag{3.47}$$

Since the energy conversion term, which comes from the work done by the pressure gradient forces have, has contributions from both layer centers and edges, we must satisfy the constraint in a global (column integrated) sense. The vertical sum of the work done by the pressure gradient forces times the layer thickness is

$$\begin{aligned}\sum_{k=1}^{K}\left[m\mathbf{v}\cdot(\mathbf{HGPF})\right]_k\left(\delta\eta\right)_k+\sum_{k=0}^{K-1}\left[mw\cdot(\mathrm{VGPF})\right]_{k+1/2}\left(\delta\eta\right)_{k+1/2}=\\ -\sum_{k=1}^{K}m_k\alpha_k\mathbf{v}_k\cdot\nabla p_k\left(\delta\eta\right)_k-\sum_{k=1}^{K-1}\frac{\hat{\rho}_{k+1/2}}{g}\theta_{k+1/2}\left(\tilde{\phi}_{k+1}-\tilde{\phi}_k\right)\dot{\eta}_{k+1/2}\frac{\Pi_{k+1}-\Pi_k}{\left(\delta\eta\right)_{k+1/2}}\\ -\sum_{k=1}^{K-1}\frac{\partial\phi_{k+1/2}}{\partial t}\frac{\hat{\rho}_{k+1/2}}{g}\theta_{k+1/2}\left(\Pi_{k+1}-\Pi_k\right)+\sum_{k=1}^{K}\frac{1}{\mathrm{g}}(m\mathbf{v})_k\cdot\widetilde{\left(\frac{\rho}{m}\theta\frac{\partial\Pi}{\partial\eta}\nabla\phi\right)}_k\left(\delta\eta\right)_k\\ -\sum_{k=1}^{K-1}\left(\mathbf{v}\cdot\nabla\phi\right)_{k+1/2}\frac{\hat{\rho}_{k+1/2}}{g}\theta_{k+1/2}\left(\Pi_{k+1}-\Pi_k\right)-\left(\mathbf{v}\cdot\nabla\phi\right)_{1/2}\frac{\hat{\rho}_{1/2}}{g}\theta_{1/2}\left(\Pi_1-\hat{\Pi}_{1/2}\right).\end{aligned} \tag{3.48}$$

The last three terms on the right hand side of (3.48) are analogs of terms that cancel out in the continuous equations. We require that they cancel out in the discrete system by setting

$$\begin{aligned}\sum_{k=1}^{K}\frac{1}{\mathrm{g}}(m\mathbf{v})_k\cdot\widetilde{\left(\frac{\rho}{m}\theta\frac{\partial\Pi}{\partial\eta}\nabla\phi\right)}_k\left(\delta\eta\right)_k\\ -\sum_{k=1}^{K-1}\left(\mathbf{v}\cdot\nabla\phi\right)_{k+1/2}\frac{\hat{\rho}_{k+1/2}}{g}\theta_{k+1/2}\left(\Pi_{k+1}-\Pi_k\right)-\left(\mathbf{v}\cdot\nabla\phi\right)_{1/2}\frac{\hat{\rho}_{1/2}}{g}\theta_{1/2}\left(\Pi_1-\hat{\Pi}_{1/2}\right)=0.\end{aligned} \tag{3.49}$$

If we define the horizontal geopotential advection term as

$$\left(\mathbf{v}\cdot\nabla\phi\right)_{k+1/2}\equiv\frac{\left(m\mathbf{v}\right)_{k+1/2}}{m_{k+1/2}}\cdot\nabla\phi_{k+1/2} \tag{3.50}$$

$$\text{for}\quad k=0,1,\cdots,K,$$

and use equations (3.26), (3.27), (3.31) and $\nabla\phi_{K+1/2}=0$ in (3.49), then, after adjusting the limits of the summations and rearranging terms, we obtain

$$\begin{aligned}
&\sum_{k=1}^{K}\frac{1}{\mathrm{g}}(m\mathbf{v})_k\cdot\left(\widetilde{\frac{\rho}{m}\theta\frac{\partial\Pi}{\partial\eta}\nabla\phi}\right)_k\left(\delta\eta\right)_k \\
&-\sum_{k=2}^{K}\frac{1}{g}\left(m\mathbf{v}\right)_k\cdot\frac{1}{2}\left[\begin{array}{l}\dfrac{\hat{\rho}_{k+1/2}}{m_{k+1/2}}\theta_{k+1/2}\dfrac{\Pi_{k+1}-\Pi_k}{\left(\delta\eta\right)_{k+1/2}}\nabla\phi_{k+1/2}+\\ \qquad\dfrac{\hat{\rho}_{k-1/2}}{m_{k-1/2}}\theta_{k-1/2}\dfrac{\Pi_k-\Pi_{k-1}}{\left(\delta\eta\right)_{k-1/2}}\nabla\phi_{k-1/2}\end{array}\right]\left(\delta\eta\right)_k \qquad (3.51)\\
&-\frac{1}{g}\left(m\mathbf{v}\right)_1\cdot\frac{1}{2}\left[\frac{\hat{\rho}_{3/2}}{m_{3/2}}\theta_{3/2}\frac{\Pi_2-\Pi_1}{\left(\delta\eta\right)_{3/2}}\nabla\phi_{3/2}+\frac{\hat{\rho}_{1/2}}{m_{1/2}}\theta_{1/2}\frac{\Pi_1-\hat{\Pi}_{1/2}}{\left(\delta\eta\right)_{1/2}}\nabla\phi_{1/2}\right]\left(\delta\eta\right)_1=0.
\end{aligned}$$

We can satisfy this equation by requiring each coefficient of $(m\mathbf{v})_k(\delta\eta)_k$ to be zero, which gives us the form the layer-centered interpolation of the vertical pressure gradient force times the horizontal geopotential gradient as

$$\left(\widetilde{\frac{\rho}{m}\theta\frac{\partial\Pi}{\partial\eta}\nabla\phi}\right)_k=\frac{1}{2}\left[\frac{\hat{\rho}_{k+1/2}}{m_{k+1/2}}\theta_{k+1/2}\frac{\Pi_{k+1}-\Pi_k}{\left(\delta\eta\right)_{k+1/2}}\nabla\phi_{k+1/2}+\frac{\hat{\rho}_{k-1/2}}{m_{k-1/2}}\theta_{k-1/2}\frac{\Pi_k-\Pi_{k-1}}{\left(\delta\eta\right)_{k-1/2}}\nabla\phi_{k-1/2}\right] \qquad (3.52)$$

$$\text{for}\quad k=2,3,\cdots,K,$$

and

$$\left(\widetilde{\frac{\rho}{m}\theta\frac{\partial\Pi}{\partial\eta}\nabla\phi}\right)_1=\frac{1}{2}\left[\frac{\hat{\rho}_{3/2}}{m_{3/2}}\theta_{3/2}\frac{\Pi_2-\Pi_1}{\left(\delta\eta\right)_{3/2}}\nabla\phi_{3/2}+\frac{\hat{\rho}_{1/2}}{m_{1/2}}\theta_{1/2}\frac{\Pi_1-\hat{\Pi}_{1/2}}{\left(\delta\eta\right)_{1/2}}\nabla\phi_{1/2}\right]. \qquad (3.53)$$

So (3.52) and (3.53) guarantee that equation (3.49) is satisfied.

Now use (3.49) in (3.48), then add and subtract $\sum_{k=1}^{K} m_k \alpha_k \frac{\partial p_k}{\partial t}\left(\delta\eta\right)_k$ to the right hand side, combine with (3.42), apply the product rule of differentiation in t, and rearrange terms to obtain

$$\begin{aligned}
&\sum_{k=1}^{K}\left[m\mathbf{v}\cdot(\mathbf{HGPF})\right]_k\left(\delta\eta\right)_k+\sum_{k=0}^{K-1}\left[mw\cdot(\mathrm{VGPF})\right]_{k+1/2}\left(\delta\eta\right)_{k+1/2}\\
&\qquad=-\sum_{k=1}^{K} m_k\alpha_k\left(\frac{\partial p_k}{\partial t}+\mathbf{v}_k\cdot\nabla p_k\right)\left(\delta\eta\right)_k\\
&\qquad\quad-\sum_{k=1}^{K-1}\frac{\hat{\rho}_{k+1/2}}{g}\theta_{k+1/2}\left(\tilde{\phi}_{k+1}-\tilde{\phi}_k\right)\dot{\eta}_{k+1/2}\frac{\Pi_{k+1}-\Pi_k}{\left(\delta\eta\right)_{k+1/2}}\\
&\qquad\quad-\sum_{k=1}^{K-1}\frac{\partial\phi_{k+1/2}}{\partial t}\frac{\hat{\rho}_{k+1/2}}{g}\theta_{k+1/2}\left(\Pi_{k+1}-\Pi_k\right)\\
&\qquad\quad-\sum_{k=1}^{K}\frac{p_k}{g}\frac{\partial}{\partial t}\left(\phi_{k+1/2}-\phi_{k-1/2}\right)+\sum_{k=1}^{K}\frac{\partial}{\partial t}\left[\frac{p_k}{g}\left(\phi_{k+1/2}-\phi_{k-1/2}\right)\right].
\end{aligned}\tag{3.54}$$

Comparing equations (3.54) and (2.35), we identify the energy conversion term as

$$\begin{aligned}
\sum_{k=1}^{K}\left(m\alpha\omega\right)_k\left(\delta\eta\right)_k&=\sum_{k=1}^{K} m_k\alpha_k\left(\frac{\partial p_k}{\partial t}+\mathbf{v}_k\cdot\nabla p_k\right)\left(\delta\eta\right)_k\\
&\quad+\sum_{k=1}^{K-1}\frac{\hat{\rho}_{k+1/2}}{g}\theta_{k+1/2}\left(\tilde{\phi}_{k+1}-\tilde{\phi}_k\right)\dot{\eta}_{k+1/2}\frac{\Pi_{k+1}-\Pi_k}{\left(\delta\eta\right)_{k+1/2}}.
\end{aligned}\tag{3.55}$$

3.4.2 Vertically integrated momentum circulation constraint on the HPGF (Constraint I)

As discussed in Chapter 2, we can design the discrete form of the horizontal pressure gradient force to mimic the constraint on the vertically integrated momentum circulation. This can limit the effects of the inevitable numerical error by eliminating the development of artificial circulations associated with surface topography. In the previous

subsection, we determined the required form of the interpolated term $\left(\widetilde{\frac{\rho}{m}\theta\frac{\partial\Pi}{\partial\eta}\nabla\phi}\right)_k$ which satisfies kinetic energy conservation. The following analysis will lead to the required form of the interpolated term $\hat{\rho}_{k+1/2}$.

The layer mass-weighted HPGF can be obtained using equations (3.39)-(3.42) in (3.34) which gives

$$\begin{aligned}\left[m(\mathbf{HPGF})\right]_k\left(\delta\eta\right)_k = &-\nabla\left[\frac{p_k}{g}\left(\phi_{k+1/2}-\phi_{k-1/2}\right)\right]\\ &+\frac{p_k}{g}\left(\nabla\phi_{k+1/2}-\nabla\phi_{k-1/2}\right)+\frac{m_k}{\mathrm{g}}\left(\widetilde{\frac{\rho}{m}\theta\frac{\partial\Pi}{\partial\eta}\nabla\phi}\right)_k\left(\delta\eta\right)_k \qquad (3.56)\end{aligned}$$

$$\text{for} \quad k=1,2,\cdots,K.$$

Following the derivation in the continuous equations, analogous to equation (2.24), we require that the last two terms of (3.56), when summed over the column, equal the "mountain torque" term. That is

$$\sum_{k=1}^{K}\frac{p_k}{g}\left(\nabla\phi_{k+1/2}-\nabla\phi_{k-1/2}\right)+\sum_{k=1}^{K}\frac{m_k}{\mathrm{g}}\left(\widetilde{\frac{\rho}{m}\theta\frac{\partial\Pi}{\partial\eta}\nabla\phi}\right)_k\left(\delta\eta\right)_k=-\frac{\hat{p}_{1/2}}{g}\nabla\phi_{1/2}. \qquad (3.57)$$

Using (3.24), (3.25), (3.31), (3.52) and (3.53) in equation (3.57), along with $\nabla\phi_{K+1/2}=0$, we get

$$\begin{aligned}&\left[\hat{p}_{1/2}-p_1+\hat{\rho}_{1/2}\theta_{1/2}\left(\Pi_1-\hat{\Pi}_{1/2}\right)\right]\nabla\phi_{1/2}\\ &\quad+\sum_{k=1}^{K-1}\left[p_k-p_{k+1}+\hat{\rho}_{k+1/2}\theta_{k+1/2}\left(\Pi_{k+1}-\Pi_k\right)\right]\nabla\phi_{k+1/2}=0.\end{aligned} \qquad (3.58)$$

This sum can be satisfied by requiring that each term in the summation equal zero. Then solving for $\hat{\rho}_{k+1/2}$ we have

$$\hat{\rho}_{k+1/2} = \frac{1}{\theta_{k+1/2}} \frac{p_{k+1} - p_k}{\Pi_{k+1} - \Pi_k} \qquad \text{for} \quad k = 1, 2, \cdots, K-1, \tag{3.59}$$

and

$$\hat{\rho}_{1/2} = \frac{1}{\theta_{1/2}} \frac{p_1 - \hat{p}_{1/2}}{\Pi_1 - \hat{\Pi}_{1/2}}. \tag{3.60}$$

Note that if we define $\left(\frac{\kappa\Pi}{p}\right)_{k+1/2} \equiv \frac{1}{\hat{\rho}_{k+1/2}\theta_{k+1/2}}$, then (3.59) and (3.60) are discrete analogs of the relation $\frac{d\Pi}{dp} = \frac{\kappa\Pi}{p}$. Finally, using (3.57) in (3.56), the vertical sum of the mass-weighted HPGF is

$$\sum_{k=1}^{K}\left[m(\mathbf{HPGF})\right]_k \left(\delta\eta\right)_k = -\nabla\sum_{k=1}^{K}\left[\frac{p_k}{g}\left(\phi_{k+1/2} - \phi_{k-1/2}\right)\right] - \frac{\hat{p}_{1/2}}{g}\nabla\phi_{1/2}, \tag{3.61}$$

which is analogous to equation (2.24). As in the continuous case, the only contribution to the vertically summed circulation of momentum is due to the last term, which is the "mountain torque" term. When the closed curve is a contour of surface topography, it is zero.

3.4.3 Conservation of total energy (Constraint II)

In the vertically discrete system of equations, total energy can be conserved through consistent forms of the energy conversion terms. Using the results of the vertically integrated momentum circulation conservation constraint on the HPGF in the previous subsection, we can derive the discrete form of the conversion term between thermodynamic and kinetic energy as given by the kinetic energy equation.

3.4.3.1 Work done by the pressure gradient forces: Part II

We have determined the form of the horizontal and vertical pressure gradient forces in subsections 3.4.1 and 3.4.2. We now complete the analysis of the work done by these forces. What remains to be shown is that the third and fourth terms on the right hand side of equation (3.54) do not contribute to the vertical sum of the production of kinetic energy by the pressure gradient forces. This is analogous to the vertical integral of the second term on the right hand side of equation (2.35) being equal to zero for non-moving upper and lower boundaries. That is, we require

$$\sum_{k=1}^{K-1} \frac{\partial \phi_{k+1/2}}{\partial t} \frac{\hat{\rho}_{k+1/2}}{g} \theta_{k+1/2} \left(\Pi_{k+1} - \Pi_k \right) + \sum_{k=1}^{K} \frac{p_k}{g} \frac{\partial}{\partial t} \left(\phi_{k+1/2} - \phi_{k-1/2} \right) = 0 , \tag{3.62}$$

for non-moving boundaries. Using equation (3.59) in (3.62), the sums of the internal terms cancel out and the result is the expression

$$\begin{aligned} \sum_{k=1}^{K-1} \frac{\partial \phi_{k+1/2}}{\partial t} \frac{\hat{\rho}_{k+1/2}}{g} \theta_{k+1/2} \left(\Pi_{k+1} - \Pi_k \right) \\ + \sum_{k=1}^{K} \frac{p_k}{g} \frac{\partial}{\partial t} \left(\phi_{k+1/2} - \phi_{k-1/2} \right) = \frac{p_K}{g} \frac{\partial \phi_{K+1/2}}{\partial t} - \frac{p_1}{g} \frac{\partial \phi_{1/2}}{\partial t} , \end{aligned} \tag{3.63}$$

which is identically zero for $\partial \phi_{K+1/2} / \partial t = \partial \phi_{1/2} / \partial t = 0$. So the required form of $\hat{\rho}_{k+1/2}$ given by (3.59), which is consistent with Constraint I on the HPGF, is also consistent with kinetic energy conservation.

3.4.3.2 Thermodynamic energy equation

We are free to specify the thermodynamic energy equation, in the form of the potential temperature tendency equation, such that total energy is conserved. This is done by using the form of the energy conversion term between kinetic and

thermodynamic energy which we derived in subsection 3.4.1. We start by writing the vertically discrete form of the vertically integrated enthalpy tendency equation (2.39) as

$$\sum_{k=1}^{K}\frac{\partial}{\partial t}\left(mc_pT\right)_k\left(\delta\eta\right)_k+\sum_{k=1}^{K}\nabla\cdot\left(m\mathbf{v}c_pT\right)_k\left(\delta\eta\right)_k+\sum_{k=1}^{K}\left[\left(m\dot{\eta}c_pT\right)_{k+1/2}-\left(m\dot{\eta}c_pT\right)_{k-1/2}\right]$$
$$=\sum_{k=1}^{K}\left(m\alpha\omega\right)_k\left(\delta\eta\right)_k+\sum_{k=0}^{K}\left(mQ\right)_{k+1/2}\left(\delta\eta\right)_{k+1/2}. \tag{3.64}$$

Note that we have defined the diabatic heating Q to be located at layer edges. This is consistent with the "N grid "of Konor and Arakawa (2000), who showed that there is an advantage of carrying condensational heating at levels carrying the vertical mass flux. Using (3.55) in (3.64) and applying mass continuity equation (3.19), the diagnostic relations (3.39) and (3.41), and rearranging terms, we get

$$\sum_{k=1}^{K}m_k\Pi_k\left(\frac{\partial\tilde{\theta}_k}{\partial t}+\mathbf{v}_k\cdot\nabla\tilde{\theta}_k\right)\left(\delta\eta\right)_k-\sum_{k=1}^{K}\tilde{\theta}_k\Pi_k\left[\left(m\dot{\eta}\right)_{k+1/2}-\left(m\dot{\eta}\right)_{k-1/2}\right]$$
$$-\sum_{k=1}^{K-1}\frac{\hat{\rho}_{k+1/2}}{g}\theta_{k+1/2}\left(\tilde{\phi}_{k+1}-\tilde{\phi}_k\right)\dot{\eta}_{k+1/2}\frac{\Pi_{k+1}-\Pi_k}{\left(\delta\eta\right)_{k+1/2}}=\sum_{k=0}^{K}\left(mQ\right)_{k+1/2}\left(\delta\eta\right)_{k+1/2}. \tag{3.65}$$

Now we have an expression with the appearance of a prediction equation for potential temperature, however, some work needs to be done to get into a useable form which is a prediction equation for θ at the layer edges. First we choose the form of the potential temperature interpolated to layer centers to be

$$\tilde{\theta}_k=\frac{1}{2}\left(\theta_{k+1/2}+\theta_{k-1/2}\right)\qquad\text{for}\quad k=1,2,\cdots,K. \tag{3.66}$$

Using this relation and (3.20) in equation (3.65), and rearranging terms, we can write

$$
\begin{aligned}
&\frac{1}{2}\Pi_1\left[m_1\frac{\partial\theta_{1/2}}{\partial t}+\left(m\mathbf{v}\right)_1\cdot\nabla\theta_{1/2}\right]\left(\delta\eta\right)_1\\
&+\sum_{k=1}^{K-1}\left\{\begin{array}{l}\frac{1}{2}\left[\Pi_k m_k\left(\delta\eta\right)_k+\Pi_{k+1}m_{k+1}\left(\delta\eta\right)_{k+1}\right]\frac{\partial\theta_{k+1/2}}{\partial t}\\ +\frac{1}{2}\left[\Pi_k\left(m\mathbf{v}\right)_k\left(\delta\eta\right)_k+\Pi_{k+1}\left(m\mathbf{v}\right)_{k+1}\left(\delta\eta\right)_{k+1}\right]\cdot\nabla\theta_{k+1/2}\end{array}\right\}\\
&+\frac{1}{2}\Pi_K\left[m_K\frac{\partial\theta_{K+1/2}}{\partial t}+\left(m\mathbf{v}\right)_K\cdot\nabla\theta_{K+1/2}\right]\left(\delta\eta\right)_K\\
&+\sum_{k=1}^{K-1}\frac{1}{2}\left(\begin{array}{l}\Pi_{k+1}\left\{\theta_{k+3/2}-\left[2\frac{\hat{\rho}_{k+1/2}}{g\,m_{k+1/2}}\frac{\tilde{\phi}_{k+1}-\tilde{\phi}_k}{\left(\delta\eta\right)_{k+1/2}}-1\right]\theta_{k+1/2}\right\}\\ +\Pi_k\left\{\left[2\frac{\hat{\rho}_{k+1/2}}{g\,m_{k+1/2}}\frac{\tilde{\phi}_{k+1}-\tilde{\phi}_k}{\left(\delta\eta\right)_{k+1/2}}-1\right]\theta_{k+1/2}-\theta_{k-1/2}\right\}\end{array}\right)\left(m\dot{\eta}\right)_{k+1/2}\\
&=\sum_{k=0}^{K}\left(mQ\right)_{k+1/2}\left(\delta\eta\right)_{k+1/2}.
\end{aligned}
\tag{3.67}
$$

Now we can write a potential temperature tendency equation which satisfies equation (3.67), which is the requirement for total energy conservation, level by level as

$$
\frac{\partial\theta_{k+1/2}}{\partial t}+\frac{\left(m\Pi\mathbf{v}\delta\eta\right)_{k+1/2}}{\left(m\Pi\delta\eta\right)_{k+1/2}}\cdot\nabla\theta_{k+1/2}+\frac{\left(\Pi\delta\theta\right)_{k+1/2}}{\left(m\Pi\delta\eta\right)_{k+1/2}}\left(m\dot{\eta}\right)_{k+1/2}=\frac{\left(mQ\delta\eta\right)_{k+1/2}}{\left(m\Pi\delta\eta\right)_{k+1/2}}
\tag{3.68}
$$

$$
\text{for}\quad k=1,2,\cdots,K-1,
$$

$$
\frac{\partial\theta_{1/2}}{\partial t}+\frac{\left(m\mathbf{v}\right)_1}{m_1}\cdot\nabla\theta_{1/2}=\frac{Q_{1/2}}{\Pi_1},
\tag{3.69}
$$

and

$$
\frac{\partial\theta_{K+1/2}}{\partial t}+\frac{\left(m\mathbf{v}\right)_K}{m_K}\cdot\nabla\theta_{K+1/2}=\frac{Q_{K+1/2}}{\Pi_K},
\tag{3.70}
$$

where

$$\left(m\Pi\delta\eta\right)_{k+1/2} \equiv \frac{1}{2}\left[\left(m\Pi\right)_k\left(\delta\eta\right)_k + \left(m\Pi\right)_{k+1}\left(\delta\eta\right)_{k+1}\right] \tag{3.71}$$

$$\text{for} \quad k = 1, 2, \cdots, K-1,$$

$$\left(m\Pi\mathbf{v}\delta\eta\right)_{k+1/2} \equiv \frac{1}{2}\left[\Pi_k\left(m\mathbf{v}\right)_k\left(\delta\eta\right)_k + \Pi_{k+1}\left(m\mathbf{v}\right)_{k+1}\left(\delta\eta\right)_{k+1}\right] \tag{3.72}$$

$$\text{for} \quad k = 1, 2, \cdots, K-1,$$

and

$$\left(\Pi\delta\theta\right)_{k+1/2} \equiv \frac{1}{2}\left(\begin{array}{c} \Pi_{k+1}\left\{\theta_{k+3/2} - \left[2\dfrac{\hat{\rho}_{k+1/2}}{g\,m_{k+1/2}}\dfrac{\tilde{\phi}_{k+1}-\tilde{\phi}_k}{\left(\delta\eta\right)_{k+1/2}} - 1\right]\theta_{k+1/2}\right\} \\ +\Pi_k\left\{\left[2\dfrac{\hat{\rho}_{k+1/2}}{g\,m_{k+1/2}}\dfrac{\tilde{\phi}_{k+1}-\tilde{\phi}_k}{\left(\delta\eta\right)_{k+1/2}} - 1\right]\theta_{k+1/2} - \theta_{k-1/2}\right\} \end{array}\right) \tag{3.73}$$

$$\text{for} \quad k = 1, 2, \cdots, K-1.$$

This form of the thermodynamic energy equation is similar to that of KA97. In fact, the horizontal advection and diabatic heating terms are the same. This is to be expected because their discretization is also based on the CP grid. The vertical advection term differs from theirs, however, because our model is nonhydrostatic and the pressure is calculated at layer centers instead of at the edges. In equation (3.73), there is an unusual looking coefficient which involves the geopotential. From equation (2.15), it can be seen that in the continuous limit the coefficient is

$$\left[2\frac{\hat{\rho}_{k+1/2}}{g\,m_{k+1/2}}\frac{\tilde{\phi}_{k+1}-\tilde{\phi}_k}{\left(\delta\eta\right)_{k+1/2}} - 1\right] \to 1 \quad \text{as} \quad \delta\eta \to 0\,. \tag{3.74}$$

Therefore, in the continuous limit, equation (3.73) becomes

$$\frac{1}{2}\left(\begin{array}{l}\Pi_{k+1}\left\{\theta_{k+3/2}-\left[2\dfrac{\hat{\rho}_{k+1/2}}{g\,m_{k+1/2}}\dfrac{\tilde{\phi}_{k+1}-\tilde{\phi}_{k}}{\left(\delta\eta\right)_{k+1/2}}-1\right]\theta_{k+1/2}\right\} \\ \quad +\Pi_{k}\left\{\left[2\dfrac{\hat{\rho}_{k+1/2}}{g\,m_{k+1/2}}\dfrac{\tilde{\phi}_{k+1}-\tilde{\phi}_{k}}{\left(\delta\eta\right)_{k+1/2}}-1\right]\theta_{k+1/2}-\theta_{k-1/2}\right\}\end{array}\right)\rightarrow\Pi d\theta \tag{3.75}$$

$$\text{as } \delta\eta\rightarrow 0.$$

The vertical advection of θ in the thermodynamic equation (3.68) involves the vertical mass flux at just one level, i.e., the level at which potential temperature is predicted. This is a result of using the CP grid instead of the Lorenz grid. As pointed out by AK96 this has the advantage of allowing conservation of quasigeostrophic potential vorticity as in the vertically discrete equations of Charney and Phillips (1953). In our nonhydrostatic model, this conservation is not relevant for small-scale motion, but it may still be a factor for large-scale motion. A disadvantage of (3.68)-(3.73) is that the mass-weighted potential temperature is not globally conserved, and as in AK96, the vertical advection of θ does not vanish for an isentropic atmosphere.

The use of the discrete vertical potential temperature advection term in (3.68) leads to large dispersion errors in high-resolution simulations, because it is centered in form. Such dispersion error can be reduced by using upstream-weighted schemes, e.g., Takacs (1985). This is not as much of an issue for large-scale flow, where vertical motions are small, but on the small-scale where vertical advection of potential temperature is significant, these errors can be reduced with the upstream-weighted schemes. Figure 3.4 shows the reduction in dispersion error in the perturbation θ field resulting from using the upstream-weighted scheme of Takacs (1985) versus a simple centered scheme. The simulation is a 2D rising thermal in a neutrally buoyant

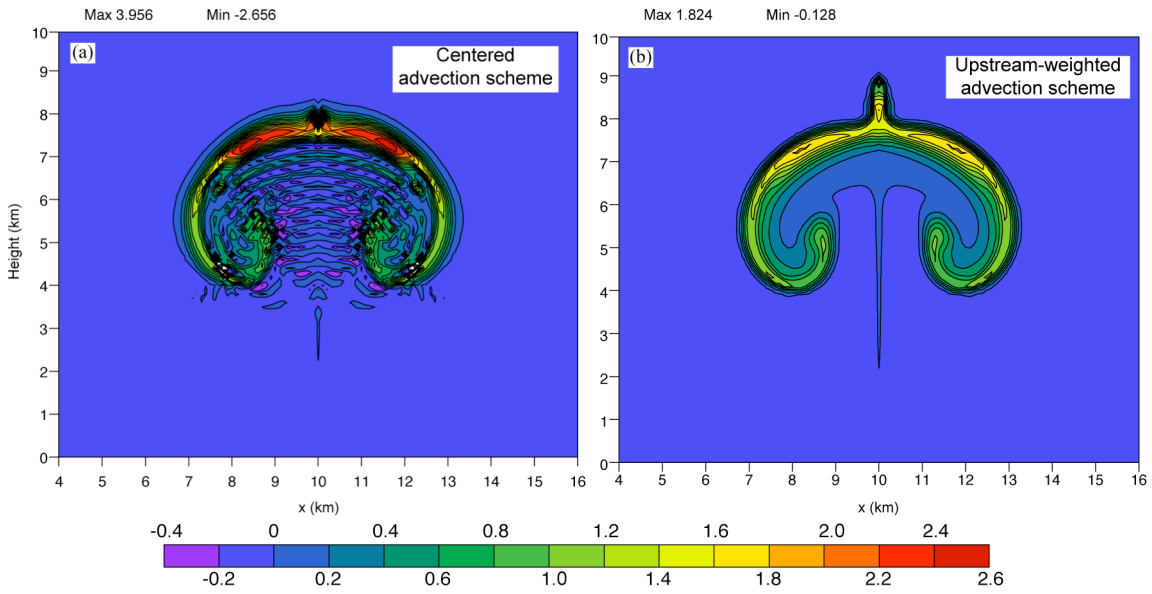


Figure 3.4: Perturbation potential temperature at time $t = 1000$ seconds for a rising thermal experiment performed with an early σ-coordinate version of the model using (a) a centered advection scheme, and (b) an upstream-weighted advection scheme (Takacs 1985) for the potential temperature.

environment using σ coordinates and is based on Bryan and Fritsch (2002). Upstream-weighted advection schemes typically require the mass flux at multiple levels. Therefore, the appearance of the vertical mass flux at one level, as in equation (3.68), does not facilitate the use of such schemes.

We wish to use an upstream-weighted potential temperature advection scheme in order to reduce dispersion error. Therefore, we need to derive an alternate form of the potential temperature prediction equation which uses the vertical mass flux at multiple levels in the vertical advection term. This alternate form will be required to conserve total energy as in the original form. To derive the alternate θ-prediction equation, start again from the total energy conservation requirement of equation (3.65). As before, use (3.20) and (3.66), but rearrange the terms differently to arrive at

$$
\begin{aligned}
&\frac{1}{2}\Pi_1\left[m_1\frac{\partial\theta_{1/2}}{\partial t}+\left(m\mathbf{v}\right)_1\cdot\nabla\theta_{1/2}\right]\left(\delta\eta\right)_1\\
&\quad+\sum_{k=1}^{K-1}\left\{\begin{aligned}&\frac{1}{2}\left[\Pi_k m_k\left(\delta\eta\right)_k+\Pi_{k+1}m_{k+1}\left(\delta\eta\right)_{k+1}\right]\frac{\partial\theta_{k+1/2}}{\partial t}\\&+\frac{1}{2}\left[\Pi_k\left(m\mathbf{v}\right)_k\left(\delta\eta\right)_k+\Pi_{k+1}\left(m\mathbf{v}\right)_{k+1}\left(\delta\eta\right)_{k+1}\right]\cdot\nabla\theta_{k+1/2}\end{aligned}\right\}\\
&\quad+\frac{1}{2}\Pi_K\left[m_K\frac{\partial\theta_{K+1/2}}{\partial t}+\left(m\mathbf{v}\right)_K\cdot\nabla\theta_{K+1/2}\right]\left(\delta\eta\right)_K\\
&\quad+\sum_{k=1}^{K-1}\left[\left(m\dot{\eta}\right)_{k+1}\left(\Pi\tilde{\theta}\right)_{k+1}-\left(m\dot{\eta}\right)_k\left(\Pi\tilde{\theta}\right)_k\right]\\
&\quad-\left\{\begin{aligned}&\sum_{k=1}^{K-1}\theta_{k+1/2}\left[\Pi_{k+1}\left(m\dot{\eta}\right)_{k+1}-\Pi_k\left(m\dot{\eta}\right)_k\right]\\&+\Pi_1\left(\theta_{1/2}-\tilde{\theta}_1\right)\left(m\dot{\eta}\right)_1+\Pi_K\left(\tilde{\theta}_K-\theta_{K+1/2}\right)\left(m\dot{\eta}\right)_K\end{aligned}\right\}\\
&\quad-\sum_{k=1}^{K-1}\left[\frac{\hat{\rho}_{k+1/2}}{g\,m_{k+1/2}}\frac{\tilde{\phi}_{k+1}-\tilde{\phi}_k}{\left(\delta\eta\right)_{k+1/2}}-1\right]\left(\Pi_{k+1}-\Pi_k\right)\theta_{k+1/2}\left(m\dot{\eta}\right)_{k+1/2}\\
&\quad=\sum_{k=0}^{K}\left(mQ\right)_{k+1/2}\left(\delta\eta\right)_{k+1/2}.
\end{aligned}
\tag{3.76}
$$

The θ-tendency equation which satisfies (3.76) can be written as

$$
\begin{aligned}
&\frac{\partial\theta_{k+1/2}}{\partial t}+\frac{\left(m\Pi\mathbf{v}\delta\eta\right)_{k+1/2}}{\left(m\Pi\delta\eta\right)_{k+1/2}}\cdot\nabla\theta_{k+1/2}\\
&\qquad+\frac{\left(m\dot{\eta}\right)_{k+1}\left(\Pi\tilde{\theta}\right)_{k+1}-\left(m\dot{\eta}\right)_k\left(\Pi\tilde{\theta}\right)_k}{\left(m\Pi\delta\eta\right)_{k+1/2}}-\theta_{k+1/2}\frac{\Pi_{k+1}\left(m\dot{\eta}\right)_{k+1}-\Pi_k\left(m\dot{\eta}\right)_k}{\left(m\Pi\delta\eta\right)_{k+1/2}}\\
&\qquad-\left[\frac{\hat{\rho}_{k+1/2}}{g\,m_{k+1/2}}\frac{\tilde{\phi}_{k+1}-\tilde{\phi}_k}{\left(\delta\eta\right)_{k+1/2}}-1\right]\frac{\Pi_{k+1}-\Pi_k}{\left(m\Pi\delta\eta\right)_{k+1/2}}\theta_{k+1/2}\left(m\dot{\eta}\right)_{k+1/2}\\
&\qquad\qquad=\frac{\left(mQ\delta\eta\right)_{k+1/2}}{\left(m\Pi\delta\eta\right)_{k+1/2}}\\
&\qquad\qquad\qquad\text{for}\quad k=1,2,\cdots,K-1,
\end{aligned}
\tag{3.77}
$$

$$
\frac{\partial\theta_{1/2}}{\partial t}+\frac{\left(m\mathbf{v}\right)_1}{m_1}\cdot\nabla\theta_{1/2}+\frac{\left(\tilde{\theta}_1-\theta_{1/2}\right)\left(m\dot{\eta}\right)_1}{m_{1/2}\left(\delta\eta\right)_{1/2}}=\frac{Q_{1/2}}{\Pi_1},
\tag{3.78}
$$

and

$$\frac{\partial \theta_{K+1/2}}{\partial t} + \frac{\left(m\mathbf{v}\right)_K}{m_K} \cdot \nabla \theta_{K+1/2} + \frac{\left(\theta_{K+1/2} - \tilde{\theta}_K\right)\left(m\dot{\eta}\right)_K}{m_{K+1/2}\left(\delta\eta\right)_{K+1/2}} = \frac{Q_{K+1/2}}{\Pi_K}, \tag{3.79}$$

where (3.71) and (3.72) apply to (3.77). From equation (3.74) we can see that (3.77)-(3.79) are finite-difference analogs of $\partial\theta/\partial t + \mathbf{v}\cdot\nabla\theta + \partial\left(\dot{\eta}\theta\right)/\partial\eta - \theta\,\partial\dot{\eta}/\partial\eta = Q/\Pi$.

3.4.3.3 Geopotential energy equation

We now derive a flux-form geopotential energy conservation equation and determine whether the conversion term between geopotential and kinetic energy is consistent with that derived from the kinetic energy equation. Multiplying equation (3.36) by $m_{k+1/2}\, w_{k+1/2}$ we identify the energy conversion term, given by the kinetic energy equation, as $(-m_{k+1/2}\, g\, w_{k+1/2})$. Now multiply the geopotential tendency equations (3.37) and (3.38) by $m_{k+1/2}$ and add $\phi_{k+1/2}$ times the layer-edge continuity equations (3.21)-(3.23). Using (3.50), the resulting geopotential energy equation is

$$\frac{\partial}{\partial t}(m\phi)_{k+1/2} + \nabla\cdot\left(m\mathbf{v}\phi\right)_{k+1/2} + \frac{\left(\widetilde{m\dot{\eta}\phi}\right)_{k+1} - \left(\widetilde{m\dot{\eta}\phi}\right)_k}{\left(\delta\eta\right)_{k+1/2}} = m_{k+1/2} g w_{k+1/2} \tag{3.80}$$

$$\text{for} \quad k = 1, 2, \cdots, K-1,$$

$$\frac{\partial}{\partial t}(m\phi)_{1/2} + \nabla\cdot\left(m\mathbf{v}\phi\right)_{1/2} + \frac{\left(\widetilde{m\dot{\eta}\phi}\right)_1}{\left(\delta\eta\right)_{1/2}} = m_{1/2} g w_{1/2}, \tag{3.81}$$

and

$$\frac{\partial}{\partial t}(m\phi)_{K+1/2} + \nabla\cdot\left(m\mathbf{v}\phi\right)_{K+1/2} - \frac{\left(\widetilde{m\dot{\eta}\phi}\right)_K}{\left(\delta\eta\right)_{K+1/2}} = m_{K+1/2} g w_{K+1/2}, \tag{3.82}$$

where the vertical flux of geopotential energy at layer centers is defined as

$$\left(\widetilde{m\dot{\eta}\phi}\right)_k \equiv \frac{1}{2}\left[\left(m\dot{\eta}\right)_{k-1/2}\phi_{k+1/2} + \left(m\dot{\eta}\right)_{k+1/2}\phi_{k-1/2}\right] \quad \text{for} \quad k = 1, 2, \cdots, K\,. \tag{3.83}$$

In (3.83), note that the geopotential flux terms involve products of the mass flux and geopotential at different levels. In deriving (3.80)-(3.82) we defined the geopotential interpolated to layer centers as

$$\tilde{\phi}_k \equiv \frac{1}{2}\left(\phi_{k+1/2} + \phi_{k-1/2}\right) \qquad \text{for} \quad k = 1, 2, \cdots, K, \tag{3.84}$$

which is the final interpolated variable that needed to be defined. Equations (3.80)-(3.82) are in flux-form, so that geopotential energy is internally conserved, and the energy conversion term $m_{k+1/2}\, g w_{k+1/2}$ appears with the same form but opposite sign as that derived from the kinetic energy equation above, so total energy is conserved.

3.4.4 Implications of the "η-scheme"

It turns out that the vertical discretization just derived, which satisfies integral Constraints I and II, leads to the "*p*-form" of the discrete vertical pressure gradient term, as shown below. Therefore, a computational mode in the potential temperature field exists as shown in Figure 3.1. This results from the form of $\hat{\rho}_{k+1/2}$ in equations (3.59) and (3.60). Plugging these expressions into (3.32) and (3.33), the VPGF becomes

$$\left(\text{VPGF}\right)_{k+1/2} = -\frac{1}{m_{k+1/2}}\frac{p_{k+1} - p_k}{\left(\delta\eta\right)_{k+1/2}} \qquad \text{for} \quad k = 1, 2, \cdots, K-1, \tag{3.85}$$

and

$$(\mathrm{VPGF})_{1/2} = -\frac{1}{m_{1/2}} \frac{p_1 - \hat{p}_{1/2}}{(\delta\eta)_{1/2}}. \tag{3.86}$$

Equations (3.85) and (3.86) are direct discretizations of the continuous equation (2.27), which is the "*p*-form" of the VPGF. The issue is that $\hat{\rho}_{k+1/2}$ is not evaluated from a discretized form of equation (2.15). If it were, then the VPGF would be expressed as a direct discretization of the equation $\mathrm{VPGF} = -\theta\partial\Pi/\partial z$ in which the computational mode is not supported and the expression is in terms of the difference in Exner function. In the following section, we derive a scheme using such an alternative specification of $\hat{\rho}_{k+1/2}$, which we use in the model. The result is a trade-off of the satisfaction of integral Constraints I and II in generalized vertical coordinates for the avoidance of the computational mode in θ.

3.5 Alternative scheme: The "*z*-scheme"

Using the scheme derived in the previous section as a starting point, we derive an alternate scheme which turns out to satisfy integral Constraints I and II for $\eta=z$ only. The integral constraints are not satisfied for systems in which coordinate surfaces may slant, such as θ and σ, due to nonzero geopotential gradient terms. These terms are assumed to be zero in the development of the present scheme.

In the following analysis we retain the designation of the vertical coordinate as η with the understanding that it represents *z*. Likewise the vertical velocity *w* is now synonymous with $\dot{\eta}$ and density ρ is synonymous with *m*. For simplicity we assume that there is no topography so that the lower boundary is a constant-coordinate surface, with

the boundary condition $\dot{\eta}_S = w_S = 0$. The basic difference in the present analysis is that we ignore terms involving time derivatives and horizontal gradients of geopotential as ϕ is constant on *z*-coordinate surfaces.

3.5.1 Vertically integrated momentum circulation constraint on the HPGF

For the *z*-coordinate, in which $\nabla\phi = 0$, the horizontal pressure gradient force expressed in equation (3.34) becomes

$$(\mathbf{HPGF})_k = -\tilde{\theta}_k \nabla \Pi_k \quad \text{for} \quad k = 1, 2, \cdots, K. \tag{3.87}$$

Using equations (3.39)-(3.42) in (3.87) we can write the layer mass-weighted HPGF as

$$\left[m(\mathbf{HPGF}) \right]_k \left(\delta\eta \right)_k = -\nabla \left[\frac{p_k}{g} \left(\phi_{k+1/2} - \phi_{k-1/2} \right) \right]. \tag{3.88}$$

Since the right hand side of (3.88) is a pure gradient term, it generates zero circulation of momentum when integrated about a closed curve, therefore, the vertically integrated momentum circulation integral constraint is satisfied.

3.5.2 Conservation of total energy

3.5.2.1 Work done by the pressure gradient forces

Applying $\nabla\phi = 0$ to equation (3.43) the work done by the HPGF can now be written as

$$\left[m\mathbf{v} \cdot (\mathbf{HGPF}) \right]_k = -m_k \alpha_k \mathbf{v}_k \cdot \nabla p_k \quad \text{for} \quad k = 1, 2, \cdots, K. \tag{3.89}$$

The work done by the VPGF is still expressed by equation (3.44), however, due to the lower boundary condition, equation (3.45) becomes

$$\left[mw\cdot(\text{VGPF})\right]_{1/2}=0\,. \tag{3.90}$$

After some rearrangement of terms as in the derivation of equation (3.54), the vertical sum of the work done by the pressure gradient forces is

$$\begin{aligned}\sum_{k=1}^{K}\left[m\mathbf{v}\cdot(\mathbf{HGPF})\right]_k\left(\delta\eta\right)_k+\sum_{k=0}^{K-1}\left[mw\cdot(\text{VGPF})\right]_{k+1/2}\left(\delta\eta\right)_{k+1/2}\\ =-\sum_{k=1}^{K}\left(m\alpha\omega\right)_k\left(\delta\eta\right)_k+\sum_{k=1}^{K}\frac{\partial}{\partial t}\left[\frac{p_k}{g}\left(\phi_{k+1/2}-\phi_{k-1/2}\right)\right],\end{aligned} \tag{3.91}$$

where the vertical sum of the energy conversion term is given by

$$\begin{aligned}\sum_{k=1}^{K}\left(m\alpha\omega\right)_k\left(\delta\eta\right)_k=\sum_{k=1}^{K}m_k\alpha_k\left(\frac{\partial p_k}{\partial t}+\mathbf{v}_k\cdot\nabla p_k\right)\left(\delta\eta\right)_k\\ +\sum_{k=1}^{K-1}w_{k+1/2}\hat{\rho}_{k+1/2}\theta_{k+1/2}\left(\Pi_{k+1}-\Pi_k\right).\end{aligned} \tag{3.92}$$

3.5.2.2 Thermodynamic energy equation

We use the energy conversion term given by (3.92) in the vertically summed enthalpy tendency equation (3.64), which gives

$$\begin{aligned}\sum_{k=1}^{K}\frac{\partial}{\partial t}\left(mc_pT\right)_k\left(\delta\eta\right)_k+\sum_{k=1}^{K}\nabla\cdot\left(m\mathbf{v}c_pT\right)_k\left(\delta\eta\right)_k+\sum_{k=1}^{K}\left[\left(m\dot{\eta}c_pT\right)_{k+1/2}-\left(m\dot{\eta}c_pT\right)_{k-1/2}\right]\\ =\sum_{k=1}^{K}m_k\alpha_k\left(\frac{\partial p_k}{\partial t}+\mathbf{v}_k\cdot\nabla p_k\right)\left(\delta\eta\right)_k+\sum_{k=1}^{K-1}w_{k+1/2}\hat{\rho}_{k+1/2}\theta_{k+1/2}\left(\Pi_{k+1}-\Pi_k\right)\\ +\sum_{k=0}^{K}\left(mQ\right)_{k+1/2}\left(\delta\eta\right)_{k+1/2}.\end{aligned} \tag{3.93}$$

Combining mass continuity equation (3.19), equations (3.20), (3.39), and (3.41) we get

$$\sum_{k=1}^{K} m_k \Pi_k \left(\frac{\partial \tilde{\theta}_k}{\partial t} + \mathbf{v}_k \cdot \nabla \tilde{\theta}_k \right) \left(\delta\eta \right)_k - \sum_{k=1}^{K} \tilde{\theta}_k \Pi_k \left[\left(m\dot{\eta} \right)_{k+1/2} - \left(m\dot{\eta} \right)_{k-1/2} \right]$$
$$- \sum_{k=1}^{K-1} w_{k+1/2} \hat{\rho}_{k+1/2} \theta_{k+1/2} \left(\Pi_{k+1} - \Pi_k \right) = \sum_{k=0}^{K} \left(mQ \right)_{k+1/2} \left(\delta\eta \right)_{k+1/2}. \tag{3.94}$$

which is the requirement for total energy conservation. Note that up to this point we have not been required to specify the form of $\hat{\rho}_{k+1/2}$ to satisfy the integral constraints. Therefore we are free to specify it any way we wish. The most straightforward way is to simply define it from equation (2.15) such that

$$\hat{\rho}_{k+1/2} \equiv g m_{k+1/2} \frac{\left(\delta\eta \right)_{k+1/2}}{\tilde{\phi}_{k+1} - \tilde{\phi}_k}, \tag{3.95}$$

and

$$\hat{\rho}_{1/2} \equiv g m_{1/2} \frac{\left(\delta\eta \right)_{1/2}}{\tilde{\phi}_1 - \phi_{1/2}}, \tag{3.96}$$

which, for *z*-coordinates gives

$$\hat{\rho}_{k+1/2} = m_{k+1/2} \qquad \text{for} \quad k = 0, 1, \cdots, K-1. \tag{3.97}$$

Finally, using (3.20), (3.66) and (3.97) in (3.94) we get the requirement for total energy conversion in terms of potential temperature at layer edges, which is

$$
\begin{aligned}
&\frac{1}{2}\Pi_1\left[m_1\frac{\partial\theta_{1/2}}{\partial t}+\left(m\mathbf{v}\right)_1\cdot\nabla\theta_{1/2}\right]\left(\delta\eta\right)_1\\
&+\sum_{k=1}^{K-1}\left\{\begin{array}{l}\frac{1}{2}\left[\Pi_k m_k\left(\delta\eta\right)_k+\Pi_{k+1}m_{k+1}\left(\delta\eta\right)_{k+1}\right]\frac{\partial\theta_{k+1/2}}{\partial t}\\ +\frac{1}{2}\left[\Pi_k\left(m\mathbf{v}\right)_k\left(\delta\eta\right)_k+\Pi_{k+1}\left(m\mathbf{v}\right)_{k+1}\left(\delta\eta\right)_{k+1}\right]\cdot\nabla\theta_{k+1/2}\end{array}\right\}\\
&+\frac{1}{2}\Pi_K\left[m_K\frac{\partial\theta_{K+1/2}}{\partial t}+\left(m\mathbf{v}\right)_K\cdot\nabla\theta_{K+1/2}\right]\left(\delta\eta\right)_K\\
&+\sum_{k=1}^{K-1}\frac{1}{2}\left[\Pi_{k+1}\left(\theta_{k+3/2}-\theta_{k+1/2}\right)+\Pi_k\left(\theta_{k+1/2}-\theta_{k-1/2}\right)\right]\left(m\dot{\eta}\right)_{k+1/2}\\
&=\sum_{k=0}^{K}\left(mQ\right)_{k+1/2}\left(\delta\eta\right)_{k+1/2}
\end{aligned}
\tag{3.98}
$$

The potential temperature tendency equation which satisfies equation (3.98) is exactly the same as equations (3.68)-(3.72), with

$$
\left(\Pi\delta\theta\right)_{k+1/2}\equiv\frac{1}{2}\left[\Pi_{k+1}\left(\theta_{k+3/2}-\theta_{k+1/2}\right)+\Pi_k\left(\theta_{k+1/2}-\theta_{k-1/2}\right)\right]
\qquad \text{for} \quad k=1,2,\cdots,K-1. \tag{3.99}
$$

Note the simplified form of (3.99) compared to (3.73).

Equation (3.98) provides the "single vertical mass flux" form of the potential temperature advection as in AK96. We can rearrange the summation terms differently to rewrite (3.94) as

$$
\begin{aligned}
&\frac{1}{2}\Pi_1\left[m_1\frac{\partial\theta_{1/2}}{\partial t}+\left(m\mathbf{v}\right)_1\cdot\nabla\theta_{1/2}\right]\left(\delta\eta\right)_1\\
&\quad+\sum_{k=1}^{K-1}\left\{\begin{aligned}&\frac{1}{2}\left[\Pi_k m_k\left(\delta\eta\right)_k+\Pi_{k+1}m_{k+1}\left(\delta\eta\right)_{k+1}\right]\frac{\partial\theta_{k+1/2}}{\partial t}\\&+\frac{1}{2}\left[\Pi_k\left(m\mathbf{v}\right)_k\left(\delta\eta\right)_k+\Pi_{k+1}\left(m\mathbf{v}\right)_{k+1}\left(\delta\eta\right)_{k+1}\right]\cdot\nabla\theta_{k+1/2}\end{aligned}\right\}\\
&\quad+\frac{1}{2}\Pi_K\left[m_K\frac{\partial\theta_{K+1/2}}{\partial t}+\left(m\mathbf{v}\right)_K\cdot\nabla\theta_{K+1/2}\right]\left(\delta\eta\right)_K\\
&\quad+\sum_{k=1}^{K-1}\left[\left(m\dot{\eta}\right)_{k+1}\left(\Pi\tilde{\theta}\right)_{k+1}-\left(m\dot{\eta}\right)_k\left(\Pi\tilde{\theta}\right)_k\right]\\
&\quad-\left\{\begin{aligned}&\sum_{k=1}^{K-1}\theta_{k+1/2}\left[\Pi_{k+1}\left(m\dot{\eta}\right)_{k+1}-\Pi_k\left(m\dot{\eta}\right)_k\right]\\&+\Pi_1\left(\tilde{\theta}_1-\theta_{1/2}\right)\left(m\dot{\eta}\right)_1-\Pi_K\left(\theta_{K+1/2}-\tilde{\theta}_K\right)\left(m\dot{\eta}\right)_K\end{aligned}\right\}\\
&\quad=\sum_{k=0}^{K}\left(mQ\right)_{k+1/2}\left(\delta\eta\right)_{k+1/2}.
\end{aligned}
\tag{3.100}
$$

The potential temperature tendency equation which satisfies equation (3.100) is

$$
\begin{aligned}
&\frac{\partial\theta_{k+1/2}}{\partial t}+\frac{\left(m\Pi\mathbf{v}\delta\eta\right)_{k+1/2}}{\left(m\Pi\delta\eta\right)_{k+1/2}}\cdot\nabla\theta_{k+1/2}\\
&\qquad+\frac{\left(m\dot{\eta}\right)_{k+1}\left(\Pi\tilde{\theta}\right)_{k+1}-\left(m\dot{\eta}\right)_k\left(\Pi\tilde{\theta}\right)_k}{\left(m\Pi\delta\eta\right)_{k+1/2}}-\theta_{k+1/2}\frac{\Pi_{k+1}\left(m\dot{\eta}\right)_{k+1}-\Pi_k\left(m\dot{\eta}\right)_k}{\left(m\Pi\delta\eta\right)_{k+1/2}}\\
&\qquad=\frac{\left(mQ\delta\eta\right)_{k+1/2}}{\left(m\Pi\delta\eta\right)_{k+1/2}}\\
&\qquad\qquad\text{for}\quad k=1,2,\cdots,K-1,
\end{aligned}
\tag{3.101}
$$

and equations (3.78) and (3.79) still apply to the bottom and top layers respectively.

3.5.2.3 Geopotential energy equation

The geopotential energy equation for $\eta=z$ is the same as in subsection 3.4.3.3. In height coordinates, geopotential energy conservation is closely tied to mass continuity.

3.5.3 Implications of the "z-scheme"

With the modified form of $\hat{\rho}_{k+1/2}$ given by (3.95) and (3.96), the VPGF given by equations (3.32) and (3.33) becomes

$$(\text{VPGF})_{k+1/2} = -g\theta_{k+1/2}\frac{\Pi_{k+1}-\Pi_k}{\tilde{\phi}_{k+1}-\tilde{\phi}_k} \qquad \text{for} \quad k = 1, 2, \cdots, K-1, \tag{3.102}$$

and

$$(\text{VPGF})_{1/2} = -g\theta_{1/2}\frac{\Pi_1-\hat{\Pi}_{1/2}}{\tilde{\phi}_1-\phi_{1/2}}. \tag{3.103}$$

The VPGF now has the "Π-form", so the computational mode in potential temperature is avoided (see Figure 3.1). As shown in Appendix B, this form of the VPGF leads to a reduction in the truncation error. Again, the trade-off with using this scheme is that in general, for $\eta \neq z$, integral constraints I and II are not satisfied. We consider the avoidance of the computational mode to be more important than unconditionally satisfying the integral constraints, and therefore use the *z*-scheme in the model.

3.6 Summary of the design features of the two vertical schemes

We have derived two vertical discretization schemes which mainly differ in their specification of the vertical pressure gradient in the vertical momentum equation. In the "η-scheme", the discrete VPGF is expressed in terms of pressure, while in the "*z*-scheme", it is expressed in terms of the Exner function. We use the latter scheme in the model, even though integral Constraints I and II are not generally satisfied. The overriding benefit to the "*z*-scheme" is the avoidance of a computational mode in the

potential temperature field. In addition, Thuburn (2006) and Toy and Randall (2007) demonstrated that the representation of linear wave propagation is more accurate with the Exner function form of the VPGF. Table 3.1 summarizes the main characteristics of the two schemes.

Table 3.1: Comparison of the characteristics of the "z-scheme" and the "η-scheme". (Note that the integral constraints refer to satisfaction for the generalized vertical coordinate. The "z-scheme" satisfies Constraints I and II for the specific case $\eta = z$.)

	Discrete form of the VPGF	z-coord. computational mode in θ?	Mass conservation (Constraint 0)	Momentum circulation constraint on the HPGF (Constraint I)	Conservation of total energy (Constraint II)	Conservation of θ (Constraint III)
z-scheme	$-\theta \frac{\delta \Pi}{\delta z}$	No	Satisfied	Not satisfied	Not satisfied	Not satisfied
η-scheme	$-\frac{1}{m}\frac{\delta p}{\delta \eta}$	Yes	Satisfied	Satisfied	Satisfied	Not satisfied

3.7 Summary of the "z-scheme" vertically discrete governing equations

This section summarizes the vertically discrete governing equations of the "z-scheme" which the model is based on. The scheme was developed using centered differences. In the actual model, we use upstream-weighted advection schemes for mass, potential temperature, and geopotential. These are presented in Appendix A. The use of these uncentered schemes means that the model equations do not formally satisfy the integral constraints.

Continuity equation:

$$\frac{\partial m_k}{\partial t} + \nabla \cdot \left(m\mathbf{v} \right)_k + \frac{\left(m\dot{\eta} \right)_{k+1/2} - \left(m\dot{\eta} \right)_{k-1/2}}{\left(\delta\eta \right)_k} = 0 \qquad \text{for} \quad k = 1, 2, \cdots, K. \tag{3.104}$$

Boundary conditions:

$$\dot{\eta}_{1/2} = \dot{\eta}_{K+1/2} = 0 \,. \tag{3.105}$$

Vertical pressure gradient force:

$$(\text{VPGF})_{k+1/2} = -g\theta_{k+1/2} \frac{\Pi_{k+1} - \Pi_k}{\tilde{\phi}_{k+1} - \tilde{\phi}_k} \qquad \text{for} \quad k = 1, 2, \cdots, K-1, \tag{3.106}$$

and

$$(\text{VPGF})_{1/2} = -g\theta_{1/2} \frac{\Pi_1 - \hat{\Pi}_{1/2}}{\tilde{\phi}_1 - \phi_{1/2}} \,, \tag{3.107}$$

where

$$\tilde{\phi}_k \equiv \frac{1}{2}\left(\phi_{k+1/2} + \phi_{k-1/2} \right) \qquad \text{for} \quad k = 1, 2, \cdots, K. \tag{3.108}$$

Horizontal pressure gradient force:

$$(\mathbf{HPGF})_k = -\tilde{\theta}_k \nabla\Pi_k + \frac{1}{\mathrm{g}} \left(\widetilde{\frac{\rho}{m}\theta \frac{\partial\Pi}{\partial\eta} \nabla\phi} \right)_k \qquad \text{for} \quad k = 1, 2, \cdots, K, \tag{3.109}$$

where

$$\left(\widetilde{\frac{\rho}{m}\theta\frac{\partial\Pi}{\partial\eta}\nabla\phi}\right)_k = \frac{1}{2}\left[g\theta_{k+1/2}\frac{\Pi_{k+1}-\Pi_k}{\tilde{\phi}_{k+1}-\tilde{\phi}_k}\nabla\phi_{k+1/2} + g\theta_{k-1/2}\frac{\Pi_k-\Pi_{k-1}}{\tilde{\phi}_k-\tilde{\phi}_{k-1}}\nabla\phi_{k-1/2}\right] \tag{3.110}$$

$$\text{for} \quad k = 2, 3, \cdots, K-1,$$

$$\left(\widetilde{\frac{\rho}{m}\theta\frac{\partial\Pi}{\partial\eta}\nabla\phi}\right)_1 = \frac{1}{2}\left[g\theta_{3/2}\frac{\Pi_2-\Pi_1}{\tilde{\phi}_2-\tilde{\phi}_1}\nabla\phi_{3/2} + g\theta_{1/2}\frac{\Pi_1-\hat{\Pi}_{1/2}}{\tilde{\phi}_1-\phi_{1/2}}\nabla\phi_{1/2}\right], \tag{3.111}$$

$$\left(\widetilde{\frac{\rho}{m}\theta\frac{\partial\Pi}{\partial\eta}\nabla\phi}\right)_K = \frac{1}{2}\left[g\theta_{K+1/2}\frac{\hat{\Pi}_{K+1/2}-\Pi_K}{\phi_{K+1/2}-\tilde{\phi}_K}\nabla\phi_{K+1/2} + g\theta_{k-1/2}\frac{\Pi_k-\Pi_{k-1}}{\tilde{\phi}_k-\tilde{\phi}_{k-1}}\nabla\phi_{k-1/2}\right], \tag{3.112}$$

$$\tilde{\theta}_k = \frac{1}{2}\left(\theta_{k+1/2}+\theta_{k-1/2}\right) \qquad \text{for} \quad k = 1, 2, \cdots, K, \tag{3.113}$$

$$\left(\delta\eta\right)_{k+1/2} \equiv \frac{1}{2}\left[\left(\delta\eta\right)_k + \left(\delta\eta\right)_{k+1}\right] \tag{3.114}$$

$$\text{for} \quad k = 1, 2, \cdots, K-1,$$

and

$$\left(\delta\eta\right)_{1/2} \equiv \frac{1}{2}\left(\delta\eta\right)_1, \qquad \left(\delta\eta\right)_{K+1/2} \equiv \frac{1}{2}\left(\delta\eta\right)_K. \tag{3.115}$$

Thermodynamic equation:

$$\begin{aligned}\frac{\partial\theta_{k+1/2}}{\partial t} &+ \frac{\left(m\Pi\mathbf{v}\delta\eta\right)_{k+1/2}}{\left(m\Pi\delta\eta\right)_{k+1/2}}\cdot\nabla\theta_{k+1/2} \\ &+ \frac{\left(m\dot{\eta}\right)_{k+1}\left(\Pi\tilde{\theta}\right)_{k+1} - \left(m\dot{\eta}\right)_k\left(\Pi\tilde{\theta}\right)_k}{\left(m\Pi\delta\eta\right)_{k+1/2}} - \theta_{k+1/2}\frac{\Pi_{k+1}\left(m\dot{\eta}\right)_{k+1} - \Pi_k\left(m\dot{\eta}\right)_k}{\left(m\Pi\delta\eta\right)_{k+1/2}} \\ &= \frac{\left(mQ\delta\eta\right)_{k+1/2}}{\left(m\Pi\delta\eta\right)_{k+1/2}}\end{aligned} \tag{3.116}$$

$$\text{for} \quad k = 1, 2, \cdots, K-1,$$

$$\frac{\partial \theta_{1/2}}{\partial t} + \frac{\left(m\mathbf{v}\right)_1}{m_1} \cdot \nabla \theta_{1/2} + \frac{\left(\tilde{\theta}_1 - \theta_{1/2}\right)\left(m\dot{\eta}\right)_1}{m_{1/2}\left(\delta\eta\right)_{1/2}} = \frac{Q_{1/2}}{\Pi_1}, \tag{3.117}$$

and

$$\frac{\partial \theta_{K+1/2}}{\partial t} + \frac{\left(m\mathbf{v}\right)_K}{m_K} \cdot \nabla \theta_{K+1/2} + \frac{\left(\theta_{K+1/2} - \tilde{\theta}_K\right)\left(m\dot{\eta}\right)_K}{m_{K+1/2}\left(\delta\eta\right)_{K+1/2}} = \frac{Q_{K+1/2}}{\Pi_K}, \tag{3.118}$$

where

$$\left(m\Pi\delta\eta\right)_{k+1/2} \equiv \frac{1}{2}\left[\left(m\Pi\right)_k\left(\delta\eta\right)_k + \left(m\Pi\right)_{k+1}\left(\delta\eta\right)_{k+1}\right] \qquad \text{for} \quad k = 1, 2, \cdots, K-1, \tag{3.119}$$

$$\left(m\Pi\mathbf{v}\delta\eta\right)_{k+1/2} \equiv \frac{1}{2}\left[\Pi_k\left(m\mathbf{v}\right)_k\left(\delta\eta\right)_k + \Pi_{k+1}\left(m\mathbf{v}\right)_{k+1}\left(\delta\eta\right)_{k+1}\right] \qquad \text{for} \quad k = 1, 2, \cdots, K-1, \tag{3.120}$$

$$\left(m\dot{\eta}\right)_k \equiv \frac{1}{2}\left[\left(m\dot{\eta}\right)_{k+1/2} + \left(m\dot{\eta}\right)_{k-1/2}\right] \qquad \text{for} \quad k = 2, 3, \cdots, K-1, \tag{3.121}$$

and

$$\left(m\dot{\eta}\right)_1 \equiv \frac{1}{2}\left(m\dot{\eta}\right)_{1/2}, \qquad \left(m\dot{\eta}\right)_K \equiv \frac{1}{2}\left(m\dot{\eta}\right)_{K-1/2}. \tag{3.122}$$

Geopotential tendency equation:

$$\frac{\partial \phi_{k+1/2}}{\partial t} + \frac{\left(m\mathbf{v}\right)_{k+1/2}}{m_{k+1/2}} \cdot \nabla \phi_{k+1/2} + \dot{\eta}_{k+1/2}\frac{\tilde{\phi}_{k+1} - \tilde{\phi}_k}{\left(\delta\eta\right)_{k+1/2}} = g w_{k+1/2} \qquad \text{for} \quad k = 1, 2, \cdots, K-1, \tag{3.123}$$

where

$$\left(m\mathbf{v}\right)_{k+1/2} \equiv \frac{1}{2}\frac{\left(\delta\eta\right)_k \left(m\mathbf{v}\right)_k + \left(\delta\eta\right)_{k+1}\left(m\mathbf{v}\right)_{k+1}}{\left(\delta\eta\right)_{k+1/2}} \qquad \text{for} \quad k = 1, 2, \cdots, K-1, \tag{3.124}$$

and

$$m_{k+1/2} \equiv \frac{1}{2}\frac{\left(\delta\eta\right)_k m_k + \left(\delta\eta\right)_{k+1} m_{k+1}}{\left(\delta\eta\right)_{k+1/2}} \qquad \text{for} \quad k = 1, 2, \cdots, K-1. \tag{3.125}$$

Diagnostic equation for temperature:

$$T_k = \frac{\tilde{\theta}_k \Pi_k}{c_p} \qquad \text{for} \quad k = 1, 2, \cdots, K\,. \tag{3.126}$$

Equation of state:

$$p_k = \rho_k R T_k \qquad \text{for} \quad k = 1, 2, \cdots, K\,. \tag{3.127}$$

Diagnostic equation for density:

$$\rho_k = \frac{m_k g\left(\delta\eta\right)_k}{\phi_{k+1/2} - \phi_{k-1/2}} \qquad \text{for} \quad k = 1, 2, \cdots, K. \tag{3.128}$$

Relationship between Exner function and pressure:

$$\Pi_k = c_p \left(\frac{p_k}{p_0}\right)^{\kappa} \text{ for} \quad k = 1, 2, \cdots, K\,. \tag{3.129}$$

Definition of the height-based, terrain-following coordinate σ:

$$\sigma_{k+1/2} = \frac{z_{k+1/2} - z_S(x,y)}{z_T - z_S(x,y)} \qquad \text{for} \quad k = 0, 1, \cdots, K, \tag{3.130}$$

where z_S is the surface height, and z_T is the model top height (which we define as a constant value).

Chapter 4 VERTICAL VELOCITY DIAGNOSIS AND ADVECTION IN THE DISCRETE EQUATIONS

4.1 Introduction

In Chapter 2, we presented the vertical coordinate used in the model, along with the diagnosis of the vertical velocity, $\dot{\eta}$, in the continuous framework. In this chapter we describe the method for diagnosing the vertical velocity in the discrete system of equations. As our handling of the generalized vertical coordinate is based mainly on KA97, the vertical velocity diagnosis is similar to their technique. However, our method differs as a result of our use of an adaptive grid and upstream-weighted, uncentered vertical advection schemes in the prognostic equations for θ and ϕ – the two variables which are the basis of the vertical coordinate η. To accommodate this, we will split the "target-seeking" component of the generalized vertical velocity, introduced in equation (2.70), into additional components and apply each one in either a centered or an upstream-weighted advection scheme. We begin by developing the framework for determining the appropriate scheme to use.

4.2 A closer look at the advection of θ and z by the generalized vertical velocity

An implicit fact regarding the vertical coordinate in a system of hydrodynamic equations is that its value is constant in time, i.e., $\partial\eta/\partial t=0$. This means that for systems based on "pure" vertical coordinates based on a single property such as height, potential temperature or pressure, an explicit prognostic equation for that property is not needed. However, such an equation is implicitly satisfied by the specification of the vertical velocity in each coordinate system. For example, in height coordinates, we could write

$$\frac{\partial z}{\partial t} = 0 = w - \mathbf{v}\cdot\nabla z - \dot{z}\frac{\partial z}{\partial z}. \tag{4.1}$$

Since $\nabla z=0$ and $\partial z/\partial z=1$, this simply expresses the Lagrangian relationship $\dot{z} = w$. Similarly, in isentropic coordinates, we could write

$$\frac{\partial \theta}{\partial t} = 0 = \frac{Q}{\Pi} - \mathbf{v}\cdot\nabla\theta - \dot{\theta}\frac{\partial \theta}{\partial \theta} \tag{4.2}$$

Since $\nabla\theta=0$ and $\partial\theta/\partial\theta=1$, this reduces to the Lagrangian form of the first law of thermodynamics $\dot{\theta} = Q/\Pi$.

In the framework of the hybrid vertical coordinate model, the coordinate is a function of more than one property. In our case, these are the potential temperature and geopotential height. As a result, prognostic equations for both of these properties must be explicitly expressed. We showed in Chapter 2 that the main role of the generalized vertical velocity is to maintain the constant value of the coordinate. In the following discussion, we will show that the roles performed by the vertical advection terms in each of the prognostic equations, i.e., $\dot{\eta}\partial z/\partial\eta$ and $\dot{\eta}\partial\theta/\partial\eta$, change in the vertical transition

from z-based to θ coordinates. This affects the way these terms are handled in the vertically discrete equations – whether upstream-weighted or centered-difference advection schemes are applied, for example.

4.2.1 The role of the vertical θ-advection term in the z-coordinate domain

The prognostic equation for potential temperature in height coordinates may be written as

$$\frac{\partial \theta}{\partial t} = \frac{Q}{\Pi} - \mathbf{v} \cdot \nabla \theta - w \frac{\partial \theta}{\partial z} . \tag{4.3}$$

The vertical advection term (the last term on the right-hand side) physically represents the θ-tendency due to the advection of potential temperature across surfaces of constant z. In the vertically discrete model, an upstream-weighted treatment of this term is justified in order to reduce dispersion error as demonstrated in Figure 3.4. So, in the discrete equations, we want

$$\left(\dot{\eta} \frac{\partial \theta}{\partial \eta} \right)_{k+1/2} \rightarrow \left(\dot{\eta} \frac{\partial \theta}{\partial \eta} \right)_{\substack{UPSTREAM \\ WEIGHTED}} \quad \text{for} \quad \eta \rightarrow z . \tag{4.4}$$

4.2.2 The role of the vertical θ-advection term in the θ-coordinate domain

As mentioned above, equation (4.2) shows that the role of the vertical advection of potential temperature in isentropic equations is to cancel out the diabatic heating term in order to keep θ constant on coordinate surfaces. The way we achieve this in the model is to specify a centered form of the vertical advection term in the limit of isentropic coordinates, specifically

$$\left(\dot{\eta}\frac{\partial\theta}{\partial\eta}\right)_{k+1/2} \rightarrow \dot{\eta}_{k+1/2}\frac{\left(\delta\theta\right)_{k+1/2}}{\left(\delta\eta\right)_{k+1/2}} \quad \text{for} \quad \eta\rightarrow\theta\,. \tag{4.5}$$

Equation (4.2) is satisfied provided that $\dot{\eta}_{k+1/2}\rightarrow\left(Q/\Pi\right)_{k+1/2}$ and $(\delta\theta)_{k+1/2}/(\delta\eta)_{k+1/2}\rightarrow 1$ for $\eta\rightarrow\theta$. The vertical velocity diagnostic procedure developed in this chapter satisfies the former requirement, while the latter is satisfied by equations (3.113) and (3.114).

4.2.3 The role of the vertical z-advection term in the θ-coordinate domain

The prognostic equation for geopotential height in isentropic coordinates may be written as

$$\frac{\partial z}{\partial t} = w - \mathbf{v}\cdot\nabla z - \dot{\theta}\frac{\partial z}{\partial\theta}\,. \tag{4.6}$$

The vertical advection term physically represents the z-tendency due to the advection of geopotential height across surfaces of constant θ. In the vertically discrete model, an upstream-weighted treatment of this term is justified in order to reduce dispersion error in a manner analogous to the advection of θ in z-coordinates. Therefore, in the model, we want

$$\left(\dot{\eta}\frac{\partial z}{\partial\eta}\right)_{k+1/2} \rightarrow \left(\dot{\eta}\frac{\partial z}{\partial\eta}\right)_{\substack{UPSTREAM\\WEIGHTED}} \quad \text{for} \quad \eta\rightarrow\theta\,. \tag{4.7}$$

4.2.4 The role of the vertical z-advection term in the z-coordinate domain

As mentioned above, equation (4.1) shows that the role of the vertical advection of geopotential height in z-coordinates is to cancel out the vertical velocity w in order to

keep z constant on coordinate surfaces. The way we achieve this in the model is to specify a centered form of the vertical advection term in the limit of height coordinates, specifically

$$\left(\dot{\eta}\frac{\partial z}{\partial \eta}\right)_{k+1/2} \to \dot{\eta}_{k+1/2}\frac{\left(\delta z\right)_{k+1/2}}{\left(\delta \eta\right)_{k+1/2}} \quad \text{for} \quad \eta \to z\,. \tag{4.8}$$

Equation (4.1) is satisfied provided that $\dot{\eta}_{k+1/2} \to w_{k+1/2}$ and $(\delta z)_{k+1/2}/(\delta \eta)_{k+1/2} \to 1$ for $\eta \to z$. The vertical velocity diagnostic procedure developed in this chapter satisfies the former requirement, while the latter is satisfied by equations (3.108) and (3.114).

4.2.5 Two components of the generalized vertical velocity

The way we vary the vertical advection of θ and z between centered and upstream-weighted schemes, as described above, is by splitting the generalized vertical velocity into components and parceling these to the appropriate scheme. In the current simplified analysis, there are two components to the vertical velocity – one is the contribution from the "z-like" nature of the coordinate ($\dot{\eta}_z$), and the other is the contribution from the "θ-like" nature of the coordinate ($\dot{\eta}_\theta$). The proportion of the contributions from each of these components "automatically" vary with height as η transitions from z to θ. The two components sum to the total vertical velocity $\dot{\eta}$, i.e.,

$$\dot{\eta} = \dot{\eta}_z + \dot{\eta}_\theta\,, \tag{4.9}$$

and they have the properties

$$\left.\begin{array}{llll} \dot{\eta}_z \to w, & \dot{\eta}_\theta \to 0 & \text{for} & \eta \to z \\ \dot{\eta}_z \to 0, & \dot{\eta}_\theta \to \dfrac{Q}{\Pi} & \text{for} & \eta \to \theta \end{array}\right\}. \tag{4.10}$$

Letting $\eta = F(\theta, z)$, and requiring $(\partial/\partial t)_\eta F = 0$, we can write

$$\left(\frac{\partial}{\partial t}\right)_\eta F(\theta,z) = 0 = \left(\frac{\partial F}{\partial \theta}\right)_z \frac{\partial \theta}{\partial t} + \left(\frac{\partial F}{\partial z}\right)_\theta \frac{\partial z}{\partial t}. \tag{4.11}$$

Applying the tendency equations for θ and z in η coordinates,

$$\frac{\partial \theta}{\partial t} = \frac{Q}{\Pi} - \mathbf{v}\cdot\nabla\theta - \dot{\eta}\frac{\partial \theta}{\partial \eta}, \tag{4.12}$$

and

$$\frac{\partial z}{\partial t} = w - \mathbf{v}\cdot\nabla z - \dot{\eta}\frac{\partial z}{\partial \eta}, \tag{4.13}$$

respectively, in equation (4.11) and solving for $\dot{\eta}$, we get

$$\dot{\eta} = \left(\frac{\partial F}{\partial z}\right)_\theta \left(w - \mathbf{v}\cdot\nabla z\right) + \left(\frac{\partial F}{\partial \theta}\right)_z \left(\frac{Q}{\Pi} - \mathbf{v}\cdot\nabla\theta\right). \tag{4.14}$$

Here we used

$$\frac{\partial F}{\partial \eta} = \left(\frac{\partial F}{\partial \theta}\right)_z \frac{\partial \theta}{\partial \eta} + \left(\frac{\partial F}{\partial z}\right)_\theta \frac{\partial z}{\partial \eta} = 1. \tag{4.15}$$

Finally, comparing equations (4.9) and (4.14) we can write

$$\dot{\eta}_z \equiv \left(\frac{\partial F}{\partial z}\right)_\theta \left(w - \mathbf{v}\cdot\nabla z\right), \tag{4.16}$$

and

$$\dot{\eta}_\theta \equiv \left(\frac{\partial F}{\partial \theta}\right)_z \left(\frac{Q}{\Pi} - \mathbf{v}\cdot\nabla\theta\right). \tag{4.17}$$

These expressions satisfy (4.10).

Now, we can use these two components of the generalized vertical velocity to define vertical advection schemes for θ and z whose roles adapt in the manner described above in Subsections 4.2.1-4.2.4. These are:

⟨θ-advection⟩

$$\left(\dot{\eta}\frac{\partial\theta}{\partial\eta}\right)_{k+1/2} \equiv \left(\dot{\eta}_\theta\right)_{k+1/2}\frac{\left(\delta\theta\right)_{k+1/2}}{\left(\delta\eta\right)_{k+1/2}} + \left[\left(\dot{\eta}_z\frac{\partial\theta}{\partial\eta}\right)_{\substack{UPSTREAM\\WEIGHTED}}\right]_{k+1/2}; \tag{4.18}$$

⟨z-advection⟩

$$\left(\dot{\eta}\frac{\partial z}{\partial\eta}\right)_{k+1/2} \equiv \left(\dot{\eta}_z\right)_{k+1/2}\frac{\left(\delta z\right)_{k+1/2}}{\left(\delta\eta\right)_{k+1/2}} + \left[\left(\dot{\eta}_\theta\frac{\partial z}{\partial\eta}\right)_{\substack{UPSTREAM\\WEIGHTED}}\right]_{k+1/2}. \tag{4.19}$$

The above expressions accommodate the specific roles of the vertical advection terms specified in equations (4.4), (4.5), (4.7) and (4.8).

4.3 Vertical velocity diagnosis and the advection of θ and ϕ in the model

In the previous section, we described the method of vertically advecting potential temperature and geopotential height in a simplified framework of a vertical coordinate based on θ and z. In the model, the coordinate is based on θ and the terrain-following σ coordinate, so the procedure is slightly more complicated, but the overall concept is the same. In this section we outline the vertical velocity diagnosis, and the advection of θ and ϕ in the model.

4.3.1 Advection of θ and ϕ by the "target-seeking" vertical velocity component

Recall from Section 2.5 (equation (2.70)) that we broke the vertical velocity into two components – $\dot{\eta}_T$, which is responsible for relaxing $F(\theta,\sigma)$ toward and maintaining its target value η, and $\dot{\eta}_S$, which involves the spatial smoothing of the coordinate surfaces (and generally causes $F(\theta,\sigma)$ to deviate from its target value). Here $F(\theta,\sigma)$ was defined in equation (2.58). We examine the first component, expressed by equation (2.72), and consider $\eta=F$, so that $\partial F/\partial\eta=1$. The vertically discrete form is

$$\left(\dot{\eta}_T\right)_{k+1/2} = \left\{\left[\left(\frac{\partial F}{\partial\theta}\right)_\sigma\left(\frac{Q}{\Pi}-\mathbf{v}\cdot\nabla\theta\right)+\left(\frac{\partial F}{\partial\sigma}\right)_\theta\left(\frac{w}{H}-\frac{1}{gH}\mathbf{v}\cdot\nabla\phi\right)+\frac{F(\theta,\sigma)-\eta}{\tau}\right]\right\}_{k+1/2} \quad (4.20)$$

Similarly to the previous section, we break the vertical velocity into the following components:

$$\left(\dot{\eta}_T\right)_{k+1/2} = \left(\dot{\eta}_{T,\sigma}\right)_{k+1/2} + \left(\dot{\eta}_{T,Q}\right)_{k+1/2} + \left(\dot{\eta}_{T,\theta}\right)_{k+1/2} + \left(\dot{\eta}_{T,R}\right)_{k+1/2}, \quad (4.21)$$

where

$$\left(\dot{\eta}_{T,\sigma}\right)_{k+1/2} = \left[\left(\frac{\partial F}{\partial\sigma}\right)_\theta\right]_{k+1/2}\frac{1}{gH}\left(wg-\mathbf{v}\cdot\nabla\phi\right)_{k+1/2}, \quad (4.22)$$

$$\left(\dot{\eta}_{T,Q}\right)_{k+1/2} = \left[\left(\frac{\partial F}{\partial\theta}\right)_\sigma\right]_{k+1/2}\left(\frac{Q}{\Pi}\right)_{k+1/2}, \quad (4.23)$$

$$\left(\dot{\eta}_{T,\theta}\right)_{k+1/2} = -\left[\left(\frac{\partial F}{\partial\theta}\right)_\sigma\right]_{k+1/2}\left(\mathbf{v}\cdot\nabla\theta\right)_{k+1/2}, \quad (4.24)$$

and

$$\left(\dot{\eta}_{T,R}\right)_{k+1/2} = \frac{F(\theta_{k+1/2},\sigma_{k+1/2}) - \eta_{k+1/2}}{\tau}\,. \tag{4.25}$$

Note that similarly to equation (4.10) the first three components have the following properties:

$$\left.\begin{array}{llll} \dot{\eta}_{T,\sigma} \to \dot{\sigma}, & \dot{\eta}_{T,Q} \to 0, & \dot{\eta}_{T,\theta} \to 0 & \text{for} \quad \eta \to \sigma \\ \dot{\eta}_{T,\sigma} \to 0, & \dot{\eta}_{T,Q} \to \dfrac{Q}{\Pi}, & \dot{\eta}_{T,\theta} \to 0 & \text{for} \quad \eta \to \theta \end{array}\right\}. \tag{4.26}$$

Accordingly, we handle the vertical advection of θ and ϕ by these components as

$$\left[\left(\dot{\eta}_{T,\sigma} + \dot{\eta}_{T,Q} + \dot{\eta}_{T,\theta}\right)\frac{\partial\theta}{\partial\eta}\right]_{k+1/2} = \left[\left(\dot{\eta}_{T,\sigma}\frac{\partial\theta}{\partial\eta}\right)_{\substack{UPSTREAM\\WEIGHTED}}\right]_{k+1/2} + \left(\dot{\eta}_{T,Q} + \dot{\eta}_{T,\theta}\right)_{k+1/2}\frac{\left(\delta\theta\right)_{k+1/2}}{\left(\delta\eta\right)_{k+1/2}}, \tag{4.27}$$

and

$$\left[\left(\dot{\eta}_{T,\sigma} + \dot{\eta}_{T,Q} + \dot{\eta}_{T,\theta}\right)\frac{\partial\phi}{\partial\eta}\right]_{k+1/2} = \left(\dot{\eta}_{T,\sigma}\right)_{k+1/2}\frac{\left(\delta\phi\right)_{k+1/2}}{\left(\delta\eta\right)_{k+1/2}} + \left\{\left[\left(\dot{\eta}_{T,Q} + \dot{\eta}_{T,\theta}\right)\frac{\partial\phi}{\partial\eta}\right]_{\substack{UPSTREAM\\WEIGHTED}}\right\}_{k+1/2}, \tag{4.28}$$

respectively. Equations (4.26)-(4.28) assure that $(\partial\phi_{k+1/2}/\partial t) \to 0$ for $\eta \to \sigma$, and $(\partial\theta_{k+1/2}/\partial t) \to 0$ for $\eta \to \theta$.

When coordinate smoothing has taken place at a given model grid point, then $\eta \neq F(\theta,\sigma)$ and, therefore, from equation (4.25) we have $\left(\dot{\eta}_{T,R}\right)_{k+1/2} \neq 0$. The purpose of this vertical velocity component is to advect θ and ϕ in such a way as to return F to its

target value η through a relaxation process with time constant τ. In the model, we use centered schemes, for simplicity, to advect θ and ϕ, in this process i.e.,

$$\left(\dot{\eta}_{T,R}\frac{\partial\theta}{\partial\eta}\right)_{k+1/2} = \left(\dot{\eta}_{T,R}\right)_{k+1/2}\frac{\left(\delta\theta\right)_{k+1/2}}{\left(\delta\eta\right)_{k+1/2}}, \tag{4.29}$$

and

$$\left(\dot{\eta}_{T,R}\frac{\partial\phi}{\partial\eta}\right)_{k+1/2} = \left(\dot{\eta}_{T,R}\right)_{k+1/2}\frac{\left(\delta\phi\right)_{k+1/2}}{\left(\delta\eta\right)_{k+1/2}}. \tag{4.30}$$

A summary of the vertical advection schemes for θ and ϕ associated with each of the four components of the "target-seeking" vertical velocity is shown in Table 4.1. The upstream-weighted advection schemes are based on Takacs (1985) and the details are shown in Appendix A.

Table 4.1: Type of scheme used for the discrete vertical advection of θ and ϕ by each "target-seeking" vertical velocity component.

Vertical velocity component	θ	ϕ
$\dot{\eta}_{T,\sigma}$	Upstream-weighted	Centered
$\dot{\eta}_{T,Q}$	Centered	Upstream-weighted
$\dot{\eta}_{T,\theta}$	Centered	Upstream-weighted
$\dot{\eta}_{T,R}$	Centered	Centered

4.3.2 Advection of θ and ϕ by the "smoothing" vertical velocity component

The purpose of the $\dot{\eta}_S$ component of the vertical velocity is to maintain the "smoothness" criteria for the model coordinate surfaces. To do this, it has to force

$F(\theta,\sigma)$ away from its target value, η. The geopotential height tendency is directly calculated from the "smoothness" criteria given by equations (2.79) and (2.80). When these criteria are met, the results are used in the finite-difference form of equation (2.78) to calculate the "smoothing" component of the vertical velocity. A simple centered form of $\partial\eta/\partial z$ is used, so that

$$\left(\dot{\eta}_S\right)_{k+1/2} = -\left[\left(\frac{\partial z}{\partial t}\right)_{\text{smoothing},h} + \left(\frac{\partial z}{\partial t}\right)_{\text{smoothing},v}\right]_{k+1/2} \frac{\left(\delta\eta\right)_{k+1/2}}{\left(\delta z\right)_{k+1/2}}. \tag{4.31}$$

This has the effect of vertically advecting ϕ with a simple centered scheme. The vertical velocity values generated by this algorithm are then used to advect θ in an upstream-weighted scheme.

4.3.3 The final determination of the vertical velocity

KA97 diagnose the vertical velocity in two steps. First, all the processes which affect θ and σ, except for vertical advection, are determined. These include horizontal advection and diabatic heating. Generally, this will force $F(\theta,\sigma)$ from its target value, η. The second step is to determine, through an iterative procedure, the vertical mass flux required to bring $F(\theta,\sigma)$ back to the target value.

We follow the same general procedure, except that in the first step, we include the vertical advection of θ and ϕ, just presented, as an explicit forcing. Another difference is that in our method, the target value for $F(\theta_{k+1/2},\sigma_{k+1/2})$ at a given time step is not necessarily $\eta_{k+1/2}$, but instead is

$$F^{n}{}_{k+1/2} = F^{n-1}{}_{k+1/2} + \left(\Delta t\right)\frac{\eta_{k+1/2} - F^{n-1}{}_{k+1/2}}{\tau}, \tag{4.32}$$

where n and n-1 refer to the current and previous time steps, respectively. This a time-integration of equation (2.64) with $\dot{\eta}_S$ set to zero, i.e.,

$$\left(\frac{\partial}{\partial t}\right)_{\eta} F(\theta,\sigma) = \frac{\eta - F(\theta,\sigma)}{\tau}. \tag{4.33}$$

Where in KA97, the vertical velocity determined by the iterative solution is the total velocity, in our case, it is the residual required to exactly set $F(\theta_{k+1/2},\sigma_{k+1/2})$ to $F^{\mathrm{n}}{}_{\mathrm{k+1/2}}$ at the current time step.

In the first step of the iterative procedure, we find the tendency of $F_{k+1/2}$ due to the processes of horizontal advection, diabatic heating, vertical displacements by w, and the vertical advection by $\dot{\eta}_T$. This is done by calculating

$$\theta_{k+1/2}{}^{*} \equiv \theta_{k+1/2} + \Delta t\left[\begin{array}{l} \dfrac{Q}{\Pi} - \mathbf{v}\cdot\nabla\theta \\ \quad -\left(\dot{\eta}_{T,\sigma}\dfrac{\partial\theta}{\partial\eta}\right)_{\substack{UPSTREAM\\WEIGHTED}} - \left(\dot{\eta}_{T,Q}\dfrac{\partial\theta}{\partial\eta}\right)_{CENTERED} \\ \quad -\left(\dot{\eta}_{T,\theta}\dfrac{\partial\theta}{\partial\eta}\right)_{CENTERED} - \left(\dot{\eta}_{T,R}\dfrac{\partial\theta}{\partial\eta}\right)_{CENTERED} \end{array}\right]_{k+1/2}, \tag{4.34}$$

and

$$\sigma_{k+1/2}{}^{*} \equiv \sigma_{k+1/2} + \frac{\Delta t}{gH}\left[\begin{array}{l} wg - \mathbf{v}\cdot\nabla\phi \\ \quad -\left(\dot{\eta}_{T,\sigma}\dfrac{\partial\phi}{\partial\eta}\right)_{CENTERED} - \left(\dot{\eta}_{T,Q}\dfrac{\partial\phi}{\partial\eta}\right)_{\substack{UPSTREAM\\WEIGHTED}} \\ \quad -\left(\dot{\eta}_{T,\theta}\dfrac{\partial\phi}{\partial\eta}\right)_{\substack{UPSTREAM\\WEIGHTED}} - \left(\dot{\eta}_{T,R}\dfrac{\partial\phi}{\partial\eta}\right)_{CENTERED} \end{array}\right]_{k+1/2}, \quad (4.35)$$

where the superscript * denotes perturbed values. From these values, we calculate

$$F_{k+1/2}{}^{*} \equiv F(\theta_{k+1/2}{}^{*}, \sigma_{k+1/2}{}^{*}). \quad (4.36)$$

We then define

$$\left(\Delta\eta\right)_{k+1/2} \equiv F_{k+1/2}{}^{*} - F^{n}{}_{k+1/2}. \quad (4.37)$$

Finally, we determine $\dot{\eta}'_{k+1/2}$ through iterations of

$$\left[\left(\frac{\partial F^{*}}{\partial\theta^{*}}\right)_{\sigma}\right]_{k+1/2}\left(\frac{\partial\theta_{k+1/2}}{\partial t}\right)_{VERT'} + \left[\left(\frac{\partial F^{*}}{\partial\sigma^{*}}\right)_{\theta}\right]_{k+1/2}\left(\frac{\partial\sigma_{k+1/2}}{\partial t}\right)_{VERT'} = -\frac{\left(\Delta\eta\right)_{k+1/2}}{\Delta t}, \quad (4.38)$$

until $\Delta\eta$, recalculated at each iteration, becomes sufficiently small. Note that

$$\left(\frac{\partial\theta_{k+1/2}}{\partial t}\right)_{VERT'} \equiv -\dot{\eta}'_{k+1/2}\frac{\left(\delta\theta\right)_{k+1/2}}{\left(\delta\eta\right)_{k+1/2}}, \quad (4.39)$$

and

$$\left(\frac{\partial\sigma_{k+1/2}}{\partial t}\right)_{VERT'} \equiv -\dot{\eta}'_{k+1/2}\frac{1}{gH}\frac{\left(\delta\phi\right)_{k+1/2}}{\left(\delta\eta\right)_{k+1/2}}. \quad (4.40)$$

The final value of $\dot{\eta}'_{k+1/2}$ is the cumulative value calculated in the iterations.

4.3.4 *Final forms of the vertical advection of θ and ϕ and the vertical velocity*

In view of the previous subsections, the form of the vertical advection of θ and ϕ are, respectively,

$$\left(\dot{\eta}\frac{\partial\theta}{\partial\eta}\right)_{k+1/2} = \left[\begin{array}{l} \left(\dot{\eta}_{T,\sigma}\frac{\partial\theta}{\partial\eta}\right)_{\substack{UPSTREAM\\WEIGHTED}} + \left(\dot{\eta}_{T,Q}\frac{\partial\theta}{\partial\eta}\right)_{CENTERED} \\ +\left(\dot{\eta}_{T,\theta}\frac{\partial\theta}{\partial\eta}\right)_{CENTERED} + \left(\dot{\eta}_{T,R}\frac{\partial\theta}{\partial\eta}\right)_{CENTERED} \\ +\left(\dot{\eta}_{S}\frac{\partial\theta}{\partial\eta}\right)_{\substack{UPSTREAM\\WEIGHTED}} + \dot{\eta}'\frac{(\delta\theta)}{(\delta\eta)} \end{array}\right]_{k+1/2}, \tag{4.41}$$

and

$$\left(\dot{\eta}\frac{\partial\phi}{\partial\eta}\right)_{k+1/2} = \left[\begin{array}{l} \left(\dot{\eta}_{T,\sigma}\frac{\partial\phi}{\partial\eta}\right)_{CENTERED} + \left(\dot{\eta}_{T,Q}\frac{\partial\phi}{\partial\eta}\right)_{\substack{UPSTREAM\\WEIGHTED}} \\ +\left(\dot{\eta}_{T,\theta}\frac{\partial\phi}{\partial\eta}\right)_{\substack{UPSTREAM\\WEIGHTED}} + \left(\dot{\eta}_{T,R}\frac{\partial\phi}{\partial\eta}\right)_{CENTERED} \\ +\left(\dot{\eta}_{S}\frac{\partial\phi}{\partial\eta}\right)_{CENTERED} + \dot{\eta}'\frac{(\delta\phi)}{(\delta\eta)} \end{array}\right]_{k+1/2} \tag{4.42}$$

The total vertical velocity is given by

$$\dot{\eta}_{k+1/2} = \left(\dot{\eta}_T\right)_{k+1/2} + \left(\dot{\eta}_S\right)_{k+1/2} + \dot{\eta}'_{k+1/2}, \tag{4.43}$$

where $\left(\dot{\eta}_T\right)_{k+1/2}$ is defined in (4.21). It is used for vertically advecting the remaining prognostic variables, i.e., mass, momentum, and tracers. Details of the advection schemes for these variables are given in Appendix A.

4.4 Summary

In this chapter, we developed a method for diagnosing the vertical velocity in the hybrid vertical coordinate of the model. In the vertically discrete system of equations, the diagnostic procedure is complicated by the fact that different vertical advection schemes are used for θ and ϕ, depending on the coordinate regime in which a given layer is located. These schemes are designed to transition from centered-in-space to upstream-weighted from one regime to the other. The method we chose to achieve this was to partition the vertical velocity into separate components, each one allocated to the appropriate advection scheme. The sum of these components is then used as a unit in the vertical transport of the remaining prognostic variables in the model, i.e., mass, momentum, and tracers.

Chapter 5 RESULTS

5.1 Introduction

Model tests with various two-dimensional mountain wave simulations are presented in this chapter. We compare the results of the model run with the Eulerian σ-coordinate versus the hybrid vertical coordinate. The first three tests are idealized isothermal cases, and the fourth test is a simulation of the 11 January 1972 Boulder, Colorado windstorm. Two of the idealized tests are linear cases whose results can be compared to analytical solutions. The Boulder windstorm results are compared with those of previous modeling studies. We will compare the two coordinate systems in regard to processes such as vertical momentum and passive tracer transport, as well as wave breaking, and point out the strengths and weaknesses of each system.

5.2 Mountain waves in an isothermal atmosphere

These experiments involve uniform flow over an isolated mountain. For isothermal atmospheres, in which the Brunt-Väisälä frequency $N = \sqrt{(g/\theta)\partial\theta/\partial z}$ $\left(\text{or } N = g/\sqrt{c_p T}\right)$ is constant, analytic solutions are readily obtained. Linear wave theory applies when the mountain is small, that is, when $Nh/\bar{u} \ll 1$, where h is the

mountain height and $\bar{u}$ is the zonal wind speed. The overbar represents the horizontal-domain average. Note that $Nh/\bar{u}$ is the inverse Froude number. Linear mountain wave analyses include Alaka (1960), Smith (1979), Holton (2004). Analytic studies of finite-amplitude (non-linear) waves associated with taller mountains include Long (1953) and Laprise and Peltier (1989a,b,c).

From linear wave theory (Eliassen and Kleinschmidt 1957; Eckart 1960), the steady-state solution for compressible, isothermal, uniform flows can be as written as

$$\left(1-\frac{\bar{u}^2}{{c_S}^2}\right)\frac{\partial^2 w''}{\partial x^2}+\frac{\partial^2 w''}{\partial z^2}+l^2 w''=0\,, \tag{5.1}$$

(see Appendix C for a derivation of this equation) where $w''\equiv w'\sqrt{\bar{\rho}}$ is the perturbation vertical velocity scaled by the square root of the basic-state density, ${c_S}^2=\gamma R\bar{T}$ is the square of the speed of sound, and l is the Scorer parameter, an inverse length given by

$$l^2=\frac{N^2}{\bar{u}^2}-\frac{1}{4}\frac{g^2}{R^2\bar{T}^2}\,. \tag{5.2}$$

The solutions to (5.1) are waves of the form

$$w''(x,z)=\hat{w}e^{i(kx+mz)} \tag{5.3}$$

where $\hat{w}$ is the complex amplitude, and k and m are the horizontal and vertical wave numbers, respectively, which are related by the dispersion relation (see Appendix C)

$$m^2=l^2-k^2\left(1-\frac{\bar{u}^2}{{c_S}^2}\right). \tag{5.4}$$

For low Mach number, $m^2\cong l^2-k^2$. Equations (5.3) and (5.4) show that vertically propagating internal waves are supported when $m^2>0$, which is the case for

$$k^2 < \frac{l^2}{1 - \frac{\bar{u}^2}{c_S^{\,2}}}. \tag{5.5}$$

Otherwise, the waves decay in the vertical. Therefore, the Scorer parameter, which is a property of the flow only, is an intrinsic spatial scale which approximates the upper limit of the horizontal wave number in which vertically propagating waves are supported. It is also the vertical wave number of hydrostatic mountain waves (Alaka 1960; Smith 1979). As k is determined by the surface topography, this means that vertically propagating waves are more likely to occur over broad mountain ranges where the dominant Fourier components are associated with large wave numbers.

Since equation (5.1) has constant coefficients, it is evident that the amplitude of the w'' wave field is constant for vertically propagating waves. This means that the amplitude of the actual perturbation vertical velocity field (w') varies as the inverse square root of the basic state density, which is an exponentially increasing function of height. This is a consequence of wave-energy conservation. The phase lines of these waves tilt upwind, as required by the radiative lower boundary condition. This ensures that the group velocity is upward, away from the surface topography, i.e., the energy source.

In our idealized experiments, the model is initialized with constant temperature $\bar{T} = 287$ K, and constant zonal wind speed $\bar{u}=20\ m/s$. The reference pressure (i.e., at $z=0$) is 1000 hPa. The buoyancy frequency is $N=0.0183$ s^{-1}, and the characteristic wave length of the flow, as given by the Scorer parameter, is

$\lambda_G \equiv 2\pi/l \approx 6890$ m. The mountain profile is prescribed as a "witch of Agnesi" curve, given by

$$z_S(x) = \frac{ha^2}{x^2 + a^2}, \tag{5.6}$$

where $z_S(x)$ is the surface height and a is the half-width. This profile has been used in numerous studies (e.g., Queney 1948, Alaka 1960, Smith 1979), and lends itself to Fourier analysis. The nature of the wave behavior which develops is strongly determined by the values of mountain height and half-width.

The horizontal boundary conditions are periodic, and the domain size is sufficiently large to minimize upstream contamination of the flow field near the mountain for the time period under study. The model top is a rigid lid at z_T=30 km. In the small-amplitude wave simulations, a Rayleigh damping layer is used in the upper layers to avoid wave-reflection off the upper boundary. The damping terms, which are added to the right-hand sides of the zonal and vertical velocity tendency equations, are given by

$$\left.\begin{aligned} D_u(z) &= \nu(z)\left(u - \bar{u}\right) \\ D_w(z) &= \nu(z) w \end{aligned}\right\}. \tag{5.7}$$

Following Klemp and Lilly (1978), the inverse decay time ν varies smoothly with height according to the relation

$$\nu(z) = \begin{cases} 0, & \text{for} \quad z \le z_D \\ \nu_0 \sin^2\left[\dfrac{\pi}{2}\left(1 - \dfrac{z_T - z}{z_T - z_D}\right)\right], & \text{for} \quad z_D < z \le z_T, \end{cases} \tag{5.8}$$

where ν_0 is a constant with the value 0.025 s^{-1}, and z_D is the height of the lower edge of the absorbing layer. The layer thickness $z_T - z_D$ is chosen to be 7 km, which is on the order of the characteristic wavelength.

For the hybrid-coordinate runs, we use the following parameters for the vertical coordinate: $\theta_{\min}=270\,\mathrm{K}$, $(\partial\theta/\partial\sigma)_{\min}=0\,\mathrm{K}$, and $r=64$. As shown in Figure 5.1, this provides a rapid transition with height from the terrain-following coordinate to the θ-coordinate. At $z\approx 3$ km and above, the coordinate is basically isentropic.

Finally, the horizontal grid spacing for each experiment is based on the half-width of the mountain, and is chosen as $\Delta x=0.1a$. There are 600 grid points in the horizontal,

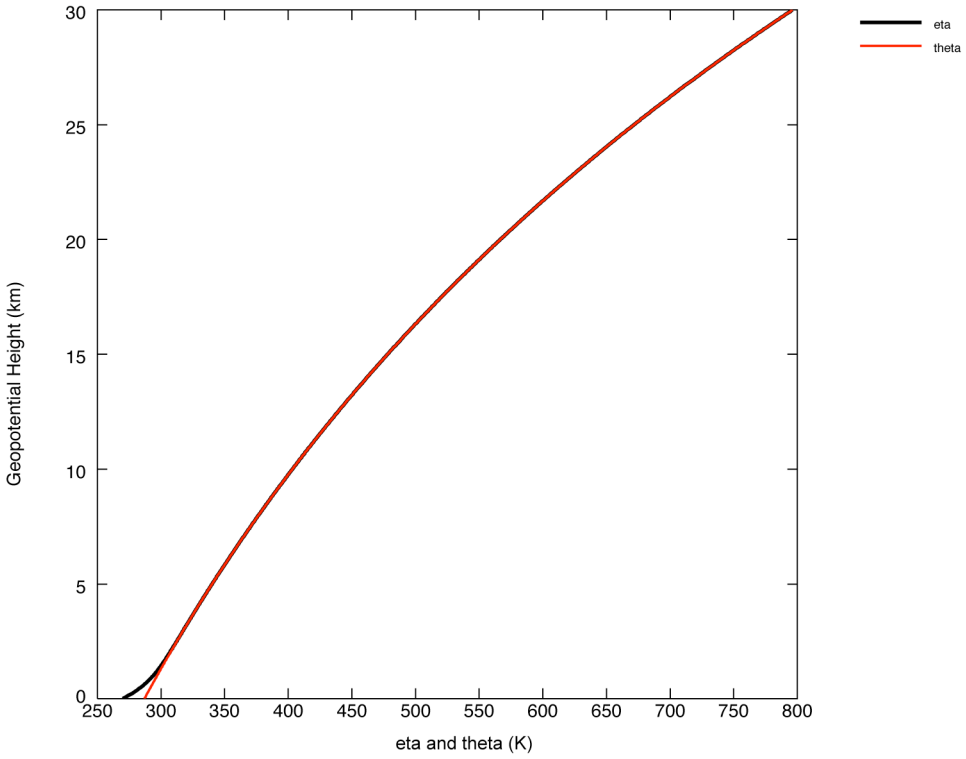


Figure 5.1: Vertical profiles of the hybrid vertical coordinate (black curve) and the basic-state potential temperature (red curve) for the isothermal mountain wave experiments. Coordinate is isentropic above ~3 km.

which provides a horizontal domain length of $60a$. We use 120 levels which, with the model top height of 30 km, gives an average layer thickness of 250 m. The free-slip boundary condition is applied at the surface.

5.2.1 Linear hydrostatic waves

Choosing the mountain height to be $h=10$ m gives $Nh/\bar{u}=0.00915\ll 1$, so the developing wave is approximately linear, and we can compare the numerical results to the analytic linear solution. For broad mountains, in which $Na/\bar{u}\gg 1$, the vertical acceleration is small, and the flow is approximately hydrostatic. Setting the mountain half-width to $a=20$ km gives $Na/\bar{u}=18.3\gg 1$, which meets this criterion. Our horizontal grid spacing is, therefore, $\Delta x=2$ km, and the domain length is $L=800$ km. We will compare our model results to nonhydrostatic analytic theory which is discussed in Appendix C. To obtain the analytical results, we included the first 90 Fourier modes in the representation of the surface topography, which provides the lower boundary condition for the vertical velocity. As expected, these agree well with the hydrostatic analytic results (e.g., Queney 1948) presented in Durran and Klemp (1983) and He (2002). A distinct feature of hydrostatic mountain waves is the vertical arrangement of wave packets directly above the mountain top. This is due to the group velocity of hydrostatic mountain waves having only a vertical component.

In order to compare with the steady-state analytic solution, the model is run until an approximate steady-state is reached, which takes about 40 of the characteristic time units given by $a/\bar{u}$. Figures 5.2 and 5.3 show the perturbation zonal and vertical velocities, respectively, for the analytic solution, and the σ-coordinate and hybrid-

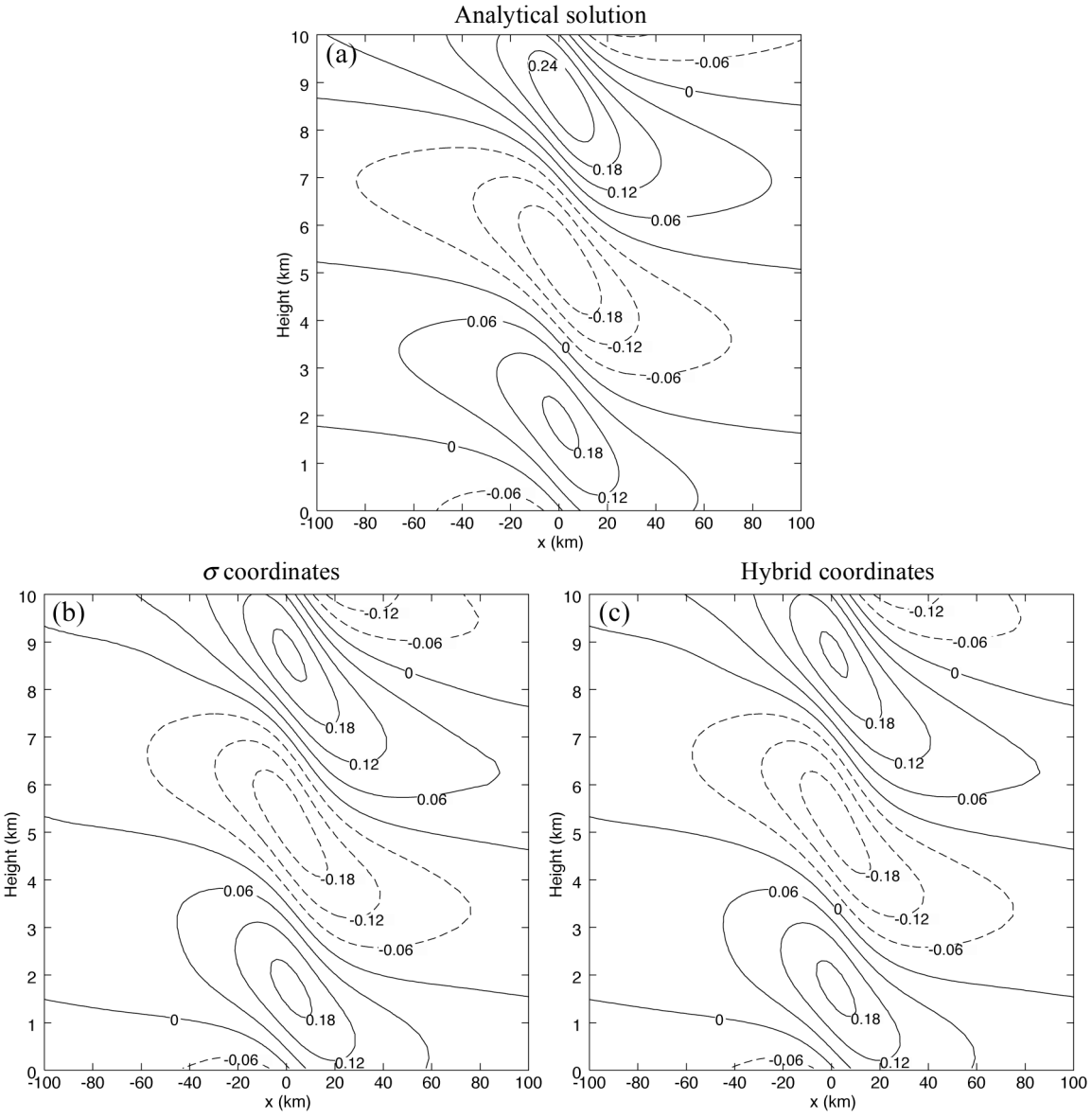


Figure 5.2: Perturbation zonal wind ($\mathrm{m\,s^{-1}}$) in the vicinity of the 10 m high, 20 km half-wide mountain from (a) the steady-state analytical solution, and from model simulations at $t = 40a/\bar{u}$ (11.1 hours) with (b) the σ vertical coordinate and (c) the hybrid vertical coordinate. The horizontal axis represents distance relative to the mountain center.

coordinate model runs. The portion of the domain in the vicinity of the mountain is shown. The model solutions agree well with each other as well as with analytical theory.

While the first moments of the velocities are reasonably accurate, a more stringent test of the model is to compare second moments of the velocity with theory. We

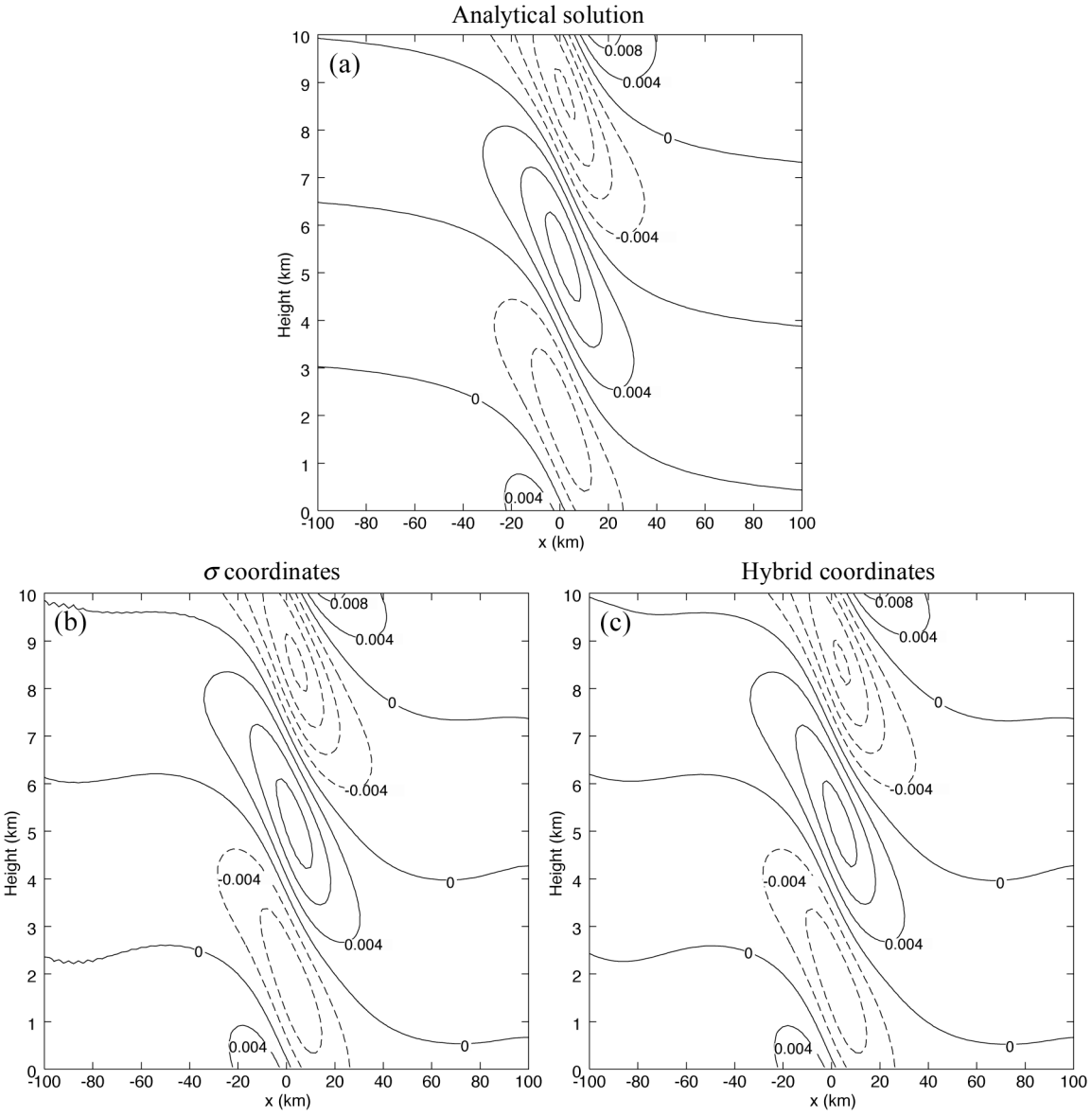


Figure 5.3: Same as in Figure 5.2, except fields plotted are perturbation vertical velocity ($m\,s^{-1}$).

therefore examine the vertical transport of horizontal momentum by the mountain wave. This has significance in terms of the effect of surface topography on the mean flow at upper levels via gravity wave drag. Following Eliassen and Palm (1960), the momentum flux is written as

$$M(z) = \int_{-L/2}^{L/2} \bar{\rho} u' w' dx = L \bar{\rho} \overline{u'w'} . \tag{5.9}$$

Figure 5.4 shows the vertical distribution of the model's diagnosed momentum flux, given by (5.9), for each coordinate system at various nondimensional times $\bar{u}t/a$. The model profiles are compared to analytical results, both nonhydrostatic, and that calculated from hydrostatic theory (Smith 1979), given by

$$M_H = -\frac{\pi}{4} \rho_0 N \bar{u} h^2 , \tag{5.10}$$

where ρ_0 is the density at the surface. These two analytical profiles are in close agreement which verifies that the flow is nearly hydrostatic. Also, the model results

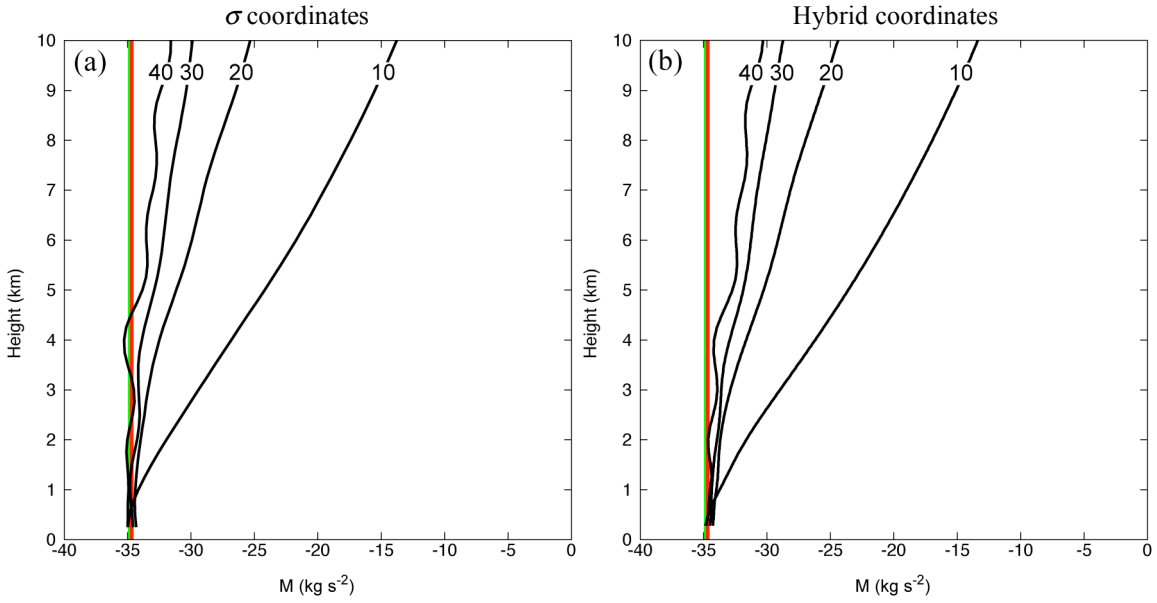


Figure 5.4: Profiles of vertical flux of horizontal momentum in $\mathrm{kg\,s^{-2}}$ at various non-dimensional times (black curves) for the linear, hydrostatic mountain wave experiment: (a) σ vertical coordinate, and (b) hybrid vertical coordinate. The analytical value for the nonhydrostatic system of equations is shown by the red lines, and that for the hydrostatic system of equations (M_H) is shown by the green lines. Labels indicate nondimensional time units of $a/\bar{u}$.

agree well with the analytical values. They are nearly constant with height, as predicted by theory.

It is interesting to contrast the form of the vertical momentum fluxes of the two coordinate systems by diagnosing the actual, non-linear fluxes of the model. As discussed in Section 2.6, with the Eulerian z coordinate, the transport is due to the eddy flux $\overline{(\rho w)'u'}$, while in the quasi-Lagrangian θ coordinate, it is expressed as the form drag on quasi-material layers, given by $-\overline{p'\partial z'/dx}$. Recall that in the generalized vertical coordinate, the vertical divergence of the 2D Eliassen-Palm flux, which determines the tendency of the zonally averaged zonal flow, is

$$\nabla^{(\eta)} \cdot \mathbf{F}^{(\eta)} = \frac{\partial}{\partial \eta}\left[\overline{p' \frac{\partial z'}{\partial x}} - \overline{(m\dot{\eta})'u'} \right]. \tag{5.11}$$

Define the "eddy-flux" component of the momentum flux as

$$M_{EF}(z) \equiv \int_{-L/2}^{L/2} (m\dot{\eta})'u'\, dx = L\overline{(m\dot{\eta})'u'}, \tag{5.12}$$

the "form drag" component of the momentum "flux" as

$$M_{FD}(z) \equiv -\int_{-L/2}^{L/2} p' \frac{\partial z'}{\partial x} dx = -L\,\overline{p' \frac{\partial z'}{\partial x}}, \tag{5.13}$$

and the surface drag as

$$M_{SD} \equiv M_{FD}(z = 0). \tag{5.14}$$

For steady-state flow, the following relation should apply at all levels

$$M_{EF}(z) + M_{FD}(z) = M_{SD} = \text{constant}. \tag{5.15}$$

Figure 5.5 shows the vertical profiles of the eddy and form-drag contributions to the momentum flux at time $t = 40\, a/\bar{u}$. The sum of these, shown by the black curve,

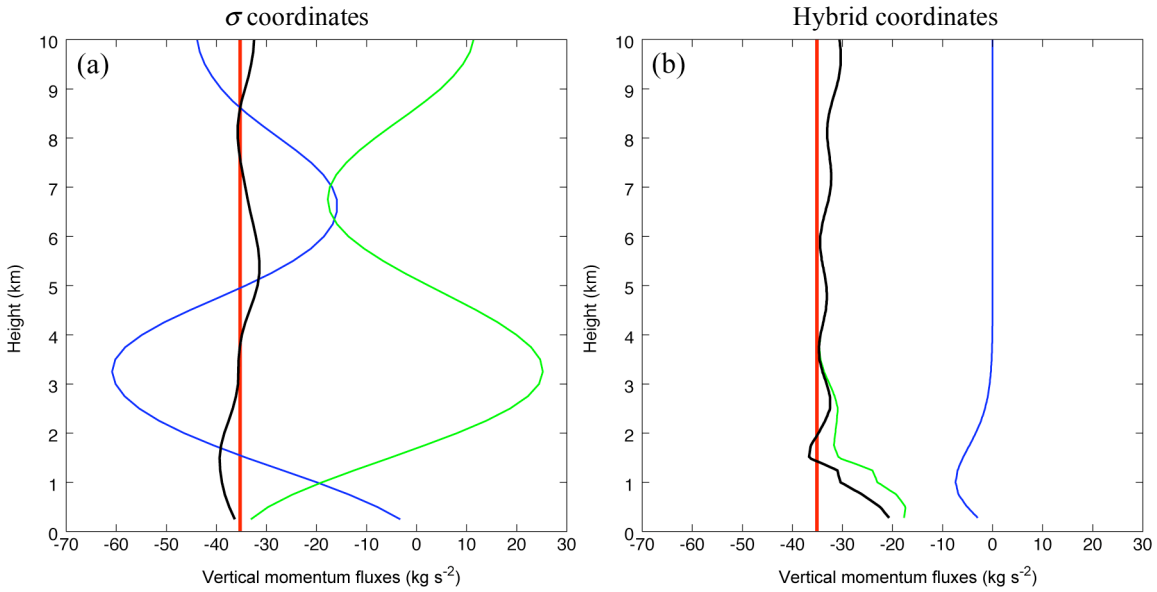


Figure 5.5: Actual vertical fluxes of horizontal momentum diagnosed from (a) σ vertical coordinate, and (b) hybrid vertical coordinate runs for the linear, hydrostatic mountain wave experiment at $t=40\,a/\bar{u}$ (11.1 hours). The blue curves are eddy momentum fluxes M_{EF}, the green curves are the form drag M_{FD}, the black curves are the sum of these, and the red lines are the diagnosed surface drag which is the theoretical, steady-state, constant momentum flux M_{SD}.

theoretically equals the surface drag (plotted as the red line for reference). For each coordinate system, the total momentum flux is nearly constant with height and is close to the theoretical surface-drag value. However, with the hybrid coordinate (Figure 5.5b), there is a large deviation of the total momentum flux from the theoretical value in the lowest 1.5 km. The cause for this is not known at this time. The sign of the total momentum flux is negative, which means that the surface imparts a drag force on the atmosphere, as expected. Note the non-zero contribution of the form-drag in σ coordinates, which is due to the sloping of the coordinate surfaces with respect to z. In the hybrid-coordinate, the flux is due entirely to the form-drag component above ~3 km.

This is because the coordinate is almost purely isentropic, so the vertical velocity is zero and, therefore, the eddy flux is zero as well.

With the σ coordinate, the form drag on coordinate surfaces and the eddy flux vertically oscillate – the form drag about its mean of zero and the eddy flux about its mean equal to the value of the total momentum flux. These oscillations are approximately 180° out of phase so that their sum is nearly constant with height. The variation of the form drag is explained by the horizontal phase shift, with height, of the pressure perturbations along coordinate surfaces. At the lower boundary, the amplitude of the form drag equals the surface drag. The amplitude decreases with height because both the pressure perturbations and the horizontal gradient of the coordinate surface height decrease. Since the sum of the form drag and the eddy momentum flux should be constant with height per equation (5.15), in order to maintain the flow in a steady state, the "purpose" of the eddy momentum flux oscillations is to cancel the oscillations of the form drag. Since the mean value of the eddy flux is the total momentum flux, it is the primary contributor to vertical momentum transport, which is expected for an Eulerian coordinate. The form drag results from the sloping coordinate surfaces, and its mean effect in the vertical is zero. With the hybrid coordinate, however, the roles are reversed, and the form drag plays the primary role in the momentum balance. The eddy flux has a small contribution near the surface where there is some σ-contribution to the vertical coordinate, but this becomes zero where the coordinate is quasi-Lagrangian and the vertical velocity vanishes. Here the form drag on coordinate surfaces has the fundamental physical significance as the net force along material surfaces, since the coordinate surfaces are material surfaces.

5.2.2 *Linear nonhydrostatic waves*

Now consider the flow over a narrower mountain with a half-width of $a = 2\,\text{km}$, and with the same height of 10 m. The flow is still considered linear, but now we have $Na/\bar{u} = 1.83 \sim 1$, so the flow is nonhydrostatic. The main difference in the wave structure, compared to hydrostatic waves, is that the group velocity has a larger relative downwind horizontal component. Therefore wave packets are arranged in an downwind-tilted direction as shown in Figures 5.6 and 5.7. For this experiment, we use a horizontal grid spacing of $\Delta x = 200$ m, and the domain length is $L = 80$ km. As with the hydrostatic case, the model perturbation velocity fields agree quite well with the analytical values.

The vertical momentum flux profiles shown in Figures 5.8 and 5.9 have very similar characteristics to their hydrostatic counterparts. The time-dependence of the vertical momentum flux shown in Figure 5.8 (as well as Figure 5.4) represents the transient wave growth. Steady-state is reached at about the time $t = 40\,a/\bar{u}$. The main difference between the two cases is that the vertical momentum flux and surface drag have lower values in the nonhydrostatic case.

5.2.3 *Finite-amplitude nonhydrostatic waves*

Wave development over tall mountains is nonlinear and the amplitude can grow to the point that isentropic surfaces become vertical and overturn. Long (1953) calculated analytical, steady-state solutions for these finite-amplitude waves for stratified Boussinesq flow. Laprise and Peltier (1989a,b,c) analyzed the linear stability of Long's steady-state solutions, as well as the structure and energetics of wave breaking. In this

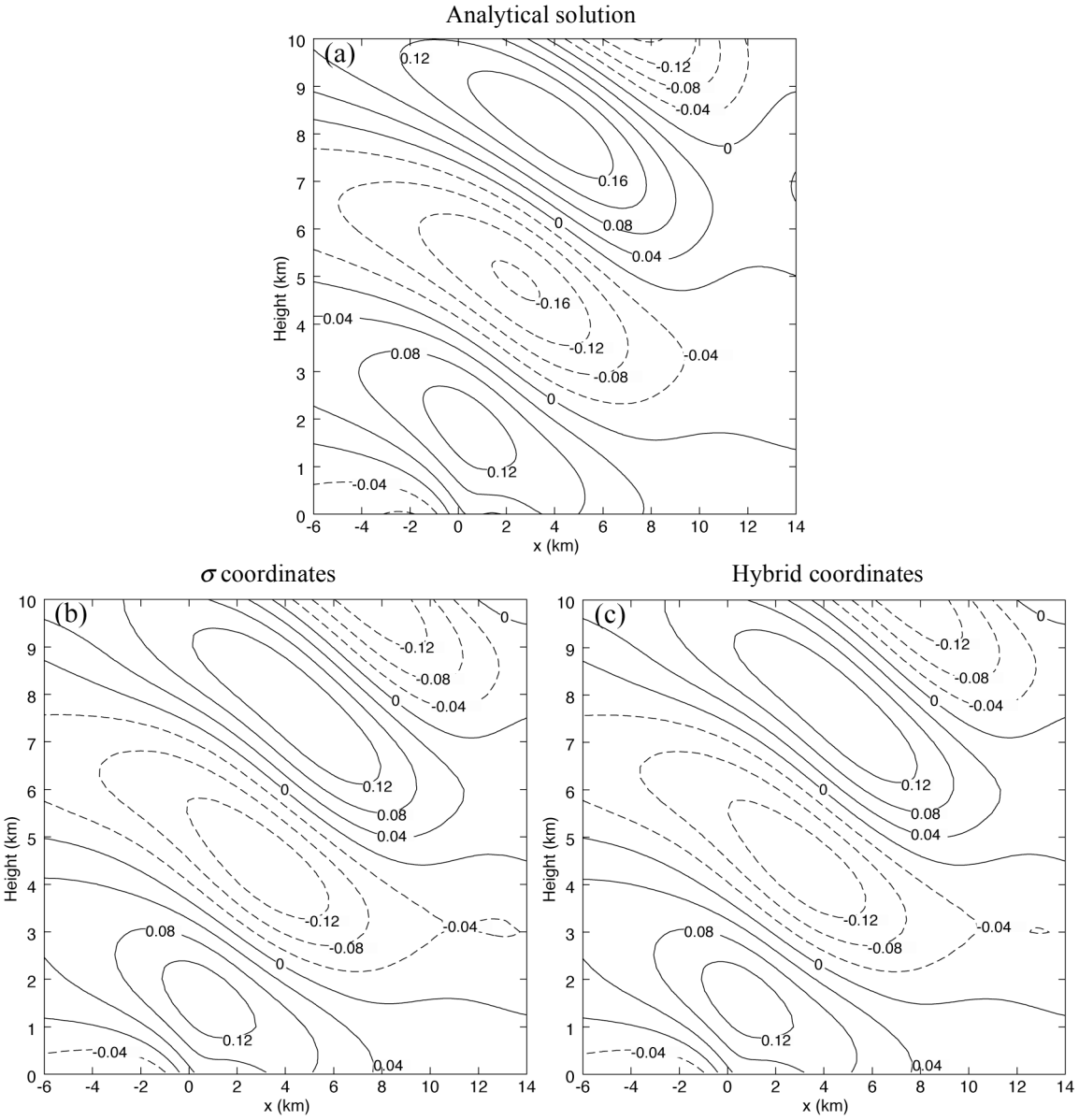


Figure 5.6: Perturbation zonal wind ($m\,s^{-1}$) in the vicinity of the 10 m high, 2 km half-wide mountain from (a) the steady-state analytical solution, and from model simulations at $t = 40a/\bar{u}$ (1.11 hours) with (b) the σ vertical coordinate and (c) the hybrid vertical coordinate. The horizontal axis represents distance relative to the mountain center.

subsection we simulate conditions in which wave breaking occurs. We will avoid a detailed comparison of our model results with the analytical solution for two reasons: 1) our model solves a different set of equations, i.e., the compressible system; and 2) our initial condition is the unperturbed basic state with the zonal flow impulsively introduced

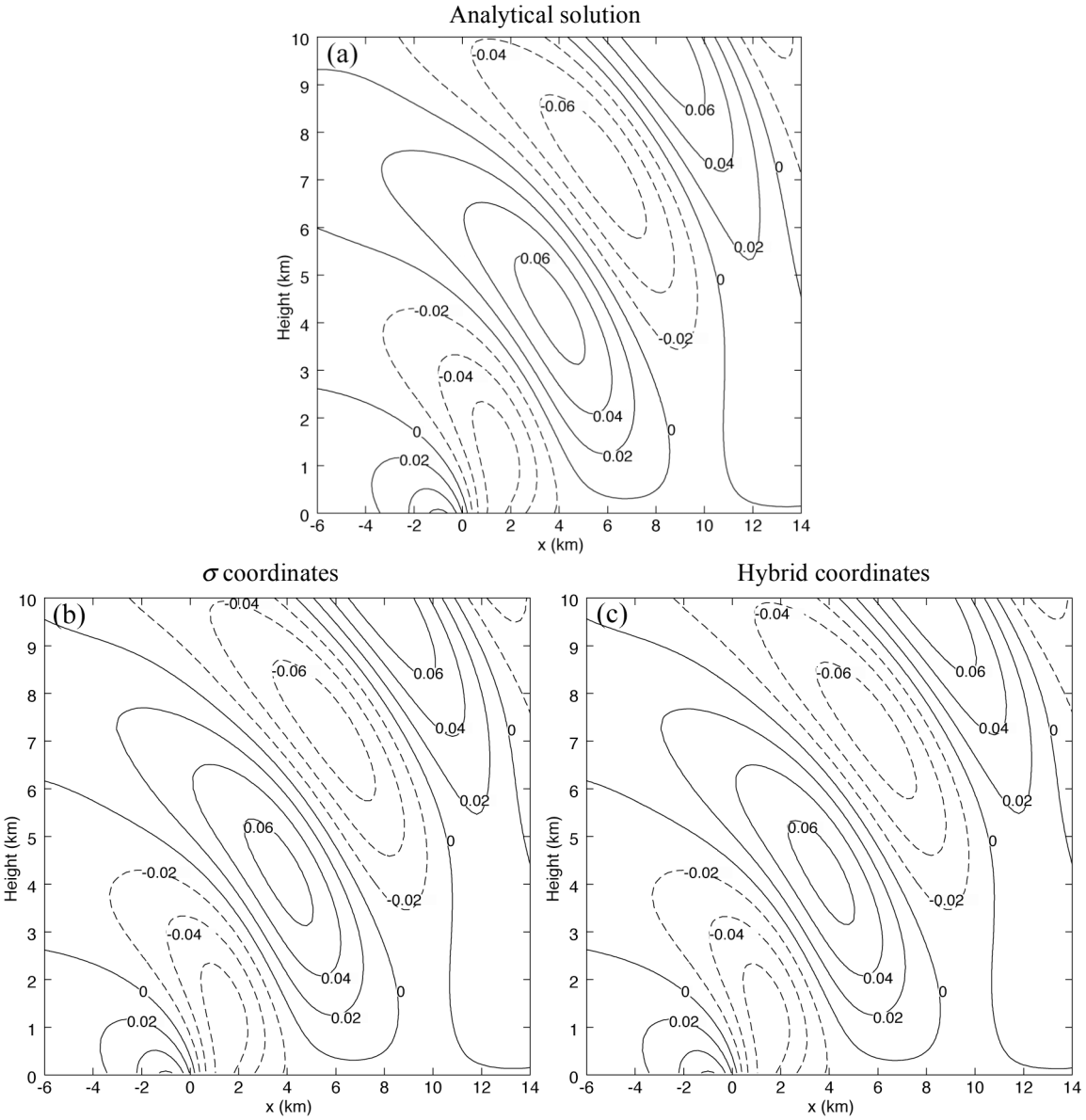


Figure 5.7: Same as in Figure 5.6, except fields plotted are perturbation vertical velocity (m/s).

(as pointed out in Laprise and Peltier (1989b), it is more suitable to initialize the model with Long's steady-state). Rather, our purpose here is to test the model's ability to simulate a breaking wave and, in particular, test how the hybrid-vertical coordinate handles isentropic overturning.

In this experiment we set the mountain height at $h = 1500\,\mathrm{m}$. This gives $N h/\bar{u} = 1.37 \sim 1$, so the mountain wave is expected to be nonlinear. As in the previous

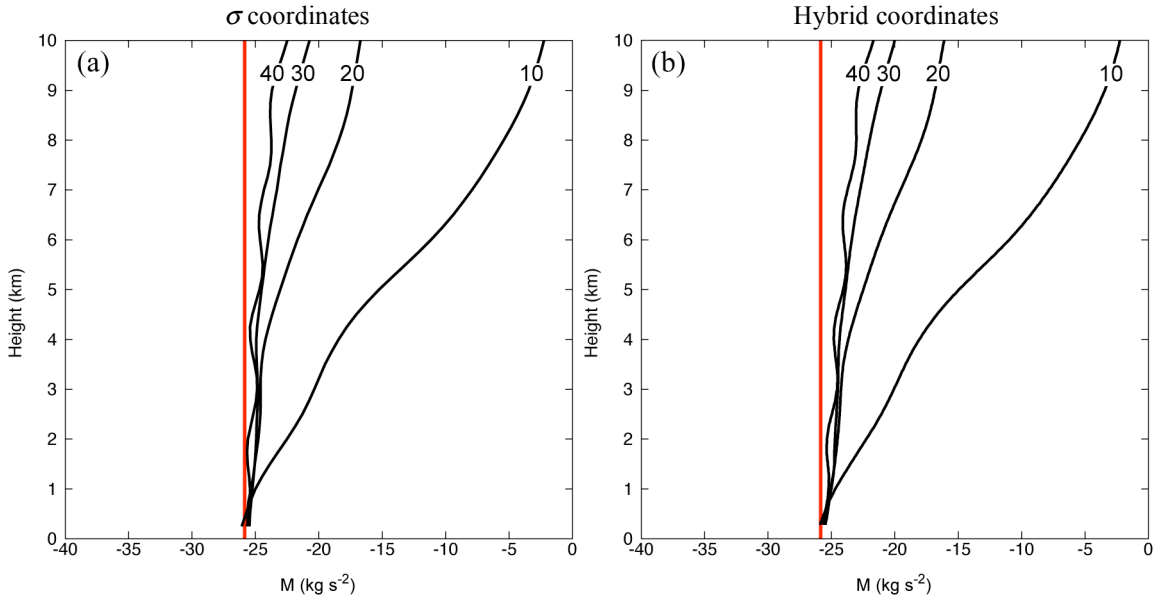


Figure 5.8: Profiles of vertical flux of horizontal momentum at various non-dimensional times (black curves) for the linear, nonhydrostatic mountain wave experiment: (a) σ vertical coordinate, and (b) hybrid vertical coordinate. The analytical values are shown by the red lines. Labels indicate nondimensional time units of $a/\bar{u}$.

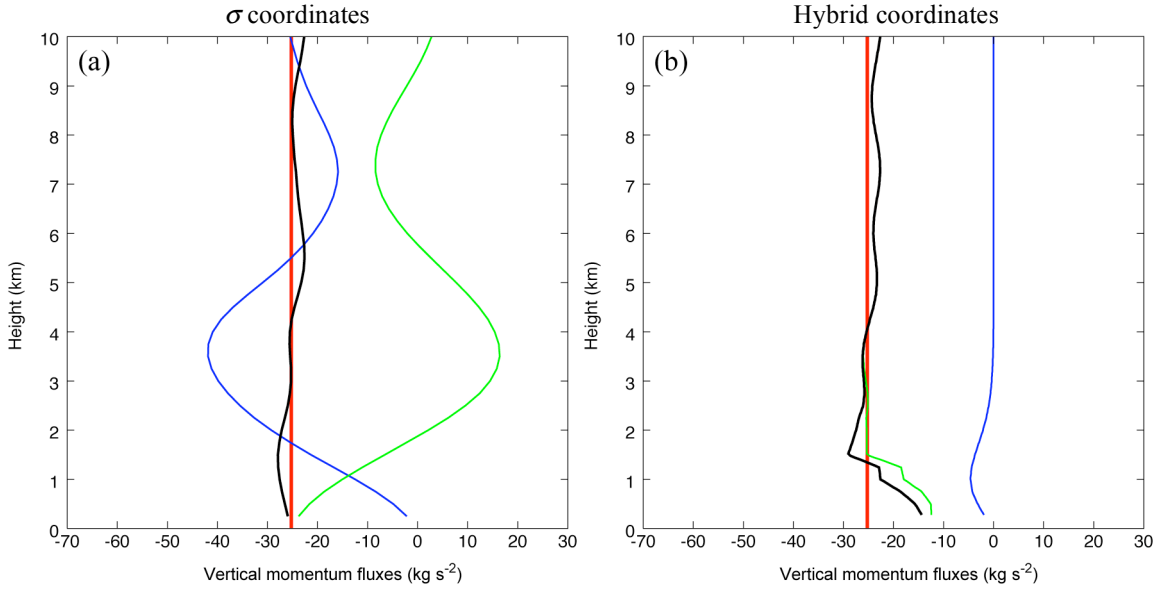


Figure 5.9: Actual vertical fluxes of horizontal momentum diagnosed from (a) σ vertical coordinate, and (b) hybrid vertical coordinate runs for the linear, nonhydrostatic mountain wave experiment at $t = 40\,a/\bar{u}$ (1.11 hours). The blue curves are eddy momentum fluxes M_{EF}, the green curves are the form drag M_{FD}, the black curves are the sum of these, and the red lines are the diagnosed surface drag which is the theoretical, steady-state, constant momentum flux M_{SD}.

experiment, we use the "narrow" mountain ($a = 2\,\text{km}$), so the flow is nonhydrostatic. We run the model in 3 configurations: (a) the σ coordinate, (b) the hybrid coordinate with no coordinate surface smoothing, and (c) the hybrid coordinate with coordinate smoothing applied.

Recall that with coordinate smoothing, the heights of model surfaces are adjusted, as necessary, to maintain both a smooth, monotonic vertical distribution of layer thickness, and a smooth horizontal profile of coordinate surface height. The parameter that quantifies the vertical smoothness is the relative difference in the thickness of adjacent layers given by $\left(\delta^2 z/\delta z\right)$ as defined in equation (2.67). For the horizontal smoothing we use the discrete analog of $\nabla^4 z$. As described earlier, there is an induced vertical mass flux associated with the smoothing process that provides an Eulerian component to the quasi-Lagrangian coordinate and allows isentropes to overturn.

In the previous linear experiments coordinate height perturbations were small, so coordinate smoothing was not needed. In this experiment, however, we expect it to be necessary, so thresholds for the absolute values of the smoothing parameters are assigned. These are $\left|\delta^2 z/\delta z\right|_{\max} = 0.4$ and $\left|\nabla^4 z\right|_{\max} = 2.1 \times 10^{-8}\,\text{m}^{-3}$. When the parameters exceed these values, coordinate smoothing occurs. The diffusion coefficients for the vertical and horizontal smoothing, shown in equations (2.79) and (2.80), are $\kappa_v = 1000\,\text{m/s}$ and $\kappa_h = 3.2 \times 10^9\,\text{m}^4/\text{s}$ respectively. For the coordinate "overturning parameter" introduced in equation (2.76) we use $\beta = 0.7$, and the relaxation time constant introduced in equation (2.64) is $\tau = 0.5\,\text{hours}$.

The transient wave growth in the vicinity of the mountain is shown in Figures 5.10 thru 5.12. These are snapshots of the positions of isentropic and model surfaces at three different times. Figure 5.10 shows that at $t = 8.5\, a/\bar{u}$ (14.17 minutes) the wave has amplified significantly. There is a region of isentropic steepening located approximately

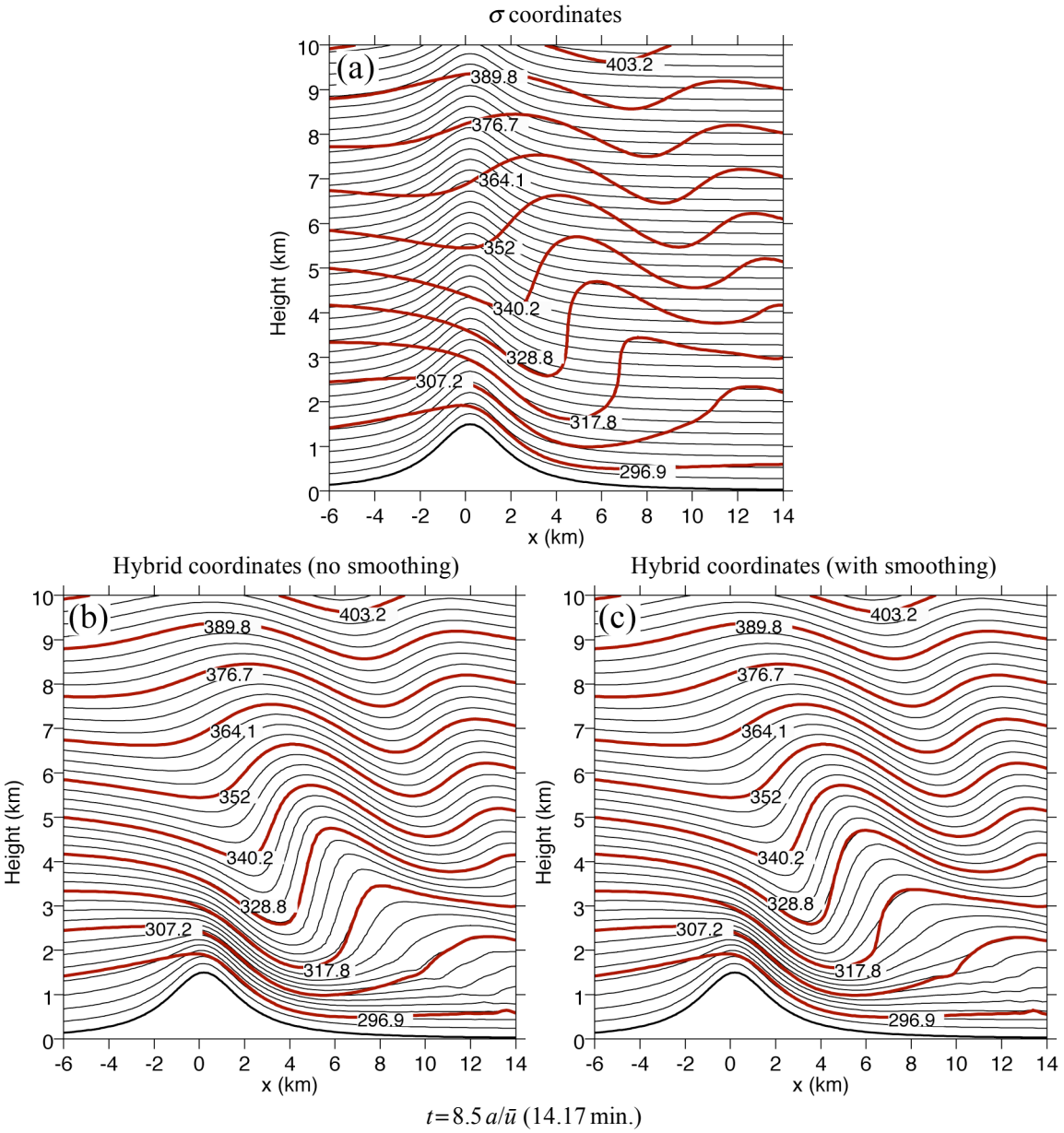


Figure 5.10: Position of model coordinate surfaces (black curves) and selected isentropic surfaces (bold red curves) at $t = 8.5\, a/\bar{u}$ (14.17 minutes): (a) σ-coordinate run, (b) hybrid-coordinate run with no smoothing, and (c) hybrid-coordinate run with coordinate smoothing.

4 km downstream of the mountain top and at a height of 4 km. This is in rough agreement with Long's steady-state solution, as described in Laprise and Peltier (1989c), where this region is theoretically positioned on the order of a mountain half-width (in our case 2 km) downstream of the mountain top and at a height of 0.75 λ_G (in our case 5.2 km).

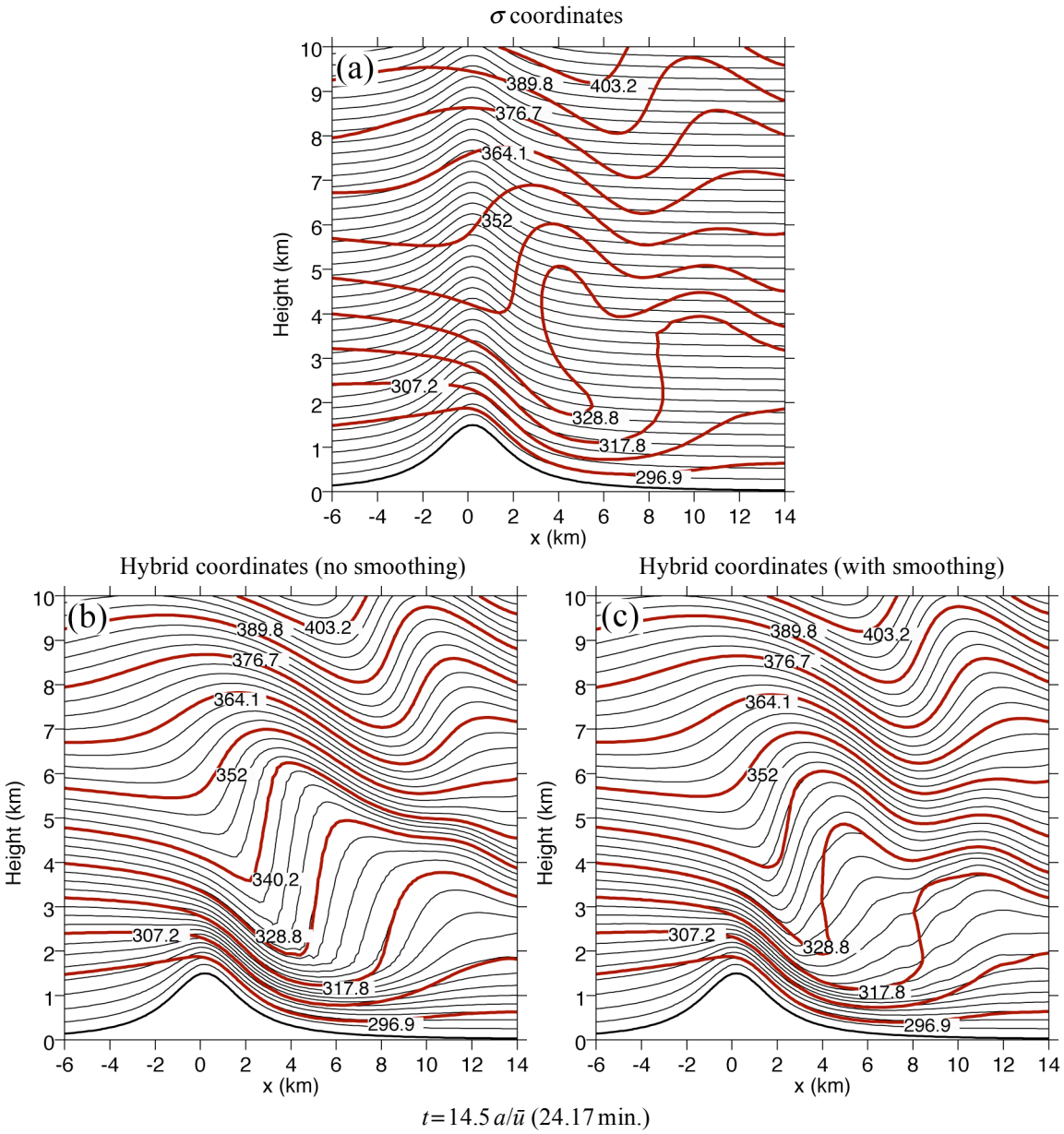


Figure 5.11: Same as Figure 10 except $t = 14.5\, a/\bar{u}$ (24.17 minutes).

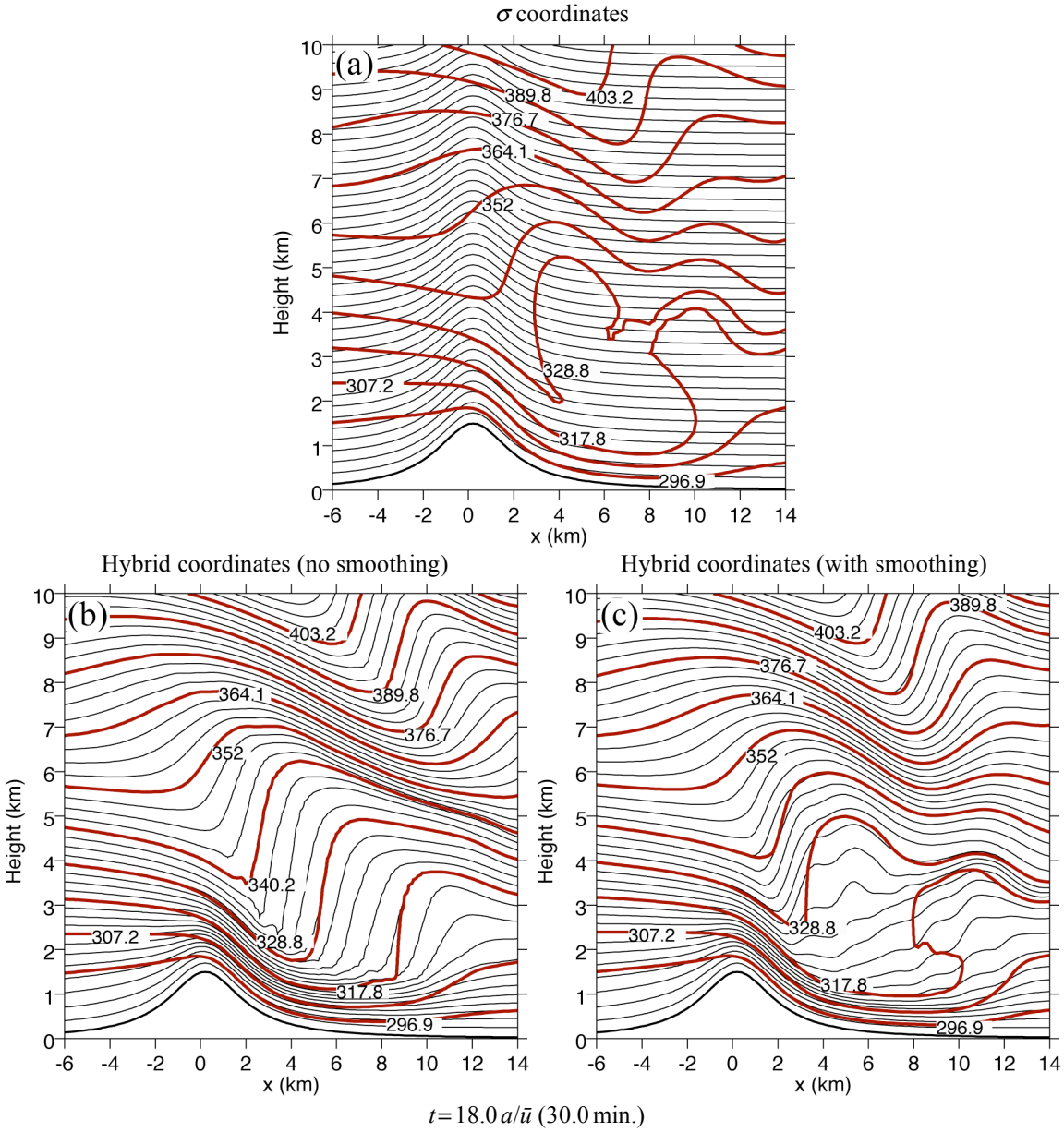


Figure 5.12: Same as Figure 10 except $t = 18.0\, a/\bar{u}$ (30.0 minutes).

The most noticeable difference among the three simulations is that with σ coordinates, the isentropes have already become vertically arranged in the steepening region, whereas with the hybrid coordinate, the steepening is not as advanced. This difference is more evident at $t = 14.5\, a/\bar{u}$ (24.17 minutes) as shown in Figure 5.11. With the σ coordinate, the isentropic overturning is pronounced. With the hybrid coordinate,

for the case without smoothing, overturning has not occurred, but with coordinate smoothing applied, isentropes are able to overturn, yet not as much as with the σ coordinate. At the later time $t = 18.0\, a/\bar{u}$ (30 minutes), shown in Figure 5.12, the wave is breaking in the σ-coordinate run, as well as with the hybrid coordinate with smoothing. With the hybrid vertical coordinate without smoothing, overturning remains suppressed.

The lack of wave overturning with the purely isentropic coordinate model is due to the fact that the sign reversal of the vertical potential temperature gradient, i.e., negative static stability, cannot be mathematically represented in θ coordinates. Another way of viewing this is in terms of mass conservation. In isentropic coordinates, for adiabatic processes, the local time tendency of the pseudo-density is equal to horizontal mass flux convergence (see equation (2.19) with $\eta = \theta$ applied). In the overturning region, the convergence is positive, so m increases (in theory, asymptotically to infinity). Given the definition of pseudo-density, $m \equiv \rho \partial z/\partial \theta$, this means that the layer thickness Δz gets big, as evident in Figure 5.12b. In order to represent the true physical occurrence of static instability, i.e., $\partial z/\partial \theta < 0$, m would have to suddenly jump from positive infinity to negative infinity, which is numerically impossible. For this reason, isentropic coordinates are not useful for representing wave breaking, and result in a nonphysical representation of wave development.

The compromise is to apply the adaptive grid technique of coordinate smoothing. Figures 5.11c and 5.12c show that isentropic overturning is represented through the separation of the coordinate and isentropic surfaces where the wave breaks. However, in regions where the wave is not overturning, the coordinate is isentropic, and the benefit of the QL coordinate is still achieved. Associated with this compromise is a degree of

distortion in the representation of wave breaking, as evidenced by the delay in isentropic overturning with the adaptive grid compared to the σ coordinate (Figure 5.10c vs. 5.10a) and the lessening of the severity of the wave breaking (Figure 5.12c vs. 5.12a). A possible explanation for this is the difference in vertical resolution between the simulations. (This explanation was also given by Skamarock (1998), He (2002) and Zangl (2007), who observed similar behavior in their models.) In the case of the smoothed hybrid vertical coordinate, layers expand in the overturning region, so this feature is less resolved. With the σ coordinate there is significantly more resolution, as seen in the plots, so we can assume that this solution is the "true" solution compared to the hybrid coordinate. The converse, however, may be true. While layers expand with this coordinate in the wave breaking region, there is enhanced resolution in the regions of high static stability (i.e., closely spaced isentropes). It is in these regions where the hybrid coordinate has an advantage over the σ coordinate. This will be demonstrated in the following section.

A downslope windstorm occurs in this idealized experiment as shown in the zonal wind fields in Figure 5.13. From an initial uniform zonal wind of 20 m/s, the surface winds on the leeward side of the mountain exceed 50 m/s at $t = 14.5\, a/\bar{u}$ (24.17 minutes). Above the location of maximum surface winds, the zonal wind component has reversed sign (or is close to zero). This is in the region of isentropic overturning where the streamlines have a westward tilt. So there has been a transfer of westerly momentum down to the surface.

Numerous studies have described the wind storm phenomenon in relationship to amplifying waves. These include Scorer and Klieforth (1959), Klemp and Lilly (1975),

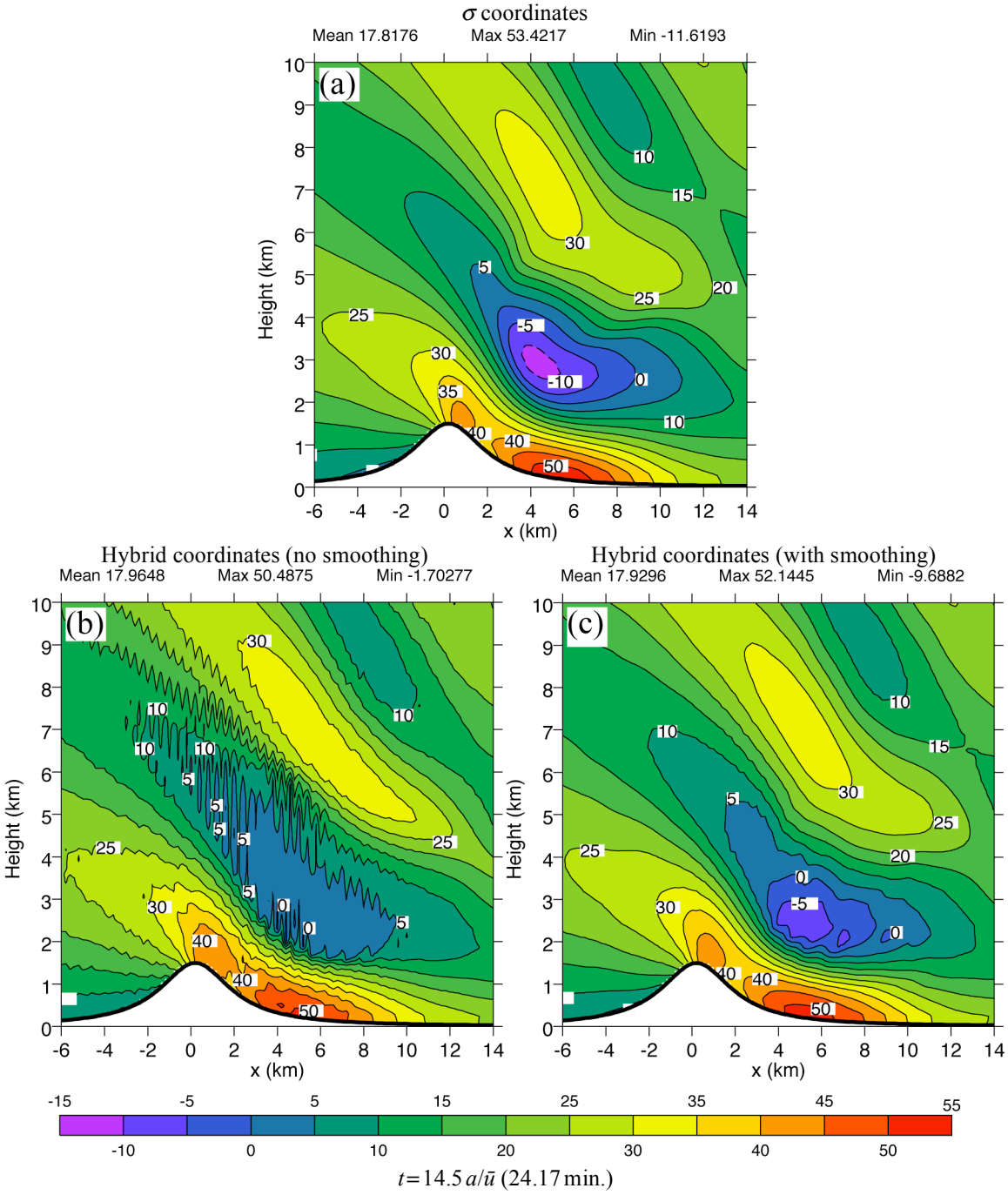


Figure 5.13: Zonal wind ($m\,s^{-1}$) at $t = 14.5\,a/\bar{u}$ (24.17 minutes): (a) σ-coordinate run, (b) hybrid-coordinate run with no smoothing, and (c) hybrid-coordinate run with coordinate smoothing.

Peltier and Clark (1979) and Laprise and Peltier (1989a). In the latter two papers, the flow reversal associated with wave overturning and breaking has been theorized as creating a resonant cavity which confines the wave energy near the surface. This

enhances the strength of the surface winds. In Figure 5.13b, there is little or no flow reversal, which is associated with the lack of wave overturning in the purely isentropic coordinate. The surface winds in this case are also the weakest of the three cases, so it is possible that this is in support of the wave energy trapping theory, however, further study would be needed to confirm this. On the other hand, the weaker surface winds may just be a manifestation of the poorly resolved wave breaking region with the isentropic coordinate. He (2002) and Zangl (2007) also noted the relationship between suppressed wave breaking and weaker surface winds with the isentropic coordinate.

We believe the noisy zonal wind field in Figure 5.13b to be a result of large truncation errors due to the sharp spatial gradients which develop in the isentropic coordinate. This was theorized earlier, and was part of the reason for implementing the coordinate smoothing technique. The disturbances seem to be worsened by a resonant response from the acoustic modes. This is suggested by the frequency of the noise, which is close to that of sound waves characteristic of their wavelength. So filtering these modes by using the anelastic system of equations or semi-implicit time differencing, for example, may lessen the noise.

The hybrid coordinate with smoothing results in stronger leeward surface winds and more enhanced flow reversal (Figure 5.13c). However, the field is somewhat noisy in the isentropic steepening region and indicates that there is still an issue with the acoustic modes. Again, filtering these could help to solve this.

The results of this experiment gives us the opportunity to compare our method of handling the isentropic coordinate with that of other nonhydrostatic models based on this coordinate. First, it should be noted that He (2002) and Zangl (2007) obtained the same

relationship between the suppression of wave overturning and its effect on the zonal wind field with the isentropic coordinate. They, along with Skamarock (1998), also attributed this to poor vertical resolution in the wave breaking regions.

Among these models, our method of vertical coordinate handling is most similar to Zangl (2007). However, our source for this experimental setup was He (2002), so we will compare our results directly with that model. Table 5.1 provides a brief comparison of the general features of each model. In terms of the vertical coordinate handling, He (2002) specified upper and lower bounds on the layer thickness. The lower bound (100 m) was designed to prevent model layers from crossing each other, and the upper bound (400 m) provided some vertical resolution in regions of static instability by eliminating the tendency for the layer thickness to become large. Figure 5.14 shows the location of isentropic and model surfaces in He's model at time $t = 14.5\, a/\bar{u}$ (24.17 minutes). This corresponds to our model results shown in Figure 5.11c. Overall, the pattern of isentropes is similar in both models. However, the wave overturning in He (2002) is more pronounced than in our model, which is probably due to finer vertical

Table 5.1: Comparison of general features of our model and that of He (2002).

	Our model	He (2002) model
Prognostic variables	$\mathbf{v}, w, \theta, z, \sigma$	$\mathbf{v}, w, \theta, z, p$
Vertical staggering	Charney-Phillips	Lorenz
Vertical coordinate	$\eta = F(\theta, \sigma)$ Based on Konor and Arakawa (1997)	Primarily θ Based on Bleck and Benjamin (1993)
Adaptive grid technique	Conditional diffusive smoothing of layer thickness distribution in the vertical and coordinate surface height in the horizontal	Max/Min layer thickness specification and $2\Delta x$ horizontal smoothing of coordinate surface height

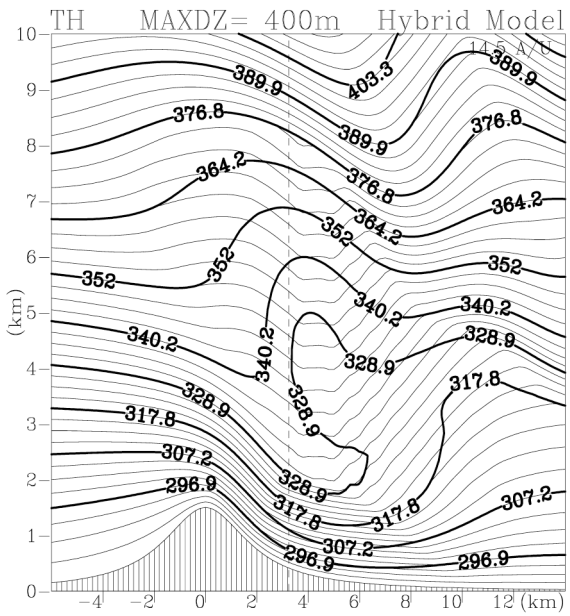


Figure 5.14: Model results from He (2002) for $t = 14.5\, a/\bar{u}$ (24.17 minutes).

resolution in the overturning region. In this region, according to Figure 5.15b, the vertical resolution in our model was about 1000 m, compared to 400 m as shown in Figure 5.14. Another key difference between the two models is the coordinate surface pattern just above the overturning region. In He's model, it appears that the maximum layer thickness criterion results in the separation between coordinate and isentropic surfaces up to about $z = 8$ km. This is just a geometric result and is the trade-off for having the enhanced resolution in the wave breaking region.

Figure 5.15 illustrates the indirect effect our method of applying limits on $\left|\delta^2 z/\delta z\right|$ and $|\nabla^4 z|$ has on the layer thickness in the hybrid coordinate model. Figure 5.15a shows the distribution of layer thickness for the case of no smoothing, and Figure 5.15b shows the same field for the smoothing case. There happens to be little effect on the minimum thickness which is approximately 70 m, but there is a large effect on the

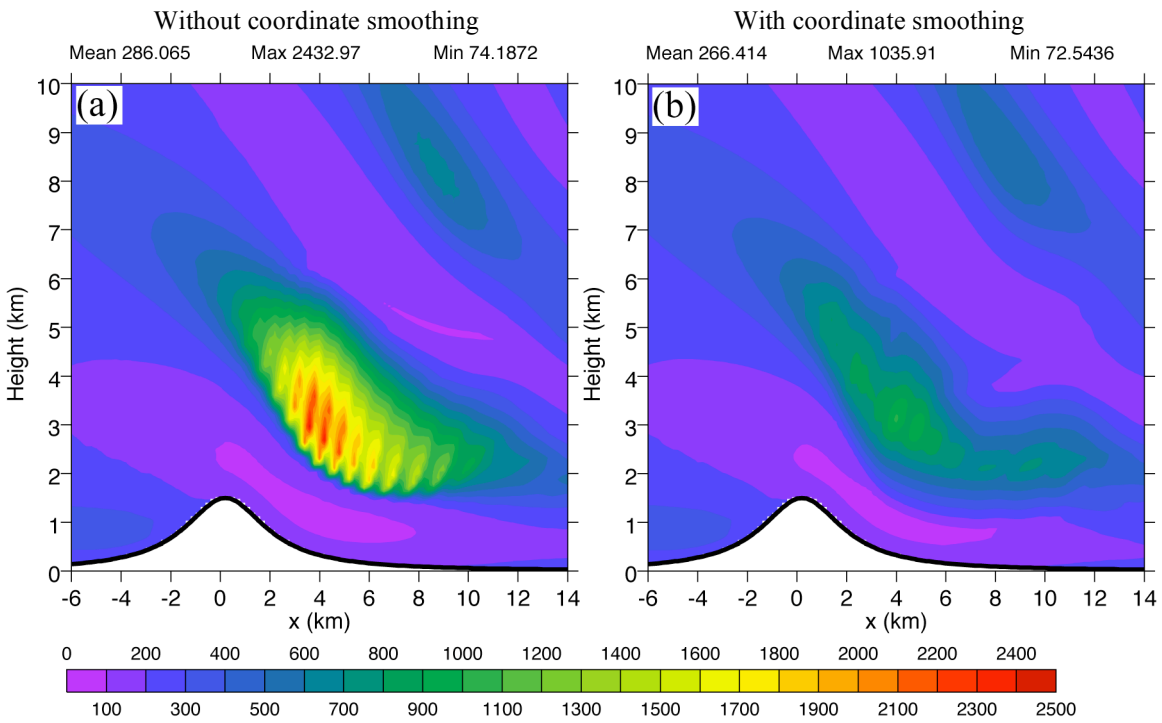


Figure 5.15: Layer thickness (m) at time $t = 14.5\, a/\bar{u}$ (24.17 minutes) for the case of (a) no coordinate smoothing (purely isentropic) and (b) with coordinate smoothing.

maximum layer thickness which is reduced from 2.4 km to 1.0 km. The reduction of the smoothness parameters $\left|\delta^2 z/\delta z\right|$ and $|\nabla^4 z|$ to their specified maximum target values is shown in Figures 5.16 and 5.17, respectively. Figure 5.16 shows the values of these parameters without coordinate smoothing, and Figure 5.17 shows them for the smoothing case.

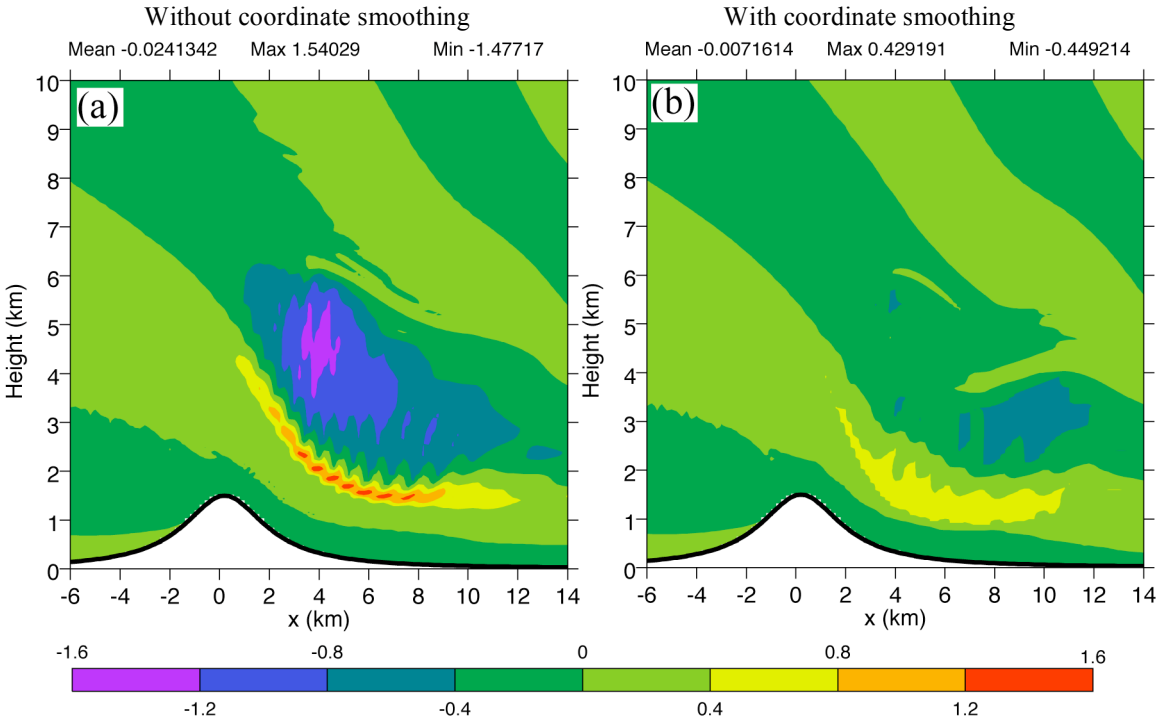


Figure 5.16: Vertical smoothness parameter $\left|\delta^2 z/\delta z\right|$ at time $t = 14.5\, a/\bar{u}$ (24.17 minutes) for the case of (a) no smoothing and (b) smoothing. Maximum specified value in the model is 0.4.

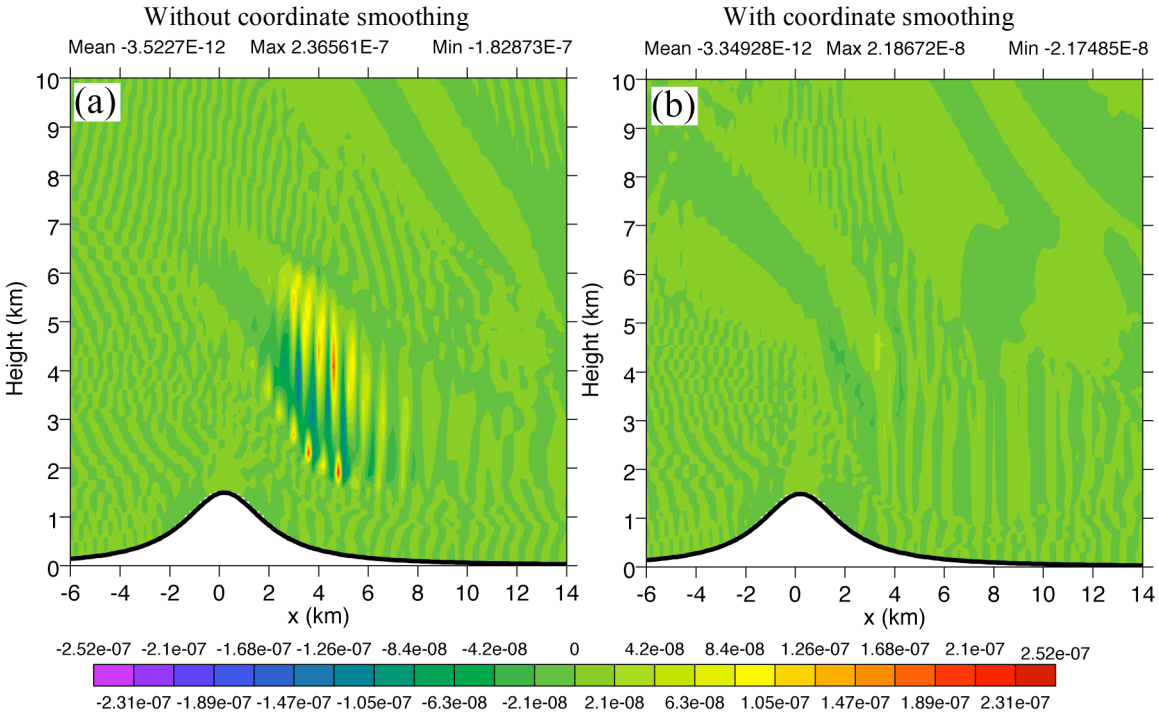


Figure 5.17: Horizontal smoothness parameter $|\nabla^4 z|$ (m^{-3}) at time $t = 14.5\, a/\bar{u}$ (24.17 minutes) for the case of (a) no smoothing and (b) smoothing. Maximum specified value in the model is $= 2.1 \times 10^{-8}\, \mathrm{m}^{-3}$.

5.3 The 11 January 1972 Boulder, Colorado Downslope Windstorm

The next step is to demonstrate the ability of the nonhydrostatic hybrid vertical coordinate model to simulate an observed event – the 11 January 1972 Boulder, Colorado downslope windstorm. Extensive observational and modeling data of this event is available which we can use to evaluate the model. We will compare the wave amplification and breaking characteristics, as well as the windstorm intensity, to those of other models.

The city of Boulder frequently experiences severe downslope windstorms due to its location on the eastern slope of the Front Range of the Rocky Mountains. The event of 11 January 1972 happened to occur during a field campaign by the National Center for Atmospheric Research (NCAR). In situ aircraft measurements provided a detailed description of the upper air structure during the storm (Lilly and Zipser, 1972). The availability of such data, along with surface observations, has provided a unique opportunity to understand the windstorm phenomenon. Through the subsequent theoretical and modeling studies (e.g., Klemp and Lilly 1975, Peltier and Clark 1979, Durran and Klemp 1983, Scinocca and Peltier, 1989), we are better able to explain the development of extreme surface wind events in relation to large-amplitude mountain waves and better predict their occurrence. Despite the availability of direct observational mountain wave data, the mechanisms of downslope windstorms are still not fully understood.

Klemp and Lilly (1975) discussed previous theories of downslope windstorm development and proposed an alternate mechanism. Some of the prior theories were

based on hydraulic jump theory (Kuettner 1959; Houghton and Isaacson 1968; Arakawa 1969) in which the atmosphere was modeled with two or more constant density layers topped by a free surface. Others attributed the extreme surface winds to the trapping of wave energy by short wavelength nonhydrostatic lee waves that form downstream of the mountain range (Scorer and Klieforth, 1959; Aanensen, 1965). Based on the observed upper air data, Klemp and Lilly noted the long horizontal wavelength, and, therefore, hydrostatic nature, of the amplifying mountain wave. From analytical and numerical model results, based on linear, two-dimensional, steady-state hydrostatic assumptions, they were able to produce realistic results. These supported their theory that the dominant effect is the partial reflection of vertically propagating wave energy by layers of varying static stability. The resulting downward westerly momentum transport by the wave is responsible for the high surface winds that develop.

It should be pointed out that Klemp and Lilly used the isentropic vertical coordinate in their numerical model. They did so expressly to take advantage of the enhanced vertical resolution that develops in regions of high static stability which is where the phase of the wave changes more rapidly. In our nonhydrostatic hybrid coordinate model we also found that regions of high static stability were more accurately represented with the isentropic coordinate.

Peltier and Clark (1979) analyzed the role of nonlinear, nonhydrostatic, transient effects on downslope windstorms. Their numerical results showed that isentropic steepening and breaking lee waves, along with the associated flow reversal, causes a breakdown in the upward propagation of wave energy. This revisits the earlier theories

of the role of lee waves in trapping wave energy and contributing to windstorm formation.

5.3.1 Model configuration and initialization

Our experimental setup is based on Doyle et al (2000) which compared the Boulder windstorm simulations generated by various models. The simulation is performed on a two-dimensional (x-z) plane with no rotation. The Front Range of Colorado is represented by a witch of Agnesi curve with the height and half-width set at $h = 2\,\text{km}$ and $a = 10\,\text{km}$, respectively. The free-slip condition is applied at the lower boundary. The horizontal domain is 220 km in extent, and in our case we use periodic lateral boundary conditions. The horizontal grid spacing is $\Delta x = 1\,\text{km}$.

The model top is a rigid lid at $z = 48\,\text{km}$. We placed the model at this height in lieu of using an absorbing layer. For simulation periods of ~ 3 hours, we found that, in the region of interest which lies below 25 km, there is little evidence of artificial wave reflection from the upper boundary. In fact, model results with the model top at 25 km, in this time period, produced nearly the same results as with the higher top. This may be due to internal wave reflection and absorption, which occurs below the 25 km level, that is associated with critical layers and sharp gradients in the wind shear and stability profiles.

At the initial condition, the average vertical grid spacing is constant up to 35 km in height. Above this we employ a stretched vertical grid to save on the computational

cost by reducing the total number of model levels. This is done in a smooth manner by gradually increasing layer thickness up to the model top of 48 km.

We performed two runs using the hybrid vertical coordinate with the same number of levels as in Doyle et al (2000), i.e., 125 levels in the lowest 25 km, giving an average vertical grid spacing of 200 m. The two cases differ in the way the coordinate transitions from terrain-following σ to isentropic coordinates. This was done by running the model with two different values for $\theta_{\min}$ in the specification of the hybrid vertical coordinate (see equation (2.61)).

In the σ coordinate runs, we used the same number of levels as in the hybrid case, but we also performed simulations with a higher vertical resolution of 500 levels in the lowest 25 km (grid spacing $\sim$50 m). We use these as benchmarks representing more accurate (or "true") solutions with which to compare the lower resolution runs. Table 5.2 lists the model configurations and names are assigned to each run to be used for reference.

The initial conditions, shown in Figure 5.18, are uniformly applied in the horizontal. They are from Doyle et al (2000) and are based on the upstream 1200 UTC 11 January 1972 Grand Junction, Colorado sounding up to 25 km. For model levels above this height, a constant zonal wind of 7.5 m s^{-1} is applied and the temperature profile smoothly merges with that of the U. S. Standard Atmosphere. The reference surface pressure corresponding to $z=0$ is 850 mb. The zonal wind refers to the cross-mountain flow, that is, the wind component normal to the Front Range which basically runs north-south.

Table 5.2: Model configurations for the 11 January 1972 Boulder, Colorado windstorm simulations.

Model run	Vertical coordinate	# levels in lowest 25 km	Average Δz in lowest 25 km	Δx	z_{TOP}	Total # levels
Hybrid125_20K	Hybrid ($\theta_{min}=20$ K)	125	200 m	1 km	48 km	205
Hybrid125_270K	Hybrid ($\theta_{min}=270$ K)	125	200 m	1 km	48 km	205
Sigma125	σ	125	200 m	1 km	48 km	205
Sigma500	σ	500	50 m	1 km	48 km	820
Sigma500fine_dx	σ	500	50 m	250 m	25 km	500

The temperature sounding (Figure 5.18b) indicates that the tropopause is located at approximately 10 km. There are multiple layers of varying static stability in the stratosphere above this height. In the lower troposphere, a stable layer exists from

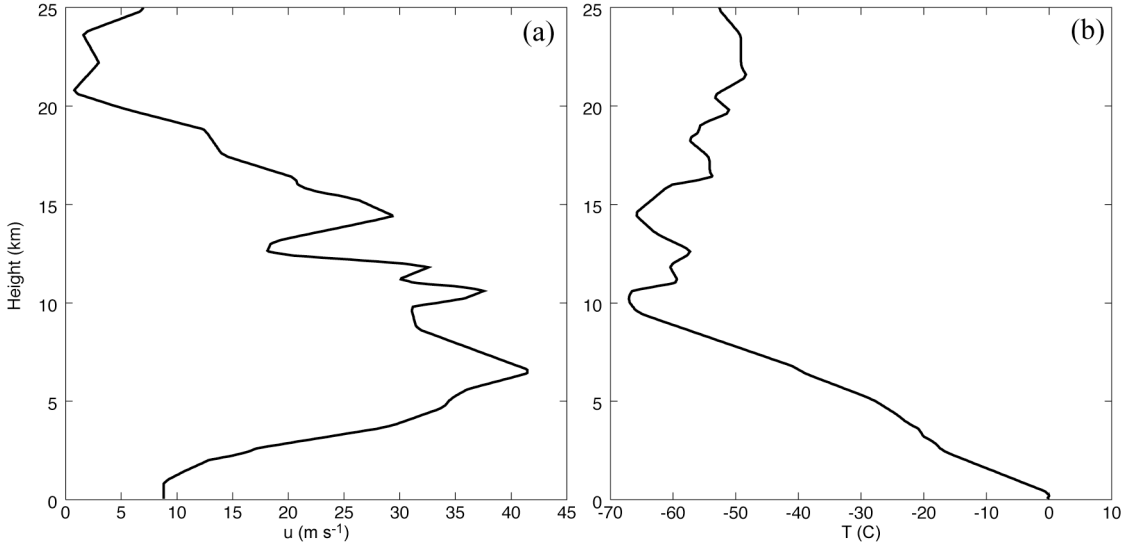


Figure 5.18: Vertical profiles of (a) the zonal wind and (b) temperature used as the initial condition for the 11 January 1972 Boulder, Colorado windstorm simulation. The data is from Doyle et al (2000) and is based on the 11 January 1200 GMT Grand Junction, Colorado sounding.

2.5 - 6 km and it is bounded on top and bottom by unstable layers. The winds throughout the troposphere are strong, though not extreme (Figure 5.18a). There are several levels of varying wind shear and at the 21 km height there is a critical level where the winds are almost zero. The presence of a stable layer with a base located just above mountain top height and strong tropospheric winds creates a favorable condition for the development of a downslope windstorm (Klemp and Lilly, 1975).

In the two hybrid-coordinate simulations, referred to as Hybrid125_20K and Hybrid125_270K, the parameter $\theta_{\min}$ is assigned a value of 20K and 270K respectively (see equation (2.61)). The effect of these two choices on the vertical coordinate profile is shown in Figure 5.19. For $\theta_{\min} = 20\text{K}$, which is obviously a value much colder than exists in the model domain, the coordinate differs considerably from the potential temperature

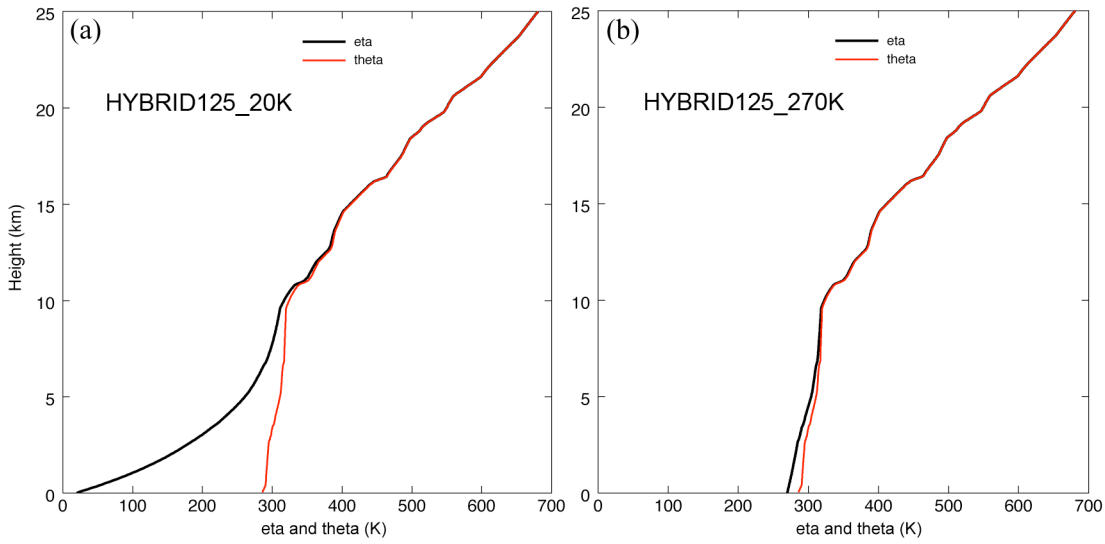


Figure 5.19: Vertical profiles of the vertical coordinate (black curves) and potential temperature (red curves) at the initial time. Panel (a) is for the hybrid coordinate with $\theta_{\min} = 20\,\text{K}$, and panel (b) is for the hybrid coordinate with $\theta_{\min} = 270\,\text{K}$.

from the surface to $\sim 7\,\text{km}$ (Figure 5.19a). This results from the system of equations (2.58)-(2.62) as well as the large difference between θ and $\theta_{\min}$. It means that the coordinate η is a function mainly of σ throughout this layer, therefore, it can remain monotonic in the presence of considerable negative static stability. On the other hand, for $\theta_{\min} = 270\text{K}$, the difference between θ and $\theta_{\min}$ is small so the coordinate is more isentropic than in the previous case (Figure 5.19b). Therefore, less negative static stability can occur near the surface before the coordinate tends to become nonmonotonic, in which case coordinate smoothing acts to prevent layer thicknesses from becoming zero. In both hybrid-coordinate simulations, the remaining coordinate parameters are set to $(\partial\theta/\partial\sigma)_{\min} = 0\,\text{K}$ and $r = 16$. Thus the coordinate is primarily isentropic above $z = 10\,\text{km}$ as shown in Figure 5.19.

5.3.2 Potential temperature field and static stability

Results after 1 hour of simulation are shown in Figure 5.20, which depicts the potential temperature field. (In these figures, the westerly flow is from left to right.) The mountain wave has substantially developed throughout the troposphere and lower stratosphere. There is generally an upwind tilt to the phase lines. A hydraulic jump feature has developed in the lower troposphere approximately $20\,\text{km}$ downstream of the mountain top with lee waves of horizontal wavelength $\sim 10\,\text{km}$ appearing just downstream of the jump. There is also considerable wave development above the hydraulic jump at the base of the stratosphere, with lee waves appearing just downstream as well.

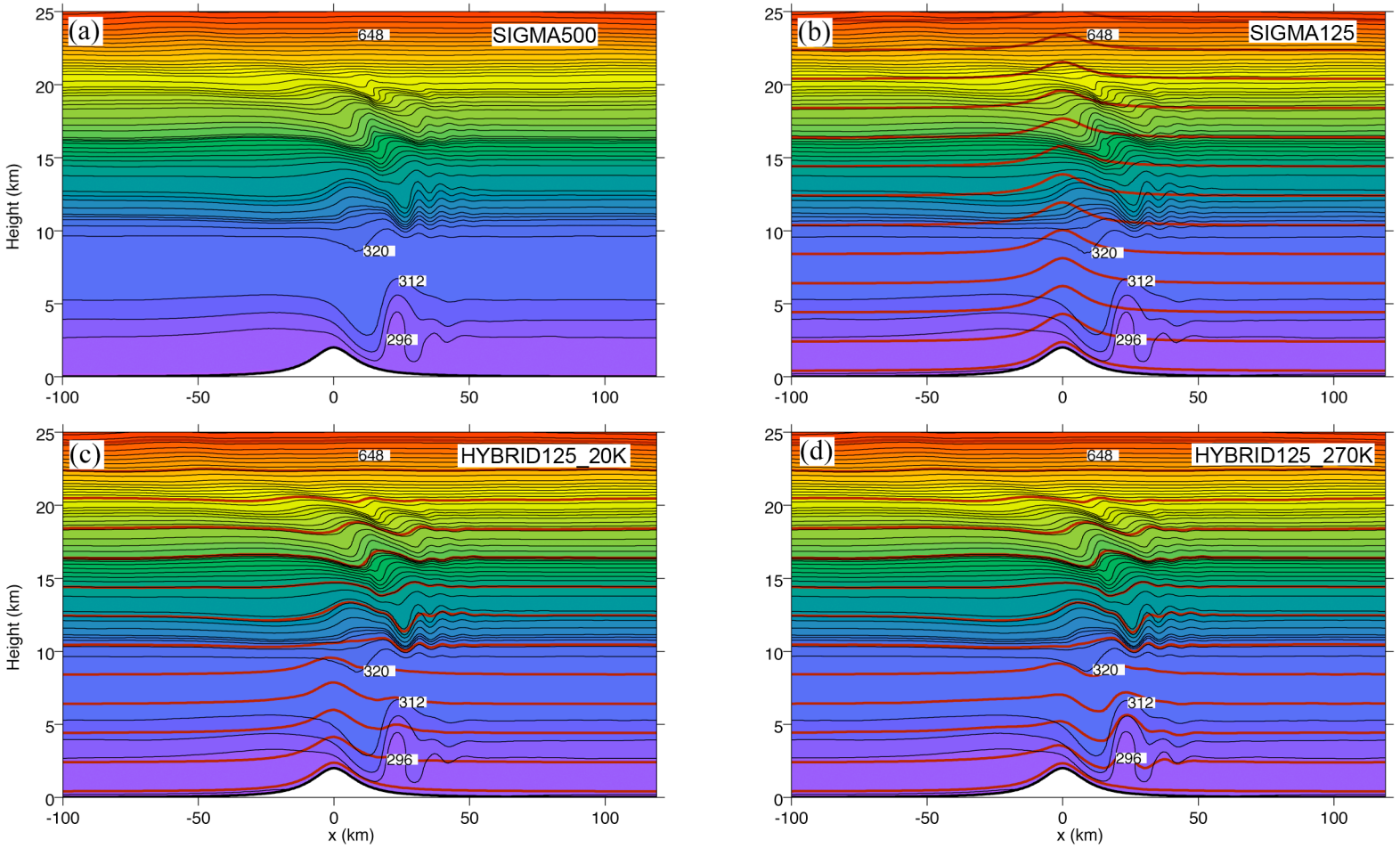


Figure 5.20: Isentropic surfaces (black curves) at time $t = 1\text{hr}\,10\text{min}$ for the 11 January 1972 Boulder windstorm simulations using the σ coordinate with (a) 500 levels and (b) 125 levels in the lowest 25 km, and the hybrid coordinate with 125 levels in the lowest 25 km for (c) $\theta_{\text{min}} = 20\,\text{K}$ and (d) $\theta_{\text{min}} = 270\,\text{K}$. The contour interval is 8 K, and selected isentropes are labeled. The bold red curves in panels (b)-(d) show the locations of every tenth model coordinate surface.

All four simulations shown in Figure 5.20 agree well with each other. The most noticeable difference is that in the σ coordinate runs, isentropes are already beginning to overturn at the 19 km level. This overturning is more advanced with the high vertical resolution Sigma500 run. In the hybrid coordinate runs, overturning has not occurred yet. This is likely due to the decreased resolution of the isentropic coordinate in areas of low static stability, and is consistent with the results of the previous finite amplitude mountain wave experiment in Subsection 5.1.3.

In the hybrid coordinate runs (Figures 5.20c and 5.20d), note that the coordinate surfaces (red curves) closely follow the isentropes above $\sim$10 km. The distinction between the vertical coordinate characteristics between the Hybrid125_20K and Hybrid125_270K runs, already discussed, is evident in these figures. In the latter simulation, where the coordinate is more θ-like near the surface, the coordinate surfaces (red curves) are more closely aligned with the isentropes in the lowest $\sim$7 km than they are in the Hybrid125_20K case.

At $t=2$ hours wave breaking is shown by the irregular isentropic surfaces in Figure 5.21, particularly at $z=15$ km just downstream of the mountain, and in the lower troposphere just downstream of the hydraulic jump. However, the wave breaking features are somewhat smoother in the hybrid coordinate simulations. Again, this is most likely due to the coarse vertical resolution in these regions as evident from the larger

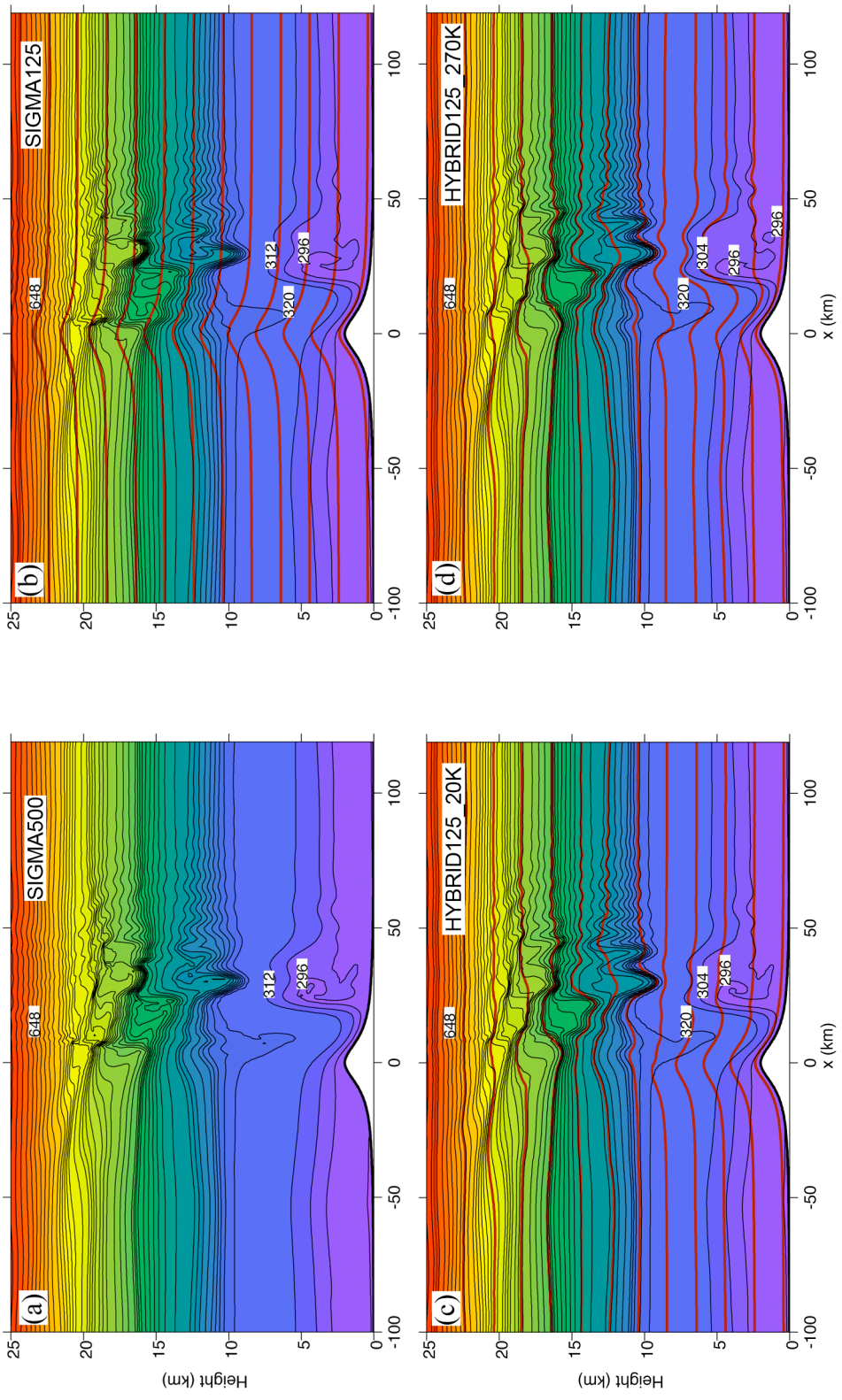


Figure 5.21: Same as in Figure 5.20 except at time t=2 hours.

vertical separation between the coordinate surfaces compared to those of the Sigma125 simulation. The effect of coarser resolution can also be seen in comparing the two hybrid coordinate simulations, where the wave overturning just downstream of the lower-troposphere hydraulic jump is more poorly resolved in the Hybrid125_270K run (Figure 5.21d) than in the Hybrid125_20K run (Figure 5.21c).

Given the same number of model levels, the hybrid coordinate does a better job than the σ coordinate at resolving regions of high static stability (i.e., where isentropes are closely spaced in the vertical). In Figures 5.21c and 5.21d there are horizontal bands of closely packed isentropes at roughly the 11 km, 12.5 km, 17 km, 19 km and 21 km levels. (These are actually features of the initial θ sounding as shown by the red curves of Figure 5.19.) These bands are more pronounced than those of the Sigma125 simulation shown in Figure 5.21b. (This is more obvious in the static stability plots of Figure 5.22.) The bands of tightly spaced isentropes in the 125 level hybrid coordinate runs are also present in the high resolution Sigma500 run, shown in Figure 5.21a. This indicates that they are physical features that are not resolved by the 125 level σ coordinate simulation. This point is reinforced by Figure 5.22 which compares the static stability as given by the square of the buoyancy frequency. In terms of the regions of positive static stability, the Hybrid125 simulations have more in common with the high resolution Sigma500 run than with the Sigma125 simulation. However, in terms of negative static stability, the Sigma125 simulation compares better to the "true" solution than does the Hybrid125 runs.

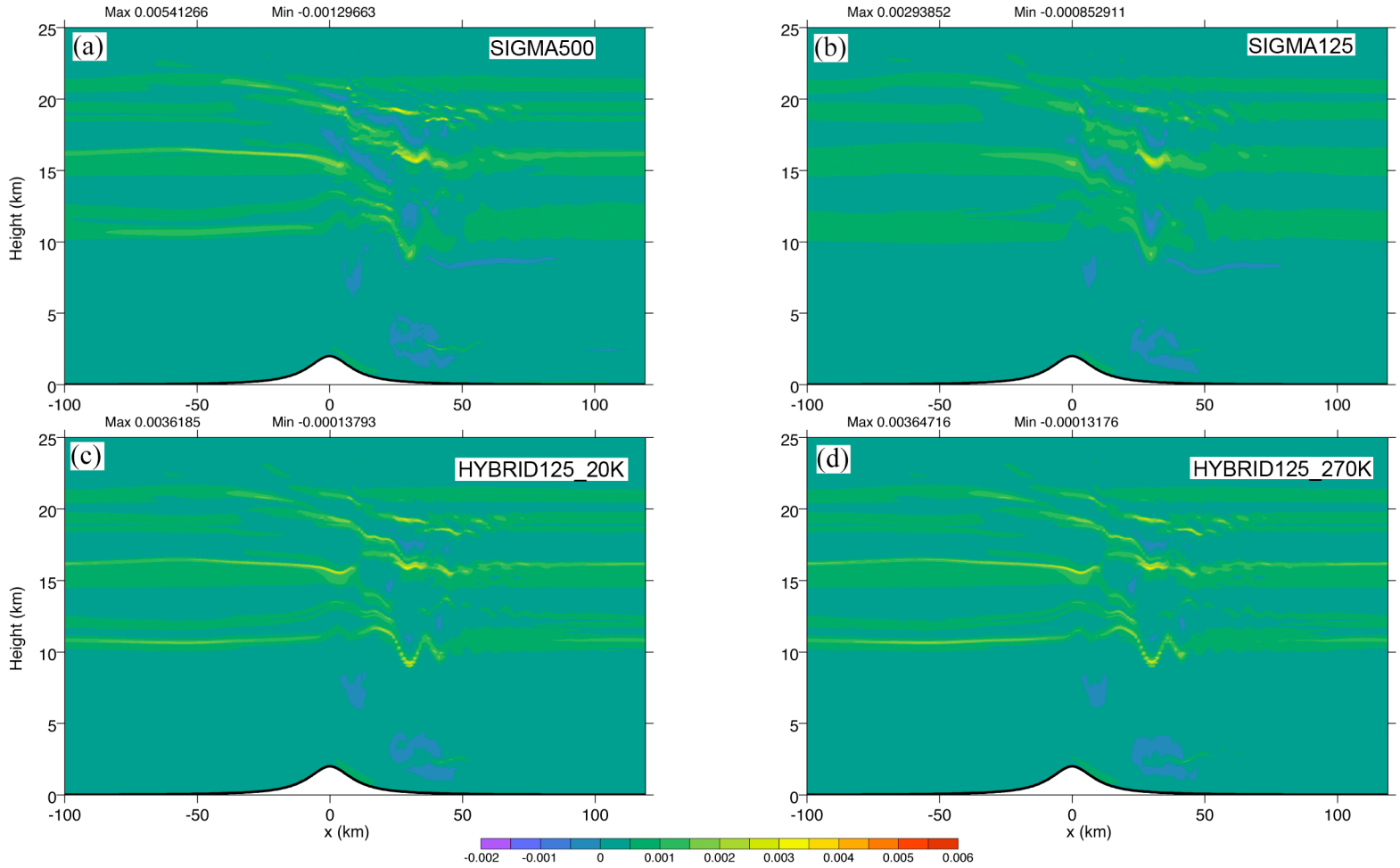


Figure 5.22: Static stability $N^2 = g\theta^{-1}\partial\theta/\partial z$ (s^{-2}) at time $t = 2$ hours for the 11 January 1972 Boulder windstorm simulations using the σ coordinate with (a) 500 levels and (b) 125 levels in the lowest 25 km, and the hybrid coordinate with 125 levels in the lowest 25 km for (c) $\theta_{min} = 20$ K and (d) $\theta_{min} = 270$ K.

Figure 5.23 shows the isentropic field at $t = 3$ hours. Again there is general agreement among the four model configurations. Our results also compare well with the models analyzed in Doyle et al (2000). Figure 5.24 shows the θ field at 3 hours for the Penn State-NCAR Mesoscale Model (MM5).

We also performed a high resolution σ coordinate run ("Sigma500fine_dx" listed in Table 5.2) in which both the vertical and horizontal resolutions are 4 times finer than the standard resolution. Figure 5.25 shows the results of this simulation at $t = 2$ hours which can be compared to the potential temperature and static stability fields in Figures 5.21 and 5.22 respectively. There is general agreement among the fields in terms of the vertical wave structure and the horizontal wave structure on scales down to ~ 10 km. This indicates that these are actual physical features resolved by the model. Finer details of the flow appear in the Sigma500fine_dx simulation which should be expected due to the finer resolution. Comparing the static stability plot of the high resolution run (Figure 5.25b) to those of the coarse horizontal resolution Hybrid125 runs (Figures 5.22c and 5.22d), we see that the hybrid coordinate accurately represents the features with high static stability.

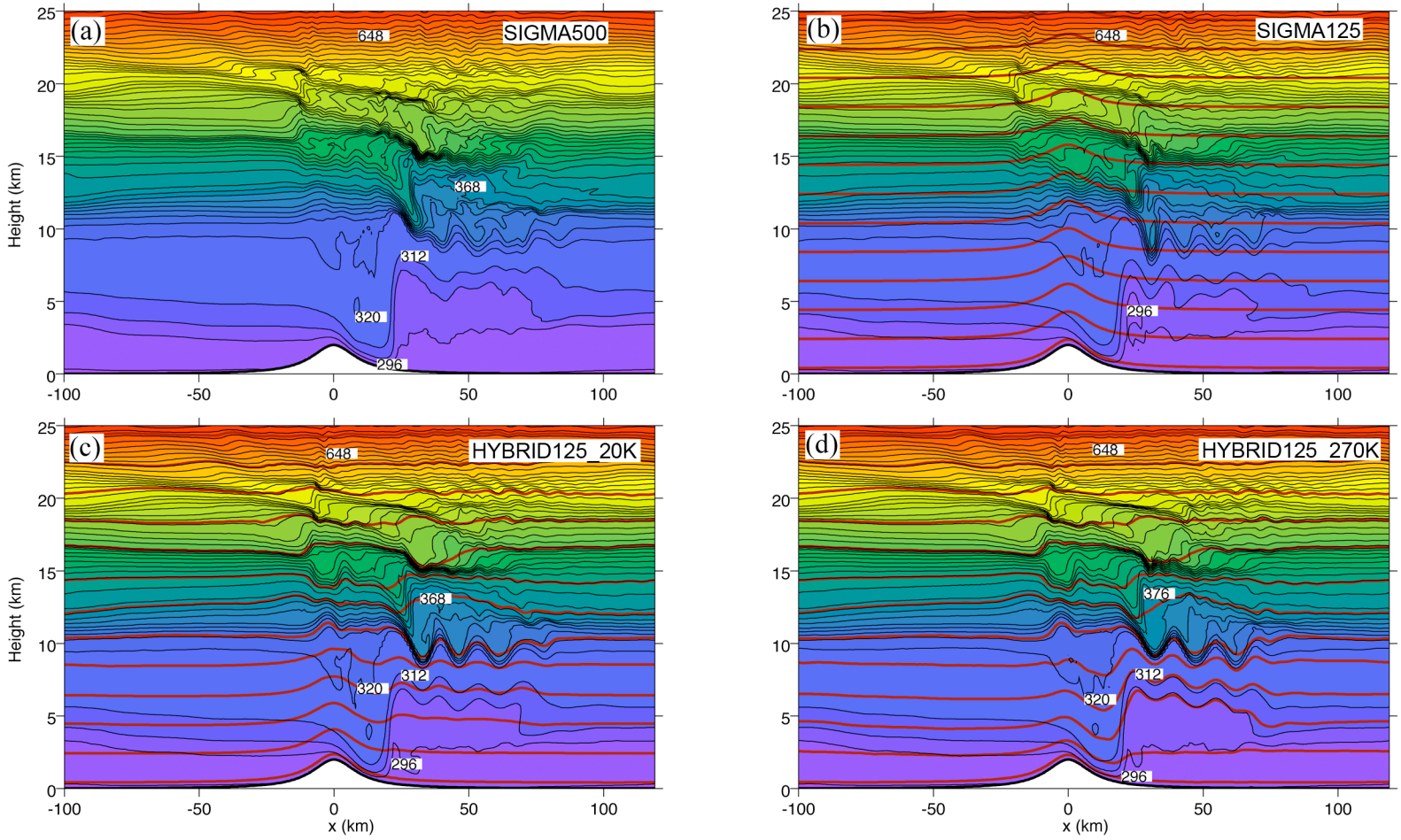


Figure 5.23: Same as in Figure 5.20 except at time $t=3$ hours.

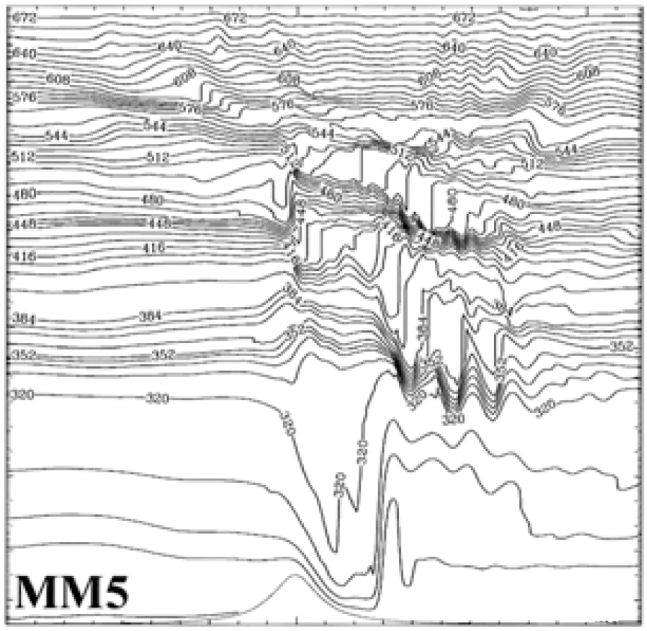


Figure 5.24: Potential temperature field at $t = 3$ hours for the Penn State-NCAR Mesoscale Model (MM5). Same contour interval as Figure 5.20. From Doyle et al (2000).

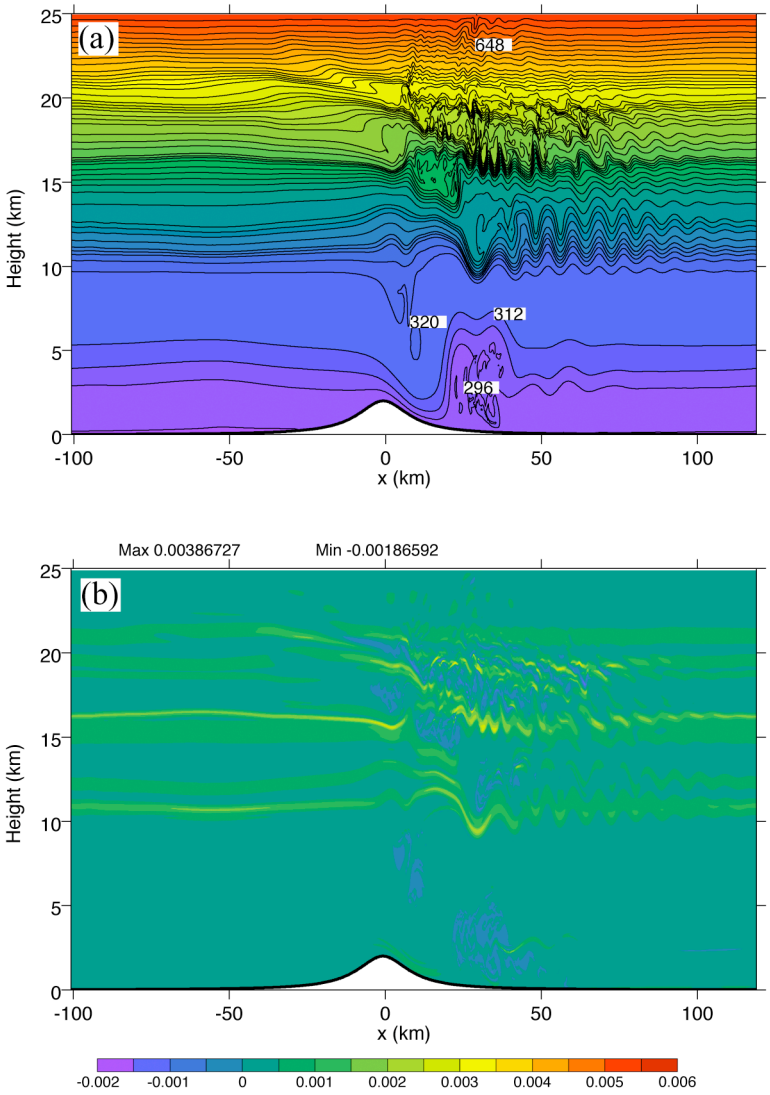


Figure 5.25: Isentropic surfaces (a) and static stability $N^2=g\theta^{-1}\partial\theta/\partial z$ (s^{-2}) (b) at time $t=2$ hours with the high vertical and horizontal resolution σ-coordinate model run (i.e., 500 levels in the lowest 25 km and $\Delta x=250$ m). The contour interval is 8 K in the isentropic plot.

5.3.3 Bulk Richardson number

Plots of the bulk Richardson number (R_B) at $t = 3$ hours are shown in Figure 5.26 (this figure actually shows $|R_B|^{0.5}\,\mathrm{sgn}(R_B)$ for graphical purposes). This dimensionless parameter is a measure of the dynamic stability of the flow field and is defined as $R_B \equiv (g/\theta)\,\delta\theta\,\delta z/(\delta u)^2$, where the δ's are vertical differences across model layers. When R_B is less than the critical value of approximately 0.25, the flow is dynamically unstable and turbulent (Stull, 1988). The regions where this condition is satisfied in Figure 5.26 correspond well to the wave breaking regions seen in the potential temperature fields in Figure 5.23. The suppression of turbulence due to the isentropic coordinate is evident in Figures 5.26c and 5.26d when compared to the σ coordinate plots in panels a and b. In the latter figures, the zones of negative R_B are larger and more coherent, particularly in the wave breaking layers in the middle stratosphere at the 16, 18 and 20 km heights.

5.3.4 Zonal wind field and surface drag

The zonal wind field at $t = 3$ hours is shown in Figure 5.27. The wave activity has redistributed the horizontal momentum from the purely westerly, horizontally uniform initial condition. Easterly winds have developed associated with wave overturning. These are more prominent in the σ coordinate runs. In other areas the westerly winds have greatly intensified. For example, in the upper troposphere at the 8 km height and

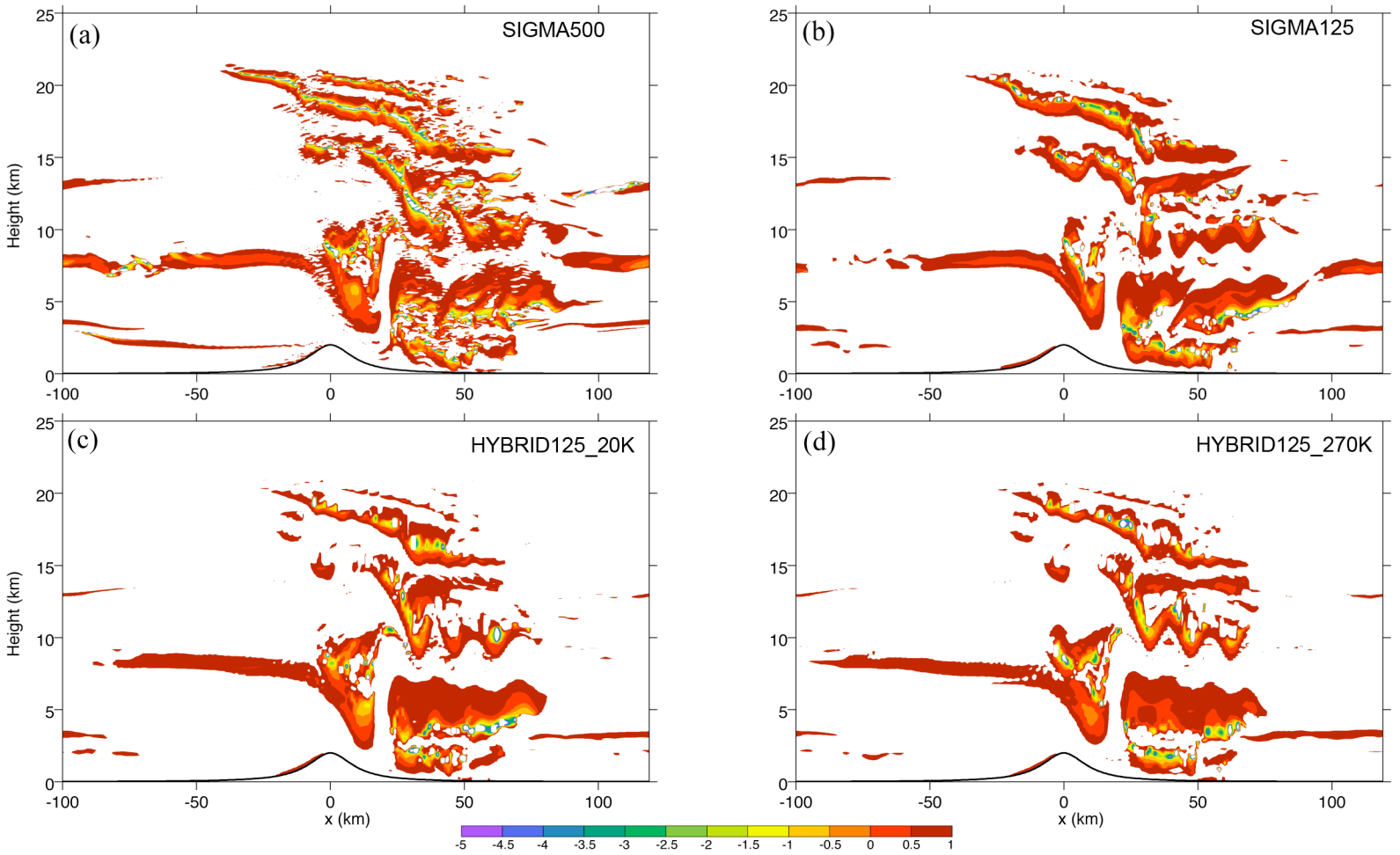


Figure 5.26: $|R_B|^{0.5}\,\mathrm{sgn}(R_B)$ at time $t=3$ hours for the 11 January 1972 Boulder windstorm simulations using the σ coordinate with (a) 500 levels and (b) 125 levels in the lowest 25 km, and the hybrid coordinate with 125 levels in the lowest 25 km for (c) $\theta_{\min}=20$ K and (d) $\theta_{\min}=270$ K.

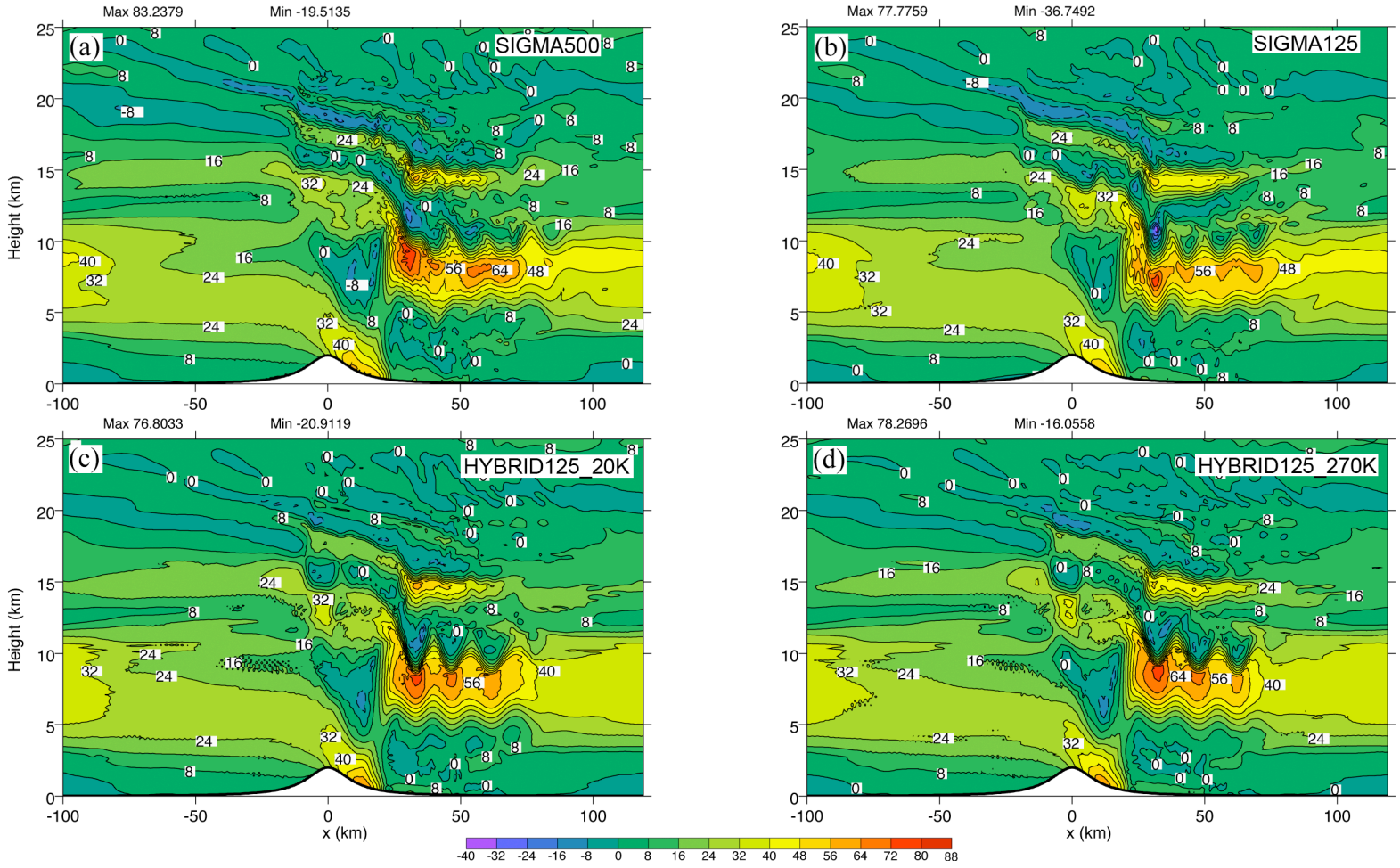


Figure 5.27: Zonal wind ($\mathrm{m\,s^{-1}}$) at time $t=3$ hours for the 11 January 1972 Boulder windstorm simulations using the σ coordinate with (a) 500 levels and (b) 125 levels in the lowest 25 km, and the hybrid coordinate with 125 levels in the lowest 25 km for (c) $\theta_{\mathrm{min}}=20$ K and (d) $\theta_{\mathrm{min}}=270$ K. The contour interval is $8\,\mathrm{m\,s^{-1}}$.

$\sim 25\,\text{km}$ downstream of the mountain top, the wind speed is $\sim 80\ \text{m s}^{-1}$ compared to the initial wind speed of $\sim 40\,\text{m s}^{-1}$.

The main feature of interest is the intense surface wind on the leeward slope of the mountain, which represents the downslope windstorm. There is a localized wind maximum located 10-15 km downstream of the mountain top in all four model simulations. This localized intensity is generally observed in downslope windstorm events. Boulder, Colorado often finds itself situated underneath the wind maxima, as was the case on January 11, 1972. The intensity of the maximum surface winds is larger in the hybrid-coordinate runs ($\sim 62\,\text{m s}^{-1}$) than in the σ-coordinate runs ($\sim 56\,\text{m s}^{-1}$). In the MM5 model (Figure 5.28) these winds were $\sim 72\,\text{m s}^{-1}$. The differences among the models may partly be attributed to the transient nature of the winds. For reference, peak

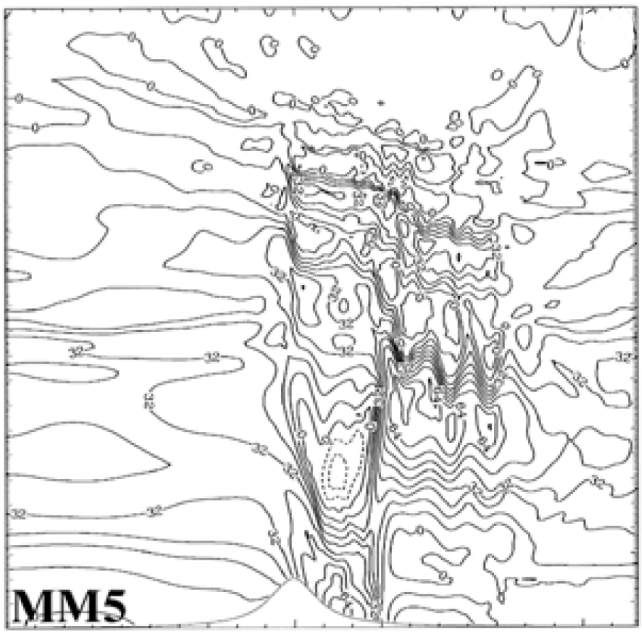


Figure 5.28: Zonal wind (m s^{-1}) at time $t = 3$ hours for the Penn State-NCAR Mesoscale Model (MM5). Same contour interval as Figure 5.27. From Doyle et al (2000).

gusts of 45-55 $\mathrm{m\,s^{-1}}$ were recorded at the surface (Lilly and Zipser, 1972). The free-slip lower boundary condition may be the reason for the overestimation of the winds by the models.

The surface pressure drag, given by $D = -\oint_x p_S \left(\partial z_S / \partial x\right) dx$, is diagnosed and plotted as a time series in Figure 5.29. Throughout most of the simulation the drag has a negative value which means that the mountain applies a net force on the atmosphere in opposition to the westerly motion. The drag peaks at about $t = 3$ hours and then decreases and becomes slightly negative after about 4.5 hours. This latter "dying-out" phase is due to the periodic lateral boundaries and that we therefore do not supply energy by way of an

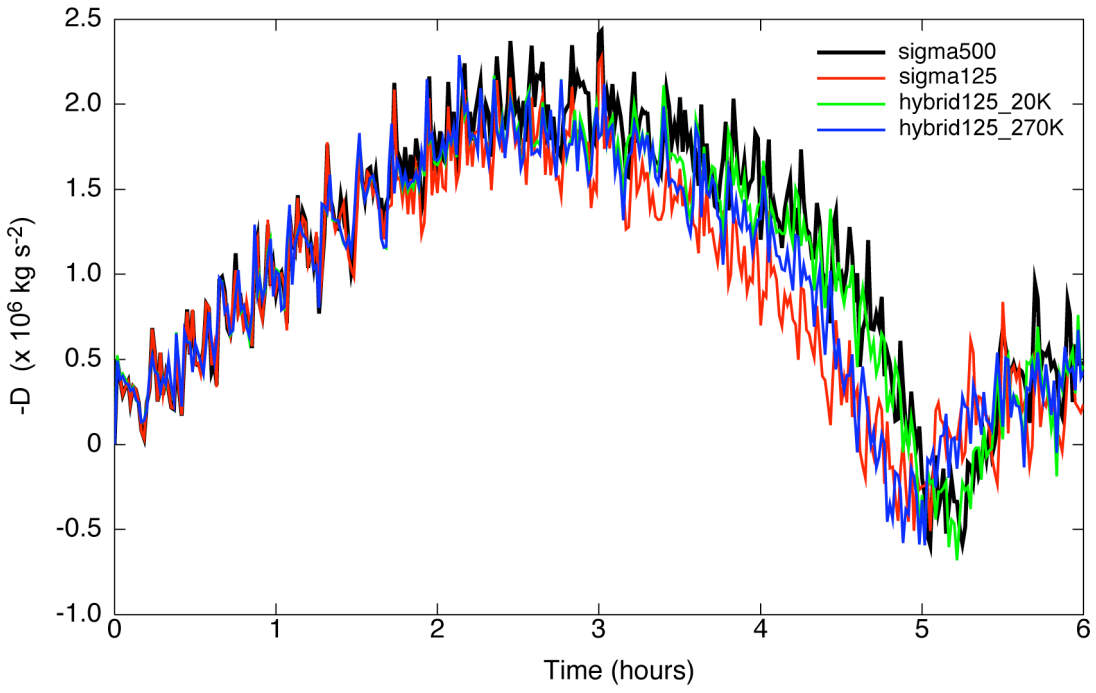


Figure 5.29: Time series of the surface pressure drag for the 11 January 1972 Boulder windstorm simulations using the σ coordinate with 500 levels (black curve) and 125 levels (red curve) in the lowest 25 km, and the hybrid coordinate with 125 levels in the lowest 25 km for $\theta_{\mathrm{min}} = 20\,\mathrm{K}$ (green curve) and $\theta_{\mathrm{min}} = 270\,\mathrm{K}$ (blue curve).

inflow upstream boundary as in Peltier and Clark (1979) and Durran and Klemp (1983). However, our surface pressure drag compares well, in order of magnitude terms, with their models.

Figure 5.29 shows that there is good agreement in the surface pressure drag among the four model simulations during the wave development period $t \cong 0\text{-}2$ hours. During the time period following this, the Hybrid125_20K simulation closely follows the "true solution" of the Sigma500 run. However, the agreement is not as good with the Hybrid125_270K simulation. Note that the Sigma125 results deviate the most from the "true solution".

A notable quasi-periodic pulsing of the surface pressure drag, with a period of about 15 minutes, can be seen in Figure 5.29. These fluctuations were analyzed by Scinocca and Peltier (1989), who attributed them to the transience of the time dependent fields associated with wave breaking. Figure 5.30 shows a time series plot of the winds in the lowest model layer of the Hybrid125_20K simulation at a location 13 km downstream of the mountain top. The pulsing begins at about $t = 1.5$ hours when wave breaking is established. The amplitude of the pulsing is large during the period from 2-4 hours when wave breaking is most active.

5.3.5 Tracer advection

The most striking difference between the hybrid and σ coordinate model runs is in the vertical advection of a passive tracer. Here we see a distinct advantage with the isentropic coordinate. In order to isolate the effects of vertical advection as much as

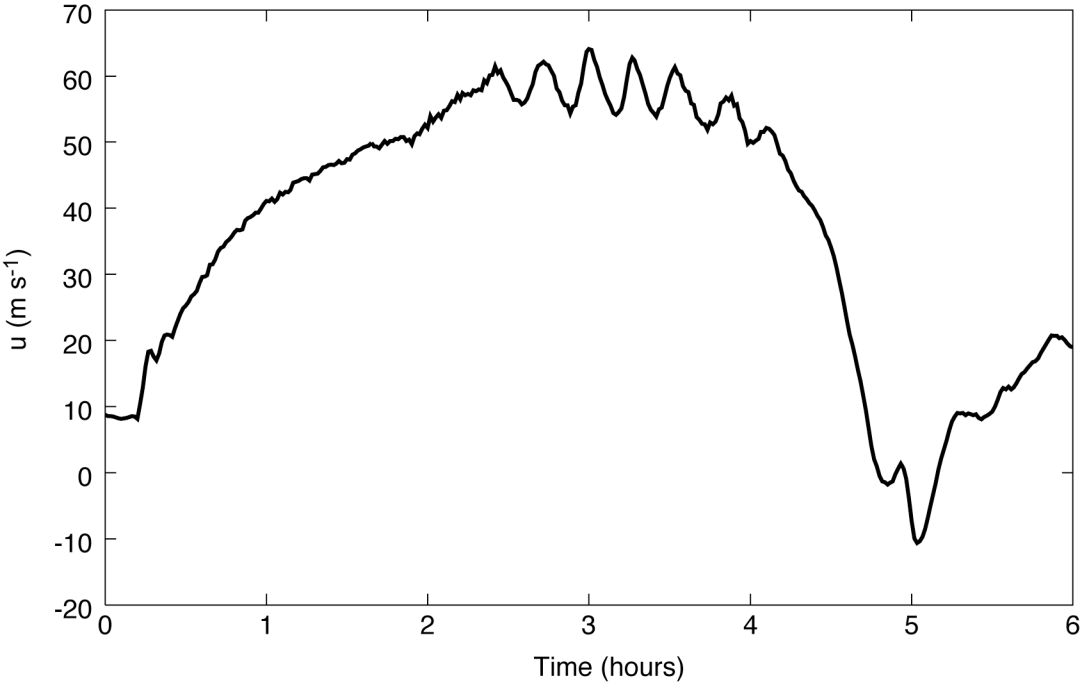


Figure 5.30: Time series of the zonal component of the surface wind at a grid point located 13 km downstream of the mountain top. Results for the Hybrid125_20K simulation are shown.

possible, the passive tracer is initialized along horizontal bands bounded by selected isentropes as shown in Figure 5.31a.[1] The tracer is assigned the arbitrary value of unity inside the bands and zero outside. This can also be viewed in a scatter plot of tracer concentration versus potential temperature for all model points as shown in Figure 5.31b. In the continuous system of equations for adiabatic processes, since θ is conserved, the

[1] With the terrain-following σ coordinate, there are nonzero vertical and horizontal gradients of the tracer along coordinate surfaces. Therefore, from the outset, this coordinate is at a disadvantage over the pure z and θ coordinates. However, we tested the model with an alternate z-based vertical coordinate based on Schar et al (2002). With this Eulerian coordinate the effects of the surface topography vanish rapidly with height and, in our case, the coordinate is basically z at a height of 10 km and above. The tracer fields (not shown here) using this alternate vertical coordinate were almost indistinguishable from those of the Eulerian σ coordinate. Therefore, the argument that the quasi-Lagrangian θ coordinate has an inherent advantage over the σ coordinate is valid.

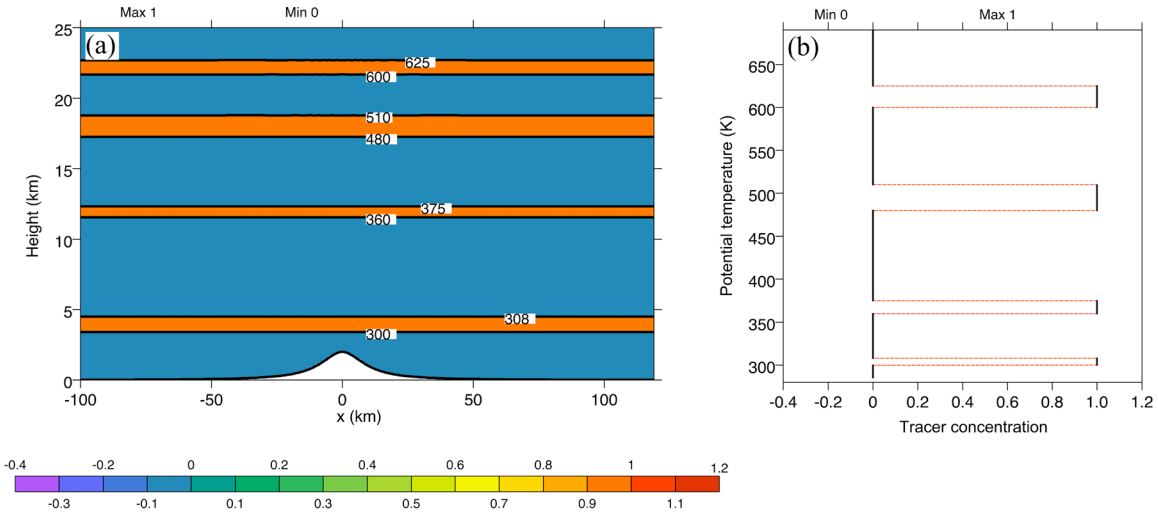


Figure 5.31: (a) Contour plot of the initial passive tracer concentration (colors) and the isentropes bounding the tracer bands (black curves). (b) Scatter plot at $t=0$ of the tracer concentration versus potential temperature.

correlation between θ and the passive tracer remains unchanged in time assuming no diffusion of either property. This means that the scatter plot of tracer concentration versus θ should remain unchanged, and there should be no other value of tracer concentration besides the initial values of 0 and 1.

Profiles of the tracer concentration after 70 minutes of simulation time are shown in Figure 5.32. In contrast to the initial condition shown in Figure 5.31a, there are now other tracer concentration values besides 0 and 1, and some of the tracer has "leaked" outside of the original isentropic bounds indicated by the bold black curves. This has occurred because of numerical dispersion associated with the vertical advection terms of the tracer tendency equation. The dispersion error is most evident where the coordinate is σ, i.e., in Figures 5.32a and 5.32b and the lowest band in the hybrid coordinate plots of Figures 5.32c and 5.32d. At $t=70$ minutes, wave overturning has not yet occurred and

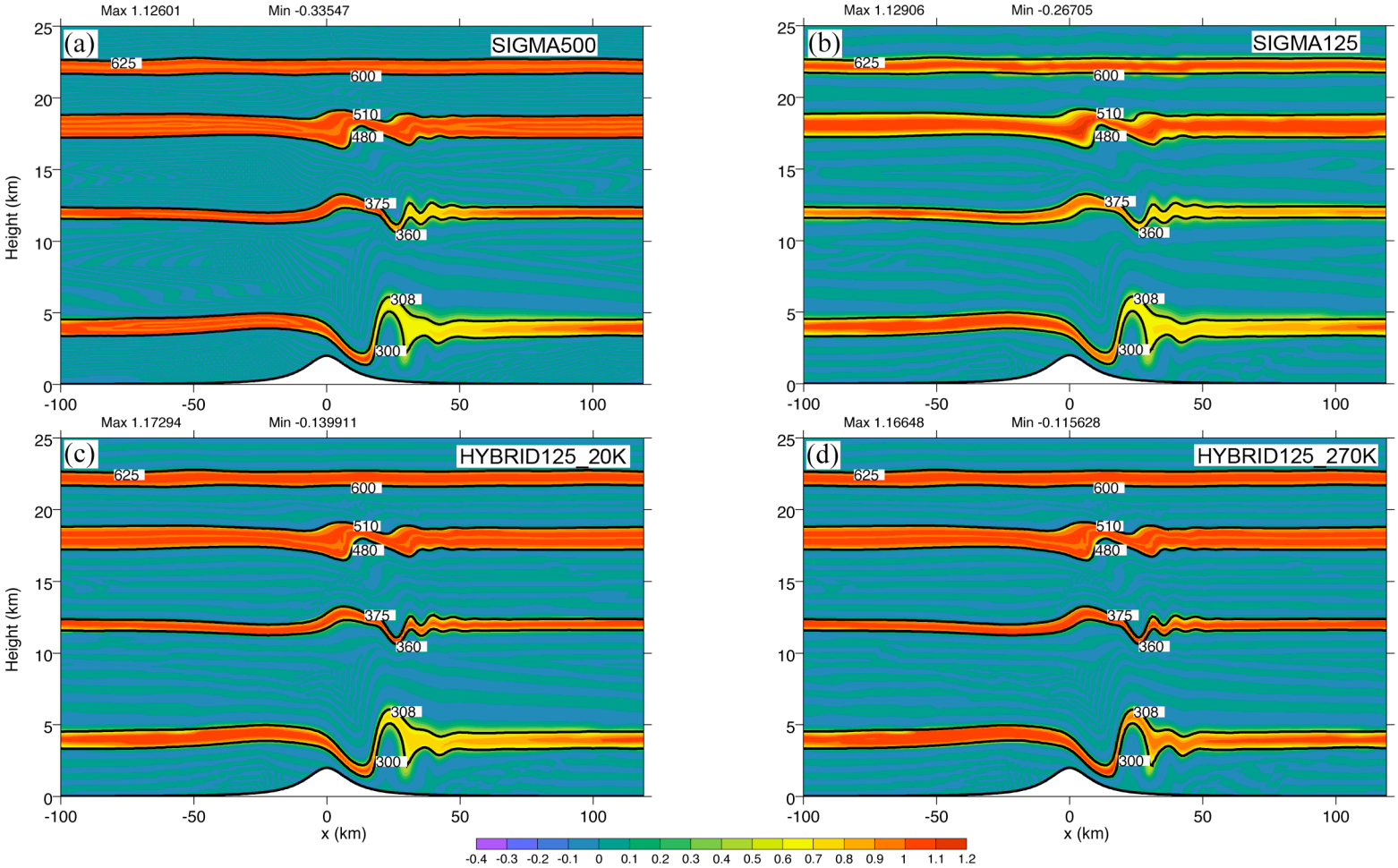


Figure 5.32: Contour plots at time t=1hr10min of the passive tracer concentration (colors) and the isentropes which originally bounded the tracer bands (black curves) using the σ coordinate with (a) 500 levels and (b) 125 levels in the lowest 25km, and the hybrid coordinate with 125 levels in the lowest 25km for (c) $\theta_{\min}$=20K and (d) $\theta_{\min}$=270K.

there has been minimal coordinate smoothing in the hybrid vertical coordinate runs. Therefore, the vertical velocity in the θ-coordinate regions of the hybrid coordinate has been virtually zero up until this time. The effect of this can be seen in Figures 5.32c and 5.32d in the upper three tracer bands as compared to those of Figures 5.32a and 5.32b.

These effects mentioned above are more noticeable in the scatter plots of Figure 5.33. The difference between the top tracer band among the four simulations is the most striking. With the hybrid vertical coordinate (Figures 5.33c and 5.33d), the scatter points lie along the theoretical profile indicated by the red lines. In the 125-level σ coordinate simulation (Figure 5.33b), the profile of the upper band differs significantly from theoretical profile due to the dispersion error. The 125-level hybrid coordinate model even has a definite advantage over the high-resolution 500-level σ coordinate simulation (Figure 5.33a), where some dispersion error is evident at the discontinuities in the original profile. It should be noted that this is a rather severe test case as we are demanding a lot of the numerical advection schemes. When advecting a property that has a sharp discontinuity, it is difficult to avoid some dispersion error. There are alternative schemes to the one we use, which is based on the upstream-weighted scheme of Takacs (1985), that minimize such error. However, our purpose here is to demonstrate the inherent advantage of the quasi-Lagrangian θ coordinate through its diminution of the vertical velocity.

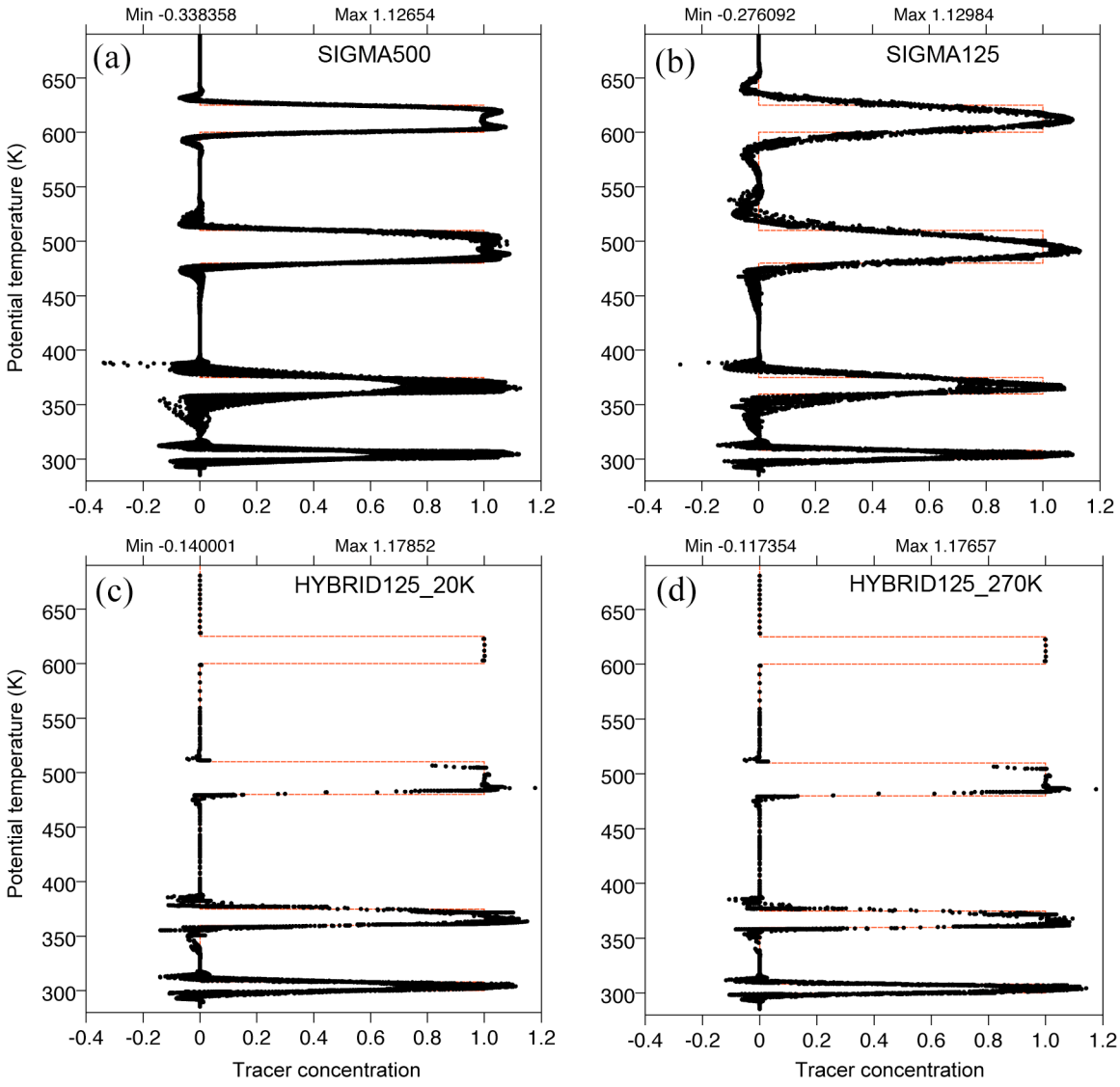


Figure 5.33: Scatter plots at time $t = 1\text{hr}10\text{min}$ of the passive tracer concentration versus potential temperature using the σ coordinate with (a) 500 levels and (b) 125 levels in the lowest 25 km, and the hybrid coordinate with 125 levels in the lowest 25 km for (c) $\theta_{\min} = 20\,\text{K}$ and (d) $\theta_{\min} = 270\,\text{K}$.

Returning to Figure 5.32, there is a noticeable difference between the appearance of the lowest band in the two hybrid coordinate simulations. In Figure 5.32d the vertical coordinate is more θ-like near the surface than in the simulation of Figure 5.32c. As a consequence, there is less dispersion error downstream of the hydraulic jump in the former case.

Figures 5.34 and 5.35 are scatter plots at simulation times 2 and 3 hours respectively. At these times, the hybrid coordinate experiences some dispersion error which is due to the vertical velocities induced by the coordinate smoothing. Despite this, the hybrid coordinate exhibits less error than the Sigma125 simulations. It is comparable to, if not better than, the high resolution Sigma500 runs, but achieves this with fewer model levels. This is an attractive feature of the hybrid coordinate.

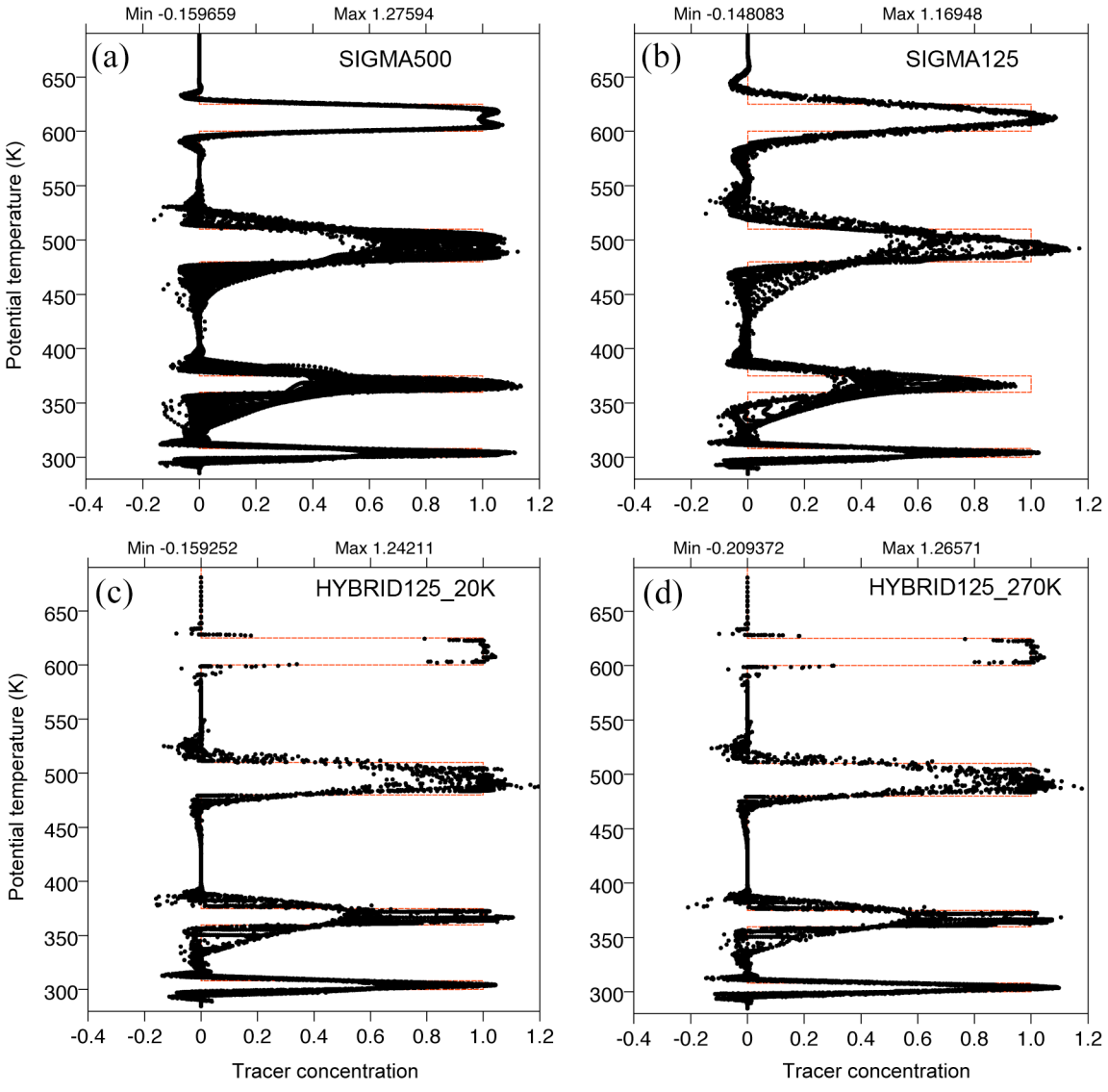


Figure 5.34: Same as Figure 5.33 except at time $t=2$ hours.

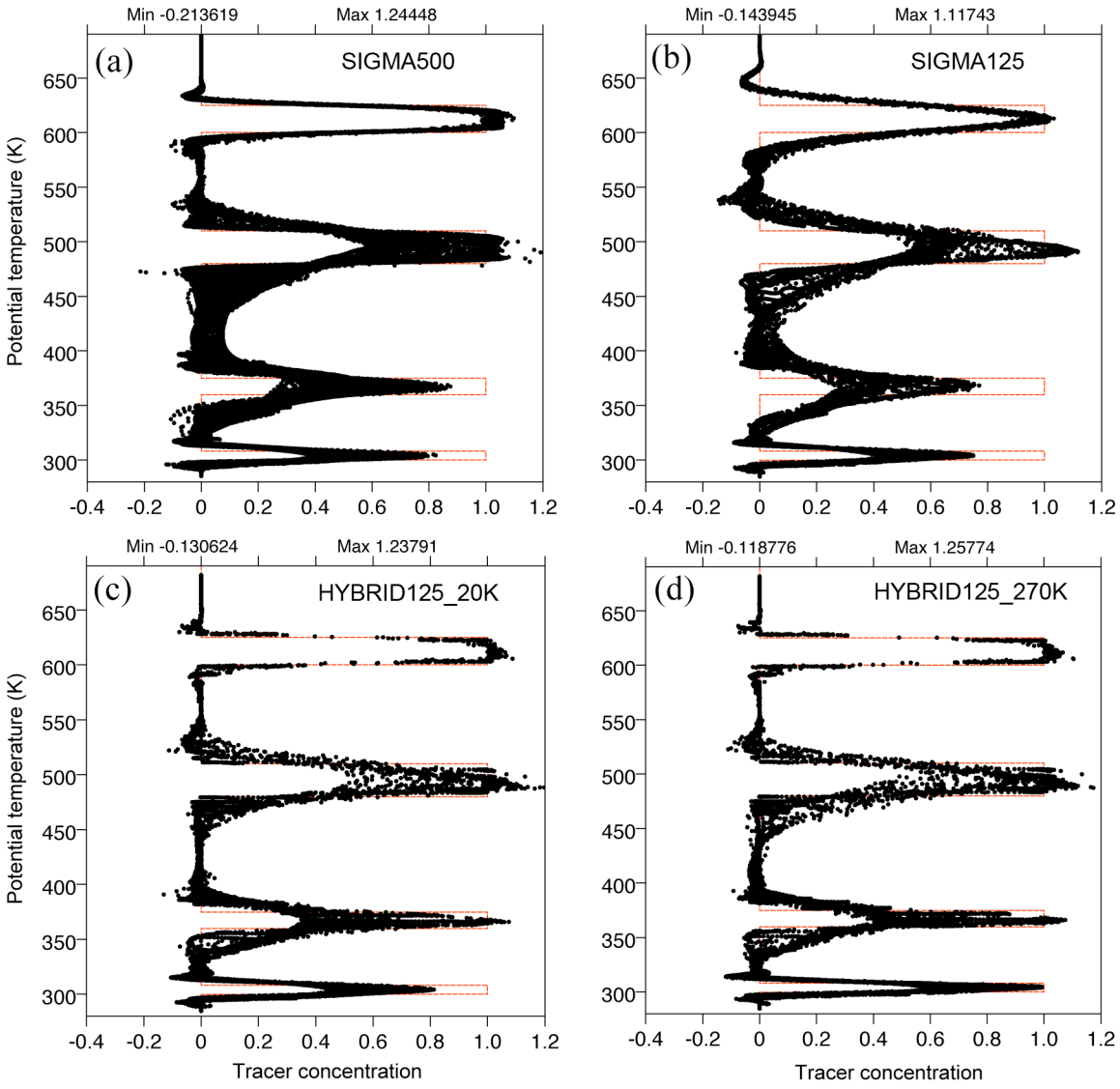


Figure 5.35: Same as Figure 5.33 except at time $t=3$ hours.

5.3.6 Integral property evaluation

In Chapter 3 we developed a vertical finite difference scheme which preserves various integral constraints found in the continuous system of equations. These include conservation of mass, conservation of total energy, and conservation of the vertically integrated momentum circulation. We verified that the model conserves mass. Conservation of potential temperature under adiabatic conditions is not satisfied,

however. The scheme was shown to satisfy these constraints only for case of z coordinates and when centered-difference advection schemes are used in the mass, potential temperature and geopotential tendency equations. In our model we do not meet these requirements because we neither use the z coordinate nor employ upstream-weighted advection schemes. In this subsection we empirically evaluate the degree to which these constraints are violated by examining time series of the mass-weighted mean total energy and potential temperature, as well as of the total zonal momentum.

The integral constraints on total energy and potential temperature were formulated assuming adiabatic, frictionless processes. Therefore, we performed model runs of the 11 January 1972 Boulder windstorm without the subgrid scale turbulence parameterization in order to evaluate the integral properties of the model. These include a σ coordinate run and a hybrid coordinate run, each with 125 levels in the lowest 25 km. The mass-weighted mean value of a given property A is calculated as $\bar{A}^* = \overline{mA}/\bar{m} = \sum_{i,k}\left[(mA)_{i,k}(\delta\eta)_k\right] \Big/ \sum_{i,k}\left[m_{i,k}(\delta\eta)_k\right]$, where the overbars are volume-weighted averages over the domain. Figure 5.36 shows the time series of the energy budget. The changes from the initial condition of the mass-weighted mean internal energy $\overline{c_v T}^*$, geopotential energy $\bar{\phi}^*$, kinetic energy $\overline{1/2 u^2}^*$ and their sum, the total energy, are plotted. If total energy were conserved then the change in total energy would be zero. Instead, there is a gradual increase in total energy with both the σ and the hybrid coordinates.

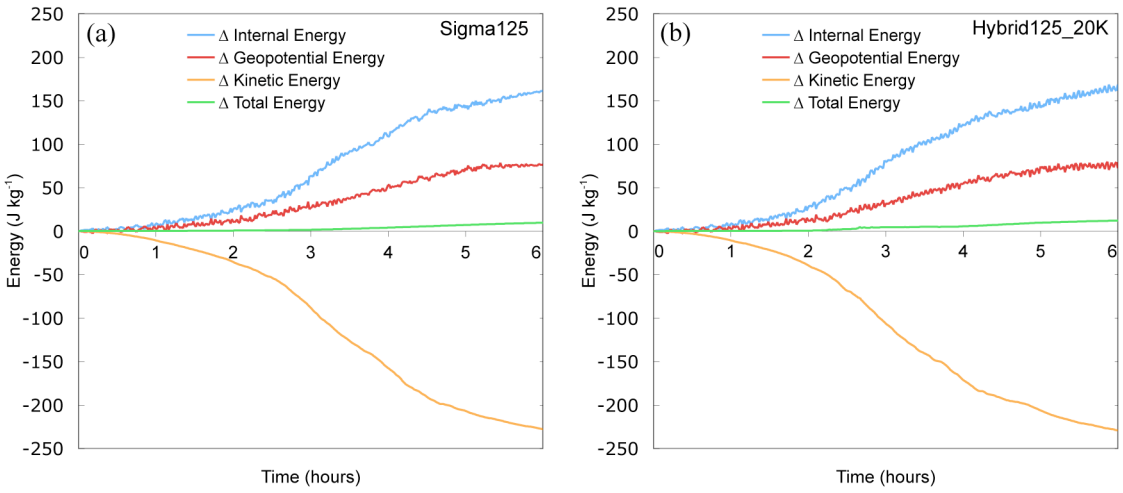


Figure 5.36: Time series of the mass-weighted mean energy budget for (a) the σ coordinate, and (b) the hybrid coordinate with $\theta_{\min} = 20\,\mathrm{K}$. The vertical resolution in each run was 125 levels in the lowest 25 km.

Figure 5.37 shows the time series of the mass-weighted mean potential temperature $\overline{\theta}^{*}$. In both runs the potential temperature is relatively constant until approximately $t = 1.5$ hours, when it starts to increase (at a higher rate in hybrid coordinate run). The increase starts at about the time wave breaking becomes active and sharp spatial gradients in the potential temperature develop. The explanation may therefore be attributed to the large error in the potential temperature advection terms resulting from these sharp gradients.

Finally, we examine the total zonal momentum budget given by $\sum_{i,k}\left[(mu)_{i,k}(\delta\eta)_k \Delta x\right]$. If the constraint on the vertically integrated momentum circulation were satisfied, then the time integral of the surface pressure drag would equal the total zonal momentum. The total zonal momentum and the zonal momentum inferred from the surface pressure drag are plotted in Figure 5.38. Figure 5.38a shows that there is close agreement between these two time series for the Sigma125 simulation. However, in both

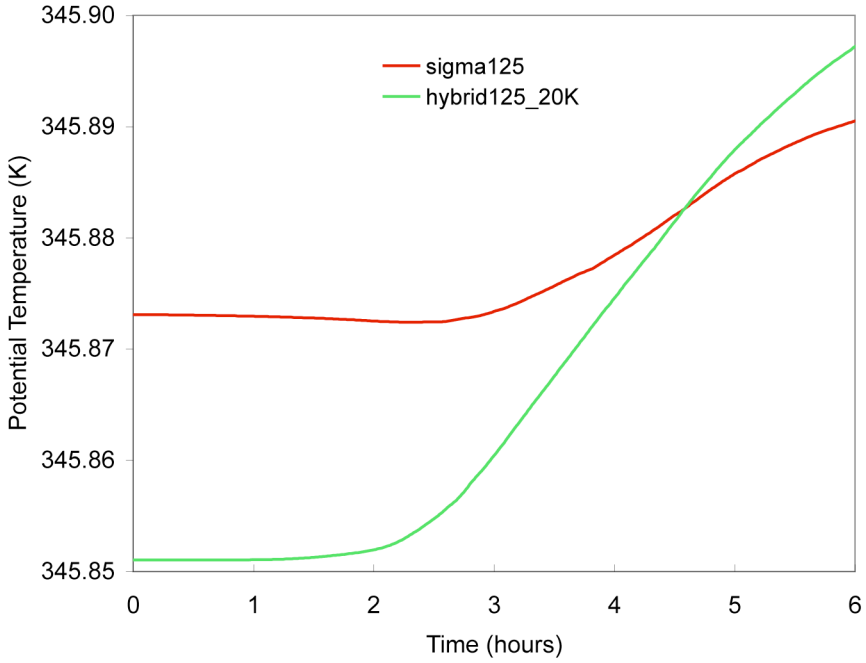


Figure 5.37: Time series of the mass-weighted potential temperature for (a) the σ coordinate, and (b) the hybrid coordinate with $\theta_{min}=20\,\mathrm{K}$. The vertical resolution in each run was 125 levels in the lowest 25 km.

the Hybrid125_20K and Hybrid125_270K runs, there is a slight deviation between the two curves. This may be due to the fact that the σ coordinate approximates the z coordinate away from the mountain, and, therefore, the momentum circulation integral constraint is satisfied in these regions. The same is not true with the hybrid coordinate which is isentropic in most of the domain.

5.4 Summary and conclusions

The hybrid (θ-σ) vertical coordinate model was extensively tested with two-dimensional mountain wave experiments and the results compared well with those of the traditional Eulerian σ coordinate. Linear experiments produced wave fields that

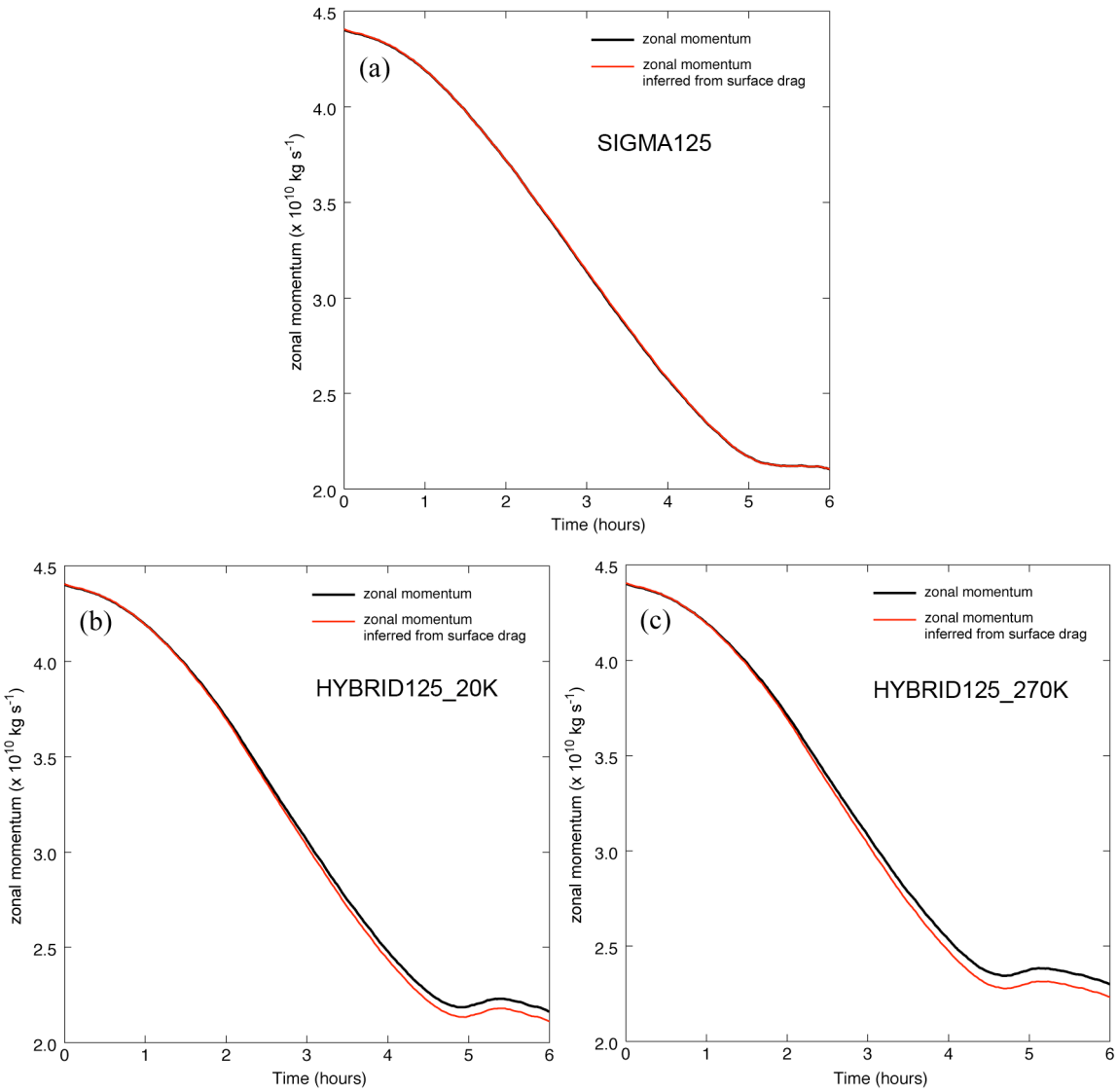


Figure 5.38: Time series of the zonal momentum (black curves) and the zonal momentum inferred from the time integration of the surface drag (red curves) for (a) the σ coordinate, (b) the hybrid coordinate with $\theta_{\min} = 20\,\mathrm{K}$, and (c) the hybrid coordinate with $\theta_{\min} = 270\,\mathrm{K}$. The vertical resolution in each case was 125 levels in the lowest 25 km.

agreed well with analytical solutions. The vertical flux of horizontal momentum was analyzed and compared between the isentropic and σ coordinate frameworks. In both cases the flux profiles were approximately the same. However, with the isentropic coordinate, the main contributor to the flux was the form drag on coordinate (isentropic)

surfaces, while with the σ coordinate, the eddy momentum flux was the primary means of momentum transport. This distinction between the two coordinate systems is readily evident in the continuous equations. The experimental analysis provided a validation of the numerical construction of the model.

Nonlinear mountain wave experiments provided an opportunity to test the ability of the hybrid coordinate to adapt to isentropic overturning. Wave breaking was handled well by the coordinate in both an idealized isothermal, uniform-flow experiment and a simulation of the 11 January 1972 Boulder, Colorado downslope windstorm. However, with the hybrid coordinate, the degree of dynamic instability associated with wave overturning is suppressed compared with the σ coordinate simulations. This is seen by comparing the bulk Richardson number fields. Tests suggest this is due to the decreased vertical resolution of the hybrid coordinate in statically unstable regions.

The hybrid coordinate gives comparable results for surface winds on the leeward slope, but does not have an advantage over the σ coordinate in this respect. Both the hybrid and σ coordinate Boulder windstorm simulations produced realistic surface winds on the leeward slope of the mountain range. These were similar to other model results (e.g., Doyle et al 2000) and to the surface winds observed during the storm. Also, both models produced similar time series of the surface pressure drag.

The hybrid vertical coordinate had an advantage over the σ coordinate in resolving features of high static stability. This results from the enhanced vertical resolution with the isentropic coordinate. Highly stable regions on plots of static stability from the hybrid coordinate compared well with those of the σ coordinate run with 4 times

the number of model levels. These features were not well resolved with the σ-coordinate run using the same number of model levels as with the hybrid coordinate simulation.

The integral properties of total energy, potential temperature and zonal momentum circulation conservation were evaluated. Simulations without the subgrid scale turbulence parameterization were performed. Time series plots from these runs indicated a gradual increase of the mass-weighted mean total energy and potential temperature. It remains to be determined how significantly this will impact performance when the dynamical core is incorporated into a weather and climate forecasting model.

For performance in the free atmosphere, where the hybrid coordinate is primarily isentropic, tracer transport tests clearly displayed the advantage of the quasi-Lagrangian θ coordinate. There was substantially less dispersion error associated with vertical advection using the hybrid coordinate, even with the high vertical resolution σ coordinate simulation at early simulations times before wave breaking occurred.

We have demonstrated that the hybrid coordinate in the nonhydrostatic framework has advantages over the σ coordinate in various situations. Further work will help to establish the extent to which benefits can be realized in practical applications.

Chapter 6 SUMMARY AND CONCLUSIONS

We have presented a new nonhydrostatic, hybrid-vertical-coordinate atmosphere model which uses the quasi-Lagrangian θ coordinate throughout much of the vertical domain. We avoided the problem of isentropic coordinate surfaces intersecting the lower boundary by using the hybrid-coordinate approach, in which a terrain-following vertical coordinate is used near the surface. Our starting point in the model design was the hybrid vertical coordinate developed by Konor and Arakawa (1997) for quasi-static models. We then modified it for nonhydrostatic modeling of fine-scale motion in which overturning of isentropic surfaces frequently occurs at any altitude. This was done by adding an adaptive grid technique which allows the coordinate to deviate from purely isentropic to allow negative static stabilities (i.e., $\partial\theta/\partial z<0$) while maintaining model layer separation. After positive static stability is restored, the coordinate is relaxed back to being isentropic.

We performed extensive model tests with two-dimensional mountain-wave experiments, and the results compared well with those of the commonly used Eulerian height-based, terrain-following σ coordinate run with very high vertical resolution. Small-amplitude wave simulations demonstrated the quasi-Lagrangian characteristics of vertical momentum transport in θ coordinates. This transport was shown to manifest itself as the pressure form drag acting on coordinate surfaces, as opposed to an eddy flux

transport as in the Eulerian framework. Such a quasi-Lagrangian view of atmospheric processes is useful for understanding the general circulation of the atmosphere.

Large-amplitude mountain wave experiments showed the ability to represent isentropic overturning and wave breaking in the θ-coordinate domain of the model, which proved the adaptive features of the coordinate. These tests included an idealized isothermal case and a simulation of the 11 January 1972 Boulder, Colorado downslope windstorm. Use of the hybrid coordinate resulted in superior performance over the σ coordinate in the following ways:

- A reduction of error in the vertical tracer transport of a passive tracer
- Improved vertical resolution of layers with high static stability

The first of these advantages is due to the elimination of the vertical velocity for adiabatic flow in the framework of isentropic coordinates. The second is due to the concentration of model layers that naturally develops with the θ coordinate in regions of high static stability. However, the turbulence and degree of instability (as measured by the bulk Richardson number) associated with wave breaking was somewhat suppressed with the hybrid coordinate. This is likely due to the decrease in vertical resolution in these regions because of the relatively large vertical separation of isentropic surfaces.

We developed a vertical discretization scheme using the generalized vertical coordinate (η) which satisfies various integral constraints found in the continuous system. These constraints include the conservation of the vertically integrated momentum circulation and the conservation of total energy. However, in the model, we use a modified version of the scheme that only satisfies the constraints for the case of $\eta=z$.

This compromise was made in order to avoid a computational mode which appears in the σ-coordinate form of the equations with the former scheme.

The use of terrain-following coordinates in numerical models is known to be problematic when the slope of the coordinate surfaces is large (e.g., Mesinger and Janjic 1985). This is due to the horizontal pressure gradient force which, in this coordinate system, is the expressed as the difference between two terms [see equation (2.14)]. The magnitude of each of the terms can become many orders of magnitude larger than their difference – the horizontal pressure gradient force – which can result in large discretization errors in the motion field. This becomes more of an issue as the horizontal resolution of weather and climate forecasting models becomes finer and highly resolved topographical features lead to steeper coordinate sloping.

The use of height coordinates avoids the problem described above. Recent developments have been made for reconciling *z*-coordinate intersections with surface topography through the use of "shaved cells" (Adroft et al. 1997). The concept is shown in Figure 6.1a, which shows a vertical cross section in the vicinity of a narrow mountain. A regular grid is featured away from the lower boundary, while cells that intersect the surface are "shaved". Through a finite-volume formulation, the shaved cells are treated the same as the regular cells except that they have reduced volumes and a different cell wall geometry through which the fluxes pass. Such a method could be used in the hybrid coordinate framework with *z* coordinates serving as the Eulerian grid near the surface in place of the terrain-following coordinate. However, another possibility may be to retain the benefits of the σ coordinate in regions where the large-scale (~100 km) topography is gently sloping, and "shave" the σ-coordinate cells only where small-scale topography is

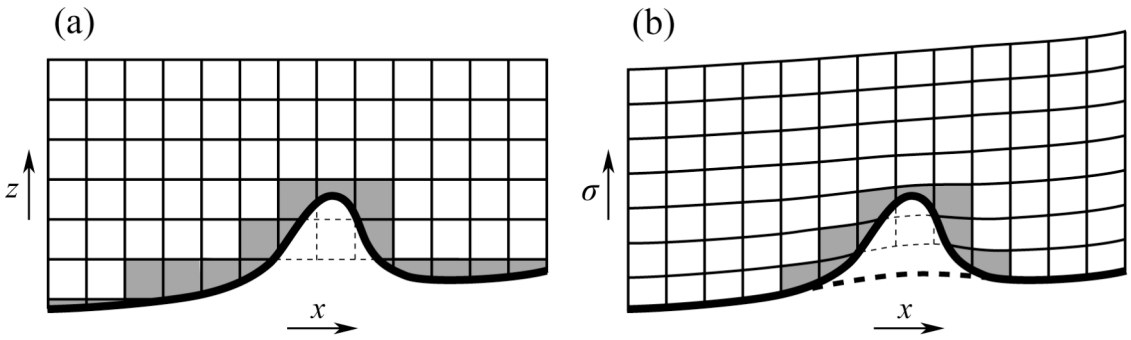


Figure 6.1: Shaved cells (shaded boxes) in (a) z coordinates and (b) a terrain-following σ coordinate based on a smoothed terrain profile (dashed bold line). Note that fewer cells are "shaved" with the σ coordinate.

encountered (for example, the buttes found occasionally in the Great Plains). Figure 6.1b illustrates how this might be done. In this configuration, fewer cells are "shaved" because the coordinate is terrain-following over the slowly varying topography.

In nonhydrostatic, compressible dynamical cores, vertically propagating acoustic waves are supported which are meteorologically insignificant. Because of the high speed at which these waves propagate and the high vertical resolution we use in the model, this limits the size of the time step we can take due to numerical instability. We currently use the explicit third-order Adams-Bashforth time-differencing scheme so these time steps are necessarily small and the acoustic waves are actually resolved. The relatively thin layers which develop in the θ coordinate limited our simulations to 2D for practical reasons. The model is capable of running in 3D, so a next step is to test the model in that capacity. (Three-dimensional test results of an early version of the σ-coordinate model are included in Appendix D.) For a 3D test of the hybrid-coordinate to be feasible, it will be necessary to run the model with longer time steps. Therefore, the next step in the model development will be to either implement a semi-implicit time differencing method

to stabilize the vertically propagating acoustic waves or to use an alternative system of equations (such as the anelastic system) which filters them or eliminates them all together.

The eventual goal is to build a cloud system resolving model based on the nonhydrostatic, hybrid-vertical-coordinate dynamical core we developed. Inclusion of moist processes is essential for producing realistic simulations of weather and climate. Clouds and precipitation have a profound impact on the energy budget of the atmosphere through radiative and latent heating effects. As we demonstrated, using the isentropic vertical coordinate increases the accuracy of vertical tracer transport. When moisture and cloud physics parameterizations are introduced in the model, we expect this strength to provide an advantage over conventional Eulerian-coordinate models in providing more accurate vertical cloud distributions.

Nonhydrostatic atmospheric models using potential temperature as the vertical coordinate have been successfully developed in the past decade. The present model further proves the feasibility of representing fine-scale motion in this coordinate framework. This scheme has distinct advantages, as illustrated, which are open to future development and application.

Appendix A SUPPLEMENTAL MODEL INFORMATION

A.1 Upstream-weighted vertical advection schemes for θ and ϕ

Recall from Chapter 4 that potential temperature and geopotential are advected in the model by portions of the total generalized vertical velocity using upstream-weighted schemes. These are based on the scheme of Takacs (1985) which is third-order accurate in space and time for uniform flow and grid spacing. In the present schemes, we prescribe upstream-weighted fluxes similar to those of Takacs. However, instead of a using a predictor-corrector sequence, we use Adams-Bashforth third-order accurate time-differencing. The following subsections describe the model's vertical advection schemes for θ and ϕ. Except where noted, we use the variables and notation defined in Chapter 3.

A.1.1 Vertical θ-advection scheme

Potential temperature is advected using an upstream-weighted scheme by the portion of the generalized vertical velocity given by $\dot{\eta}_{T,\sigma} + \dot{\eta}_S$ (see Table 4.1 and Section 4.3.2). (To simplify the notation in the following equations, we will use $\dot{\eta}$ to represent this portion.) In the scheme, the vertical advection term for θ is written

$$\left(\dot{\eta}\frac{\partial\theta}{\partial\eta}\right)_{k+1/2} = \theta_{k+1/2}\frac{\Pi_{k+1}\left(m\dot{\eta}\right)_{k+1} - \Pi_k\left(m\dot{\eta}\right)_k}{\left(m\Pi\delta\eta\right)_{k+1/2}} - \frac{\left(m\dot{\eta}\right)_{k+1}\left(\Pi\tilde{\theta}\right)_{k+1} - \left(m\dot{\eta}\right)_k\left(\Pi\tilde{\theta}\right)_k}{\left(m\Pi\delta\eta\right)_{k+1/2}} - \frac{1}{m_{k+1/2}}\frac{\left(G_{\theta\eta}\right)_{k+1} - \left(G_{\theta\eta}\right)_k}{\left(\delta\eta\right)_{k+1/2}} \tag{A.1}$$

$$\text{for} \quad k = 1, 2, \cdots, K-1,$$

$$\left(\dot{\eta}\frac{\partial\theta}{\partial\eta}\right)_{1/2} = \theta_{1/2}\frac{\Pi_1\left(m\dot{\eta}\right)_1}{\left(m\Pi\delta\eta\right)_{1/2}} - \frac{\left(m\dot{\eta}\right)_1\left(\Pi\tilde{\theta}\right)_1}{\left(m\Pi\delta\eta\right)_{1/2}} - \frac{1}{m_{1/2}}\frac{\left(G_{\theta\eta}\right)_1}{\left(\delta\eta\right)_{1/2}}, \tag{A.2}$$

and

$$\left(\dot{\eta}\frac{\partial\theta}{\partial\eta}\right)_{K+1/2} = -\theta_{K+1/2}\frac{\Pi_K\left(m\dot{\eta}\right)_K}{\left(m\Pi\delta\eta\right)_{K+1/2}} + \frac{\left(m\dot{\eta}\right)_K\left(\Pi\tilde{\theta}\right)_K}{\left(m\Pi\delta\eta\right)_{K+1/2}} + \frac{1}{m_{K+1/2}}\frac{\left(G_{\theta\eta}\right)_K}{\left(\delta\eta\right)_{K+1/2}}, \tag{A.3}$$

where

$$\left(G_{\theta\eta}\right)_k \equiv -\frac{1}{6}\left\{\left[\left(m\dot{\eta}\right)^+_k - \left(m\dot{\eta}\right)^-_k\right]\left(\theta_{k+1/2} - \theta_{k-1/2}\right) - \widehat{\left(m\dot{\eta}\right)}^+_k\left(\theta_{k-1/2} - \theta_{k-3/2}\right) + \widehat{\left(m\dot{\eta}\right)}^-_k\left(\theta_{k+3/2} - \theta_{k+1/2}\right)\right\} \tag{A.4}$$

$$\text{for} \quad k = 2, 3, \cdots, K-1,$$

$$\left(G_{\theta\eta}\right)_1 \equiv -\frac{1}{6}\left\{\widehat{\left(m\dot{\eta}\right)}^-_1\left(\theta_{5/2} - \theta_{3/2}\right) - \left(m\dot{\eta}\right)^-_1\left(\theta_{3/2} - \theta_{1/2}\right)\right\}, \tag{A.5}$$

and

$$\left(G_{\theta\eta}\right)_K \equiv -\frac{1}{6}\left\{\left(m\dot{\eta}\right)^+_K\left(\theta_{K+1/2} - \theta_{K-1/2}\right) - \widehat{\left(m\dot{\eta}\right)}^+_K\left(\theta_{K-1/2} - \theta_{K-3/2}\right)\right\}. \tag{A.6}$$

The vertical mass fluxes used in (A.4)-(A.6) are defined as

$$\left(m\dot{\eta}\right)^{+}_{k} \equiv \frac{\left(m\dot{\eta}\right)_k + \left|\left(m\dot{\eta}\right)_k\right|}{2}, \qquad \left(m\dot{\eta}\right)^{-}_{k} \equiv \frac{\left(m\dot{\eta}\right)_k - \left|\left(m\dot{\eta}\right)_k\right|}{2} \qquad \text{for} \quad k = 1, 2, \cdots, K, \tag{A.7}$$

$$\widehat{\left(m\dot{\eta}\right)}^{+}_{k} \equiv \sqrt{\left(m\dot{\eta}\right)^{+}_{k}\left(m\dot{\eta}\right)^{+}_{k-1}} \quad \text{for} \quad k = 2, 3, \cdots, K, \tag{A.8}$$

and

$$\widehat{\left(m\dot{\eta}\right)}^{-}_{k} \equiv -\sqrt{\left|\left(m\dot{\eta}\right)^{-}_{k}\right|\left|\left(m\dot{\eta}\right)^{-}_{k+1}\right|} \qquad \text{for} \quad k = 1, 2, \cdots, K-1. \tag{A.9}$$

The $G_{\theta\eta}$ terms in (A.1)-(A.3) are the upstream-weighted contributions to the potential temperature flux. Note that if these are assumed to be zero, the scheme reduces to the centered scheme in equations (3.116)-(3.118). Also, note that in an isentropic atmosphere where $\theta_{k+1/2}$ is a constant for all k, the contribution to the potential temperature tendency by the advection scheme is zero.

A.1.2 Vertical ϕ-advection scheme

Potential temperature is advected using the upstream-weighted scheme by the portion of the generalized vertical velocity given by $\dot{\eta}_{T,Q} + \dot{\eta}_{T,\theta}$ (see Table 4.1). (To simplify the notation in the following equations, we will use $\dot{\eta}$ to represent this portion.) In the scheme, the vertical advection term for ϕ is written

$$\left(\dot{\eta}\frac{\partial\phi}{\partial\eta}\right)_{k+1/2} = \frac{\phi_{k+1/2}}{m_{k+1/2}}\frac{\left(m\dot{\eta}\right)_{k+1} - \left(m\dot{\eta}\right)_k}{\left(\delta\eta\right)_{k+1/2}} - \frac{1}{m_{k+1/2}}\frac{\left(F_{\phi\eta}\right)_{k+1} - \left(F_{\phi\eta}\right)_k}{\left(\delta\eta\right)_{k+1/2}} \qquad \text{for} \quad k = 1, 2, \cdots, K-1, \tag{A.10}$$

where

$$\left(F_{\phi\eta}\right)_k \equiv \left(m\dot{\eta}\right)_k \tilde{\phi}_k + \left(G_{\phi\eta}\right)_k \qquad \text{for} \quad k = 1, 2, \cdots, K, \tag{A.11}$$

$$\left(G_{\phi\eta}\right)_k \equiv -\frac{1}{6}\left\{\begin{array}{l}\left[\left(m\dot{\eta}\right)^+_k - \left(m\dot{\eta}\right)^-_k\right]\left(\phi_{k+1/2} - \phi_{k-1/2}\right) - \\ \qquad \widehat{\left(m\dot{\eta}\right)}^+_k\left(\phi_{k-1/2} - \phi_{k-3/2}\right) + \widehat{\left(m\dot{\eta}\right)}^-_k\left(\phi_{k+3/2} - \phi_{k+1/2}\right)\end{array}\right\} \tag{A.12}$$

$$\text{for} \quad k = 2, 3, \cdots, K-1,$$

$$\left(G_{\phi\eta}\right)_1 \equiv -\frac{1}{6}\left\{\widehat{\left(m\dot{\eta}\right)}^-_1\left(\phi_{5/2} - \phi_{3/2}\right) - \left(m\dot{\eta}\right)^-_1\left(\phi_{3/2} - \phi_{1/2}\right)\right\}, \tag{A.13}$$

and

$$\left(G_{\phi\eta}\right)_K \equiv -\frac{1}{6}\left\{\left(m\dot{\eta}\right)^+_K\left(\phi_{K+1/2} - \phi_{K-1/2}\right) - \widehat{\left(m\dot{\eta}\right)}^+_K\left(\phi_{K-1/2} - \phi_{K-3/2}\right)\right\}. \tag{A.14}$$

A.2 Horizontal finite-difference schemes used in the model

A.2.1 The horizontal grid

The horizontal grid staggering is based on the Arakawa C-grid (Arakawa and Lamb 1977) shown in Figure A.1. Note that the thermodynamic variables and geopotential are horizontally colocated with the mass grid points. The variable q, used in the horizontal momentum advection scheme, is defined as $q \equiv (f+\zeta)/m$. In θ coordinates, this becomes Ertel's potential vorticity in the hydrostatic limit.

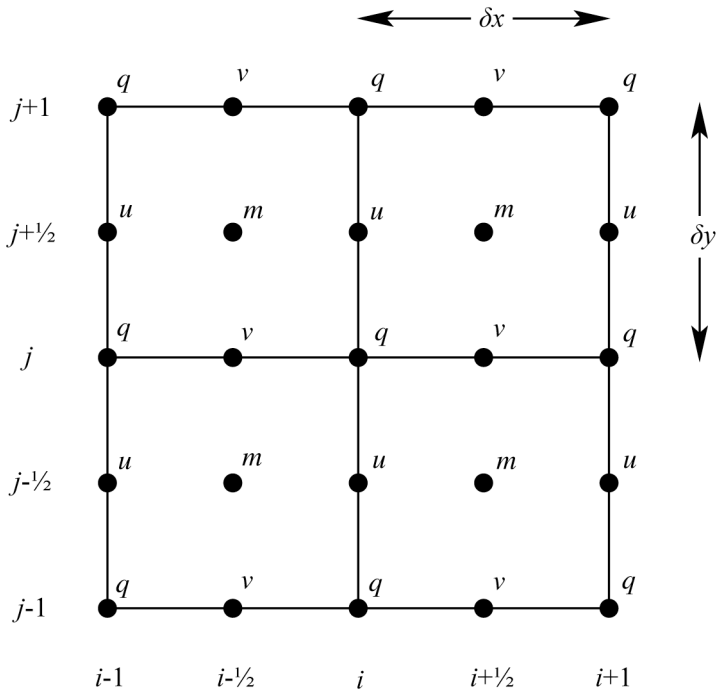


Figure A.1: The Arakawa C-grid used for the horizontal staggering.

A.2.2 Horizontal momentum advection

The horizontal momentum advection in the model is based on the scheme developed for the shallow water equations by Arakawa and Lamb (1981). In place of the shallow water depth h, we use the pseudo-density m.

A.2.3 Horizontal mass advection

We use an upstream-weighted scheme for the advection of pseudo-density in the continuity equation. The form of the fluxes are based on Takacs (1985). Here we present the x-component advective contribution to the mass tendency. The y-component

equations are similar, but are not shown for brevity. The *x*-component portion of the scheme is

$$\left[\frac{\partial}{\partial x}(mu)\right]_{i+1/2,k} = \frac{\left(F_x\right)_{i+1,k} - \left(F_x\right)_{i,k}}{\delta x}, \tag{A.15}$$

where the upstream-weighted mass fluxes are given by

$$\left(F_x\right)_{i,k} \equiv \left[u_i \frac{m_{i+1/2} + m_{i-1/2}}{2}\right]_k + \left(G_x\right)_{i,k}, \tag{A.16}$$

where

$$\left(G_x\right)_{i,k} \equiv -\frac{1}{6}\left[\begin{array}{l}\left(u^+{}_i - u^-{}_i\right)\left(m_{i+1/2} - m_{i-1/2}\right) \\ \qquad -\hat{u}_i^+\left(m_{i-1/2} - m_{i-3/2}\right) + \hat{u}_i^-\left(m_{i+3/2} - m_{i+1/2}\right)\end{array}\right]_k, \tag{A.17}$$

$$u^+{}_{i,k} \equiv \left(\frac{u_i + |u_i|}{2}\right)_k, \qquad u^-{}_{i,k} \equiv \left(\frac{u_i - |u_i|}{2}\right)_k, \tag{A.18}$$

and

$$\hat{u}^+_{i,k} \equiv \sqrt{\left(u^+{}_i u^+{}_{i-1}\right)_k}, \qquad \hat{u}^-_{i,k} \equiv -\sqrt{\left(\left|u^-{}_i\right|\left|u^-{}_{i+1}\right|\right)_k}\ . \tag{A.19}$$

A.2.4 Horizontal θ-advection

The horizontal θ-advection scheme is upstream-weighted. The form of the fluxes are based on Takacs (1985). Here we present the *x*-component advective contribution to the potential temperature tendency. The *y*-component equations are similar, but are not shown for brevity. The *x*-component portion of the scheme is

$$\left(u\frac{\partial\theta}{\partial x}\right)_{i+1/2,k+1/2}=\frac{\left[\left(F_{\Pi\theta x}\right)_{i+1}-\left(F_{\Pi\theta x}\right)_{i}\right]_{k+1/2}}{\left(m\Pi\delta\eta\right)_{i+1/2,k+1/2}\delta x}+\frac{\left[\left(G_{\theta x}\right)_{i+1}-\left(G_{\theta x}\right)_{i}\right]_{k+1/2}}{m_{i+1/2,k+1/2}\delta x}$$
$$-\frac{\theta_{i+1/2,k+1/2}}{\left(m\Pi\delta\eta\right)_{i+1/2,k+1/2}}\frac{\left[\left(F_{\Pi x}\right)_{i+1}-\left(F_{\Pi x}\right)_{i}\right]_{k+1/2}}{\delta x} \tag{A.20}$$

$$\text{for}\quad k=0,1,\cdots,K,$$

where

$$\left(F_{\Pi\theta x}\right)_{i,k+1/2}\equiv\frac{1}{2}\left\{\begin{array}{l}\left(F_x\right)_{i,k+1}\frac{1}{2}\left[\left(\Pi_{k+1}\theta_{k+1/2}\right)_{i+1/2}+\left(\Pi_{k+1}\theta_{k+1/2}\right)_{i-1/2}\right]\left(\delta\eta\right)_{k+1}+\\ \left(F_x\right)_{i,k}\frac{1}{2}\left[\left(\Pi_{k}\theta_{k+1/2}\right)_{i+1/2}+\left(\Pi_{k}\theta_{k+1/2}\right)_{i-1/2}\right]\left(\delta\eta\right)_{k}\end{array}\right\} \tag{A.21}$$

$$\text{for}\quad k=1,2,\cdots,K-1,$$

$$\left(F_{\Pi\theta x}\right)_{i,1/2}\equiv\frac{1}{2}\left\{\left(F_x\right)_{i,1}\frac{1}{2}\left[\left(\Pi_1\theta_{1/2}\right)_{i+1/2}+\left(\Pi_1\theta_{1/2}\right)_{i-1/2}\right]\left(\delta\eta\right)_1\right\}, \tag{A.22}$$

$$\left(F_{\Pi\theta x}\right)_{i,K+1/2}\equiv\frac{1}{2}\left\{\left(F_x\right)_{i,K}\frac{1}{2}\left[\left(\Pi_K\theta_{K+1/2}\right)_{i+1/2}+\left(\Pi_K\theta_{K+1/2}\right)_{i-1/2}\right]\left(\delta\eta\right)_K\right\}, \tag{A.23}$$

$$\left(G_{\theta x}\right)_{i,k+1/2}\equiv-\frac{1}{6}\left[\begin{array}{l}\left(F_x^{+}-F_x^{-}\right)_i\left(\theta_{i+1/2}-\theta_{i-1/2}\right)-\\ \left(\hat{F}_x^{+}\right)_i\left(\theta_{i-1/2}-\theta_{i-3/2}\right)+\left(\hat{F}_x^{-}\right)_i\left(\theta_{i+3/2}-\theta_{i+1/2}\right)\end{array}\right]_{k+1/2} \tag{A.24}$$

$$\text{for}\quad k=0,1,\cdots,K,$$

$$\left(F_{\Pi x}\right)_{i,k+1/2}\equiv\frac{1}{2}\left\{\left[\left(F_x\right)_i\frac{1}{2}\left(\Pi_{i+1/2}+\Pi_{i-1/2}\right)\left(\delta\eta\right)\right]_{k+1}+\left[\left(F_x\right)_i\frac{1}{2}\left(\Pi_{i+1/2}+\Pi_{i-1/2}\right)\left(\delta\eta\right)\right]_{k}\right\} \tag{A.25}$$

$$\text{for}\quad k=1,2,\cdots,K-1,$$

$$\left(F_{\Pi x}\right)_{i,1/2} \equiv \frac{1}{2}\left[\left(F_x\right)_i \frac{1}{2}\left(\Pi_{i+1/2}+\Pi_{i-1/2}\right)\left(\delta\eta\right)\right]_1, \tag{A.26}$$

$$\left(F_{\Pi x}\right)_{i,K+1/2} \equiv \frac{1}{2}\left[\left(F_x\right)_i \frac{1}{2}\left(\Pi_{i+1/2}+\Pi_{i-1/2}\right)\left(\delta\eta\right)\right]_K, \tag{A.27}$$

$$\left(F_x^+\right)_{i,k+1/2} = \frac{\left(F_x\right)_{i,k+1/2} + \left|\left(F_x\right)_{i,k+1/2}\right|}{2}, \quad \left(F_x^-\right)_{i,k+1/2} = \frac{\left(F_x\right)_{i,k+1/2} - \left|\left(F_x\right)_{i,k+1/2}\right|}{2} \tag{A.28}$$

$$\text{for} \quad k = 0, 1, \cdots, K,$$

and

$$\left(\hat{F}_x^+\right)_{i,k+1/2} \equiv \sqrt{\left[\left(F_x^+\right)_i \left(F_x^+\right)_{i-1}\right]_{k+1/2}}, \quad \left(\hat{F}_x^-\right)_{i,k+1/2} \equiv \sqrt{\left[\left|\left(F_x^-\right)_i\right|\left|\left(F_x^-\right)_{i+1}\right|\right]_{k+1/2}} \tag{A.29}$$

$$\text{for} \quad k = 0, 1, \cdots, K.$$

Note that when $\theta_{k+1/2}$ is constant on model surfaces, the right-hand side of (A.20) is zero and the potential temperature tendency by the advection scheme is zero.

A.2.5 Horizontal ϕ-advection

The upstream-weighted *x*-component horizontal geopotential advection scheme is given by

$$\left(u\frac{\partial\phi}{\partial x}\right)_{i+1/2,k+1/2} = \frac{\left[\left(F_{\phi x}\right)_{i+1} - \left(F_{\phi x}\right)_i\right]_{k+1/2}}{m_{i+1/2,k+1/2}\delta x} - \frac{\phi_{i+1/2,k+1/2}}{m_{i+1/2,k+1/2}} \frac{\left[\left(F_x\right)_{i+1} - \left(F_x\right)_i\right]_{k+1/2}}{\delta x} \tag{A.30}$$

$$\text{for} \quad k = 1, 2, \cdots, K-1,$$

where

$$\left(F_{\phi x}\right)_{i,k+1/2} \equiv \left(F_x\right)_{i,k+1/2} \frac{1}{2}\left(\phi_{i+1/2}+\phi_{i-1/2}\right)_{k+1/2} + \left(G_{\phi x}\right)_{i,k+1/2}, \tag{A.31}$$

and

$$\left(G_{\phi x}\right)_{i,k+1/2} \equiv -\frac{1}{6}\left[\begin{array}{l}\left(F_x^{+}-F_x^{-}\right)_i\left(\phi_{i+1/2}-\phi_{i-1/2}\right)- \\ \left(\hat{F}_x^{+}\right)_i\left(\phi_{i-1/2}-\phi_{i-3/2}\right)+\left(\hat{F}_x^{-}\right)_i\left(\phi_{i+3/2}-\phi_{i+1/2}\right)\end{array}\right]_{k+1/2} . \quad \text{(A.32)}$$

A.2.6 Time discretization

In the model, the third-order Adams-Bashforth time-differencing scheme is used (Durran 1991).

A.2.7 Subgrid-scale turbulence parameterization

A subgrid-scale mixing parameterization is applied to the three components of velocity as well as the potential temperature. The scheme we use follows that used in the University of Oklahoma's Advanced Research Prediction System (ARPS) (documentation at http://www.caps.ou.edu/ARPS/download/code/pub/ARPS.docs/ARPS4DOC.PDF/arpsch6.pdf). We use the modified Smagorinsky first-order closure scheme (Smagorinsky 1963) which includes Richardson number dependency.

A.2.8 Surface pressure diagnosis

The Exner function at the lower boundary appears in the horizontal pressure gradient force terms of the bottom-layer horizontal velocity tendency equations, as well as the tendency equation for the vertical velocity at the surface. Since the surface vertical velocity w is not predicted, but is diagnosed from the lower boundary condition, this latter tendency equation serves in diagnosing the surface Exner function, from which the surface pressure can be calculated. However, this must be in agreement with the

horizontal momentum tendencies through the boundary condition. Since the horizontal pressure gradient force term at each horizontal momentum grid point involves the Exner function at multiple grid points, an iterative procedure is required for its solution.

Combining equations (3.36) and (3.107), the vertical velocity tendency at the lower boundary can be written

$$\frac{\partial w_{i+1/2,j+1/2,1/2}}{\partial t} = -g\theta_{i+1/2,j+1/2,1/2}\frac{\Pi_{i+1/2,j+1/2,1} - \hat{\Pi}_{i+1/2,j+1/2,1/2}}{\tilde{\phi}_{i+1/2,j+1/2,1} - \phi_{i+1/2,j+1/2,S}} - g + \left(F_z - \mathbf{v}\cdot\nabla w - \dot{\eta}\frac{\partial w}{\partial \eta} \right)_{i+1/2,j+1/2,1/2}. \tag{A.33}$$

The vertical and horizontal velocity tendency equations are related through the lower boundary condition (3.38). We can write the horizontally discrete form of this equation as

$$\frac{\partial w_{i+1/2,j+1/2,1/2}}{\partial t} = \frac{1}{2}\left\{ \frac{\partial u_{i+1,1}}{\partial t}\frac{\left(z_S\right)_{i+3/2} - \left(z_S\right)_{i+1/2}}{\delta x} + \frac{\partial u_{i,1}}{\partial t}\frac{\left(z_S\right)_{i+1/2} - \left(z_S\right)_{i-1/2}}{\delta x} \right\}_{j+1/2} + \frac{1}{2}\left\{ \frac{\partial v_{j+1,1}}{\partial t}\frac{\left(z_S\right)_{j+3/2} - \left(z_S\right)_{j+1/2}}{\delta y} + \frac{\partial v_{j,1}}{\partial t}\frac{\left(z_S\right)_{j+1/2} - \left(z_S\right)_{j-1/2}}{\delta y} \right\}_{i+1/2}. \tag{A.34}$$

The tendency equations for the horizontal velocity components at the lowest layer are written from the combination of (3.35), (3.109) and (3.111) as

$$\frac{\partial u_{i,j+1/2,1}}{\partial t} = -\bar{\bar{\tilde{\theta}}}^{i}_{i,j+1/2,1}\left(\frac{\partial \Pi}{\partial x}\right)_{i,j+1/2,1} + \frac{1}{2}\left[\theta_{3/2}\frac{\Pi_2 - \Pi_1}{\tilde{\phi}_2 - \tilde{\phi}_1}\left(\frac{\partial \phi}{\partial x}\right)_{3/2} \right]_{i,j+1/2} + \frac{1}{2}\left[\frac{1}{2}\left(\theta_{1/2}\frac{\Pi_1 - \hat{\Pi}_{1/2}}{\tilde{\phi}_1 - \phi_S} \right)_{i+1/2} + \frac{1}{2}\left(\theta_{1/2}\frac{\Pi_1 - \hat{\Pi}_{1/2}}{\tilde{\phi}_1 - \phi_S} \right)_{i-1/2} \right]_{j+1/2}\left(\frac{\partial \phi_S}{\partial x}\right)_{i,j+1/2} + \left(F_x + fv - \mathbf{v}\cdot\nabla u - \dot{\eta}\frac{\partial u}{\partial \eta} \right)_{i,j+1/2,1}, \tag{A.35}$$

and

$$\frac{\partial v_{i+1/2,j,1}}{\partial t} = -\bar{\bar{\theta}}^{j}_{i+1/2,j,1}\left(\frac{\partial \Pi}{\partial y}\right)_{i+1/2,j,1} + \frac{1}{2}\left[\theta_{3/2}\frac{\Pi_2 - \Pi_1}{\tilde{\phi}_2 - \tilde{\phi}_1}\left(\frac{\partial \phi}{\partial y}\right)_{3/2}\right]_{i+1/2,j}$$
$$+\frac{1}{2}\left[\frac{1}{2}\left(\theta_{1/2}\frac{\Pi_1 - \hat{\Pi}_{1/2}}{\tilde{\phi}_1 - \phi_S}\right)_{j+1/2} + \frac{1}{2}\left(\theta_{1/2}\frac{\Pi_1 - \hat{\Pi}_{1/2}}{\tilde{\phi}_1 - \phi_S}\right)_{j-1/2}\right]_{i+1/2}\left(\frac{\partial \phi_S}{\partial y}\right)_{i+1/2,j} \quad \text{(A.36)}$$
$$+\left(F_y - fu - \mathbf{v}\cdot\nabla v - \dot{\eta}\frac{\partial v}{\partial \eta}\right)_{i+1/2,j,1}.$$

When (A.33)-(A.36) are combined, and the velocity tendencies eliminated, the result is a linear system of equations. The only unknowns at a given time step in the system are the surface Exner functions $\hat{\Pi}_{i+1/2,j+1/2,1/2}$. In the model, their solution is found by using the Gauss-Seidel iteration method. The surface pressure is then calculated at all grid points from the relation

$$p_{i+1/2,j+1/2,S} = p_0\left(\frac{\hat{\Pi}_{i+1/2,j+1/2,1/2}}{c_p}\right)^{1/\kappa}. \quad \text{(A.37)}$$

Appendix B EFFECT OF THE FORM OF THE DISCRETE PRESSURE GRADIENT FORCES ON ACCURACY AND SATISFACTION OF THE INTEGRAL CONSTRAINTS: "*p*- vs. Π-FORM"

B.1 Introduction

In this appendix, we compare alternative discrete forms of the horizontal and vertical pressure gradient force terms of the horizontal and vertical momentum equations, respectively. Recall that these terms can involve the gradient of pressure itself [the "*p*-form", as in equations (2.14) and (2.18)] or the gradient of the Exner function defined in equation (2.7) [the "Π-form", as in equations (2.29) and (2.30)]. In Chapter 3, we contrasted the two forms in the vertically discrete system of equations. Here, we will include an analysis of the *horizontally* discrete forms of the horizontal pressure gradient force (HPGF) in terms of accuracy and the satisfaction of the integral constraints. We also mentioned in Chapter 3 that the use of the Exner function in the vertical pressure gradient force (VPGF) leads to improved accuracy in the vertical discrete normal mode frequencies as found in Thuburn (2006) and Toy and Randall (2007). We will present a possible explanation for this by demonstrating, via a Taylor series analysis, that the truncation error of the VPGF (and additionally the HPGF) is smaller with the use of the Exner function.

In the design of vertical discretization schemes, the vertically-discrete equations are typically continuous in the horizontal spatial and time dimensions (e.g., Arakawa and Suarez 1983). Keeping the continuous forms of the terms in the dimensions not being analyzed simplifies the analysis because they are easier to manipulate than in the discrete forms. In our analysis of the horizontal discretization of the HPGF, we will consider the system of vertically continuous, horizontally discrete equations. The design of horizontal discretization schemes for atmospheric models are often based on the shallow water system of equations (e.g., Arakawa and Lamb 1981). On the other hand, Bleck (1978b, 1979) analyzed conservation properties in the vertically and horizontally discretize primitive equations. We speculate that performing integral constraint analysis in each dimension separately is sufficient to determine whether the constraints are met in the fully discrete system. This simplifies the analysis by taking advantage of the ease of manipulating continuous terms.

First, we require that the finite-difference system of equations are convergent, i.e., they converge to the continuous form when Δx, Δy, $\Delta \eta$, and Δt go to zero. We also require that as the resolution becomes infinite in a given dimension, the result represents the continuous form of the equations in that dimension. For example, in the finite-difference equations used in the model, it can be shown that as Δx, Δy, and Δt go to zero, this results in the vertically discrete system of equations in Chapter 3. One of the characteristics of the finite-differencing operator δ that makes this possible is that, given a function $\phi(x,y)$, the finite-difference analogs of second order (or more) partial derivatives of this function are the same, regardless of the order in which they are taken. That is, the difference operators should commute as in the continuous relation

$$\frac{\partial^2 \phi}{\partial x \partial y} = \frac{\partial}{\partial y}\left(\frac{\partial \phi}{\partial x}\right) = \frac{\partial}{\partial x}\left(\frac{\partial \phi}{\partial y}\right). \tag{B.1}$$

In Section B.2 we show that in the horizontally continuous, vertically discrete form of the primitive equations, the simultaneous satisfaction of Constraints I, II and III (potential temperature conservation) cannot be achieved with either form of the HPGF. There is a trade-off between Constraints I and II if Constraint III is satisfied – the "*p*-form" of the HPGF satisfies Constraint I but not II, while the "Π-form" satisfies Constraint II but not I.

In Section B.3 we show that using the "Π-form" of the hydrostatic relation, as well as the "Π-form" of the HPGF, results in reduced truncation error. Also, while Constraint I is not strictly met by the "Π-form", it leads to reduced artificial generation of vertically integrated momentum circulation due to topography

B.2 Integral constraints in the vertically continuous, horizontally discrete quasi-static (primitive) equations in the generalized vertical coordinate

The following analysis is performed in one horizontal direction without loss of generality. The domain is periodic and the staggering corresponds to the one-dimensional version of the Arakawa "C" grid (Arakawa and Lamb 1977), as shown in Figure B.1.

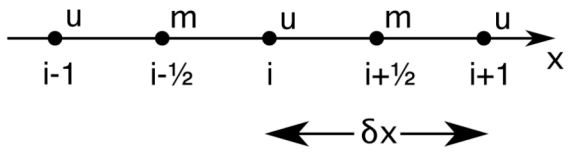


Figure B.1: Horizontal staggering of the variables corresponding to the 1D equivalent of the Arakawa "C" grid. The "*m*" points are mass points and are colocated with the variables ϕ, θ, T, Π, and $\dot{\eta}$.

B.2.1 Energy conversion term of the thermodynamic energy equation

To determine if the horizontally discrete forms of the HPGF are consistent with total energy conservation we "reverse engineer" the system of horizontally discrete equations by separately deriving the energy conversion term from both the thermodynamic energy equation and the kinetic energy generation by the HPGF. Then we check if the two results are equivalent. If they are, then total energy is conserved; otherwise, it is not. We start by deriving the energy conversion term given by the thermodynamic equation. Since this term is independent of the HPGF, it will apply to both of the discretized forms of the HPGF when testing for total energy conservation. Note that we assume adiabatic conditions.

Discretize equation (2.39) as

$$\left[\left(m\alpha\omega\right)_{\substack{\text{thermodynamic}\\ \text{energy}\\ \text{conversion}}}\right]_{i+1/2} = \frac{\partial}{\partial t}\left(mc_pT\right)_{i+1/2} + \left\{\frac{1}{\delta x}\delta_i\left[u\left(\bar{m}^i c_p \bar{T}^i\right)\right]\right\}_{i+1/2} + \frac{\partial}{\partial \eta}\left(m\dot{\eta}c_pT\right)_{i+1/2}, \tag{B.2}$$

where the differencing operator is defined as

$$\left[\delta_i(\ )\right]_i \equiv (\ )_{i+1/2} - (\ )_{i-1/2}, \quad \left[\delta_i(\ )\right]_{i+1/2} \equiv (\ )_{i+1} - (\ )_i, \tag{B.3}$$

and the overbar $\overline{(\ )}^{i}$ represents the arithmetic average of neighboring points. Use $T_{i+1/2} = (\theta\Pi)_{i+1/2} \big/ c_p$ and sum (B.2) over the horizontal domain to get

$$\begin{aligned} \sum_{m \text{ points}} \left(m\alpha\omega\right)_{\substack{\text{thermodynamic}\\ \text{energy}\\ \text{conversion}}} = & \sum_{m \text{ points}} \frac{\partial}{\partial t}\left(m\theta\Pi\right)_{i+1/2} \\ & + \sum_{m \text{ points}} \left\{\frac{1}{\delta x}\delta_i\left[u\left(\bar{m}^i\overline{\theta\Pi}^i\right)\right]\right\}_{i+1/2} \\ & + \sum_{m \text{ points}} \frac{\partial}{\partial \eta}\left(m\dot{\eta}\theta\Pi\right)_{i+1/2}. \end{aligned} \tag{B.4}$$

Since the second term on the right-hand side (r.h.s.) of (B.4) sums to zero, we are free to rewrite it as

$$\begin{aligned} 0 &= \sum_{m \text{ points}} \left\{\frac{1}{\delta x}\delta_i\left[u\left(\bar{m}^i\overline{\theta\Pi}^i\right)\right]\right\}_{i+1/2} \\ &= \sum_{m \text{ points}} \left(\Pi\left\{\frac{1}{\delta x}\delta_i\left[u\left(\bar{m}^i\bar{\theta}^i\right)\right]\right\}\right)_{i+1/2} + \sum_{u \text{ points}} \left\{\frac{1}{\delta x}\left[u\left(\bar{m}^i\bar{\theta}^i\right)\right]\delta_i\Pi\right\}_i, \end{aligned} \tag{B.5}$$

where the sums are over all the *u* and *m* (i.e., mass) points at a given level on the grid, and we have used the following relation for any two variables *a* and *b* defined at staggered points on the grid:

$$\sum_{a \text{ points}} a_{i+1/2}\left(b_{i+1} - b_i\right) + \sum_{b \text{ points}} b_i\left(a_{i+1/2} - a_{i-1/2}\right) = 0. \tag{B.6}$$

The discretized flux-form potential temperature tendency equation is

$$\frac{\partial}{\partial t}\left(m\theta\right)_{i+1/2} + \left\{\frac{1}{\delta x}\delta_i\left[u\left(\bar{m}^i\bar{\theta}^i\right)\right]\right\}_{i+1/2} + \frac{\partial}{\partial \eta}\left(m\dot{\eta}\theta\right)_{i+1/2} = 0. \tag{B.7}$$

Note that this form conserves global mass-weighted θ due to its flux form. Finally, we can combine (B.7) with (B.4) and (B.5), then use the relations $\partial\Pi/\partial t = (\partial\Pi/\partial p)(\partial p/\partial t)$, $\partial\Pi/\partial\eta = (\partial\Pi/\partial p)(\partial p/\partial\eta)$, and $\theta(\partial\Pi/\partial p) = \alpha$ to obtain

$$\sum_{m \text{ points}} \left(m\alpha\omega\right)_{\substack{\text{thermodynamic}\\ \text{energy}\\ \text{conversion}}} = \sum_{m \text{ points}} \left(m\alpha \frac{\partial p}{\partial t} \right)_{i+1/2} + \sum_{u \text{ points}} \left\{ \frac{1}{\delta x} \left[u\left(\bar{m}^i \bar{\theta}^i \right) \right] \delta_i \Pi \right\}_i + \sum_{m \text{ points}} \left(m\alpha\dot{\eta} \frac{\partial p}{\partial \eta} \right)_{i+1/2}. \tag{B.8}$$

This is the horizontal sum, at a given level, of the energy conversion term as given by the discrete thermodynamic energy equation. In the following subsections we derive the corresponding expression from the kinetic energy generation by the HPGF.

B.2.2 The "p-form" of the HPGF

First we consider the horizontally discrete form of equation (2.23), given by

$$\left[\text{HPGF}_{p\text{-form}} \right]_i = -\frac{1}{\bar{m}_i^i g} \frac{1}{\delta x} \left[\delta_i \left(p \frac{\partial \phi}{\partial \eta} \right) \right]_i + \frac{1}{\bar{m}_i^i g} \frac{\partial}{\partial \eta} \left[\bar{p}^i \frac{1}{\delta x} \left(\delta_i \phi \right) \right]_i . \tag{B.9}$$

To show that $\text{HPGF}_{p\text{-form}}$ maintains Constraint I, multiply (B.9) by $\bar{m}_i^i d\eta$, and integrate from the surface to the top of the atmosphere to get

$$\int_{\eta_S}^{\eta_T} \left[\bar{m}^i \left(\text{HPGF}_{p\text{-form}} \right) \right]_i d\eta = -\frac{1}{g} \int_{\eta_S}^{\eta_T} \frac{1}{\delta x} \left[\delta_i \left(p \frac{\partial \phi}{\partial \eta} \right) \right]_i d\eta + \frac{1}{g} \int_{\eta_S}^{\eta_T} \frac{\partial}{\partial \eta} \left[\bar{p}^i \frac{1}{\delta x} \left(\delta_i \phi \right) \right]_i d\eta. \tag{B.10}$$

When equation (B.10) is summed around the domain, the first term on the right-hand side sums to zero. Therefore, only the last term, known as the "mountain torque" term, can contribute to the circulation induced by the HPGF. When ϕ_S = constant for all *i*, the term vanishes. *Therefore Constraint I is satisfied.*

Now we determine the kinetic energy generation by the "*p*-form" HPGF discretization. Multiply (B.9) by $(\overline{m}^i u)_i$, and sum over the horizontal domain:

$$\sum_{u \text{ points}} \left[(\overline{m}^i u) \text{HPGF}_{p\text{-form}} \right]_i = - \sum_{u \text{ points}} \frac{u_i}{g} \frac{1}{\delta x} \left[\delta_i \left(p \frac{\partial \phi}{\partial \eta} \right) \right]_i + \sum_{u \text{ points}} \frac{u_i}{g} \frac{\partial}{\partial \eta} \left[\overline{p}^i \frac{1}{\delta x} \left(\delta_i \phi \right) \right]_i . \tag{B.11}$$

Note the following identity, which is the discrete analog of the product rule for differentiation (and is made possible through the use of arithmetic averaging):

$$\left[\delta_i \left(ab \right) \right]_i = \left[\overline{a}^i \delta_i b \right]_i + \left[\overline{b}^i \delta_i a \right]_i , \tag{B.12}$$

where *a* and *b* are arbitrary variables defined at mass points. Applying (B.12) to the first term on the r.h.s. of (B.11) and expanding the derivative in the second term on the r.h.s. of (B.11), we can write

$$\sum_{u \text{ points}} \left[(\overline{m}^i u) \text{HPGF}_{p\text{-form}} \right]_i = - \sum_{u \text{ points}} \frac{u_i}{g} \overline{\left(\frac{\partial \phi}{\partial \eta} \right)}^i_i \frac{1}{\delta x} \left(\delta_i p \right)_i + \sum_{u \text{ points}} \frac{u_i}{g} \overline{\left(\frac{\partial p}{\partial \eta} \right)}^i_i \frac{1}{\delta x} \left(\delta_i \phi \right)_i . \tag{B.13}$$

Next, define the discrete analog of the energy conserving terms $m\alpha\omega$ and mgw as

$$\sum_{m \text{ points}} \left(m\alpha\omega \right)_{\substack{\text{kinetic energy} \\ \text{conversion}}} \equiv \sum_{m \text{ points}} \left(m\alpha \frac{\partial p}{\partial t} \right)_{i+1/2} + \sum_{u \text{ points}} \frac{u_i}{g} \overline{\left(\frac{\partial \phi}{\partial \eta} \right)}^i_i \frac{1}{\delta x} \left(\delta_i p \right)_i + \sum_{m \text{ points}} \left(m\alpha\dot{\eta} \frac{\partial p}{\partial \eta} \right)_{i+1/2} , \tag{B.14}$$

and

$$\sum_{m \text{ points}} \left(mgw\right)_{i+1/2} \equiv -\sum_{m \text{ points}} \left(\frac{1}{g}\frac{\partial p}{\partial \eta}\frac{\partial \phi}{\partial t}\right)_{i+1/2} - \sum_{u \text{ points}} \frac{u_i}{g}\overline{\left(\frac{\partial p}{\partial \eta}\right)}^{i}_{i} \frac{1}{\delta x}\left(\delta_i \phi\right)_i - \sum_{m \text{ points}} \left(\frac{1}{g}\frac{\partial p}{\partial \eta}\dot{\eta}\frac{\partial \phi}{\partial \eta}\right)_{i+1/2}, \tag{B.15}$$

where we have used the hydrostatic relation $\partial p/\partial \eta = -mg$. Using equations (B.14) and (B.15) in (B.13), and using the relation $m\alpha = (1/g)(\partial \phi/\partial \eta)$, then upon rearranging terms, we arrive at the following discrete analog of equation (2.35):

$$\sum_{u \text{ points}} \left[(\bar{m}^i u)\text{HPGF}_{p\text{-form}}\right]_i = - \sum_{m \text{ points}} \left(m\alpha\omega\right)_{\substack{\text{kinetic energy} \\ \text{conversion}}} - \sum_{m \text{ points}} \left(mgw\right)_{i+1/2} + \sum_{m \text{ points}} \frac{\partial}{\partial t}\left(\frac{p}{g}\frac{\partial \phi}{\partial \eta}\right)_{i+1/2} - \sum_{m \text{ points}} \frac{\partial}{\partial \eta}\left(\frac{p}{g}\frac{\partial \phi}{\partial t}\right)_{i+1/2}. \tag{B.16}$$

This is the work done by the pressure gradient force. Therefore, the mechanical energy has a form consistent with the continuous equations. Now we check the consistency of the energy conversion terms between the form derived from the mechanical energy equation, given by equation (B.14), and the form derived from the thermodynamic energy equation, i.e., equation (B.8). These equations differ from each other in the horizontal difference terms. *Therefore, the use of the "p-form" of the HPGF does not lead to energy conservation.* Examining the horizontal difference term in equation (B.8) we see that it involves the difference of the Exner function, and not pressure. This is an indication that the energy conversion term derived from the mechanical energy equation should also be in terms of the difference in Exner function. This suggests that the "Π-form" of the HPGF may lead to a consistent energy conversion term.

B.2.3 The "Π-form" of the HPGF

We write the discretized form of equation (2.30) as

$$\left[\text{HPGF}_{\Pi\text{-form}}\right]_i = -\frac{1}{\delta x}\left(\delta_i \phi\right)_i - \bar{\theta}^i_i \frac{1}{\delta x}\left(\delta_i \Pi\right)_i . \tag{B.17}$$

Using this form of the HPGF leads to total energy conservation, which can be shown by multiplying (B.17) by $(\bar{m}^i u)_i$ and summing over the horizontal domain, which gives the work done by the HPGF as

$$\begin{aligned}\sum_{u \text{ points}} \left[(\bar{m}^i u)\text{HPGF}_{\Pi\text{-form}}\right]_i = \\ -\sum_{u \text{ points}}\left[\left(\bar{m}^i u\right)\frac{1}{\delta x}\left(\delta_i \phi\right)\right]_i - \sum_{u \text{ points}}\left[\left(\bar{m}^i u\right)\bar{\theta}^i \frac{1}{\delta x}\left(\delta_i \Pi\right)\right]_i .\end{aligned} \tag{B.18}$$

Now, using (B.15), and adding and subtracting the terms $\sum m\theta\,\partial\Pi/\partial t$ and $\sum m\theta\dot{\eta}\,\partial\Pi/\partial\eta$, then rearranging, equation (B.18) becomes

$$\begin{aligned}\sum_{u \text{ points}} \left[(\bar{m}^i u)\text{HPGF}_{\Pi\text{-form}}\right]_i = \\ -\left(\begin{array}{l}\displaystyle\sum_{m \text{ points}}\left(m\alpha\frac{\partial p}{\partial t}\right)_{i+1/2} + \sum_{u \text{ points}}\left\{\frac{1}{\delta x}\left[u\left(\bar{m}^i\bar{\theta}^i\right)\right]\delta_i\Pi\right\}_i \\ \qquad\qquad + \displaystyle\sum_{m \text{ points}}\left(m\alpha\dot{\eta}\frac{\partial p}{\partial \eta}\right)_{i+1/2}\end{array}\right) \\ -\sum_{m \text{ points}}\left(mgw\right)_{i+1/2} + \sum_{m \text{ points}}\frac{\partial}{\partial t}\left(\frac{p}{g}\frac{\partial\phi}{\partial\eta}\right)_{i+1/2} - \sum_{m \text{ points}}\frac{\partial}{\partial\eta}\left(\frac{p}{g}\frac{\partial\phi}{\partial t}\right)_{i+1/2} .\end{aligned} \tag{B.19}$$

Comparing equations (B.19) and (2.35) we see that the first term on the r.h.s. of (B.19) is the discrete analog of the energy conversion term, which we rewrite as

$$\begin{aligned}\sum_{m \text{ points}}\left(m\alpha\omega\right)_{\substack{\text{kinetic energy}\\ \text{conversion}}} = \\ \sum_{m \text{ points}}\left(m\alpha\frac{\partial p}{\partial t}\right)_{i+1/2} + \sum_{u \text{ points}}\left\{\frac{1}{\delta x}\left[u\left(\bar{m}^i\bar{\theta}^i\right)\right]\delta_i\Pi\right\}_i + \sum_{m \text{ points}}\left(m\alpha\dot{\eta}\frac{\partial p}{\partial\eta}\right)_{i+1/2} .\end{aligned} \tag{B.20}$$

This form of the energy conversion term is identical to the form given by the thermodynamic energy equation as in equation (B.8). *Therefore, the "Π-form" of the HPGF leads to total energy conservation (Constraint II).*

However, the "Π-form" of the HPGF does not maintain Constraint I. This can be shown by multiplying (B.17) by $\bar{m}_i^i d\eta$ and using the relation $m = -(1/g)(\partial p/\partial \eta)$ to get

$$\left[\bar{m}^i\left(\mathrm{HPGF}_{\Pi\text{-form}}\right)\right]_i d\eta = \frac{1}{g}\overline{\left(\frac{\partial p}{\partial \eta}\right)}_i^i \frac{1}{\delta x}\left(\delta_i \phi\right)_i d\eta + \frac{1}{g}\overline{\left(\frac{\partial p}{\partial \eta}\right)}_i^i \bar{\theta}_i^i \frac{1}{\delta x}\left(\delta_i \Pi\right)_i d\eta. \quad \text{(B.21)}$$

Using equation (B.12), we can rewrite (B.21) as

$$\begin{aligned}\left[\bar{m}^i\left(\mathrm{HPGF}_{\Pi\text{-form}}\right)\right]_i d\eta = {} & \frac{1}{g}\frac{1}{\delta x}\left[\delta_i\left(\frac{\partial p}{\partial \eta}\phi\right)\right]_i d\eta \\ & -\frac{1}{g}\bar{\phi}_i^i \frac{1}{\delta x}\left[\delta_i\left(\frac{\partial p}{\partial \eta}\right)\right]_i d\eta + \frac{1}{g}\overline{\left(\frac{\partial p}{\partial \eta}\right)}_i \bar{\theta}_i^i \frac{1}{\delta x}\left(\delta_i \Pi\right)_i d\eta.\end{aligned} \quad \text{(B.22)}$$

Finally, after rearranging, integrating through the depth of the atmosphere, and applying equation (B.10), we have

$$\begin{aligned}\int_{\eta_S}^{\eta_T}\left[\bar{m}^i\left(\mathrm{HPGF}_{\Pi\text{-form}}\right)\right]_i d\eta = {} & \\ & \int_{\eta_S}^{\eta_T}\left[\bar{m}^i\left(\mathrm{HPGF}_{p\text{-form}}\right)\right]_i d\eta + \\ & \frac{1}{g}\int_{\eta_S}^{\eta_T}\left\{\overline{\left(\frac{\partial p}{\partial \eta}\right)}_i^i \frac{1}{\delta x}\left(\delta_i \Pi\right)_i - \overline{\left(\frac{1}{\rho}\frac{\partial p}{\partial \eta}\right)}_i^i \frac{1}{\delta x}\left(\delta_i p\right)_i\right\} d\eta.\end{aligned} \quad \text{(B.23)}$$

In the previous subsection, we showed [equation (B.10)] that the first term on the r.h.s. of (B.23) vanishes when it is summed around the domain. However, the second term on the r.h.s. does not vanish. It is a residual term. *Therefore, the "Π-form" of the HPGF does not maintain Constraint I.* (Note, however, that if the pressure is constant along the

contour of topography, then the "Π-form" of the HPGF generates no artificial acceleration of vertically integrated circulation, as the r.h.s. of (B.23) is zero in that case.)

B.2.4 Discussion

We showed that in the vertically continuous, horizontally discrete system of quasi-static equations, the choice of the horizontally discrete form of the horizontal pressure gradient force determines the satisfaction of Constraints I and II – the "*p*-form" maintains the "mountain torque" Constraint I, but not the total energy conservation Constraint II; the "Π-form" satisfies Constraint II, but not Constraint I. Bleck (1978b) came to a similar conclusion. In both cases, the global conservation of potential temperature (Constraint III) is satisfied.

We conjecture that in order to satisfy the constraints in the same manner as above in the vertically *and* horizontally discrete system of equations, the vertical discretization must independently (i.e., as analyzed in the horizontally continuous, vertically discrete system of equations) satisfy Constraints I, II and III, as we discussed in the introduction of this appendix.

B.3 Comparison of the truncation error between the "*p*-" and "Π-forms" of the HPGF and VPGF

B.3.1 A closer look at Constraint I (the "mountain torque" constraint)

The statement of integral Constraint I on the HPGF is traditionally formulated to prevent the artificial "spin-up" or "spin-down" of the vertically integrated atmosphere

about a contour of topography, in which $\nabla z_S = 0$ [e.g., Arakawa and Lamb 1977]. An additional requirement of the HPGF along these lines can be stated. Consider a hydrostatic atmosphere in which pressure is a function only of height, i.e., $p = p(z)$. In this case, the HPGF in the continuous system is identically zero. It follows that the surface pressure p_S is a function only of the surface height z_S. For such an atmosphere, the line integral of the "mountain torque" term, given by the r.h.s. of equation (2.24), is

$$-\oint p_S(z_S)\nabla z_S \cdot \mathbf{dl} = 0\,, \tag{B.24}$$

where **dl** is the differential length vector tangent to the path of integration. Therefore, for such an atmosphere, the HPGF should generate no acceleration of circulation about *any* closed path, even if it does not follow a contour of topography. This can be thought of as a more stringent constraint on the HPGF which we refer to as Constraint I+. It can be shown that neither the "*p*-form" nor the "Π-form" of the HPGF satisfies this constraint. However, in the following analysis, we show that the numerically induced (artificial) acceleration of circulation about an arbitrary closed path is smaller with the "Π-form" of the HPGF than with the "*p*-form". We do this by analyzing the truncation error of the discretized form of the equations based on a prescribed atmosphere.

B.3.2 Analysis of HPGF truncation error

Consider a hydrostatically balanced, horizontally homogenous atmosphere with a temperature profile specified by

$$T(z) = T_0 - \Gamma z\,, \tag{B.25}$$

where T_0 is a reference temperature (15 °C) and Γ is a constant lapse rate. The pressure profile can be derived as

$$\left.\begin{aligned} p(z) &= p_0\left(1-\frac{\Gamma}{T_0}z\right)^{\frac{g}{\Gamma R}} \qquad \text{for} \quad \Gamma \neq 0 \\ p(z) &= p_0 e^{-\frac{g}{RT_0}z} \qquad\qquad \text{for} \quad \Gamma = 0 \end{aligned}\right\}, \tag{B.26}$$

where p_0 is a reference pressure (1000 mb).

Now, consider the vertically continuous, horizontally discrete system of equations. Multiply the mass by the "*p*-form" of the HPGF, given by (B.9), to obtain

$$\left[\overline{m}^i\left(\text{HPGF}_{p\text{-form}}\right)\right]_i = -\frac{1}{g}\frac{1}{\delta x}\left[\delta_i\left(p\frac{\partial\phi}{\partial\eta}\right)\right]_i + \frac{1}{g}\frac{\partial}{\partial\eta}\left[\overline{p}^i\frac{1}{\delta x}\left(\delta_i\phi\right)\right]_i. \tag{B.27}$$

Using a Taylor series expansion, we can write the horizontal finite-difference operations that appear in (B.27) as

$$\left(\overline{p}^i\right)_i \equiv \frac{1}{2}\left(p_{i+1/2}+p_{i-1/2}\right) = p_i + \frac{1}{8}\left(\frac{\partial^2 p}{\partial x^2}\right)_i\left(\delta x\right)^2 + \text{H.O.T.}, \tag{B.28}$$

$$\left(\delta_i\phi\right)_i \equiv \phi_{i+1/2}-\phi_{i-1/2} = \left(\frac{\partial\phi}{\partial x}\right)_i\left(\delta x\right) + \frac{1}{24}\left(\frac{\partial^3\phi}{\partial x^3}\right)_i\left(\delta x\right)^3 + \text{H.O.T.}, \tag{B.29}$$

and

$$\begin{aligned} \left[\delta_i\left(p\frac{\partial\phi}{\partial\eta}\right)\right]_i &\equiv \left(p\frac{\partial\phi}{\partial\eta}\right)_{i+1/2} - \left(p\frac{\partial\phi}{\partial\eta}\right)_{i-1/2} \\ &= \frac{\partial}{\partial x}\left(p\frac{\partial\phi}{\partial\eta}\right)_i\left(\delta x\right) + \frac{1}{24}\frac{\partial^3}{\partial x^3}\left(p\frac{\partial\phi}{\partial\eta}\right)_i\left(\delta x\right)^3 + \text{H.O.T.}, \end{aligned} \tag{B.30}$$

where "H.O.T." refers to "higher-order terms". Using (B.28)-(B.30) in (B.27), we obtain

$$\left[\bar{m}^i\left(\text{HPGF}_{p\text{-form}}\right)\right]_i = -\frac{1}{g}\frac{\partial}{\partial x}\left(p\frac{\partial\phi}{\partial\eta}\right)_i + \frac{1}{g}\frac{\partial}{\partial\eta}\left(p\frac{\partial\phi}{\partial x}\right)_i$$
$$-\frac{1}{24}\frac{1}{g}\left\{\frac{\partial^3}{\partial x^3}\left(p\frac{\partial\phi}{\partial\eta}\right)_i - \frac{\partial}{\partial\eta}\left(p\frac{\partial^3\phi}{\partial x^3}\right)_i - 3\frac{\partial}{\partial\eta}\left[\left(\frac{\partial^2 p}{\partial x^2}\right)_i\left(\frac{\partial\phi}{\partial x}\right)_i\right]\right\}\left(\delta x\right)^2 + \text{H.O.T.} \tag{B.31}$$

The first two terms on the r.h.s. of (B.31) represent the continuous solution at the grid point *i*. Therefore, the remaining terms on the r.h.s. represent the truncation error, written as

$$\left(\varepsilon_{p\text{-form}}\right)_i \cong$$
$$-\frac{1}{24}\frac{1}{g}\left\{\frac{\partial^3}{\partial x^3}\left(p\frac{\partial\phi}{\partial\eta}\right)_i - \frac{\partial}{\partial\eta}\left(p\frac{\partial^3\phi}{\partial x^3}\right)_i - 3\frac{\partial}{\partial\eta}\left[\left(\frac{\partial^2 p}{\partial x^2}\right)_i\left(\frac{\partial\phi}{\partial x}\right)_i\right]\right\}\left(\delta x\right)^2, \tag{B.32}$$

where we have neglected the higher-order terms. Note that the error is 2nd-order in δx.

Now, perform a similar analysis for the "Π-form" HPGF. From (B.17), can write

$$\left[\bar{m}^i\left(\text{HPGF}_{\Pi\text{-form}}\right)\right]_i = -\frac{\bar{m}_i^i}{\delta x}\left(\delta_i\phi\right)_i - \bar{\theta}_i^i\frac{\bar{m}_i^i}{\delta x}\left(\delta_i\Pi\right)_i. \tag{B.33}$$

Again, using a Taylor series expansion, we obtain

$$\bar{\theta}_i^i \equiv \frac{1}{2}\left(\theta_{i+1/2} + \theta_{i-1/2}\right) = \theta_i + \frac{1}{8}\left(\frac{\partial^2\theta}{\partial x^2}\right)_i\left(\delta x\right)^2 + \text{H.O.T.}, \tag{B.34}$$

$$\bar{m}_i^i \equiv \frac{1}{2}\left(m_{i+1/2} + m_{i-1/2}\right) = m_i + \frac{1}{8}\left(\frac{\partial^2 m}{\partial x^2}\right)_i\left(\delta x\right)^2 + \text{H.O.T.}, \tag{B.35}$$

and

$$\left(\delta_i\Pi\right)_i \equiv \Pi_{i+1/2} - \Pi_{i-1/2} = \left(\frac{\partial\Pi}{\partial x}\right)_i\left(\delta x\right) + \frac{1}{24}\left(\frac{\partial^3\Pi}{\partial x^3}\right)_i\left(\delta x\right)^3 + \text{H.O.T.} \tag{B.36}$$

Using (B.34)-(B.36) in (B.33), we get

$$\left[\overline{m}^{i}\left(\mathrm{HPGF}_{\Pi\text{-form}}\right)\right]_i = -m_i\left(\frac{\partial\phi}{\partial x}\right)_i - m_i\theta_i\left(\frac{\partial\Pi}{\partial x}\right)_i$$
$$-\frac{1}{24}\left\{\begin{array}{l} m_i\left(\frac{\partial^3\phi}{\partial x^3}\right)_i + 3\left(\frac{\partial^2 m}{\partial x^2}\right)_i\left(\frac{\partial\phi}{\partial x}\right)_i + 3m_i\left(\frac{\partial^2\theta}{\partial x^2}\right)_i\left(\frac{\partial\Pi}{\partial x}\right)_i \\ +3\theta_i\left(\frac{\partial^2 m}{\partial x^2}\right)_i\left(\frac{\partial\Pi}{\partial x}\right)_i + m_i\theta_i\left(\frac{\partial^3\Pi}{\partial x^3}\right)_i \end{array}\right\}(\delta x)^2 \qquad \text{(B.37)}$$
$$+\text{H.O.T.}$$

Here, we identify the truncation error as

$$\left(\varepsilon_{\Pi\text{-form}}\right)_i \cong -\frac{1}{24}\left\{\begin{array}{l} m_i\left(\frac{\partial^3\phi}{\partial x^3}\right)_i + 3\left(\frac{\partial^2 m}{\partial x^2}\right)_i\left(\frac{\partial\phi}{\partial x}\right)_i + 3m_i\left(\frac{\partial^2\theta}{\partial x^2}\right)_i\left(\frac{\partial\Pi}{\partial x}\right)_i \\ +3\theta_i\left(\frac{\partial^2 m}{\partial x^2}\right)_i\left(\frac{\partial\Pi}{\partial x}\right)_i + m_i\theta_i\left(\frac{\partial^3\Pi}{\partial x^3}\right)_i \end{array}\right\}(\delta x)^2. \qquad \text{(B.38)}$$

Given the temperature profile above, we can obtain analytical values of the truncation errors given by (B.32) and (B.38). First we choose a mountain profile given by

$$z_S(x) = \frac{h}{2}\left\{1-\cos\left[2\pi\left(\frac{x}{x_m}\right)^{\beta}\right]\right\}, \qquad \text{(B.39)}$$

where h is the mountain top height (5 km), β is a "skewness" factor (β=1.5) (the mountain is symmetrical with β=0), and x_m is the mountain "width" (10 km). Figure B.2 shows the mountain profile with a periodic domain, δx=500 m, and 20 grid points. We want to compare the domain-integrated (i.e., vertically integrated, horizontally summed) values of the truncation error, which are a measure of the artificial acceleration of the circulation. We set the domain top to be at 16 km. Figure B.3 shows that the domain integrated truncation error is smaller with the "Π-form" of the HPGF than with the

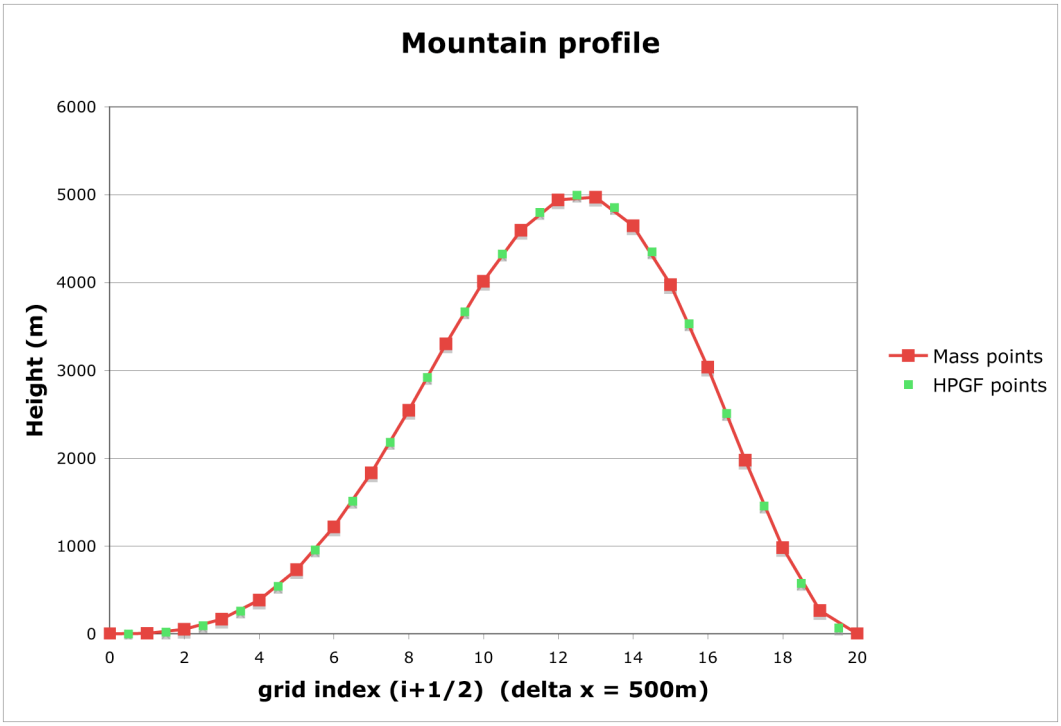


Figure B.2: Mountain profile. Periodic horizontal domain with 20 grid points.

"*p*-form" for various values of the lapse rate Γ. Figure B.4 shows that the truncation error of *m* times the HPGF itself is smaller with the "Π-form" of the HPGF as well. That is, the "Π-form" of the HPGF is more accurate. This may be due to the fact that the Exner function field is a mathematically smoother field than the pressure field, in general. Typically, numerical approximations of such fields are more accurate.

B.3.3 Analysis of the truncation error of the VPGF

We can perform an analysis of the vertical pressure gradient force similar to the one above for the HPGF. Now, consider a vertically discrete grid with indices *k* for layer centers and half-integers for layer edges where the VPGF resides. We write the "*p*-form" of the VPGF as

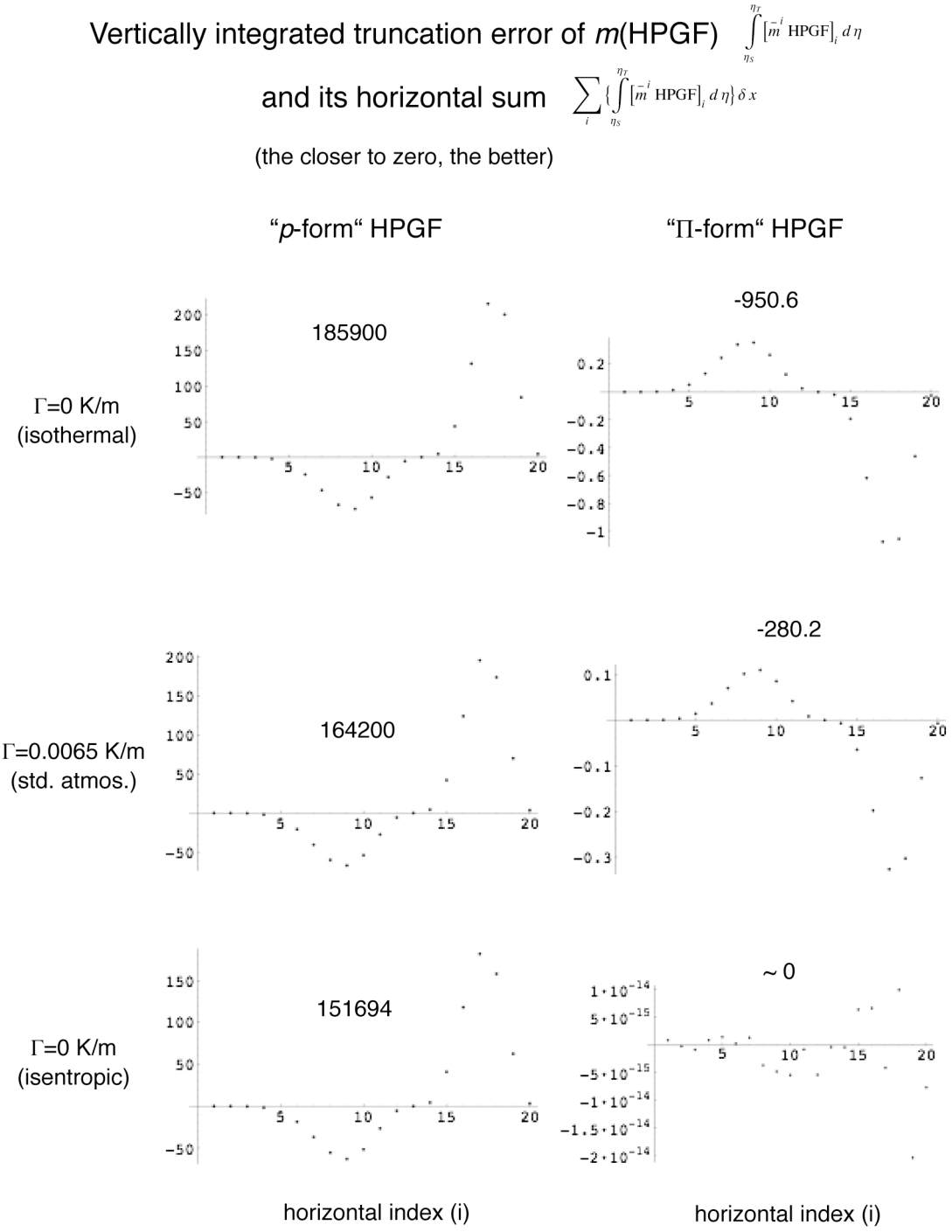


Figure B.3: Horizontal profiles of the vertically integrated truncation error of the mass-weighted HPGF ($\mathrm{N\,m^{-2}}$) (dots). Domain "integrated" truncation error ($\mathrm{kg\,s^{-2}}$) (numbers). Left-hand column: "*p*-form" HPGF; right-hand column: "Π-form" HPGF. Rows represent results for various atmospheric lapse rates.

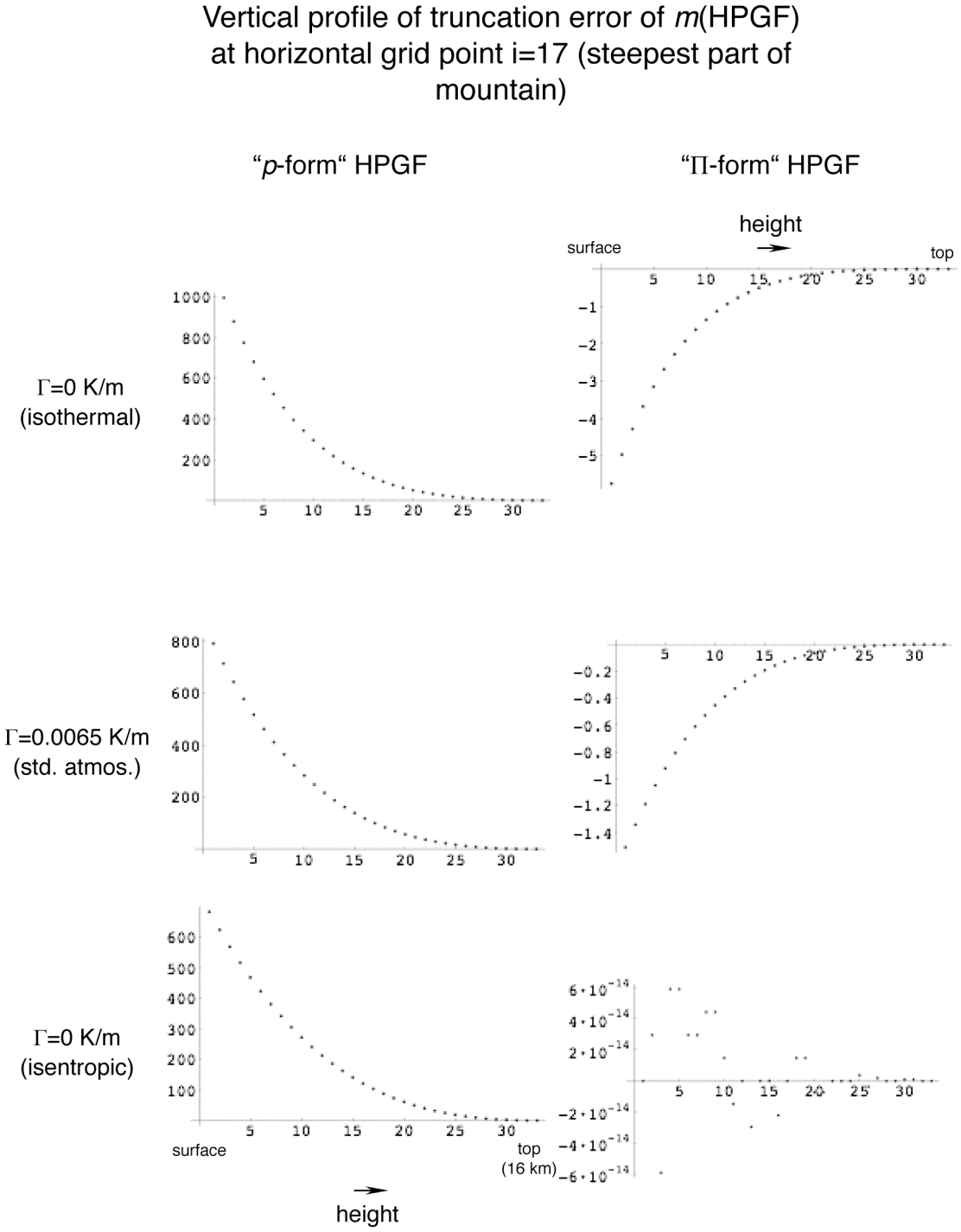


Figure B.4: Vertical profiles of the truncation error of the mass-weighted HPGF at the horizontal grid point $i=17$. ($\mathrm{N\,m^{-2}}$) (dots). Left-hand column: "*p*-form" HPGF; right-hand column: "Π-form" HPGF. Rows represent results for various atmospheric lapse rates.

$$\left(\mathrm{VPGF}_{p\text{-form}}\right)_{k+1/2} = -\frac{1}{\frac{1}{2}\left(\rho_{k+1}+\rho_k\right)}\frac{p_{k+1}-p_k}{\delta z} \tag{B.40}$$

where δz (500 m) is the layer thickness, which is assumed constant. Taylor series expansions gives

$$p_{k+1}-p_k = \left(\frac{dp}{dz}\right)_{k+1/2} + \frac{1}{24}\left(\frac{d^3p}{dz^3}\right)_{k+1/2}\left(\delta z\right)^2 + \text{H.O.T.}, \tag{B.41}$$

and

$$\frac{1}{2}\left(\rho_{k+1}+\rho_k\right) = \rho_{k+1/2} + \frac{1}{8}\left(\frac{dp}{dz}\right)_{k+1/2}\left(\delta z\right)^2 + \text{H.O.T.} \tag{B.42}$$

Using (B.41) and (B.42) in (B.40), we obtain

$$\begin{aligned}\left(\mathrm{VPGF}_{p\text{-form}}\right)_{k+1/2} = & \\ & -\frac{1}{\rho_{k+1/2}}\left(\frac{dp}{dz}\right)_{k+1/2} \\ & -\frac{1}{24}\frac{1}{\rho_{k+1/2}}\left[\left(\frac{d^3p}{dz^3}\right)_{k+1/2} - \frac{3}{\rho_{k+1/2}}\left(\frac{dp}{dz}\right)_{k+1/2}\left(\frac{d^2\rho}{dz^2}\right)_{k+1/2}\right]\left(\delta z\right)^2 \\ & +\text{H.O.T.}\end{aligned} \tag{B.43}$$

The truncation error can be identified as

$$\left(\varepsilon_{p\text{-form}}\right)_{k+1/2} \cong -\frac{1}{24}\frac{1}{\rho_{k+1/2}}\left[\left(\frac{d^3p}{dz^3}\right)_{k+1/2} - \frac{3}{\rho_{k+1/2}}\left(\frac{dp}{dz}\right)_{k+1/2}\left(\frac{d^2\rho}{dz^2}\right)_{k+1/2}\right]\left(\delta z\right)^2. \tag{B.44}$$

For the "Π-form" of the VPGF, we write

$$\left(\mathrm{VPGF}_{\Pi\text{-form}}\right)_{k+1/2} = -\theta_{k+1/2}\frac{\Pi_{k+1}-\Pi_k}{\delta z}. \tag{B.45}$$

Again, from the Taylor series, we have

$$\Pi_{k+1} - \Pi_k = \left(\frac{d\Pi}{dz}\right)_{k+1/2} + \frac{1}{24}\left(\frac{d^3\Pi}{dz^3}\right)_{k+1/2}\left(\delta z\right)^2 + \text{H.O.T.} \tag{B.46}$$

Using (B.46) in (B.45), we have

$$\left(\text{VPGF}_{\Pi\text{-form}}\right)_{k+1/2} = -\theta_{k+1/2}\left(\frac{d\Pi}{dz}\right)_{k+1/2} - \frac{1}{24}\theta_{k+1/2}\left(\frac{d^3\Pi}{dz^3}\right)_{k+1/2}\left(\delta z\right)^2 + \text{H.O.T.} \tag{B.47}$$

The truncation error is

$$\left(\varepsilon_{\Pi\text{-form}}\right)_{k+1/2} \cong -\frac{1}{24}\theta_{k+1/2}\left(\frac{d^3\Pi}{dz^3}\right)_{k+1/2}\left(\delta z\right)^2. \tag{B.48}$$

Using the same atmospheric profile as in the HPGF analysis, we can analytically calculate the vertical profile of the truncation errors given by (B.44) and (B.48). These are shown in Figure B.5 for various values of the lapse rate Γ. The results show that the "Π-form" of the VPGF has a smaller truncation error than the "*p*-form". Note that the vertical grid we used has 32 layers and a top height of 16 km.

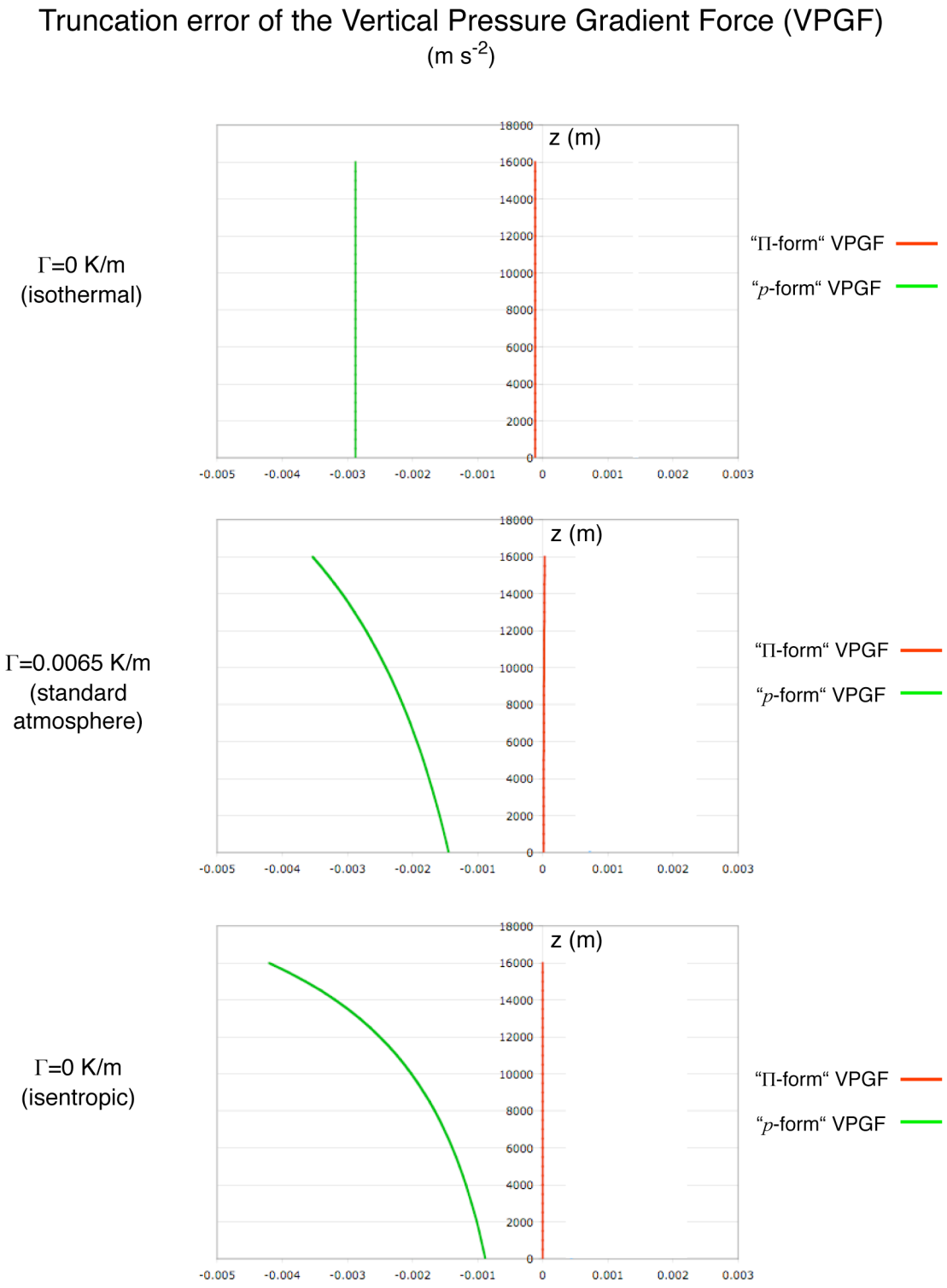


Figure B.5: Vertical profiles of the truncation error of the vertical pressure gradient force. Red curves are for the "Π-form" VPGF, green curves are for the "Π-form" VPGF. Results for various atmospheric lapse rates are shown.

Appendix C LINEAR WAVE EQUATIONS

Here we discuss the analytical solutions to the linear mountain wave experiments presented in Section 5.2. The analysis is based on the linearized, nonhydrostatic, compressible Euler equations of motion. Details of the solution method can be found in Eliassen and Kleinschmidt (1957), Eckart (1960) and, more recently, Thuburn and Woollings (2005). We will not present the complete derivation here, but instead will highlight the important steps required to obtain the analytical solutions.

The basic state is assumed to be hydrostatic, isothermal, and at rest. We can then write the linearized, z-coordinate system of 2D equations in terms of four prognostic variables as

⟨Horizontal momentum⟩

$$\frac{\partial u'}{\partial t} = -\frac{1}{\overline{\rho}}\frac{\partial p'}{\partial x}, \tag{C.1}$$

⟨Vertical momentum⟩

$$\frac{\partial w'}{\partial t} = -\frac{1}{\overline{\rho}}\left(\frac{\partial p'}{\partial z} + g\rho'\right), \tag{C.2}$$

⟨Mass continuity⟩

$$\frac{\partial \rho'}{\partial t} + \overline{\rho}\left(\frac{\partial u'}{\partial x} + \frac{\partial w'}{\partial z}\right) + \frac{d\overline{\rho}}{dz}w' = 0, \tag{C.3}$$

〈Thermodynamic equation〉

$$\frac{1}{c_S^{\,2}}\left(\frac{\partial p'}{\partial t}+\frac{d\overline{p}}{dz}w'\right)=\frac{\partial \rho'}{\partial t}+\frac{d\overline{\rho}}{dz}w', \tag{C.4}$$

where c_S is the speed of sound, and we have neglected the Coriolis terms.

Transform the dependent variables as follows:

$$u'=\frac{u''}{\sqrt{\overline{\rho}}}, \qquad w'=\frac{w''}{\sqrt{\overline{\rho}}}, \qquad \rho'=\sqrt{\overline{\rho}}\,\rho'', \qquad p'=\sqrt{\overline{\rho}}\,p''. \tag{C.5}$$

Using (C.5) in (C.1)-(C.4), the system becomes

$$\frac{\partial u''}{\partial t}=-\frac{\partial p''}{\partial x}, \tag{C.6}$$

$$\frac{\partial w''}{\partial t}=-\frac{\partial p''}{\partial z}-g\rho''+\frac{1}{2}\frac{\gamma g}{c_S^{\,2}}p'', \tag{C.7}$$

$$\frac{\partial \rho''}{\partial t}+\frac{\partial u''}{\partial x}-\frac{1}{2}\frac{\gamma g}{c_S^{\,2}}w''+\frac{\partial w''}{\partial z}=0, \tag{C.8}$$

and

$$\frac{1}{c_S^{\,2}}\frac{\partial p''}{\partial t}+\left(\gamma-1\right)\frac{g}{c_S^{\,2}}w''=\frac{\partial \rho''}{\partial t}, \tag{C.9}$$

where $\gamma=c_p/c_v$. The result of this transformation is that the system expressed by (C.6)-(C.9) has constant coefficients, which simplifies the solution procedure.

Consider wavelike solutions of the form

$$\begin{bmatrix} u''(x,z,t) \\ w''(x,z,t) \\ \rho''(x,z,t) \\ p''(x,z,t) \end{bmatrix}=\begin{bmatrix} U(z) \\ W(z) \\ R(z) \\ P(z) \end{bmatrix}e^{i(kx-\omega t)}, \tag{C.10}$$

where $U(z)$, $W(z)$, $R(z)$, and $P(z)$ are the vertical profiles of the dependent variables, k is the horizontal wave number, and ω is the frequency. Applying (C.10) in (C.6)-(C.9), we obtain

$$\omega U = kP, \tag{C.11}$$

$$-i\omega W = -\frac{dP}{dz} - gR + \frac{1}{2}\frac{\gamma g}{c_S^{\,2}}P, \tag{C.12}$$

$$-i\omega R + ikU - \frac{1}{2}\frac{\gamma g}{c_S^{\,2}}W + \frac{\partial W}{\partial z} = 0, \tag{C.13}$$

and

$$-i\frac{\omega}{c_S^{\,2}}P + (\gamma - 1)\frac{g}{c_S^{\,2}}W = -i\omega R. \tag{C.14}$$

These are the vertical structure equations. Equations (C.11)-(C.14) can be reduced to an equation for W, which is

$$\frac{d^2W}{dz^2} + \left\{(\gamma - 1)\frac{g^2}{c_S^{\,2}}\frac{k^2}{\omega^2} - \frac{1}{4}\frac{\gamma^2 g^2}{c_S^{\,4}} + \frac{\omega^2}{c_S^{\,2}} - k^2\right\}W = 0. \tag{C.15}$$

This is a wave equation which leads to the dispersion relation

$$m^2 = N^2\frac{k^2}{\omega^2} - \frac{1}{4}\frac{g^2}{R^2\bar{T}^2} + \frac{\omega^2}{c_S^{\,2}} - k^2, \tag{C.16}$$

where m is the vertical wave number, and we used the expression for the square of the buoyancy frequency for an isothermal atmosphere given by $N^2=(\gamma-1)\ g^2/\ c_S^{\,2}$. Assuming the same wavelike behavior in the remaining dependent variables, equations (C.11)-(C.14) provides their phase relationship and, therefore, the wave structure used in the analytical solutions of Section 5.2.

For flow of uniform velocity $\bar{u}$ over a mountain of wave number *k*, the frequency is given by

$$\omega = \bar{u}k\,. \tag{C.17}$$

Using this in (C.16), the dispersion relation becomes equation (5.4), i.e.,

$$m^2 = l^2 - k^2\left(1 - \frac{\bar{u}^2}{c_S{}^2}\right), \tag{C.18}$$

where *l* is the Scorer parameter given by

$$l^2 = \frac{N^2}{\bar{u}^2} - \frac{1}{4}\frac{g^2}{R^2\bar{T}^2}\,. \tag{C.19}$$

Note that through (C.10) and the vertical wave structure of the solutions, the dispersion relation (C.18) also results from

$$\left(1 - \frac{\bar{u}^2}{c_S{}^2}\right)\frac{\partial^2 w''}{\partial x^2} + \frac{\partial^2 w''}{\partial z^2} + l^2 w'' = 0\,, \tag{C.20}$$

which is the structure equation for the transformed vertical velocity used in Section 5.2.

Appendix D 3D EXPERIMENTS WITH AN EARLY VERSION OF THE σ-COORDINATE MODEL

In the initial phase of developing the hybrid-vertical-coordinate model, we built a nonhydrostatic model based on the σ coordinate. The model was a test bed for the advection schemes and for the CP-grid variable staggering. It used the "Π-form" of the vertical pressure gradient force term [see equation (3.106)], and the vertical differencing scheme was designed to conserve the global mass-weighted potential temperature. In this appendix we present results of two 3D experiments that we performed with the model.

D.1 Rising thermal experiment

This experiment was designed to simulate a rising thermal in a sheared, neutrally buoyant layer which is topped by a stable, isothermal layer. The neutrally buoyant layer extends from the surface to a height of 10 km and has a constant potential temperature of 300 K. The temperature is constant from the 10 km to the 20 km height. The horizontal domain is 10 km in extent (in both *x*- and *y*-directions) with periodic boundary conditions. The zonal velocity profile is shown in Figure D.1. The shear is constant up to the 10 km height, above which the flow is uniform. The thermal is initialized as a sphere with perturbation potential temperature given by

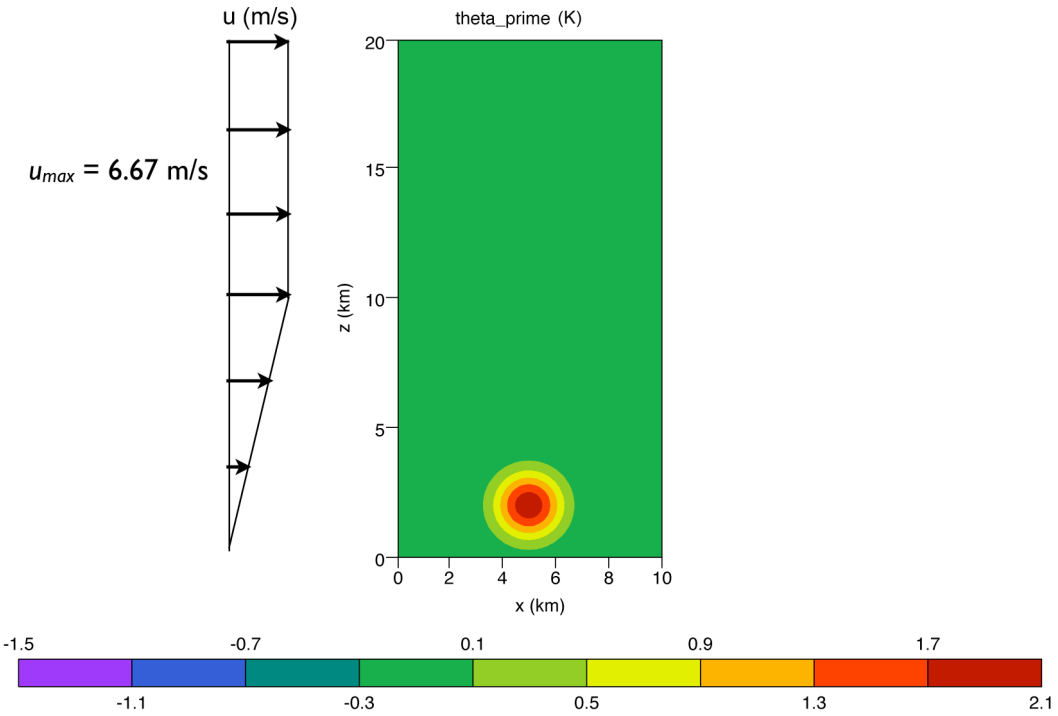


Figure D.1: Initial perturbation potential temperature field (K) and vertical profile of zonal wind (m s^{-1}) for 3D rising thermal experiment (slice through center of *y*-domain is shown).

$$\theta' = 2\cos^2\left(\frac{\pi L}{2}\right), \tag{D.1}$$

where θ' is in Kelvin and

$$L = \sqrt{\left(\frac{x - x_c}{x_r}\right)^2 + \left(\frac{y - y_c}{y_r}\right)^2 + \left(\frac{z - z_c}{z_r}\right)^2}, \tag{D.2}$$

$x_c = y_c = 5$ km, $z_c = 2$ km, and $x_r = y_r = z_r = 2$ km. Figure D.1 shows the initial condition of the thermal in an *x*-*z* plane located at the center of the thermal. The model is configured with 100 x 100 grid points in the horizontal with $\Delta x = \Delta y = 100$ m. There are 200 levels with $\Delta z = 100$ m.

Figure D.2 shows the perturbation potential temperature of an x-z slice through the center of the y-domain at simulation time $t = 14$ minutes. At this time the warm bubble has almost reached the layer interface at the 10 km height. The effects of the shear deformation on the thermal can be seen. Also, rising and sinking motion, induced by the rising thermal, is evident in the isothermal layer just above the 10 km height.

Close-up views of the thermal at $t = 14$ minutes are shown in Figure D.3. The plots show perturbation potential temperature with velocity vectors superimposed. Figure D.3a is an x-z slice through the center of the y-domain. The updraft can be seen throughout the core of the thermal, as well as the circulation at the edges associated with the vorticity ring. Figure D.3b is a horizontal slice through the thermal at $z = 6.67$ km. The effect on the mean flow field can be seen in the plot. The bubble acts as an obstacle,

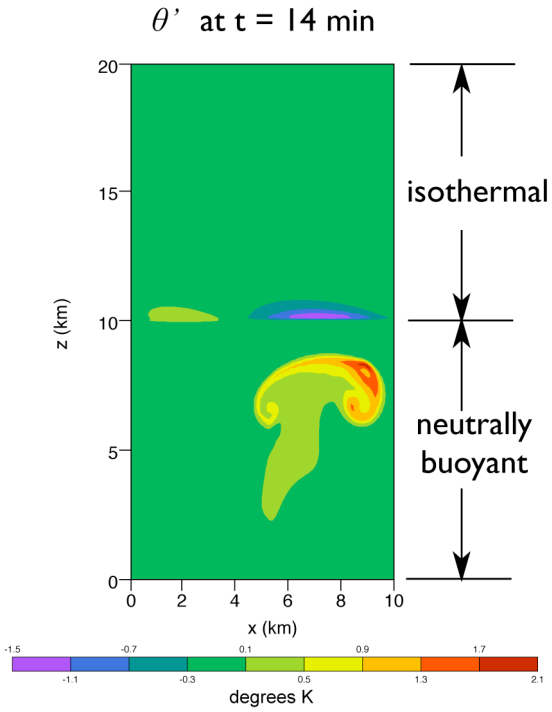


Figure D.2: Perturbation potential temperature field (K) at simulation time $t = 14$ minutes.

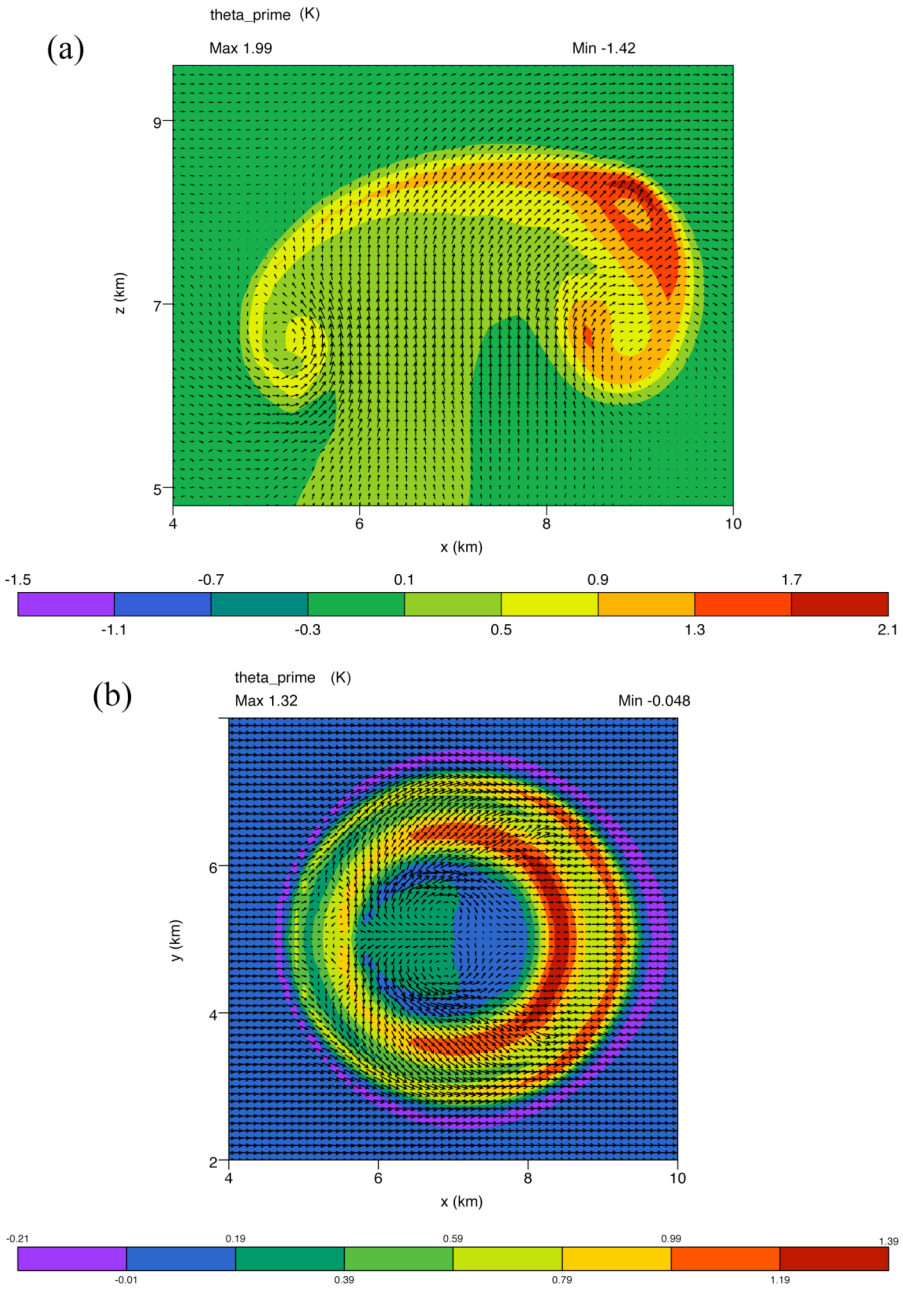


Figure D.3: Vertical (x-z) slice through center of thermal (a), and horizontal slice at height $z = 6.67\,\text{km}$ (b) at time $t = 14$ minutes. Perturbation potential temperature field (K) is plotted with velocity vectors superimposed.

causing the air to be deflected in order to pass around it. The rising thermal also acts to twist the horizontal mean-flow vorticity into the vertical as seen by the vortex dipole which straddles the y-direction center-line of the thermal at $x = 7\,\text{km}$.

This experiment shows that the model is capable of representing the 3D characteristics of a rising thermal in a sheared environment in the σ-coordinate domain. This feature is necessary for representing cloud dynamics when moisture is introduced to the model.

D.2 Amplifying 3D baroclinic wave in a β-channel

This is a synoptic-scale experiment to test the model's ability to represent the growth of a baroclinic wave. This is an important physical phenomenon which affects the general circulation of the atmosphere. Therefore, we are testing the potential of the dynamical core to be used in a global model.

The horizontal model domain is a β-channel in which the Coriolis parameter f varies in the y-direction by the relation

$$\beta = \frac{df}{dy}. \tag{D.3}$$

In the experiment, the values of β and f are set to values typical of the mid-latitudes. The y-domain is 8000 km in extent with walls at each boundary. The x-domain is 10000 km long with periodic boundary conditions. The model top is at 30 km. The model is initialized with a geostrophically balanced, zonally uniform zonal jet as shown in the y-z cross-section of Figure D.4. The potential temperature field is also initialized as zonally uniform except for a random perturbation in the lowest 2 layers of the model. Also, the model is initially in hydrostatic balance. The model is configured with 100 grid points in the x-direction ($\Delta x = 100$ km) and 80 grid points in the y-direction ($\Delta y = 100$ km). There are 30 model levels with $\Delta z = 1$ km.

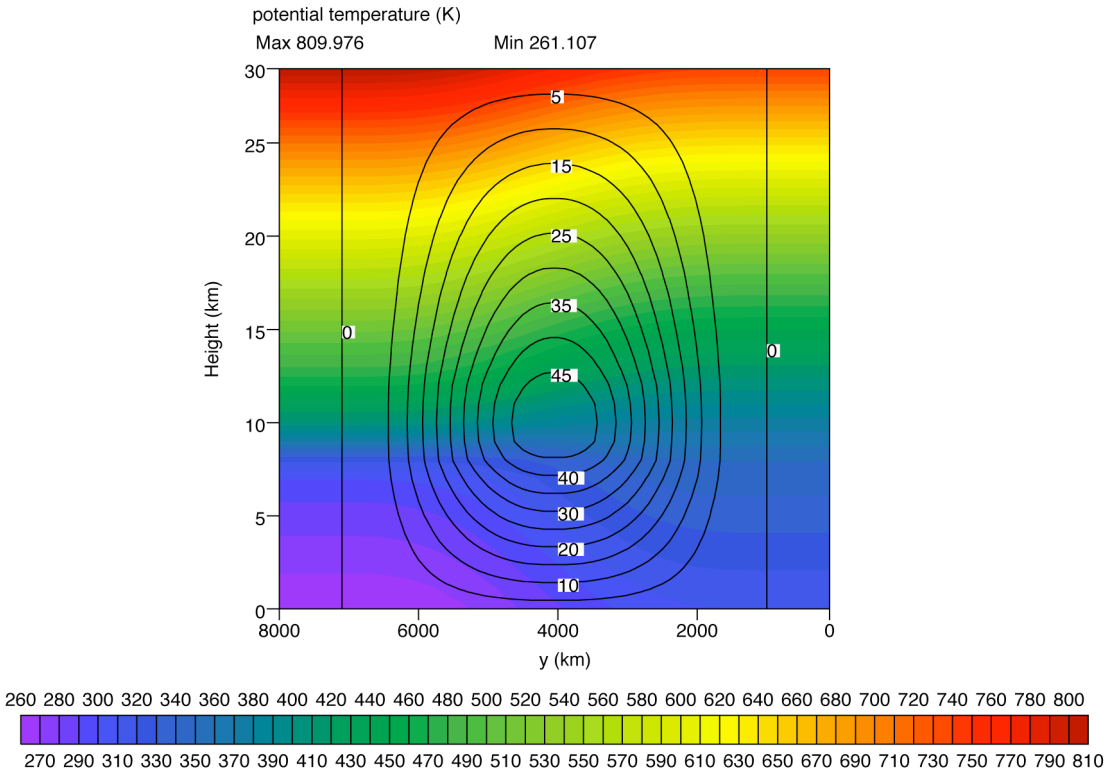


Figure D.4: Initial vertical profile of potential temperature (K) (colors) and zonal wind (m s^{-1}) (black contours) along the *y*-axis.

Figure D.5 shows the surface temperature and pressure at 14 days into the simulation. Here we see that the initial zonally-uniform, randomly perturbed temperature field has evolved into baroclinic cyclones as is expected. Sharp fronts have developed in association with the wave growth. These results are encouraging for the future development of the model in a global framework.

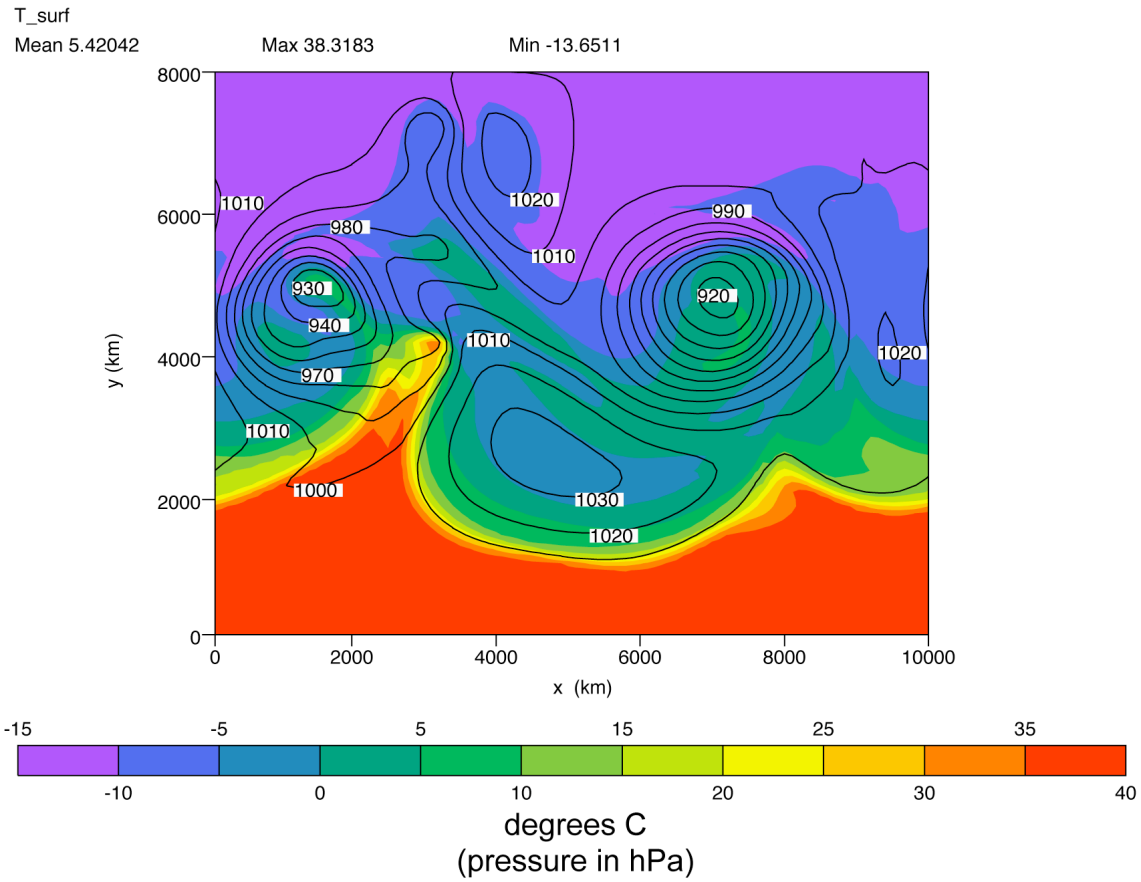


Figure D.5: Surface temperature field (degrees Celsius) (colors) and isobars (hPa) at 14 days into the simulation.

REFERENCES

Aanensen, C. J. M., 1965: Gales in Yorkshire in February 1962. *Geophys. Mem.,* **14,** 1-44.

Adcroft, A., C. Hill, and J. Marshall, 1997: Representation of topography by shaved cells in a height coordinate ocean model. *Mon. Wea. Rev.,* **125,** 2293-2315.

Alaka, M. A., Ed., 1960: *The Airflow over Mountains.* WMO Tech. Note 34, 135 pp.

Andrews, D. G., 1983: A finite-amplitude Eliassen-Palm theorem in isentropic coordinates. *J. Atmos. Sci.,* **40,** 1877-1883.

Arakawa, A., and V. Lamb, 1977: Computational design of the basic dynamical processes of the UCLA general circulation model. *Methods in Computational Physics,* Vol. 17, J. Chang, Ed., Academic Press, 173-265.

Arakawa, A., and V. Lamb, 1981: A potential enstrophy and energy conserving scheme for the shallow water equations. *Mon. Wea. Rev.,* **109,** 18-36.

Arakawa, A., and M. J. Suarez, 1983: Vertical differencing of the primitive equations in sigma coordinates. *Mon. Wea. Rev.,* **111,** 34-45.

Arakawa, A., and S. Moorthi, 1988: Baroclinic instability in vertically discrete systems. *J. Atmos. Sci.,* **45,** 1688-1707.

Arakawa, A., and C. S. Konor, 1996: Vertical differencing of the primitive equations based on the Charney-Phillips grid in hybrid σ-θ vertical coordinates. *Mon. Wea. Rev.,* **124,** 511-528.

Arakawa, S., 1969: Climatological and dynamical studies on local strong winds, mainly in Hokkaido, Japan. *Geophys. Mag.,* **34,** 359-425.

Bannon, P. R., 1995: Hydrostatic adjustment: Lamb's problem. *J. Atmos. Sci.,* **52,** 1743-1752.

Benjamin, S. G., G. A. Grell, J. M. Brown, and T. G. Smirnova, 2004: Mesoscale weather prediction with the RUC hybrid isentropic-terrain-following coordinate model. *Mon. Wea. Rev.,* **132,** 473-494.

Bleck, R., 1978a: On the use of hybrid vertical coordinates in numerical weather prediction models. *Mon. Wea. Rev.,* **106,** 1233-1244.

Bleck, R., 1978b: Finite difference equations in generalized vertical coordinates. Part I: Total energy conservation. *Beitr. Phys. Atmos.,* **51,** 360-372.

Bleck, R., 1979: Finite difference equations in generalized vertical coordinates. Part II: Potential vorticity conservation. *Beitr. Phys. Atmos.,* **52,** 95-105.

Bleck, R., 1984: An isentropic coordinate model suitable for lee cyclogenesis simulation. *Riv. Meteor. Aeronaut.,* **43,** 189-194.

Bleck, R., and S. Benjamin, 1993: Regional weather prediction with a model combining terrain-following and isentropic coordinates. Part I: Model Description. *Mon. Wea. Rev.,* **121,** 1770-1785.

Bryan, G. H., and J. M. Fritsch, 2002: Benchmark simulation for moist nonhydrostatic numerical models. *Mon. Wea. Rev.,* **130,** 2917-2928.

Charney, J. G., and N. A. Phillips, 1953: Numerical integration of the quasi-geostrophic equations for barotropic and simple baroclinic flows. *J. Meteor.,* **10,** 71-99.

Davies, T., M. J. P. Cullen, A. J. Malcolm, M. H. Mawson, A. Staniforth, A. A. White, and N. Wood, 2005: A new dynamical core for the Met Office's global and regional modelling of the atmosphere. *Q. J. R. Meteorol. Soc.,* **131,** 1759-1782.

Deaven, D. G., 1976: A solution on boundary problems in isentropic coordinate models. *J. Atmos. Sci.,* **33,** 1702-1713.

Dietachmayer, G. S., and K. K. Droegemeier, 1992: Application of continuous dynamic grid adaption techniques to meteorological modeling. Part I: Basic formulation and accuracy. *Mon. Wea. Rev.,* **120,** 1675-1706

Dowling, T. E., M. E. Bradley, E. Colón, J. Kramer, R. P. LeBeau, G. C. H. Lee, T. I. Mattox, R. Morales-Juberías, C. J. Palotai, V. K. Parimi, A. P. Showman, 2006: The EPIC atmospheric model with an isentropic/terrain-following hybrid vertical coordinate. *Icarus,* **182,** 259-273.

Doyle, J. D., D. R. Durran, C. Chen, B. A. Colle, M. Georgelin, V. Grubisic, W. R. Hsu, C. Y. Huang, D. Landau, Y. L. Lin, G. S. Poulus, W. Y. Sun, D. B. Weber, M. G. Wurtele, and M. Xue, 2000: An intercomparison of model-predicted wave breaking for the 11 January 1972 Boulder windstorm. *Mon. Wea. Rev.,* **128,** 901-914.

Durran, D. R., 1991: The third-order Adams-Bashforth method: an attractive alternative to leapfrog time differencing. *Mon. Wea. Rev.,* **119,** 702-720.

Durran, D. R., and J. B. Klemp, 1983: A compressible model for the simulation of moist mountain waves. *Mon. Wea. Rev.,* **111,** 2341-2361.

Eckart, C., 1960: *Hydrodynamics of Oceans and Atmospheres.* Pergamon, 290 pp.

Eliassen, A., 1949: The quasi-static equations of motion with pressure as independent variable. *Geofys. Publ.,* **XVII,** 3-44.

Eliassen, A., 1962: On the use of a material layer model of the atmosphere in numerical prediction. *Proc. Int. Symp. Numerical Weather Prediction.* Tokyo, Japan Meteor. Agency, 207-211.

Eliassen, A., and E. Kleinschmidt Jr., 1957: *Dynamic Meteorology.* Vol, 48, *Handbuch der Physik: Geophysik II,* Springer-Verlag, 1-154.

Eliassen, A., and E. Palm, 1961: On the transfer of energy in stationary mountain waves. *Geofys. Publ.,* **22,** No. 3, 1-23.

Eliassen, A., and E. Raustein, 1968: A numerical integration experiment with a model atmosphere based on isentropic coordinates. *Meteorologiske Annaler,* **5**(2)**,** 45-63.

Eliassen, A., and E. Raustein, 1970: A numerical integration experiment with a six-level atmospheric model with isentropic information surface. *Meteorologiske Annaler,* **5**(11)**,** 429-449.

Ertel, H., 1942: Ein neuer hydrodynamischer Wirbelsatz. *Meteorologische Zeitschrift,* **59,** 271-281.

Friend, A. L., D. Djuric, and K. C. Brundidge, 1977: A combination of isentropic and sigma coordinates in numerical weather prediction. *Beitr. Phys. Atmos.,* **50,** 290-295.

Gal-Chen, T. and R. C. J. Somerville, 1975: On the use of a coordinate transformation for the solution of the Navier-Stokes equations. *J. Comput. Phys.,* **17,** 209-228.

He, Z., 2002: A non-hydrostatic model with a generalized vertical coordinate. Ph.D. thesis, University of Miami, 99 pp.

Heikes, R., C. Konor, and D. A. Randall, 2006: A geodesic atmospheric model with a quasi-Lagrangian vertical coordinate. *J. Phys.: Conf. Ser.,* **46,** 351-355.

Hirt, C. W., A. A. Amsden, and J. L. Cook, 1974: An arbitrary Lagrangian-Eulerian computing method for all flow speeds. *J. Comput. Phys.,* **14,** 227-253.

Holton, J. R., 2004: *An Introduction to Dynamic Meteorology,* 4th ed., Elsevier Academic Press, 535 pp.

Hoskins, B. J., M. E. McIntyre, and A. W. Robertson, 1985: On the use and significance of isentropic potential vorticity maps. *Quart. J. Roy. Meteor. Soc.,* **111,** 877-946.

Houghton, D. D., and E. Isaacson, 1968: Mountain Winds. *Stud. Numer. Anal.* 2, 21-52.

Hsu, Y.-J. G., and A. Arakawa, 1990: Numerical modeling of the atmosphere with an isentropic vertical coordinate. *Mon. Wea. Rev.,* **118,** 1933-1959.

Kasahara, A., 1974: Various vertical coordinate systems used for numerical weather prediction. *Mon. Wea. Rev.,* **102,** 509-522.

Kim, Y.-J., 1992: Numerical simulation and parameterization of orographic gravity waves. Ph.D. dissertation, University of California, Los Angeles, 254 pp.

Kim, Y.-J., and A. Arakawa, 1995: Improvement of orographic gravity wave parameterization using a mesoscale gravity wave model. *J. Atmos. Sci.,* **52,** 1875-1902.

Klemp, J. B., and D. K. Lilly, 1975: The dynamics of wave-induced downslope winds. *J. Atmos. Sci.,* **32,** 320-339.

Klemp, J. B., and D. K. Lilly, 1978: Numerical simulation of hydrostatic mountain waves. *J. Atmos. Sci.,* **35,** 78-107.

Konor, C. S., and A. Arakawa, 1997: Design of an atmospheric model based on a generalized vertical coordinate. *Mon. Wea. Rev.,* **125,** 1649-1673.

Konor, C. S., and A. Arakawa, 2000: Choice of a vertical grid in incorporating condensation heating into an isentropic vertical coordinate model. *Mon. Wea. Rev.,* **128,** 3901-3910.

Kuettner, J., 1959: The rotor flow in the lee of mountains. GRD Res. Notes No. 6, AFCRL, Bedford, Mass.

Laprise, R., 1992: The Euler equations of motion with hydrostatic pressure as an independent variable. *Mon. Wea. Rev.,* **120,** 197-207.

Laprise, R., and W. R. Peltier, 1989a: The linear stability of nonlinear mountain waves: Implications for the understanding of severe downslope windstorms. *J. Atmos. Sci.,* **46,** 545-564.

Laprise, R., and W. R. Peltier, 1989b: The structure and energetics of transient eddies in a numerical simulation of breaking mountain waves. *J. Atmos. Sci.,* **46,** 565-585.

Laprise, R., and W. R. Peltier, 1989c: On the structural characteristics of steady finite-amplitude mountain waves over bell-shaped topography. *J. Atmos. Sci.,* **46,** 586-595.

Lilly, D. K., and E. J. Zipser, 1972: The front range windstorm of 11 January 1972 – a meteorological narrative. *Weatherwise,* **25,** 56-63.

Long, R. R., 1953: Some aspects of the flow of stratified fluids. I: A theoretical investigation. *Tellus,* **5,** 42-58.

Lorenz, E. N., 1955: Available potential energy and the maintenance of the general circulation. *Tellus,* **7,** 157-167.

Lorenz, E. N., 1960: Energy and numerical weather prediction. *Tellus,* **12,** 364-373.

Mesinger, F., and Z. I. Janjic, 1985: Problems and numerical methods of the incorporation of mountains in atmospheric models. *Large-Scale Computations in Fluid Mechanics,* Part 2. Lec. Appl. Math., Vol. 22, Amer. Math. Soc., 81-120.

Montgomery, R. B., 1937: A suggested method for representing gradient flow in isentropic surfaces. *Bull. Amer. Meteor. Soc.,* **18,** 210-212.

Peltier, W. R., and T. L. Clark, 1979: The evolution and stability of finite-amplitude mountain waves. Part II: Surface wave drag and severe downslope windstorms. *J. Atmos. Sci.,* **36,** 1498-1529.

Phillips, N. A., 1957: A coordinate system having some special advantages for numerical forecasting. *J. Meteor.,* **14,** 184-185.

Queney, P., 1948: The problem of airflow over mountains: A summary of theoretical studies. *Bull. Amer. Meteor. Soc.,* **29,** 16-26.

Randall, D. A., 1994: Geostrophic adjustment and the finite-difference shallow-water equations. *Mon. Wea. Rev.,* **122,** 1371-1377.

Randall, D. A., Ed., 2000: *General Circulation Model Development: Past, Present and Future.* Academic Press, 807 pp.

Randall, D. A., R. Heikes, and T. D. Ringler, 2000: Global atmospheric modeling using a geodesic grid with an isentropic vertical coordinate. In Randall, D. A., Ed., *General Circulation Model Development: Past, Present and Future*, Chapter 17, Academic Press, pp. 509-538.

Richardson, L. F., 1922: *Weather Prediction by Numerical Process.* Cambridge University Press, 236 pp.

Rossby, C.-G., 1938: On temperature changes in the stratosphere resulting from shrinking and stretching. *Beitr. Phys. D. freien Atmos.,* **24,** 53-59.

Rossby, C.-G., 1940: Planetary flow patterns in the atmosphere. *Quart. J. Roy. Meteor. Soc.,* **66** (Suppl.), 68-87.

Schär, C., D. Leuenberger, O. Fuhrer, D. Lüthi, and C. Girard, 2002: A new terrain-following vertical coordinate formulation for atmospheric prediction models. *Mon. Wea. Rev.,* **130,** 2459-2480.

Scinocca, J. F., and W. R. Peltier, 1989: Pulsating downslope windstorms. *J. Atmos. Sci.,* **46,** 2885-2914.

Scorer, R. S., and H. Klieforth, 1959: Theory of mountain waves of large amplitude. *Quart. J. Roy. Meteor. Soc.,* **85,** 131-143.

Shapiro, M. A., 1975: Simulation of upper-level frontogenesis with a 20-level isentropic coordinate primitive equation model. *Mon. Wea. Rev.,* **103,** 591-604.

Simmons, A. J., and D. M. Burridge, 1981: An energy and angular-momentum conserving vertical finite-difference scheme and hybrid vertical coordinates. *Mon. Wea. Rev.,* **109,** 758-766.

Skamarock, W. C., 1998: A hybrid-coordinate nonhydrostatic model. Preprints, *12th Conf. on Numerical Weather Prediction,* Phoenix, AZ, Amer. Meteor. Soc., 232-235.

Skamarock, W. C., J. B. Klemp, J. Dudhia, D. O. Gill, D. M. Barker, W. Wang, and J. G. Powers, 2005: A Description of the Advanced Research WRF version 2. NCAR Tech. Note TN-468+STR, 88pp.

Smagorinsky, J., 1963: General circulation experiments with the primitive equations. I: The basic experiment. *Mon. Wea. Rev.,* **91,** 99-164.

Smith, R. B., 1979: The influence of mountains on the atmosphere. *Advances in Geophysics,* Vol. 21, Academic Press, 87-230.

Starr, V. P., 1945: A quasi-Lagrangian system of hydrodynamical equations. *J. Meteor.,* **2,** 227-237.

Stull, R. B., 1988: *An Introduction to Boundary Layer Meteorology.* Kluwer Academic, 666 pp.

Sutcliffe, R. C., 1947: A contribution to the problem of development. *Quart. J. Roy. Meteor. Soc.,* **73,** 370-383.

Takacs, L. L., 1985: A two-step scheme for the advection equation with minimized dissipation and dispersion errors. *Mon. Wea. Rev.,* **113,** 1050-1065.

Thuburn, J., 2006: Vertical discretizations giving optimal representation of normal modes: Sensitivity to the form of the pressure-gradient term. *Quart. J. Roy. Meteor. Soc.,* **132,** 2809-2825.

Thuburn, J., and T. J. Woollings, 2005: Vertical discretizations for compressible Euler equation atmospheric models giving optimal representation of normal modes. *J. Comput. Phys.,* **203,** 386-404.

Tokioka, T., 1978: Some considerations on vertical differencing. *J. Meteor. Soc. Japan,* **56,** 98-111.

Toy, M. D., and D. A. Randall, 2007: Comment on the article "Vertical discretizations for compressible Euler equation atmospheric models giving optimal representation of normal modes" by Thuburn and Woollings. *J. Comput. Phys.,* **223,** 82-88.

Uccellini, L. W., D. R. Johnson, and R. E. Schlesinger, 1979: An isentropic and sigma coordinate hybrid numerical model: Model development and some initial tests. *J. Atmos. Sci.,* **36,** 390-414.

Woollings, T. J., 2004: Entropy and potential vorticity in dynamical core atmosphere models. Ph.D. thesis, University of Reading, U.K., 193 pp.

Zangl, G., 2007: An adaptive vertical coordinate formulation for a nonhydrostatic model with flux-form equations. *Mon. Wea. Rev.,* **135,** 228-239.

Zhu, Z., J. Thuburn, B. J. Hoskins, and P. H. Haynes, 1992: A vertical finite-difference scheme based on a hybrid σ-θ-p coordinate. *Mon. Wea. Rev.,* **120,** 851-862.